Universidad de Granada

Tesis doctoral

Seismic response of new reinforced concrete structures: conventional versus innovative systems using hysteretic dampers

Respuesta sísmica de estructuras nuevas de hormigón armado: soluciones convencionales frente a sistemas innovativos de disipación pasiva de energía

David Escolano Margarit

Departamento de Mecánica de Estructuras

e Ingeniería Hidráulica

Programa oficial de Posgrado en EstructuraS

Director: Dr. Amadeo Benavent Climent

Septiembre 2013

Editor: Editorial de la Universidad de Granada
Autor: David Escolano Margarit
D.L.: GR 720-2014
ISBN: 978-84-9028-893-1

Editor: Editorial de la Universidad de Granada
Autor:
D.L.: En trámite
ISBN: En trámite

Compromiso de respeto de derechos de autor

El doctorando David Escolano Margarit y el director de la tesis Amadeo Benavent Climent, garantizamos, al firmar esta tesis doctoral, que el trabajo ha sido realizado por el doctorando bajo la dirección del director de la tesis y hasta donde nuestro conocimiento alcanza, en la realización del trabajo, se han respetado los derechos de otros autores a ser citados, cuando se han utilizado sus resultados o publicaciones.

En Granada Octubre de 2013

El director de la tesis	El doctorando
Amadeo Benavent Climent	David Escolano Margarit

Agradecimientos

En primer lugar quiero agradecer a mi mujer Mª Carmen por acompañarme incondicionalmente desde el principio de este camino incierto que supone la carrera investigadora.

A mi director de tesis D. Amadeo Benavent Climent por confiar en mi para formar parte de su equipo de investigación desde el inicio del Laboratorio de Ingeniería de Estructuras de la Universidad de Granada.

Al profesor Santiago Pujol por recibirme en la Universidad de Purdue y compartir generosamente su investigación y conocimiento.

A mi padres Pepe y Mª Victoria, a mi hermana Mª Victoria, a mi sobrina Victoria y a toda mi familia.

Al Ministerio de Ciencia e Innovación sin cuya financiación económica a través de la ayuda Predoctoral de Formación de Personal Investigador BES-2009-021744 vinculada al proyecto de investigación BIA2008-00050 no hubiera podido realizarse esta tesis.

Resumen

Los elevados daños materiales provocados por los terremotos de Loma Prieta (1987) , Northridge (1994) y de Hanshin ocurridos en Estados Unidos y en Japón, pusieron de manifiesto que el proyecto sismorresistente basado exclusivamente en evitar la pérdida de vidas humanas era insuficiente y que era necesario un cambio de paradigma que considerase también y de forma explícita el control del daño. Las grandes pérdidas económicas debidas a terremotos de intensidad relativamente moderada, mostraron la necesidad de una metodología para el proyecto de los edificios basados en el comportamiento de las estructuras durante los terremotos. Después del terremoto de Northridge de 1994 la "Structural Egineering Association of California (SEAOC)" desarrolló un informe con recomendaciones para el proyecto basado en las prestaciones que se llamó "Performance Based Seismic Engineering" (PBSE) Proyecto Sismorresistente Basado en Prestaciones [85].

> "La ingeniería sísmica basada en las prestaciones enmarca todas las actividades necesarias para proyectar y construir completamente los edificios de manera que puedan resistir terremotos de distinta severidad dentro de unos niveles de daño predeterminados"

Para cumplir los objetivos marcados por la filosofía de PBSE los proyectistas necesitan poder predecir el comportamiento sísmico de las estructuras frente a diferentes niveles de intensidad sísmica. Pero esta tarea esa sujeta a numerosas fuentes de incertidumbre. En primer lugar es necesario poder identificar y definir de manera fiable la intensidad sísmica de los terremtos esperables en cada lugar con una determianda probabilidad (peligrosidad sísmica). Es fundamental también conocer la capacidad resistente, de deformación y de disipación de energía de los elementos estructurales especialmente en el rango no lineal y cuando se someten a cargas cíclicas de tipo dinámico. También es necesario identificar y cuantificar los parámetros que mejor caracterizan el daño en los elementos estructurales y sus criterios de aceptabilidad. Y finalmente es muy importante el uso de metodologías basadas en el comportamiento de las estructuras frente al sismo para poder proyectar las estructuras y comprobar si los parámetros de demanda se han excedido para un determinado nivel de intensidad sísmica. En este contexto, es absolutamente necesario disponer de datos experimentales que nos permitan conocer mejor el comportamiento de los elementos estructurales en el rango no lineal y disponer de información suficiente para poder establecer los límites de aceptabilidad en cada nivel de daño. Se necesitan nuevas metodologías de proyecto basadas en las prestaciones, en lugar de en la resistencia, para poder preparar de una manera más eficaz a las estructuras frente a los sismos. El uso de nuevas tecnologías como son los disipadores de energía, ha demostrado ser también una estrategia eficaz para proyectar estructuras de nueva planta y rehabilitar estructuras para que puedan alcanzar los objetivos de comportamiento.

Entre todos los posibles enfoques metodológicos que se pueden plantear para materializar la filosofía del proyecto basado en prestaciones, los métodos basados en el balance energético de Housner-Akiyama [3, 51] han demostrado ser muy eficaces especialmente en el proyecto de estructuras con disipadores de energía y se han incluido recientemente (2005) en la norma sismorresistente japonesa [63]. Comparada con otras metodologías de proyecto como las basadas en desplazamientos[80, 76, 67], las basadas en la energía pueden tener en cuenta el daño acumulado provocado por el terremoto. A pesar de que son unas metodologías prometedoras, existe poca información acerca de la capacidad de disipación de energía de los elementos estructurales, especialmente en elementos de hormigón armado [86, 87, 12, 14, 33, 72]. Los ensayos de estructuras en laboratorio con mesa sísmica y los ensayos estáticos nos proporcionan información de enorme valor para entender la respuesta de la estructura durante un terremoto, para definir los parámetros de respuesta y para analizar los distintos niveles de daño que experimenta una estructura bajo distintas intensidades sísmicas.

Esta investigación busca contribuir a un mejor entendimiento del comportamiento sísmico de soluciones sismorresistentes tradicionales como son los pórticos y las pantallas de hormigón armado. El comportamiento de este tipo de estructuras y de sus elementos estructurales se obtiene a través de ensayos dinámicos y estáticos llevados a cabo en las universidades de Granada y Purdue respectivamente. Para valorar mejor dicho comportamiento, éste se compara con el de las de las estructuras porticadas equipadas con disipadores de energía mediante estudios numéricos con modelos de elementos finitos. Finalmente, se evalúa la idoneidad y efectividad de diferentes herramientas de cálculo basadas en el método de empuje incremental en la predicción del comportamiento de estructuras con disipadores de energía.

Objetivos y metodología

Esta tesis persigue los siguientes objetivos principales:

1. Investigar experimentalmente el comportamiento sísmico de las estructuras porticadas convencionales de hormigón armado con mecanismo de colapso del tipo “columna fuerte-viga débil”. Evaluar la precisión de las expresiones de rotación de la parte 3 del Eurocódigo 8 y cuantificar la capacidad última de disipación de energía de elementos estructurales de hormigón armado mediante ensayos dinámicos con mesa sísmica.
2. Evaluar experimentalmente la respuesta de muros pantalla dúctiles a escala real de hormigón armado a través de dos ensayos estáticos y comparar el comportamiento histerético de las pantallas dúctiles de hormigón armado con el comportamiento de disipadores de energía histeréticos.
3. Comparar la respuesta sísmica de las estructuras porticadas convencionales de hormigón armado, diseñadas siguiendo la filosofía de proyecto “columna fuerte-viga débil” y con criterios de proyecto por capacidad, con la respuesta sísmica de las estructuras porticadas de hormigón armado con disipadores de energía histeréticos a través de los resultados de análisis dinámicos directos con modelos de elementos finitos.

4. Evaluar, sobre la base de resultados de ensayos dinámicos con mesa sísmica, la idoneidad y la precisón de tres procedimientos estáticos no lineales (el Método de los Coeficientes de desplazamiento, el Método del Espectro de Capacidad y el Método N2) de reciente incorporación en las normativas sísmicas, para predecir la respuesta de estructuras porticadas con disipadores de energía histeréticos.

La metodología aplicada para conseguir estos objetivos tiene dos enfoques. Una parte experimental consistente en ensayos estáticos y ensayos dínamicos con mesa sísmica y otra parte numérica consistente en realizar análisis estáticos no lineales de empuje incremental y análisis dinámicos directos.

Organización y principales conclusiones.

Esta tesis se divide en 6 capítulos independientes que desarrollan de una manera mas exhaustiva las conclusiones obtenidas en esta investigación:

En el capítulo 1 se revisan los conceptos en los que se fundamenta esta tesis y se enumeran los objetivos principales que se persiguen.

En el capítulo 2 se investiga el comportamiento sísmico de una estructura porticada de hormigón armado proyectada para desarrollar un mecanismo de colapso del tipo “columna fuerte-viga débil” y con criterios de proyecto por capacidad. Se realizaron cuatro ensayos dinámicos sobre una estrucura a escala 2/5 proyectada según la actual norma sismorresistente española NSCE-02, para cumplir con los parámetros de diseño de la ciudad de Granada. El nivel de peligrosidad sísmica en cada ensayo era el característico de terremotos “muy frecuentes”, “frecuentes”, “raros” y “muy raros” según la escala definida por la SEAOC [85]. La respuesta de la estructura se evalúo en términos de diversos parámetros de demanda e índices de daño, que muestran que la estructura se comportó con los niveles de daño siguientes: entre “ocupación inmediata” y “seguridad para las vidas” para el terremoto “frecuente”, “seguridad para las vidas” para el terremoto “raro” y “colapso” para el terremoto “muy raro”. La estructura se comportó tal y como se espera en la normativa NSCE-02 para el terremoto “raro” (asociado a un periodo de retorno de 500 años). Sin embargo colapsó para el terremoto “muy raro” que es el terremoto de máxima intensidad esperable en la zona. Un estudio de la respuesta obtenida mediante estos ensayos dinámicos de los elementos estructurales a nivel local de rótula plástica muestra que las fórmulas del Eurocódigo 8 parte 3 predicen con mucha exactitud la capacidad de rotacion última de las vigas y la columnas de hormigón armado bajo cargas cíclicas. Los valores obtenidos del índice de daño de Park y Ang muestran que se trata de un índice muy adecuado para cuantificar el nivel de daño en de los elementos de hormigón armado sometidos a flexión.

En el capítulo 3 se investiga el comportamiento histerético y la capacidad última de disipación de energía de muros pantalla de hormigón armado y se compara con el comportamiento de un disipador de energía histerético equivalente. Se ensayaron dos muros pantalla de hormigón armado a escala real bajo cargas estáticas de tipo cíclico hasta su rotura. Ambas pantallas tenían un refuerzo a flexión idéntico, diferenciándose únicamente en la inclusión de estribos de confinamiento en los elementos de borde de una de ellas. Los resultados de los ensayos muestran que ambas pantallas tuvieron un comportamiento prácticamente igual hasta el inicio de la fluencia. En cambio la capacidad última de la pantalla con refuerzo de confinamiento fue mucho mayor en términos de desplazamientos últimos y de capacidad de disipación de energía. Los resultados de las deformaciones unitarias obtenidas experimentalmente, mediante sensores externos, muestran que existe una gran diferencia en la distribución de las tensiones en los extremos comprimido y traccionado de las pantallas. La comparación del comportamiento histerético de la pantalla con confinamiento y el de un disipador de energía histerético equivalente, revela que la capacidad sismorresistente del disipador de energía es mucho mayor en términos cantidad de energia disipada y capacidad de deformación plástica.

En el capítulo 4 se compara el comportamiento sismorresistente de estructuras con pórticos de hormigón armado equipadas con disipadores de energía histeréticos con el de las estructuras con pórticos sismorresistentes de hormigón armado proyectados con la filosofía de proyecto “viga débil-columna fuerte”. Para ello se llevan a cabo numerosos análisis dinámicos directos con modelos numéricos de elementos finitos. Se proyectaron dos grupos de estructuras de 3 y 6 plantas de altura. El primer grupo de prototipos, estructuras con pórticos de HA sismorresistentes, se proyectó para cumplir con las especificaciones de la norma sismorresistente española NSCE-02 para resistir el terremoto de 500 años de periodo de retorno esperable en la ciudad de Granada. El segundo grupo de prototipos, estructuras con pórticos de HA (proyectados para cargas gravitatorias exclusivamente) y disipadores de energía histeréticos, se diseña para tener el mismo cortante basal, $Q_{y1,}$ requerido por los prototipos del primer grupo. La comparación se realizó a nivel de estructura global y a nivel local de rótula plástica. A nivel global se estudiaron parámetros que cuantifican el daño como son el desplazamiento entre planta id y el ratio de deformación plástica acumulada η. A nivel local se estudió la demanda de rotación en las rótulas plásticas, el índice de daño de Darwin y Nmai Di y el conocido índice de daño de Park y Ang $DI_{P\&A}$. Los resultados obtenidos en los análisis dinámicos directos sugieren que los prototipos de estructuras de pórticos de HA equipados con disipadores histeréticos tuvieron un mejor comportamiento sismorresistente. La comparación de los resultados de la respuesta a nivel local (i.e. demanda de rotación y los valores de los índices Di y $DI_{P\&A}$) obtenidos en los análisis dinámicos directos con los resultados experimentales para el ensayo de igual intensidad sísmica descrito en el capítulo 2, muestra una muy buena correlación.

En el capítulo 5 se estudia la idoneidad y la precisión de tres procedimientos estáticos no lineales para predecir la respuesta de estructuras con disipadores histeréticos. Los procedimientos estudiados son el Método de los Coeficientes de Desplazamiento (DCM) y el Método del Espectro de Capacidad (CSM) del código FEMA-440 y el Método N2 del eurocódigo 8. La respuesta sismorresistente se obtuvo para tres niveles de comportamiento estructural definidos en el FEMA 356 “ocupación inmediata”, “seguridad para las vidas” y “seguridad para las vidas limitada”. La comparación de la predicción obtenida mediante los procedimientos estáticos no linelaes y los resultados experimentales muestra que los tres métodos predicen de una manera aceptable la máxima respuesta, en términos de desplazamiento y cortante máximos, de la estructura con disipadores histeréticos. La comparativa a su vez entre las predicciones dadas por los distintos métodos muestra que el CSM subestimó la predicción de la máxima respuesta mientras que el DCM y el N2 la sobreestimaron en la mayoría de los casos.

En el capítulo 6 se resumen y recopilan las principales conclusiones obtenidas en esta investigación.

Abstract

The great economic losses suffered after several earthquakes in the last two decades showed a need for new design and construction procedures based in the performance of structures during earthquakes. But there are several sources of uncertainties to this end. Firstly the identification and definition of the potential hazard that may exist at the site. Furthermore, the knowledge of strength, deformations and energy dissipation capacities of the structural elements and the identification and quantification of the engineering demand parameters to define damage in structural elements. And finally the use of design approaches to accomplish the definition of the structural system with predictable seismic performance and the acceptability analysis procedures to verify if the performance levels are exceeded. This research aims to contribute to a better understanding of the seismic performance of RC structures through shaking table and quasi-static tests and numerical studies with non-linear finite element models.

This thesis is divided in 6 chapters. Chapter 1 reviews the framework and the main concepts in which this thesis is supported. Chapter 2 investigates the seismic performance of a "strong column-weak beam" RC framed structure in terms of several damage indexes. The study is based on the experimental results of a scaled substructure representing a three story building designed accordingly to current Spanish code and tested with shake table at the University of Granada. Chapter 3 investigates the hysteretic behaviour and ultimate energy dissipation capacity of conventional RC ductile walls, and particularly the effect of the inclusion of confinement reinforcement through quasi-static tests. Chapter 4 compares the seismic behaviour of two structural systems. On the one hand, the conventional "strong column-weak beam" RC frame . On the other the innovative stiff-flexible mixed system consisting of a RC frame equipped with hysteretic dampers. Chapter 5 studies the appropriateness and accuracy of three conventional non-linear Static Procedures (NSP) to predict the response of structures with hysteretic dampers. The NSP studied are the Displacement Coefficient Method (DCM) and Capacity Spectrum Method (CSM) from FEMA-440 and the N2 method form Eurocode 8. The prediction obtained with these methods is compared to the results of several shake table tests.

Contents

List of Figures

List of Tables

1. Introduction

After the Loma Prieta (1987), Northridge (1994) and Hanshin (1995) earthquakes that occurred in USA and Japan, the earthquake engineering community realized that the seismic design centered exclusively in the avoiding potential loss of life was insufficient. The high economic losses even for moderate earthquakes showed a need for new design procedures based in the performance of structures during earthquakes. From 1992 to 1993 the vision 2000 committee developed a preliminary framework for the next generation of performance-based building codes, with the goal of defining a new code before the 2000. But after the 1994 northridge earthquake, the Structural Engineering Association of California (SEAOC) developed a report with the recommendations for a performance based design and they referred to them as Performance Based Seismic Engineering (PBSE)[85].

> “Performance Based Seismic Engineering involves the complete design and construction support activities necessary to permit buildings to be constructed that will resist earthquakes of different severity within specified limiting levels of damage”

To fulfill the goals of the PBSE, the professional engineer needs the ability to predict the seismic performance of the structures at different seismic hazard scenarios. But there are several sources of uncertainties to this end. Firstly the identification and definition of the potential hazard that may exist at the site. Secondly the use of accurate methods and models to analyze the structural response during earthquakes, especially in the non-linear range. Thirdly the knowledge about the strength, the deformation and the energy dissipation capacity of the structural elements under dynamic loading. Fourthly the identification and quantification of the engineering demand parameters to define the damage in structural elements and its acceptability criteria. And finally, the use of design approaches to accomplish the definition of the structural system with predictable seismic performance and the acceptability analysis procedures to verify if the performance levels are exceed. Consequently there is a need for experimental data to better know the reliability of structural elements in which inelastic deformations are expected as well as information enough to establish the limiting values for each performance level. Furthermore new design methodologies based on the performance of the building rather than strength are also necessary to better prepare structures against earthquakes. Likewise, the use of new technologies as the passive energy dissipating systems can be also an alternative for the structural seismic resistant design of new buildings and rehabilitation of existing structures to achieve the performance objectives.

Among all possible performance based design approaches, the energy based methodologies have been proven as reliable tools for design and assessment of new and existing structures [3, 56, 94, 57, 4, 30, 88, 11, 17, 91, 92] and have been recently included in the Japanese building code [63].

Compared to other procedures as displacement based design [80, 76, 67], the energy based approach can take into account the damage potential of the earthquake along its duration, including the effect of cyclic response on structural elements. Although it is a promising methodology there is limited information about the energy dissipation capacity of structural elements, especially in reinforced concrete structural elements [86, 87, 12, 14, 33, 72]. The laboratory studies with shaking table and quasi-static tests help us providing realistic experimental data to assess the engineering response parameters and to define the structural performance levels for different seismic hazard levels.

This research aims to contribute to a better understanding of the seismic performance of traditional seismic resistant structures as the RC frames and RC structural walls (through shake table and quasi-static tests done at the University of Granada and Purdue University respectively) and compare their performance with that of structures with energy dissipating devices. This comparison is done by means of numerical studies with non-linear finite element models. Further, the suitability of methodologies based in pushover analysis, commonly used in PBSE, are evaluated as a design tool for structures equipped with hysteretic dampers.

1.1. Conventional and innovative strategies for earthquake resistant structures.

The seismic resistant structures can be classified on the basis of how the energy input is distributed in two groups:

1. Energy dispersing structures: In this group the energy is distributed among the structural elements of the whole structure. (i.e. beams, columns, shear walls,...) The strategies used in this group can be also considered as conventional or traditional solutions.
2. Energy concentration structures: In this group the energy is intentionally dissipated and concentrated in precise elements especially designed to this end. Within this group several types of solutions can be distinguished depending on where the energy is dissipated: i) base isolated structures ii) Structures with active control systems and iii) Flexible-stiff mixed structures. This group of structures are the new and innovative solutions on the seismic design.

1.1.1. Strong column weak beam structures. Conventional RC moment resisting frames.

The design of buildings with energy dispersion is based in two main objectives: 1) To provide to the structure a sufficient strength to behave in the elastic range for the earthquake with a return period similar to the life of the building; 2) To design the building to endure inelastic deformations without compromising human life for the earthquakes of greater return period. These two fundamental guidelines require from the structure to be able to resist the gravitational loads and a higher lateral strength to resist the earthquake action in the first case scenario. Further, the structure must dissipate the energy introduced by an earthquake, by means of inelastic deformation of the structural elements, in the second case scenario. At the design phase, these goals are accomplished by using the ductility reduction factor $R_\mu - q - \mu$, which reduce the lateral force demand and hence the strength of the structural elements. But this reduction also requires a thoughtful design of the global structure to avoid damage concentration and the correct detailing of the structural elements to ensure their energy dissipation and ductility capacity, especially at the plastic hinge regions where the majority inelastic deformations are expected.

One of the oldest and most common structural designs based in these principles are the strong column-weak beam structural systems. The main objectives in this structural type are: i) Ensure a collapse mechanism that uniformly distributes the plastic energy among the structural elements of all storeys ii) Force the formation of the plastic hinges at the beams ends, which present a greater dissipation capacity than columns because of the absence of the axial load. The formation of the plastic hinges at the columns is exclusively allowed at the base of the columns to establish the failure mechanism.

To define the dimensions and reinforcement of the structural elements it is necessary the use of a capacity design approach. Another key point to ensure that the plastic hinges are developed at the beams instead of the columns is that the sum of the bending capacities of the columns framing into a joint is larger enough than the sum of the bending capacities of the beams framing into the same joint, as expressed by equation 1.1.

$$\frac{\sum M_c}{\sum M_b} \gg 1 \tag{1.1}$$

Where M_c is the column moment strength and M_b is the beams column strength.

A detailed description and an example of these structures will be deeply described in chapter 4.

1.1.2. Flexible-stiff mixed structures. Innovative RC frame equipped with hysteretic dampers.

Among the different energy concentration type structures, the flexible-stiff mixed structure with damage concentration in all storeys is considered in this study. This structural system combines in parallel in each story of the structure two clearly different parts: the flexible part and the stiff part. The flexible part has a reduced stiffness that allows large lateral deformations within the elastic range and its main function is to resist the gravitational loads. The stiff part has larger stifness and ample inelastic deformation capacity and its main function is to resist the lateral loads and concentrate the damage exerted by the earthquake at each level of the structure. In this study the flexible part is determined by a conventional RC frame and the stiff part is constituted by passive energy dissipation devices at each level. Figure 1.1 shows the typical idealized capacity curves (i.e. force Q vs. displacement δ) for the flexible part, the stiff part and the mixed system. In figure1.1., ${}_fQ_y$ and ${}_sQ_y$ are the lateral strengths of the flexible and stiff parts respectively, while ${}_f\delta_y$, and ${}_s\delta_y$, are the corresponding inter-storey drifts at yielding.

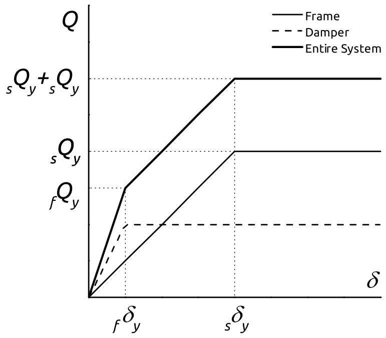

Figure 1.1.: Flexible-stiff mixed structural system at the storey level

The use of passive Energy Dissipating Devices (EDD) for seismic design of structures has increased exponentially in recent years, for both new and existing buildings. The EDD's concentrate the energy dissipation demand caused by the earthquake, reducing the damage imparted to the framing system [31]. The EDD's are capable of minimizing inter-storey drifts and increasing the overall earthquake resistance of the buildings to achieve performance-based design objectives. There are different types of passive EDD's. The most commonly used in seismic design are viscous fluid dampers, viscoelastic solid dampers, friction dampers and metallic dampers [89]. The EDD's based on the yielding of metals— commonly known as hysteretic dampers—are among the most popular. An EDD called Web Plastifying Damper (WPD) designed and patented at the University of Granada [15] has been used in this study. The WPD damper is based on the yielding of the web of I-shaped section segments under out of plane bending as shown in figure 1.2. The damper is designed to be installed as diagonal braces where several I-shaped segments, depending on the required damper strength and stiffness, are attached to two steel auxiliary bars that remain elastic during the earthquake. Figure 1.3 show a WPD damper installed on an RC frame, as a diagonal brace. The simplicity and low cost of this damper makes it very interesting to use it massively in low to moderate earthquake risk areas and developing countries.

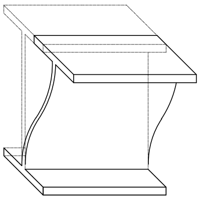

Figure 1.2.: WPD damper

Figure 1.3.: Damper assemblage

1.2. Seismic design: force-based, displacement-based and energy-based methodologies.

1.2.1. Force-based seismic design.

The force-based methods are the most generalized in seismic codes presently, for the seismic design of structures, because of its simplicity and suitability for non-specialized professional engineers. These methods use lateral forces distributed over the height of the structure with a known pattern whose values are determined by a minimum base shear strength required to resist the design earthquake. Depending on how these lateral forces are calculated, there are two different methods that use the force-based approaches [85]:

- Static Equivalent Lateral Force (ELF) Method. The elastic response base shear of a structure, V_e can be obtained as follow.

  $$V_e = C_T W \tag{1.2}$$

  Where C_T is the seismic design coefficient dependent on the seismic hazard and the fundamental period of vibration, T and W is the weight of the building.
  This elastic base shear is reduced by the appropriate reduction factor R — called $R_\mu$in the US code, q in Eurocode 8 and μ in the Spanish seismic code — depending on the plastic deformation capacity of the structural system, obtaining the design base shear force from equation 1.3

  $$V = \frac{V_e}{R} \tag{1.3}$$

  This design base shear is distributed along the height of the structure and among the different parts of the structure proportionally to their elastic stiffness. It is very common to use a distribution proportional to the height and weight at different levels as expressed in equation1.4

  $$F_i = \frac{(V - F_t)\, w_i h_i}{\sum_{i=1}^{n} w_i h_i} \tag{1.4}$$

  Where F_i is the force, w_i is weight and h_i is the height at level i respectively and F_t is a concentrated load at the top of the building that tries to represent the effect of higher modes of vibration.

- Dynamic Equivalent Lateral Force Method. The most common method is the Response Spectrum Analysis, which is the one adopted by the NSCE-02 code [35] and Eurocode-8 [38]. The design is based on the peak elastic dynamic response of the representative modes of the structure, obtained from the elastic response spectrum at the given site. The maximum modal contributions are combined statistically to obtain the maximum response of the structure.
  The design response spectrum used is obtained by dividing an elastic response spectrum by the same reduction factor R used in the ELF method.

1.2.2. Displacement-based seismic design.

Unlike the Force-Based seismic design methodologies, the Displacement-based procedures use displacements instead of forces as design parameter. The seismic performance of the structures is controlled by the storeys displacements or drifts, as it is directly related to the damage. Although these procedures are relatively new and not common among professional engineers, there has been an extensive research during the last decades. Shimazaki and Sozen [80] and Miranda [64] studied, among others, the relationship between the inelastic and elastic displacement based on the non-linear time history analysis of elastic-perfectly plastic SDOF structures. Both concluded that for short period structures the inelastic displacements exceed those of the elastic SDOF, while for medium-long period structures, the displacements were almost equal. They also noted that the limit between short and long periods SDOF can be defined in terms of the characteristic ground period T_g which is the limit period between constant velocity and constant acceleration ranges of the elastic response spectra of the ground motion. Depending on how the equivalent SDOF system that represents the real MDOF structure is defined, there have been several proposals for displacement based design of structures. The seismic design based on these proposals is commonly referred to as Direct Displacement-Based Design (DDBD) [75, 76, 29, 68]. In these procedures an inelastic equivalent SDOF is defined from a push-over analysis of the real MDOF structure, in terms of effective period, stiffness, mass and damping for an assumed maximum displacement. The effective properties are used to obtain the maximum displacement with an elastic displacement spectrum. Moehle [66, 67] studied the different factors that influence on the displacement response of RC structures. Recently three methodologies based on the pushover analysis have been developed and included in the latest seismic codes as a design and evaluation tool: The Displacement Coefficient Method (DCM), presented in FEMA-356 and reviewed in FEMA-440; the N2 method included in EC8; and the capacity spectrum method (CSM) from ATC-40. A wide comparative study among CSM, N2 and CSM methodologies based on experimental results can be found in chapter 5.

1.2.3. Energy-based seismic design.

Since Housner [51] and Akiyama [3] settled the basis of the energy based method in the second half of the last century, there has been an increasing interest among earthquake engineering research community towards these methodologies. As any other engineering design procedures, the energy based methods are rooted in the premise that the capacity of the structure (in terms of energy absorption/dissipation) should exceed the earthquake demand (in terms of seismic input energy), as expressed by Housner in the following sentence [51]:

> “If a structure can absorb a large amount of energy through so-called plastic deformation, it will be able to withstand very intense ground motion without fail”

The problem then is how to determine the energy exerted by an earthquake to the structure and how is this energy distributed among the storeys and dissipated by the structural elements.

Housner in 1956 [51] stated that the energy that contributes to damage, E_t , in a SDOF subjected to a given ground motion can be estimated by equation 1.5:

$$E_t = \frac{1}{2} m S_v^2 \tag{1.5}$$

Where m is the mass of the system and S_v is the maximum relative velocity attained by the mass, obtained from the velocity elastic response spectrum with an appropriate damping ratio ξ.

According to Housner the energy input to the structure is dissipated in part through damping and the rest stored/dissipated in the structure as kinetic energy of motion of the mass and elastic/plastic strain energy of the structural members. If the structure is not able to absorb the portion of the energy input by the earthquake not dissipated by damping in the elastic range (i.e. in form of kinetic energy and elastic strain energy) the stresses in the structural components will exceed the elastic limit, resulting in plastic strains and permanent deformations that can lead to the collapse of the structure. If the structure is provided with enough capacity to dissipate energy through inelastic deformations without collapse, it will survive the earthquake.

Akiyama [3] demonstrated that the total energy input exerted by an earthquake is a stable quantity that depends mainly on the total mass of the system and the fundamental period of vibration of the structure. According to Akiyama the energy input can be derived as follows. The equation of motion for an inelastic SDOF system subjected to a unidirectional horizontal component of an earthquake characterized by the ground acceleration $\ddot{v}_g\left(t\right)$ is:

$$M\ddot{v} + C\dot{v} + Q\left(v\right) = -M\ddot{v}_g \tag{1.6}$$

Where M is the mass of the system, C is the damping coefficient, $Q\left(y\right)$ is the restoring force. $\dot{v}$ and $\ddot{v}$, are the first and second derivatives of the relative displacement of the mass v respect to time t.

The equation 1.6 expresses the fundamental relationship which governs the vibrational response of the SDOF system. Multiplying equation 1.6 by $dv = \dot{v}dt$ and integrating over the duration of the ground motion, t_0, the equation of energy balance is obtained as follows.

$$\int_0^{t_0} M\ddot{v}\dot{v}dt + \int_0^{t_0} C\dot{v}^2 dt + \int_0^{t_0} Q\left(v\right)\dot{v}dt = -\int_0^{t_0} M\ddot{v}_g\dot{v}dt \tag{1.7}$$

Equation 1.7 can be written also as

$$W_k + W_\xi + W_s = E \tag{1.8}$$

Where:

W_k is the kinetic energy

$$W_k = M\int_0^{t_0} \ddot{v}\dot{v}dt \tag{1.9}$$

W_ξ is the energy absorbed by damping

$$W_\xi = C \int_0^{t_0} \dot{v}^2 dt \tag{1.10}$$

And W_s is the strain energy which comprises the recoverable elastic strain energy W_{se} and the irrecoverable inelastic strain energy W_p (i.e. $W_s = W_{es} + W_p$).

$$W_s = \int_0^{t_0} Q(v)\,\dot{v}dt \tag{1.11}$$

The elastic vibrational energy is by definition:

$$W_e = W_k + W_{es} \tag{1.12}$$

The equation 1.8 can be rewritten with equation 1.13 that is the fundamental equation on which the energy balance design methodology is constructed. Figure 1.4 shows a typical history of energies input by an earthquake into an elastic-plastic system:

$$W_e + W_p + W_\xi = E \tag{1.13}$$

E is by definition the total amount of energy exerted by the earthquake to the structure and can be expressed in terms of an equivalent velocity V_E by:

$$V_E = \sqrt{\frac{2E}{M}} \tag{1.14}$$

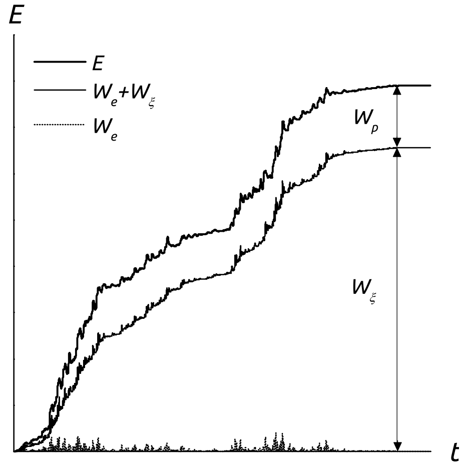

Figure 1.4.: Time history of energy of an elastic-plastic system

If we rewrite 1.13 as follows:

$$W_e + W_p = E - W_\xi = E_D \tag{1.15}$$

The second term in equation 1.15 E_D can be expressed in terms of an equivalent velocity, V_D by means of equation 1.16. When Housner stated equation 1.5, the underlying assumption in his methodology was that the maximum V_D that a SDOF could attaine is determined by the relative response velocity, S_v which is an upper bound for V_D. Akiyama, based on nonlinear time history analysis with elastic perfectly plastic models, proved that Housner assumption provides an acceptable estimation of V_D except in the short period range where V_D was clearly greater than S_V in most cases. Due to the proximity of E_D to E_t in a broad range of periods beyond the short ones, E_D is also commonly referred to as the energy that contributes to damage.

$$V_D = \sqrt{\frac{2E_D}{M}} \tag{1.16}$$

Based on the same nonlinear analyses the following relationship between V_E and V_D was proposed:

$$\frac{V_D}{V_E} = \frac{1}{1 + 3\xi + 1.2\sqrt{\xi}} \tag{1.17}$$

The elastic vibrational energy W_e of equation 1.15 can be approximated with the following equation [2]:

$$W_e = \frac{Q_y \delta_y}{2} \tag{1.18}$$

Where Q_y and δ_y are the yield strength and the yield displacement of the elastic-perfectly plastic SDOF system.

Using the base shear coefficient defined by $\alpha = {}^{Q_y}/_{Mg}$ (where g is the gravity acceleration) and taking into account that $Q_y = \alpha M g$, $\delta_y = {}^{Q_y}/_{k}$, $k = {}^{4\pi^2 M}/_{T^2}$ the equation 1.18 can be rewritten as follows:

$$W_e = \frac{M g^2 T^2}{4\pi^2} \frac{\alpha^2}{2} \tag{1.19}$$

The last term in equation 1.15 to be addressed is W_p which is the term that represents the structural damage. Whereas the elastic deformations are restored to the structural system, the inelastic deformations are accumulated monotonously until the collapsed of the structure is reached. In this sense, the cumulative inelastic deformation or cumulative inelastic strain energy directly related to damage and it is a quantitative index of the degree of damage caused by the earthquake on the structure. Equations 1.6 to 1.13 can be easily extended to MDOF systems replacing the escalar magnitudes M, C by matrices, and Q, v, $\dot{v}$,$\ddot{v}$, by vectors. In case of a MDOF system, W_e can be approximated with equation 1.19 replacing α by the base shear force coefficeint α_1 [3], and the total energy dissipated by the MDOF systems through plastic deformations, W_p, is the sum of the plastic strain energy dissipated by each story, W_{pi}, that is:

$$W_p = \sum W_{pi} \tag{1.20}$$

W_{pi} can be expressed in terms of a the non-dimensional damage ratio, η_i , which is called cumulative inelastic deformation ratio of the storey i-th , and its expressed by equation 1.21 for each domain of loading:

$$\eta_i^{\pm} = \frac{W_{pi}^{\pm}}{Q_{yi}^{\pm}\delta_{yi}^{\pm}} \tag{1.21}$$

Here, Q_{yi} and δ_{yi} are the yield shear force and interstory drift at yielding, of storey i.

Another important index to characterize the damage on the structure is the maximum plastic deformation, also called by Akiyama apparent maximum plastic deformation ratio , μ, defined as follows:

$$\mu_i^{\pm} = \frac{\delta_{max,i}^{\pm} - \delta_{yi}^{\pm}}{\delta_{yi}^{\pm}} \tag{1.22}$$

Where $\delta_{max,i}^{\pm}$ is the maximum inter-storey drift in positive and negative displacement domains of the storey i .

1.3. Future trends in seismic-design: the paradigm of Performance Based Design.

The first step in PBSE is the selection of the design Performance Objective, which is the expected performance level for the building for a given earthquake seismic hazard level (SHL). The selection of the performance objective is based on the building importance, occupancy, function, potential value as historical or cultural resource and other economic factors as the repair or rebuild costs or business interruption.

A performance level is a damage state defined in terms of the structural, non-structural and content damage, the consequences to the occupants and the continuity of the function carried on in the building. There are five discrete performance levels which are commonly used in actual standards [39, 45, 85, 6] as limit for a range of limit states. Figure 1.5 shows the damage expected at different performance levels based on the global state of the building according to the SEAOC [85].

For RC primary structural elements, the table 1.1 associates each performance level described qualitatively in figure 1.5 with a quantitative description of the allowed damage in terms of maximum inter-storey drift, determining the maximum damage permissible for each performance level. Several engineering damage parameters can be used for damage quantification but nowadays the most extended is the inter-storey drift ratio. The ranges of inter-storey drift ratio for different structural performance levels are distinct within diverse standards, the most widely used are considered herein.

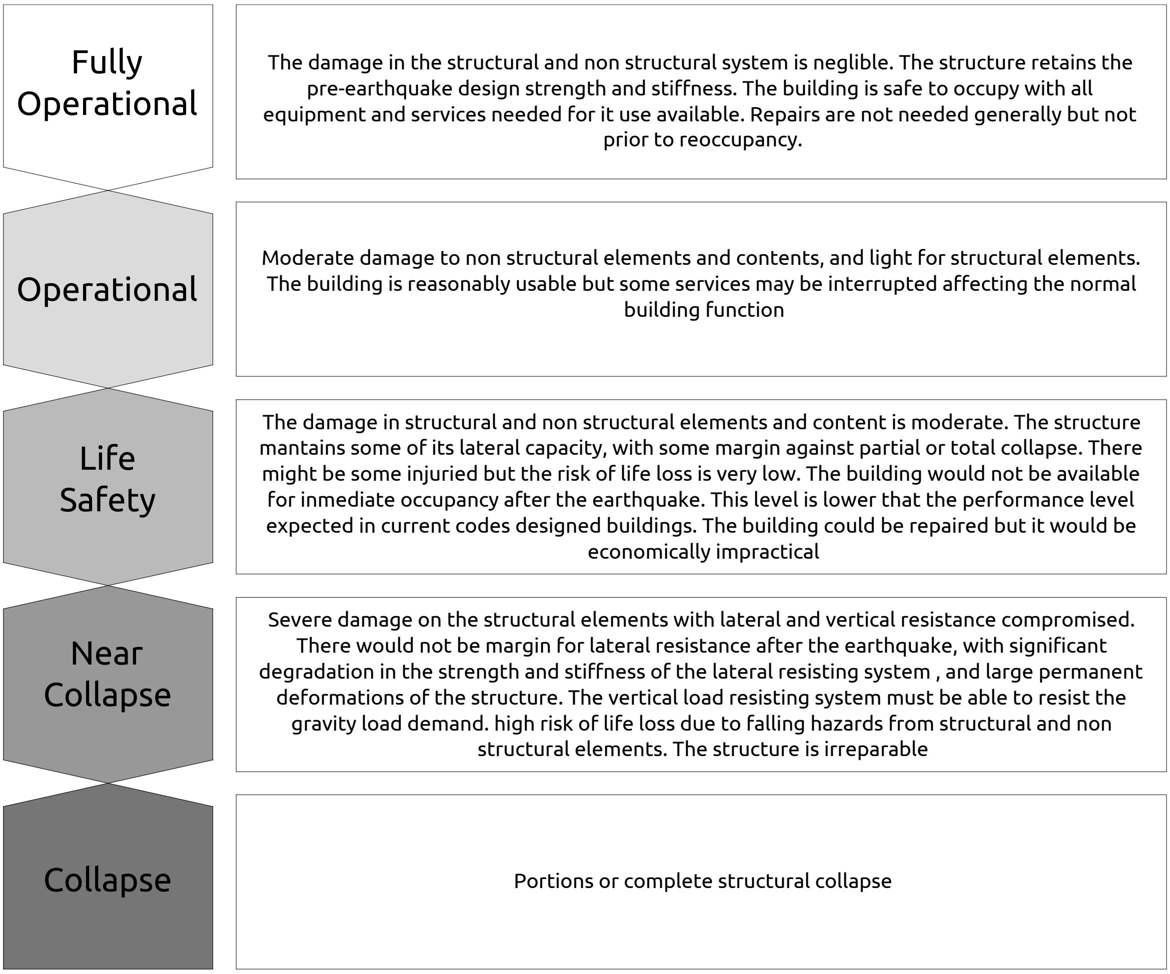

Fully Operational	The damage in the structural and non structural system is neglible. The structure retains the pre-earthquake design strength and stiffness. The building is safe to occupy with all equipment and services needed for it use available. Repairs are not needed generally but not prior to reoccupancy.
Operational	Moderate damage to non structural elements and contents, and light for structural elements. The building is reasonably usable but some services may be interrupted affecting the normal building function
Life Safety	The damage in structural and non structural elements and content is moderate. The structure mantains some of its lateral capacity, with some margin against partial or total collapse. There might be some injuried but the risk of life loss is very low. The building would not be available for inmediate occupancy after the earthquake. This level is lower that the performance level expected in current codes designed buildings. The building could be repaired but it would be economically impractical
Near Collapse	Severe damage on the structural elements with lateral and vertical resistance compromised. There would not be margin for lateral resistance after the earthquake, with significant degradation in the strength and stiffness of the lateral resisting system , and large permanent deformations of the structure. The vertical load resisting system must be able to resist the gravity load demand. high risk of life loss due to falling hazards from structural and non structural elements. The structure is irreparable
Collapse	Portions or complete structural collapse

Figure 1.5.: Performance levels definitions

	Fully Operational	Operational	Life Safety	Near Collapse	Collapse
inter-story drift					
SEAOC	$id < 0.2$	$0.2 < id < 0.5$	$0.5 < id < 1.5$	$1.5 < id < 2.5$	$id > 2.5$
FEMA 356	-	$id < 1$	$1 < id < 2$	2	$id > 4$
ATC-40	-	$id < 1$	$1 < id < 2$	$2 < id < 0.33 V_i/P_i$	$id > 0.33 V_i/P_i$
Damage observed	Negligible	Minor cracking. Limited yielding in some locations; no crushing	Extensive damage to beams; spalling of cover and shear cracking for ductile columns. Minor spalling in non-ductile columns	Extensive cracking and hinge formation in ductile elements. Limited cracking and/or splice failure in some non-ductile columns. Severe damage in short columns	

Table 1.1.: Performance levels and permissible structural damage in RC structures

The seismic hazard level at the building site is defined by a set of ground motions and their associate hazards with different probabilities of occurrence. The seismic hazard level is expressed in terms of probability of exceedance or mean recurrence interval, which is the averaged period of time between the occurrences of earthquakes that produce effects of similar or greater intensity. Four Seismic hazard levels are proposed by the SEAOC and ATC [6, 85] and summarized in table 1.2.

Seismic Hazard Level	Recurrence interval	Probability of Exceedance
Frequent	43 years	50% in 30 years
Occasional	72 years	50% in 50 years
Rare	475 years	10% in 50 years
Very rare	970 years	10% in 100 years

Table 1.2.: Seismic hazard levels

Given a Seismic hazard level the building is designed to meet a performance objective, establishing the acceptability criteria for the design. As the different performance levels are related to several engineering demand parameters (e.g. drift, ductility, cumulative inelastic deformation ratio) this parameters become the acceptability criteria in later checking states of the design. The selection of different performance objectives for a given seismic hazard level depends on the importance of the building, their use and occupancy. Figure 1.6 summarizes the recommended performance objectives for Safety Critical Facilities, Essential/Hazardous Facilities and Basic Facilities. Safety Critical Facilities are those that contain large quantities of hazardous material as toxins, explosive and radioactive materials. Essential/Hazardous Facilities are those that are important after the earthquake as hospital, fire stations, police stations, etc. Basic facilities are the rest of building not included in previous categories.

After the structural performance levels are selected for the different Seismic Hazard Levels, a seismic hazard analysis must be done to determine the suitability of the structure at the site. The hazard analysis must take into account any potential hazard at the site, seismicity and soil type. This analysis will define the seismic ground motion at different seismic hazard levels. The ground motion can be represented as time histories, acceleration response spectra, displacement response spectra, velocity response spectra, energy input response spectra or any other mean that could be required in design and check procedures.

Once the performance objectives are selected and ground motion characteristics are determined at the site, the structural design can be started. The possible approaches to accomplish the definition of the structural system with predictable seismic performance are mainly based on force/strength, displacement or energy approaches. The objective is to define the dimensions and detailing of the structural elements to meet the performance objectives for the different seismic hazard levels. The performance levels here are determined by engineering demand parameters that define the acceptability criteria. The acceptability criteria can be defined in several terms, as stress ratios, inter-story drift, ductility or energy demand that need to be achieved in order to meet the established performance objectives. Finally the structural design needs to be checked, to ensure that the acceptability limits are not exceeded and the structure behaved with the expected performance level by means of inelastic analysis methods. The most accurate procedure is the non linear time history analysis but other simplified methodologies as the non-linear static procedures based on pushover analysis or energy based methods could also be used.

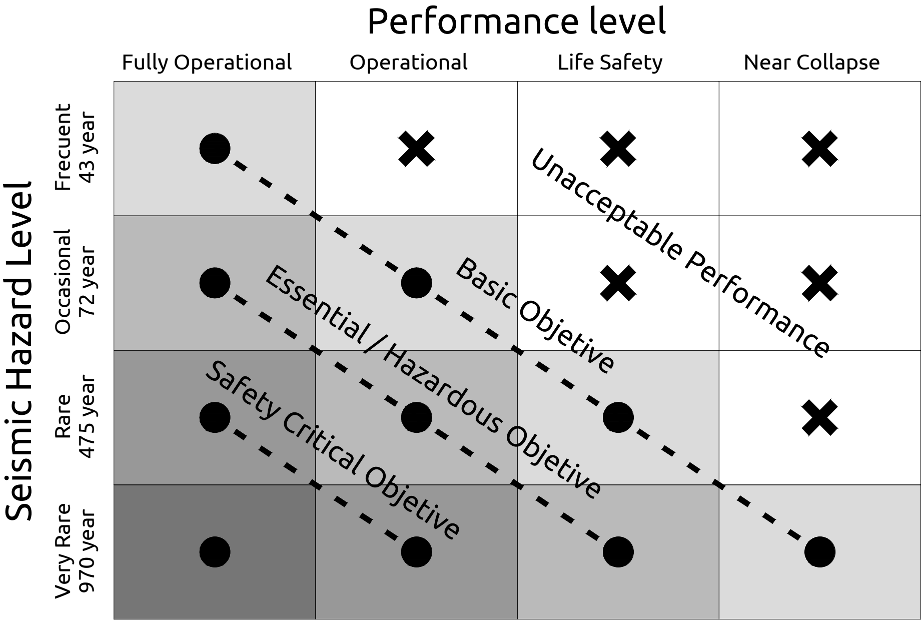

Figure 1.6.: Recommended seismic performance objectives for buildings

1.4. Objectives and methodology.

This thesis pursues the following main objectives:

1. Investigate experimentally the seismic performance of conventional “strong column-weak beam” RC framed structure. Evaluate the accuracy of the chord rotations expressions included in Eurocode-8 Part 3 and quantify the energy dissipation capacity of RC structural members, through shaking table tests.
2. Investigate experimentally the seismic performance of RC ductile structural walls based on the results of cyclic loading tests and compare the hysteretic behaviour of conventional RC ductile walls with that of innovative hysteretic dampers.
3. Compare the seismic response of conventional RC frames, designed following the strong column-weak beam philosophy and capacity design criteria, with the innovative solution of RC frames with hysteretic dampers by means of non-linear numerical analyses within the framework of the Performance Based Design.
4. Evaluate and compare through shaking table tests, the applicability and accuracy of the prediction given by three common non-linear static procedures (the displacement coefficient method, the N2 method and the Capacity Spectrum Method) to predict the response of frames with hysteretic dampers.

The methodology applied to pursue these objectives is two folded. It comprises an experimental approach consisting on static and dynamic tests, and a numerical approach consisting basically on conducting nonlinear static and dynamic time history analyses.

1.5. Main original contributions

The new contributions of this Thesis to the field of earthquake engineering can be summarized as follows:

1. Related to the main objective 1 and based on dynamic shaking table tests:
    - New quantitative experimental information on the actual performance of RC frames designed according to modern seismic codes.
    - Evaluation of the level of damage on the columns of "strong column-weak beam systems" that have been designed to meet the column-to-beam bending strength ratio, prescribed by ACI-318-08 and by Eurocode-8.
    - Quantitative evaluation of the ultimate chord rotation capacities of RC beams and columns under realistic dynamic loads, and comparison with the prediction provided by the empirical equations of Eurocode 8 (Part 3).
    - Quantitative evaluation of the ultimate energy dissipation capacities of well-designed RC beams and columns under realistic dynamic loads.
2. Related to the second objective and based on static cyclic tests:
    - Quantitative evaluation of the seismic performance of covencional RC walls, in terms of yield displacements, maximum displacements and energy disipation capacity.
    - Quantitative evaluation of the lengths of the regions in which inelastic compressive and tensile strains are concentrated.
    - Evaluation of the influence of the reinforcement pattern of the wall on their cyclic behavior.
    - Comparison of the RC walls with the response of hysteretic dampers in terms of energy dissipation capacity.
3. Related to the third main objective and based on non-linear time history analyses:
    - A quantitative comparison of the response of conventional RC frames designed for sustaining seismic loads through the formation of a strong column-weak beam mechanism, and that of the RC frames designed only for gravity loads equiped with hysteretic dampers.
4. Related to the fourth objective and based on shaking table tests:
    - Experimental information on how the NSPs apply to systems with hysteretic dampers

- Quantitative comparison among three NSPs: (1) the improved version of the Capacity Spectrum Method (CSM) from FEMA 440; (2) the improved version of the Displacement Coefficient Method (DCM) from FEMA 440; and (3) the N2 Method implemented in Eurocode 8.

1.6. Organization of the thesis.

This thesis is divided in 6 chapters. All chapters aim to be independent to each other although the findings made in each of them are helpful to understand and consolidate the rest of them.

Chapter 1 revises the framework and the main concepts in which this thesis is supported.

Chapter 2 investigates the seismic performance of a "strong column weak beam" RC framed structure in terms of several damage indexes. The study is based on the experimental results of a scaled substructure representing a three story building designed accordingly to current Spanish code tested with shaking table at University of Granada.

Chapter 3 investigates the hysteretic behaviour and ultimate energy dissipation capacity of conventional RC ductile walls, and particularly the effect of the inclusion of confinement reinforcement through quasi-static tests.

Chapter 4 compares the seismic behaviour of two structural systems. In one hand the conventional "strong column weak beam" RC frame . In the other the innovative stiff-flexible mixed system configured by a RC frame equipped with hysteretic dampers.

Chapter 5 studies the appropriateness and accuracy of three conventional non-linear Static Procedures (NSP) to predict the response of structures with hysteretic dampers. The NSP studied are the displacement coefficient method (DCM) and Capacity Spectrum Method (CSM) from FEMA-440 and the N2 method form Eurocode 8. The prediction obtained with these methods is compared with the results of several tests done with shake table.

2. Performance assessment of a reinforced concrete framed structure based on shake table tests

One of the most common seismic force-resisting systems for building structures is the reinforced concrete (RC) frame. In the framework of the Performance Based Seismic design the structure must satisfy different seismic performance levels (SPL) under different seismic hazard levels (SHL) as seen in chapter 1. For SHLs associated with rare or very rare earthquakes (i.e. with return periods P_r of the order of about 475 and 2000 years, respectively), the RC frame is allowed to dissipate energy through plastic deformations (i.e. undergoing structural damage) at special regions called plastic hinges by developing a stable plastic "strong column-weak beam" mechanism.To this end, brittle failures must be prevented at the locations where plastic hinges are expected, by applying capacity design criteria.Although the frame is allowed to enter into the nonlinear range in the case of severe ground motions, common seismic design procedures nowadays, are aimed at converting the complicated nonlinear dynamic behavior of the structure into an equivalent linear problem. This simplification is accomplished by the use of force reduction factors that depend on the inelastic response characteristics of the structural system, and that rely strongly on the formation of the aforementioned "strong column-weak beam" mechanism.

There is a need to assess the inelastic response characteristics and performance of typical structures designed in view of provisions established by current seismic codes, and to verify the adequacy of these provisions to meet the design performance objectives [7] under prescribed SHLs. Of paramount importance among these provisions is the ratio of the moment capacity of columns to beams framing into a joint, to assure the formation of a "strong column-weak beam" mechanism. It is also important to quantify the level of damage expected in a structure in each scenario of seismic hazard, not only in terms of maximum deformations (i.e. maximum chord rotation or interstory drift), but also in terms of cumulative damage (i.e. dissipated energy).). Progress in all these aspects calls for laboratory data and experimental evidence, and the best source for such information is the dynamic shake-table test. Shaking table tests reproduce in a most realistic way the seismic demands on structures subjected to ground motions, particularly within the nonlinear range, and include cumulative damage effects. The behavior of real structures can be sensitive to rate-of-loading effects hardly captured with numerical models. Strain rate effects can modify the nominal resistance of the structural members and alter the intended hierarchy of strengths that guarantee the formation of a "strong column-weak beam" mechanism. Furthermore, a computationally effective modeling of the hysteretic behavior of RC elements requires introducing many simplifications (regarding the pinching effects, the strength and stiffness degradation, etc.) that may condition the actual response of the structure. The use of such analytical models entails calibration and verification through experimental data.

The general objective of this chapter is to assess experimentally, through shake-table tests, the seismic performance of RC frames with ductile reinforcement details designed according to modern codes. The study focuses on the quantitative evaluation of damage (in terms of maximum deformation, dissipated energy, chord rotations and damage indexes) imparted to the structure under each SHL, examining the ratio of moment capacity of columns to beams framing into a joint to guarantee the formation of a "strong column-weak beam mechanism". To this end, shake-table tests of a sub-structure corresponding to a three-story, three-bay RC framed stucture were conducted in the Laboratory of Dynamics of Structures of the University of Granada. The specimen was a 2/5-scale model of a prototype building representative of conventional RC frame structures with regular and symmetric configuration, designed in view of current seismic codes in the Mediterranean area. The specimen was subjected to four seismic simulations of increasing intensity until collapse. The test results provide a quantitative evaluation of the global and local damage, the energy dissipation demands for each SHL, and a recommendation on the minimum ratio of column-to-beam moment capacity required in the joints to guarantee the formation of the strong column-weak beam mechanism, that is larger than that required by Eurocode 8[38] and ACI 318 [5].

2.1. Prototype and test model description.

The three-story and three-bay RC moment resisting frame shown in figure 2.1 is considered as prototype structure in this study. The structure is representative of existing modern buildings in the Mediterranean area. It is designed with the limit state design method considering gravity loads (dead loads of $3.22\,\mathrm{kN/m^2}$ for floors and $2.95\,\mathrm{kN/m^2}$ for the roof; and live loads of $2\,\mathrm{kN/m^2}$ for floors and $1\,\mathrm{kN/m^2}$ for the roof), and lateral seismic loading following the provisions of the current Spanish Seismic Code NCSE-02 [35]. The prototype building is assumed to be located in Granada (Spain), where the design ground acceleration (associated with a design earthquake of 500 years return period), a_b, is $a_b = 0.23g$ (g is the gravity acceleration). The concrete compressive strength f_c assumed in the calculations was $f_c = 25\,\mathrm{MPa}$, and the yield strength for the steel $f_y = 500\,\mathrm{MPa}$. The floor system consisted of one-way joists spaced 80 cm supported by the main beams (joist-band floor system). In turn, the one-way joists supported a thin concrete slab of 6 cm thickness. The cross section of the RC columns was $40 \times 40\,\mathrm{cm}$. The section of the main beams that supported the joist was $30 \times 40\,\mathrm{cm}$; the cross section of the beams perpendicular to the main beams was $25 \times 35\,\mathrm{cm}$. Ductile reinforcement details and capacity design criteria were used so that the frame develops a ductile strong column-weak beam plastic mechanism under lateral loads. The behavior factor q adopted for the seismic design was $q = 3.0$, and the resulting base shear force coefficient of the prototype structure was 0.22. The required strength of columns so that the structure develops the weak beam-strong column plastic mechanism shown in Figure 2.2 was based on the following considerations: (i) an inverted triangle distribution of lateral loads was adopted; (ii) the plastic hinges at beam ends are concentrated at a distance $d_R = 0.5h_c + h_b$, where h_c and h_b are the depth of the column and of the beam respectively; (iii) the ultimate bending capacity of beams at plastic hinge regions, M_{ub}, was determined assuming that its actual yield stress was $1.25f_y$. Capacity design was applied also at the plastic hinge level to prevent shear failure before the members reached their ultimate flexural capacity.

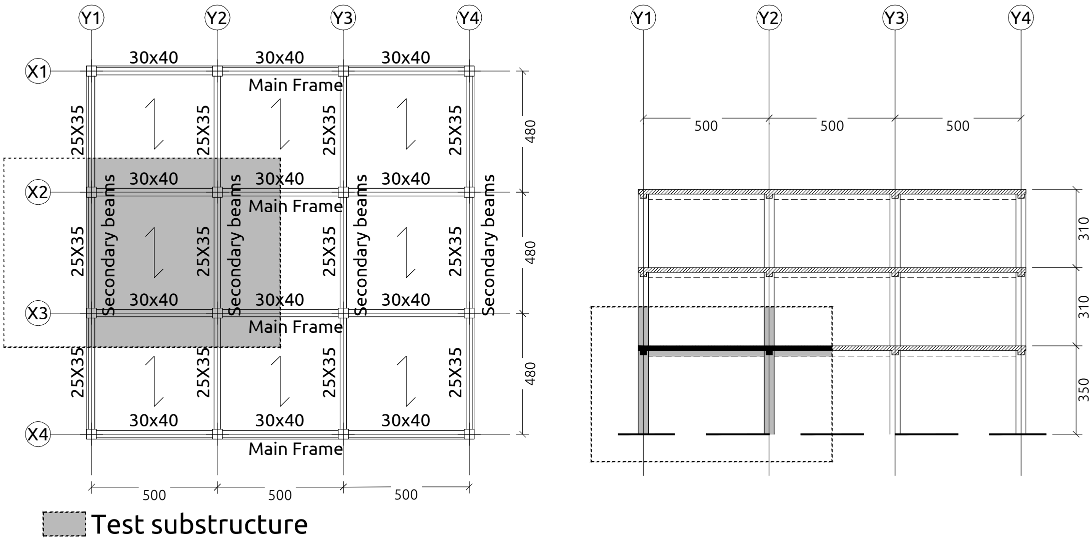

Figure 2.1.: Prototype structure

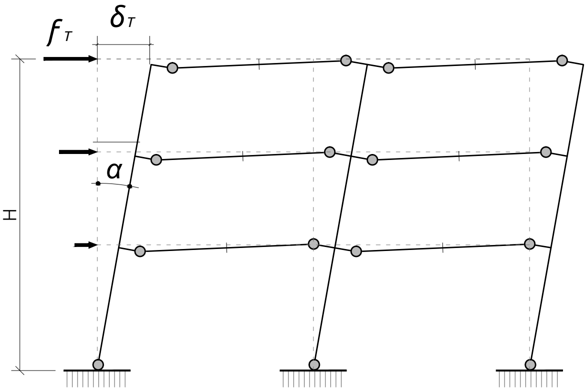

Figure 2.2.: Weak beam strong column failure mechanism

From the prototype, a substructure was separated from the original prototype by cutting through points of nominal zero bending moment under lateral loads. These lines are plotted with dash in figure 2.1. The substructure has the height of one story and a half, and the width of one-bay and a half in the direction of the main beams (i.e. those supporting the gravity loading). The test specimen was defined by applying scale factors of $\lambda_L = 2/5$ for length, $\lambda_a = 1$ for acceleration and $\lambda_\sigma = 1$ for stress. Scale factors for the rest of the physical quantities were set to satisfy similitude requirement[50]. Figures 2.3 to 2.8 show the geometry and reinforcing details of the test model. The test model consist in two parallel primary frame conected by secondary beams and the one-way joist-band floor system. Figure 2.3 shows the conection of the colummns with the footing. All columns were equal with a RC cross section of $16 \times 16\,\mathrm{cm}$ and a reinforcing ratio of $\rho = 0.016$. Figure 2.4 show a detailed definition of the one-way joist-band floor system supported by the main beams. The joists were spaced 32 cm each and their section was $2.8 \times 7.2\,\mathrm{cm}$ with $\phi 6$ flexion reinforcement bars on top and bottom. Figure 2.4 shows the definition of the 2.5 cm thik slab suported by the joists. Figure 2.6 and 2.7 show the geometry and reinforcement details of the main frames and secondary frames respectivelly. All beams primary and secondary were equal with a cross section of $120 \times 160\,\mathrm{cm}$ and a reinforcement ratio of $\rho = 0.008$. A detail of the main RC sections can be found in Figure 2.8.Coupon tension tests were conducted on samples of reinforcing bars of each batch and size, giving a yield stress of 551 MPa for the longitudinal reinforcement and 636 MPa for the stirrups. Compression tests were conducted on normalized concrete cylinders on the 28th day and the day of the tests, giving 35 MPa and 41 MPa, respectively.

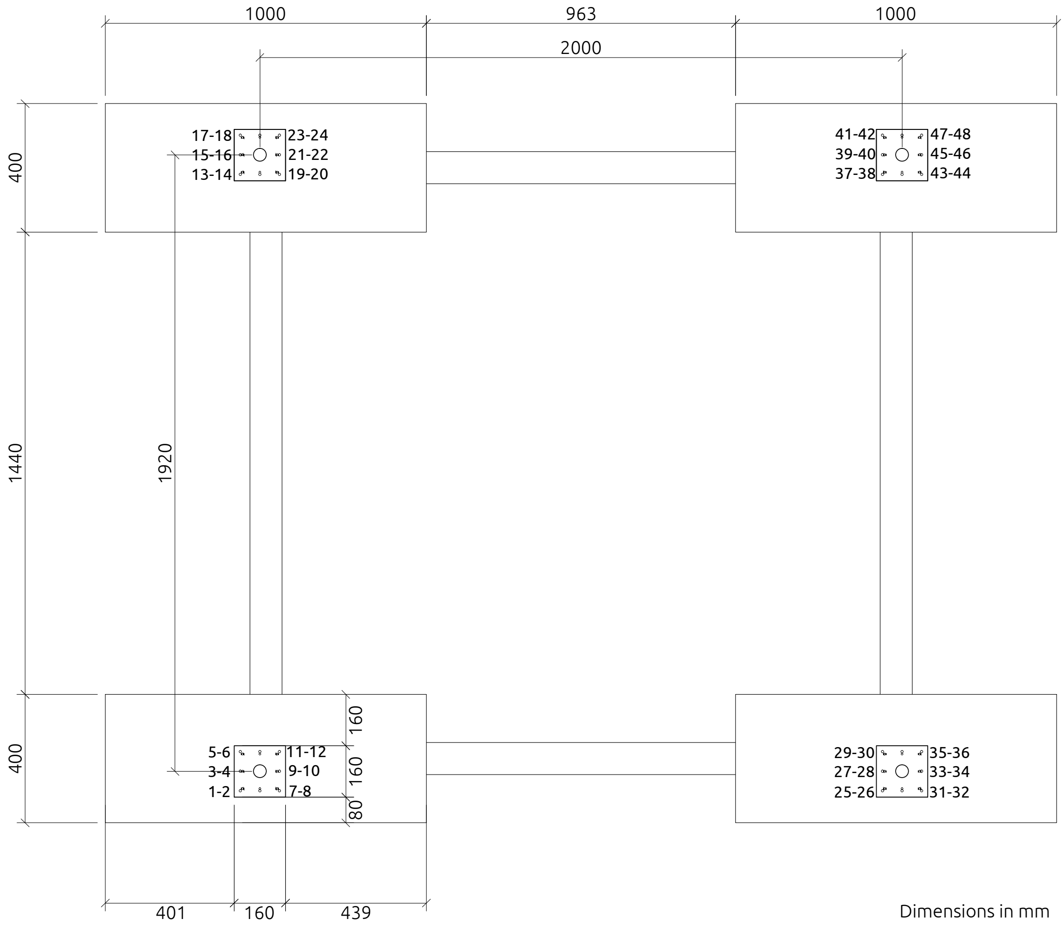

Figure 2.3.: Model geometry. Foundation

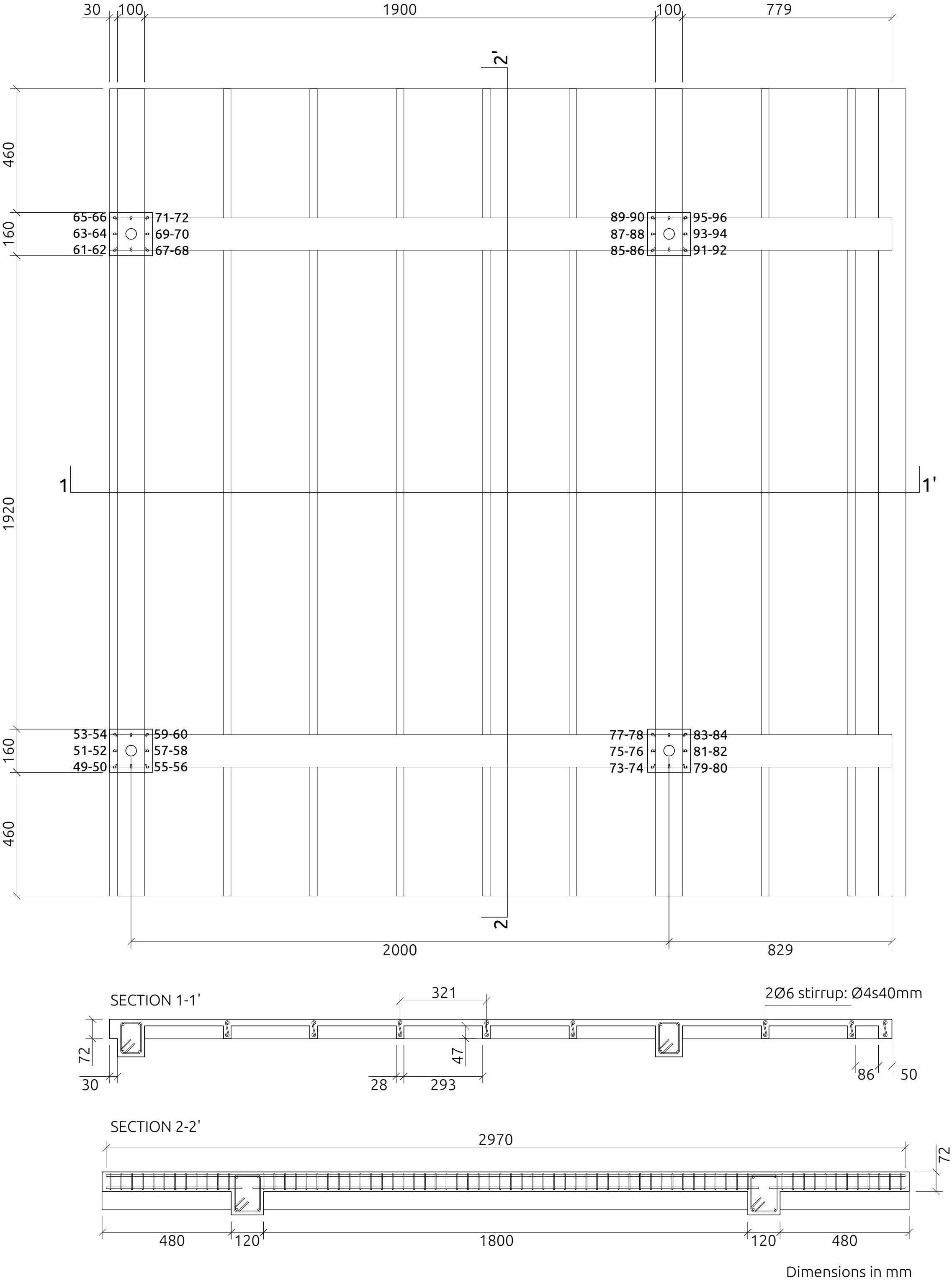

Figure 2.4.: Model geometry. Ground floor columns top sections. Joist-band floor system definition

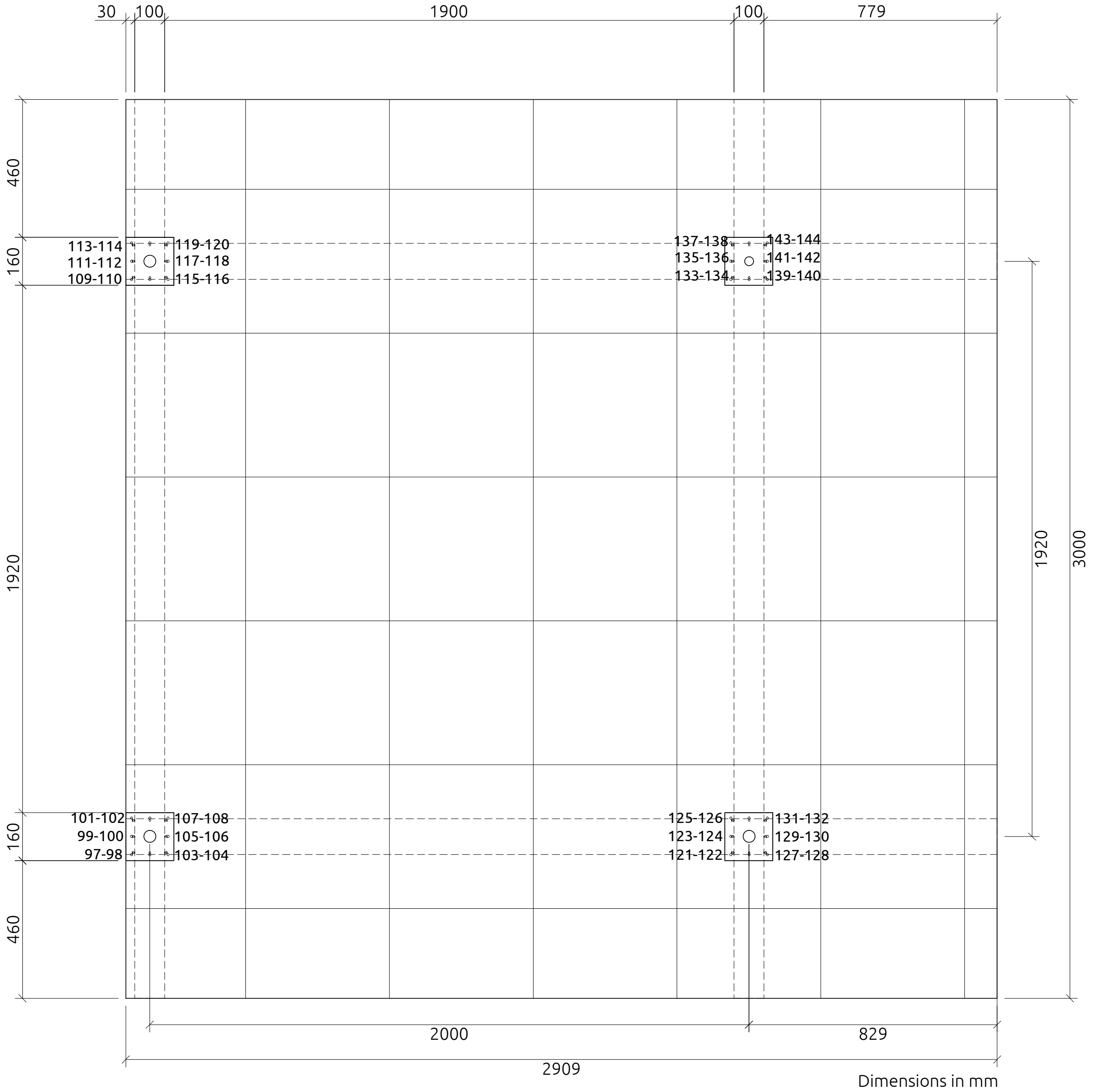

Figure 2.5.: Model geometry. First floor column base sections.

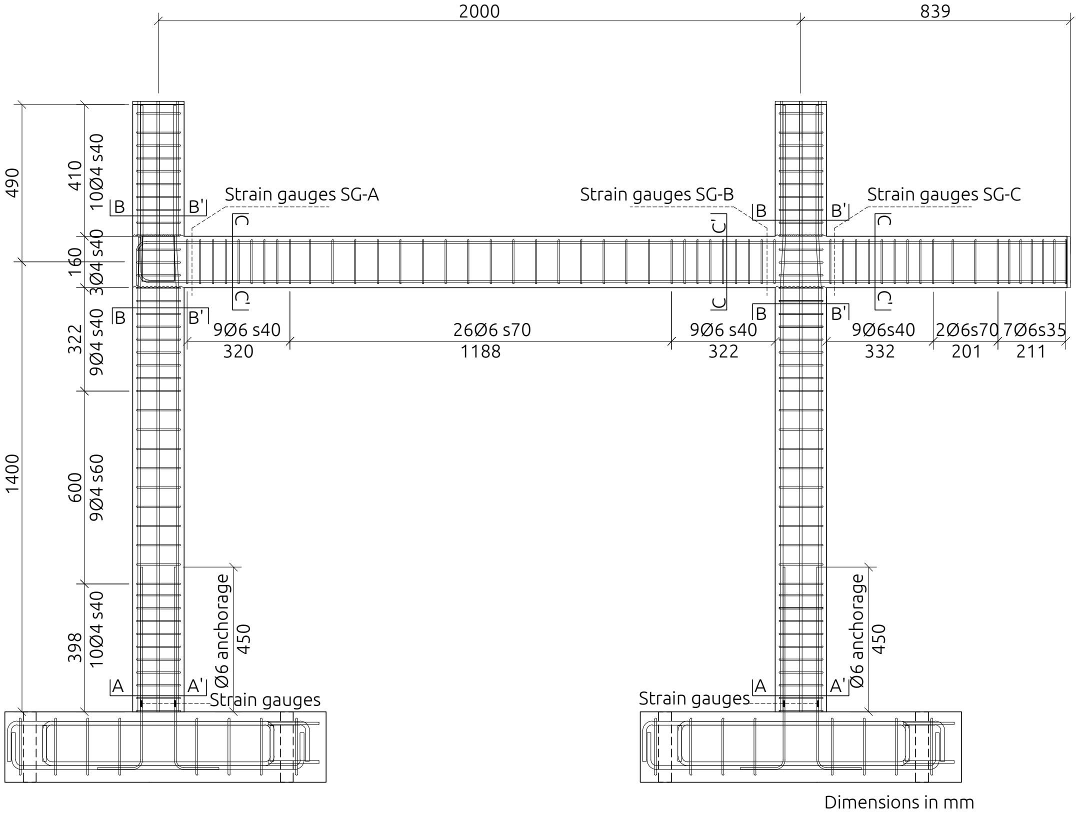

Figure 2.6.: Model geometry. Main frame

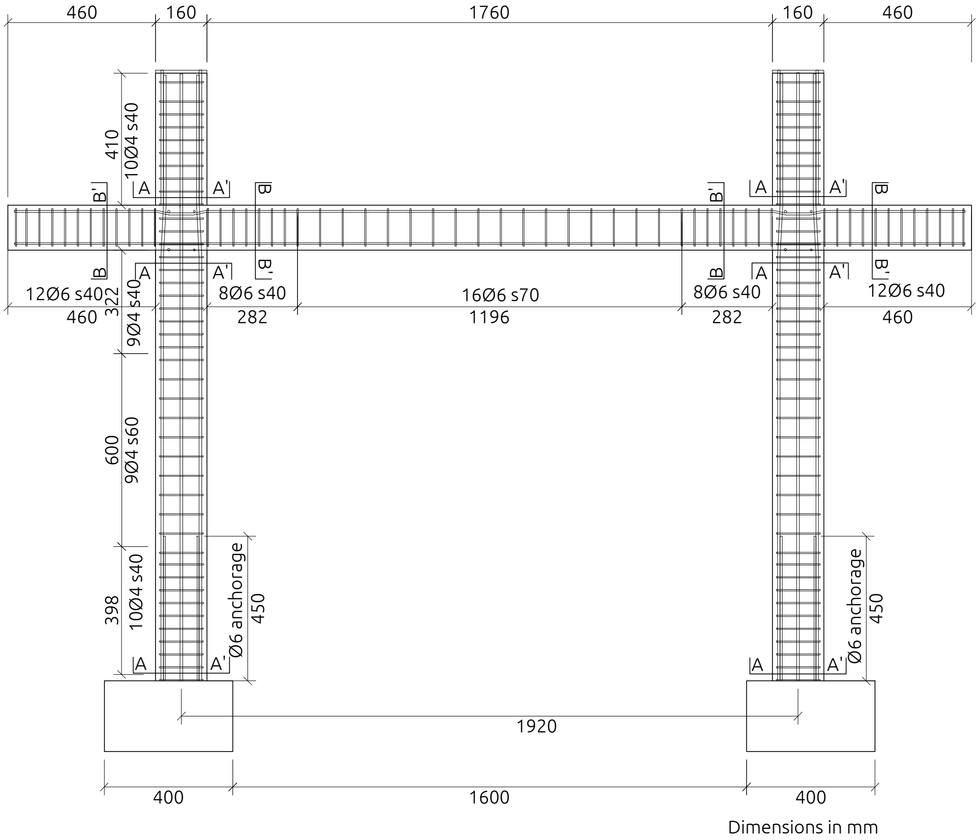

Figure 2.7.: Model geometry. Secondary frames

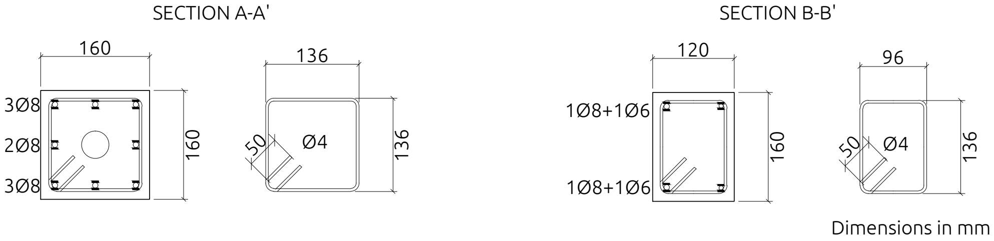

Figure 2.8.: Model geometry. Reinforcement details

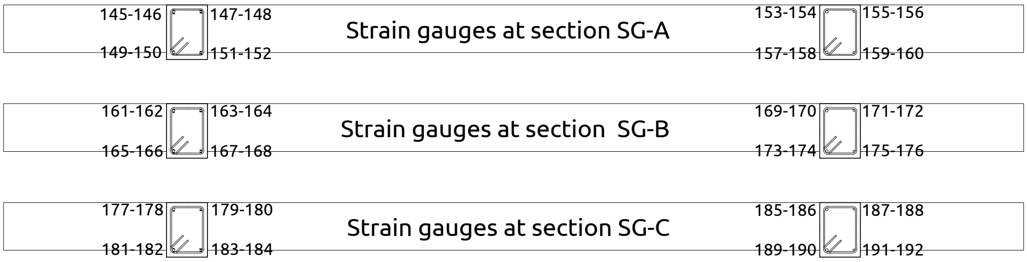

Figure 2.9.: Beam sections detail.

2.2. Set-up, instrumentation and load history.

2.2.1. Set-up and instrumentation.

The specimen was placed on the uniaxial MTS $3 \times 3\,\mathrm{m}^2$ shake table of the University of Granada (Spain) as shown in Figures 2.10 to 5.6. The structure was oriented so that the direction of the uniaxial movement of the shaking table coincided with that of the main frames. To represent the gravity loads acting on the floors and to satisfy similitude requirements between prototype and test model, steel blocks were attached at the top the RC slab and at the top of half columns of the second story as shown in Fig. 2.10 and 2.11 (added weight). To reproduce the boundary conditions (i.e. zero bending moment) of the substructure when the overall prototype building is subjected to lateral forces, pin joint connections were used at the top of the half-columns of the second story, and at the ends of the half-beams of the first floor. The restriction against vertical movements of the ends of the half-beams of the first floor was accomplished by means of pin-ended steel bars that connected the end of the beams with the steel plates (added weight) located on the top of the specimen, which have a very large flexural stiffness in comparison with that of the RC frame. When the shake table was accelerated, the inertial force generated in these steel blocks dynamically loaded the test model. The total mass of the test specimen (including the additional masses) was 10070kg.

During each seismic simulation, displacements, strains and accelerations were acquired simultaneously. Data was continuously collected by a HBM MGC Plus data acquisition system using a sampling rate of 200 Hz. The model was instrumented with the following sensors:

1. 192 Tokyo Sokki Kenkyujo 120Ω electrical resistance strain gages were atached to the surface of longitudinal reinforcement prior to casting the concrete. They were located at column and beam ends and labeled as shown in figures 2.3,2.4,2.5 and2.9.
2. Two HBM inductive displacement transducers model WA-500, indicated as LVDT-1 and LVDT-2 in figures 2.10 and 2.11. These sensors measured the relative horizontal displacement, v_1, between the shake table and the floor system in the direction of the seismic loading. One HBM inductive displacement transducer model WA-100, indicated as LVDT-3 in figures 2.10 and 2.11. measured the relative displacement between the shake table and the floor system in the direction perpendicular to the seismic loading.
3. Two HBM inductive displacement transducers model WA-500, indicated as LVDT-4 and LVDT-5 in figures 2.10 and 2.11. These sensors measured the relative horizontal displacement, v_2, between the floor system and the added weight at the top of the model in the direction of the seismic loading. One HBM inductive displacement transducer model WA-100, indicated as LVDT-6 in figures 2.10 and 2.11 measured the relative displacement between the added weight and the floor system in the direction perpendicular to the seismic loading.
4. Two pairs of Bruel & Kjaer piezoelectric and seismic accelerometers, labeled as seisimic and piezoelectric 1 and 2 in figures 2.10 and 2.11 were fixed to the floor system to measure the absolute response acceleration at the floor system, $\ddot{v}_1^t$ in the direction of the seismic loading. One Bruel & Kjaer seismic accelerometer labeled as seismic 3 measured the absolute response acceleration in the direction perpendicular to the seismic loading.
5. Two pairs of Bruel & Kjaer piezoelectric and seismic accelerometers, labeled as seisimic and piezoelectric 5 and 6 in figures 2.10 and 2.11 were fixed to the floor system to measure the absolute response acceleration at the floor system, $\ddot{v}_2^t$ in the direction of the seismic loading. One Bruel & Kjaer seismic accelerometer labeled as seismic 7 measured the absolute response acceleration in the direction perpendicular to the seismic loading.
6. One Bruel & Kjaer piezoelectric accelerometer lindicated as piezoelectric 4 was attached to the shaking table to measure the absolute acceleration, $\ddot{v}_g$ at the shaking table during the tests in the direction of the seismic loading.
7. Five video cameras recorded the experiments, four of them focusing columns bases, beam ends and beam-column joints.

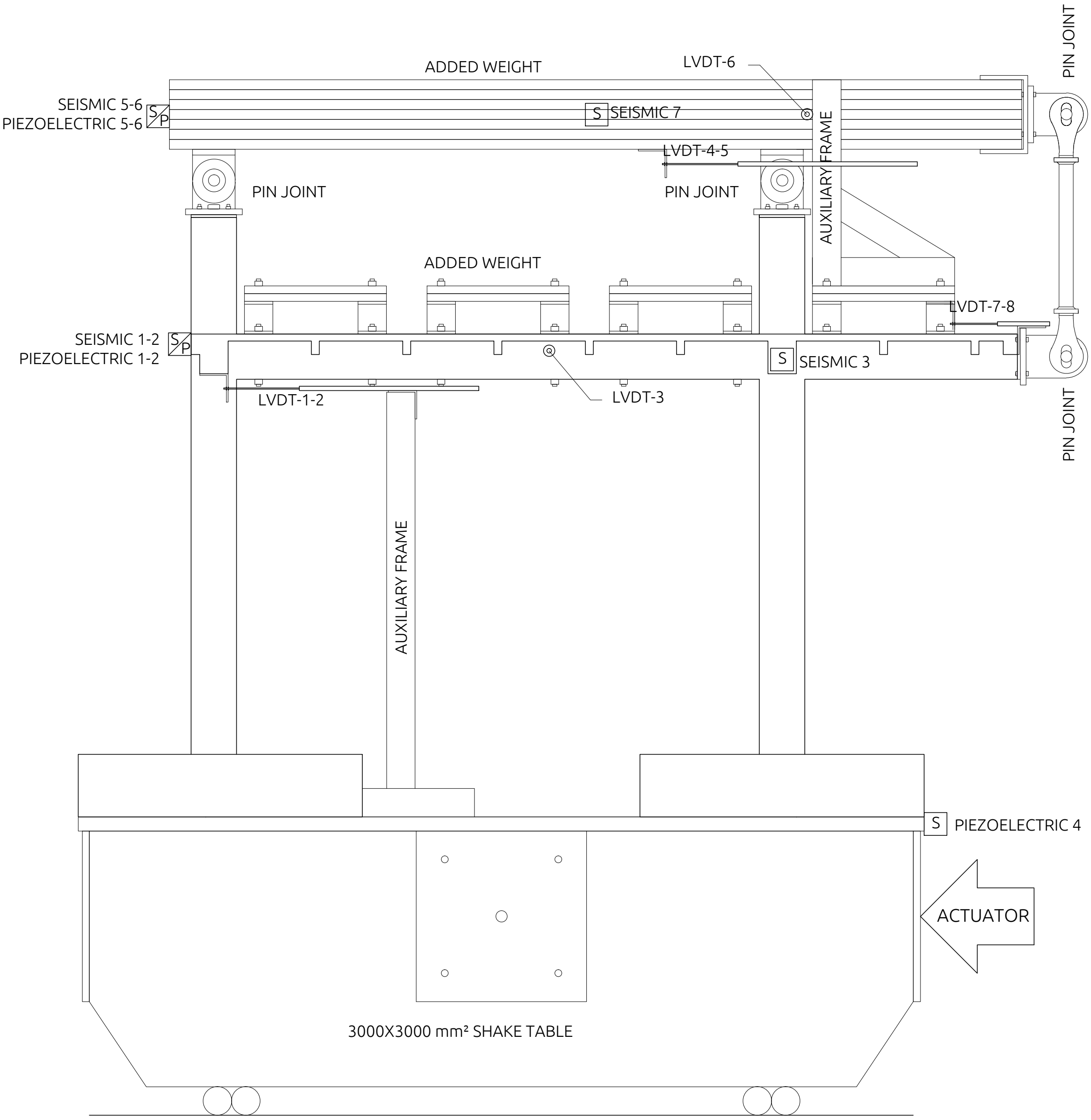

Figure 2.10.: Test set-up and instrumentation. Main frames view.

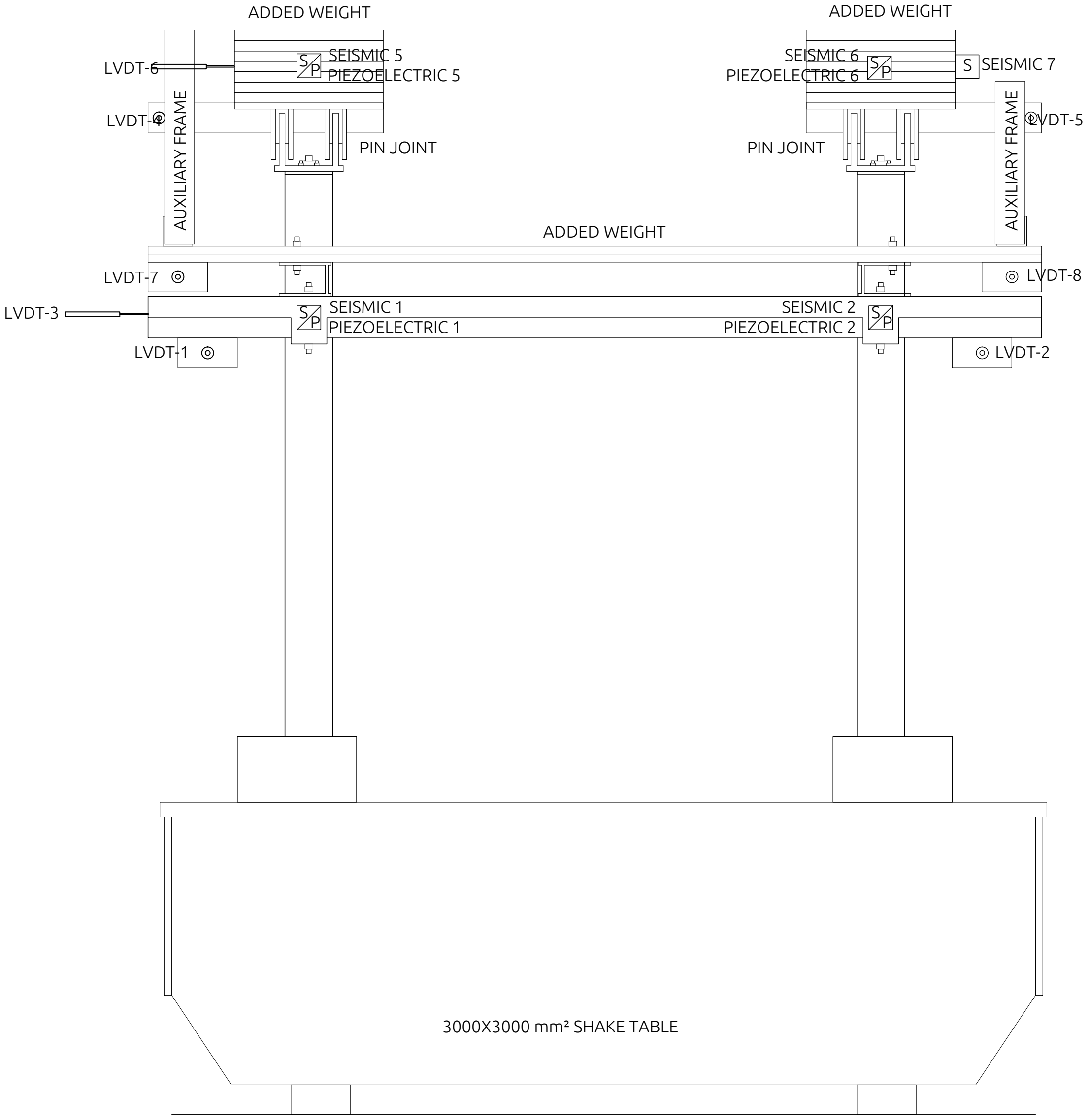

Figure 2.11.: Test set-up and instrumentation. Secondary frames view

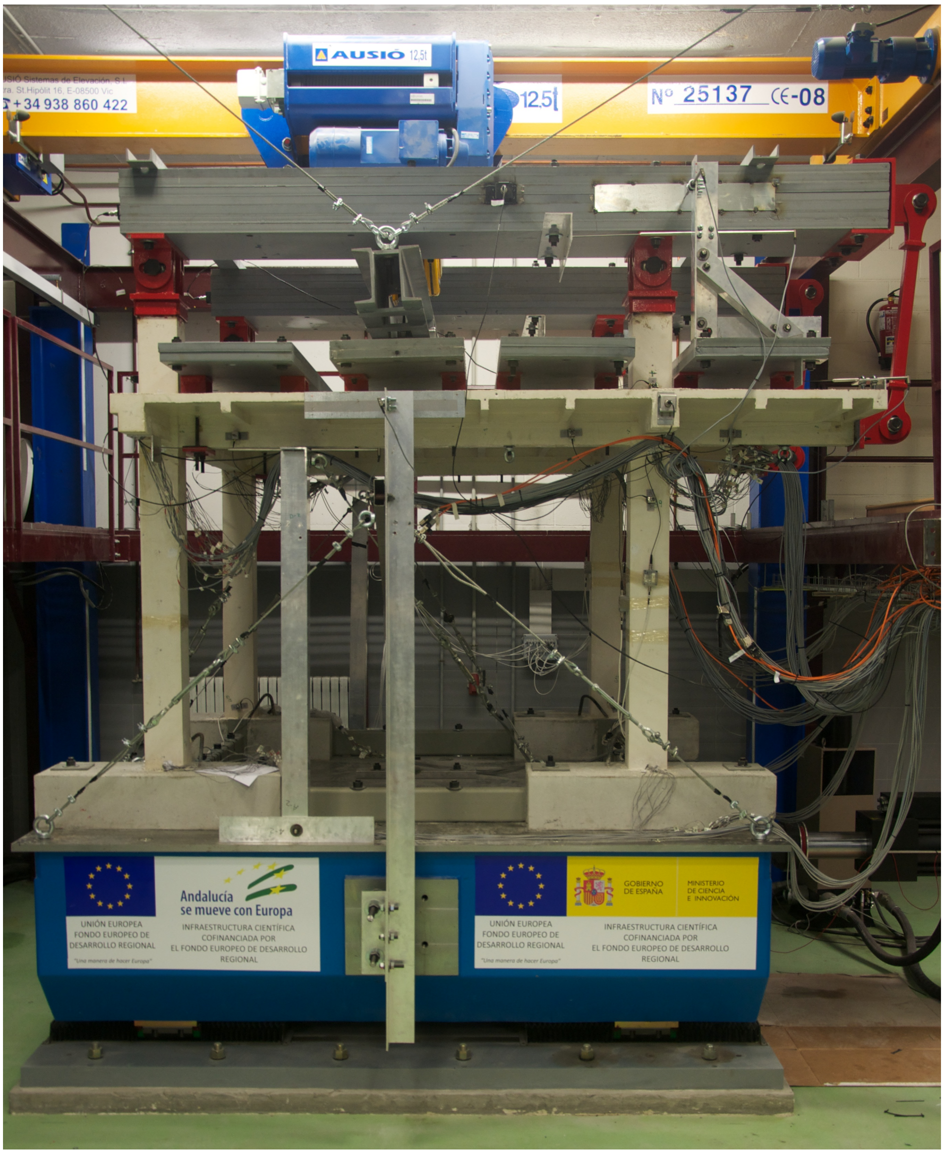

Figure 2.12.: Set-up overview

2.2.2. Seismic simmulations

The specimen was subjected to dynamic tests that consisted of four seismic simulations referred to as C50, C100, C200 and C300 herein, in which the shake table reproduced the ground motion recorded at Calitri during the Campano Lucano (1980) earthquake. Figure shows the time history ground acceleration $\ddot{v}_g$ and the 5% damped elastic response spectrum in terms of absolute acceleration, S_a and absolute velocity, S_v. The time history acceleration from figure 2.13 was respectively scaled in time by the scaling factor $\lambda_t = \sqrt{\lambda_L/\lambda_a} = 0.63$, and in amplitude to 50%, 100%, 200% and 300%. Their corresponding peak ground accelerations, PGAs, were 0.08g, 0.16g, 0.31g and 0.47g, respectively. Each PGA represents a different Seismic Hazard Level (SHL) at the site (Granada) that will be referred to hereafter as SHL-1, SHL-2, SHL-3 and SHL-4 respectively. SHL-1 represents a "very frequent" earthquake, SHL-2 a "frequent" earthquake, SHL-3 a "rare" earthquake, and SHL-4 a "very rare" or the "maximum considered" earthquake. Each SHL can be associated with a return period P_r of 17 years, 97 years, 500 years and 1435 years, respectively. The relation between P_r and PGA was obtained from the Spanish seismic code NCSE-02 [35] on the basis that: (i) the basic acceleration $a_{b,Pr}$ for a given P_r is $a_{b,Pr} = a_b(P_r/500)^{0.4}$, where a_b is the basic acceleration prescribed by NSCE-02 for $P_r = 500$ years; and (ii) the building is of ordinary importance and it is located in soft soil (type IV). According to NSCE-02, for this type of soil $PGA = 1.34\,a_{b,Pr}$. Free vibration tests were performed before and after each simulation.

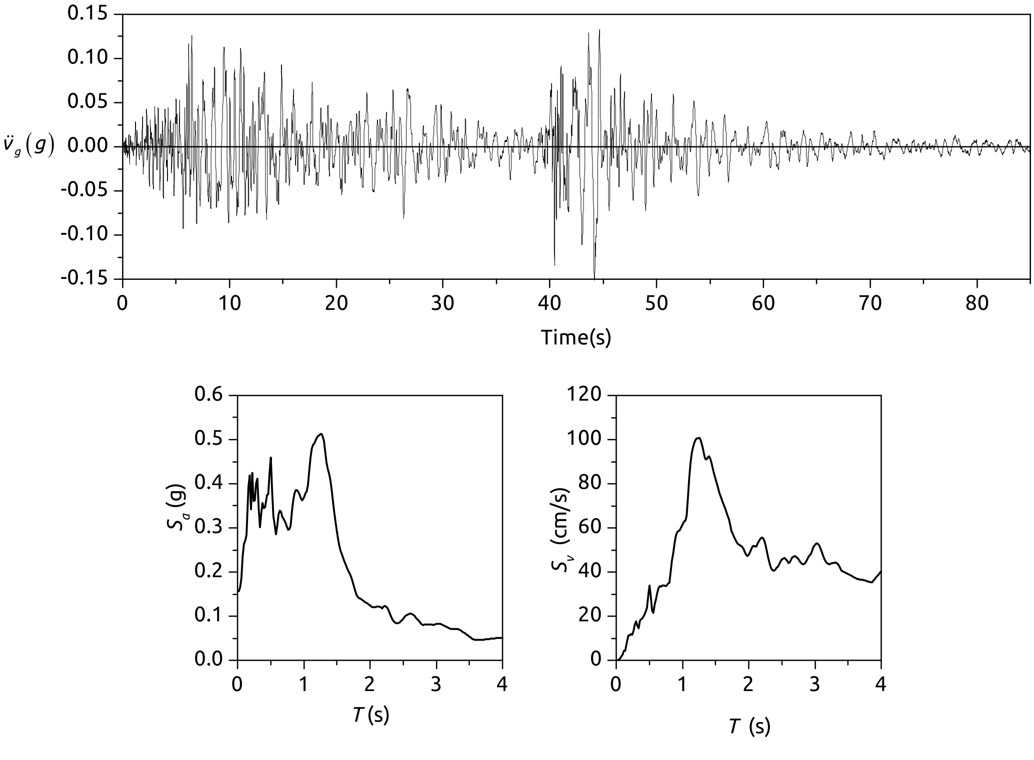

Figure 2.13.: Campano Lucano (1980) earthquake (Calitri). Unscaled history of accelerations and response spectra

2.3. Test results and discussion.

2.3.1. Dynamic characterization.

The third and fourth columns of Table 2.1 show the fundamental period $T_1$and the damping ratio ξ obtained from from the free vibration tests conducted prior and after each seismic simulation. $T_1$was calculated by averaging the time between response peaks for several cycles and dividing by the number of cycles.ξ was determined using the logarithmic decrement method. $T_1$and ξ increased with the intensity of the table motion reflecting increasing levels of damage. Before the seismic simulation C200, T_1 and ξ remained basically unchanged, indicating an undamaged structure that kept its initial lateral stiffness. After seismic simulation C200 the period T_1enlarged of about 70% and ξ about 40%, what reflects the occurrence of plastic deformations on the structure (damage) and an drop of the lateral stiffness up to about a 35% $\left(= 100\left({}^{0.32}/_{0.54}\right)^2\right)$of the initial value, as discussed later.

2.3.2. Overall response.

Figure 2.14 shows the time histories of the interstory drift, id, at each level in the direction of the shaking, for each seismic simulation. It was obtained by averaging the measurement provided by the displacements transducers LVDT-1 y LVDT-2 for story 1 and LVDT-4 and LVDT-5 for story 2. Figure 2.15 shows the corresponding time histories of absolute response acceleration $\ddot{v}_i^t = \ddot{v}_g + \ddot{v}$ at i-th story in the direction of the shaking.I

A detailed examination of the maximum response values response of the specimen after each seismic simulation is summarized in table 2.1. For each seismic simulation, Table 1 shows in columns five to ten the maximum response acceleration $\ddot{v}_{max}^t$ and maximum interstory drift id and the remanent interstory drift id_{rem} of each story. In case of simulation C300 there are two rows in the Table 4; the first one corresponds to the instant of collapse, as discussed latter, and the second one to the end of the seismic simulation. The strucutral performace level (SPL) of the structure is presented in column 11 accordingly to the id limiting values proposed by the SEAOC [85], ATC-40 [6] and FEMA-356 [45].

Seismic simulation	SHL	T_1 (s)	ξ %	story 1 $\ddot{v}^t_{max}$ (g)	story 1 id %	story 1 id_{rem} %	story 2 $\ddot{v}^t_{max}$ (g)	story 2 id %	story 2 id_{rem} %	SPL	SEAOC %	ATC %	FEMA %
C50	SHL-1	0.31	2.7	0.13	0.24	0.00	0.18	0.20	0.00	IO	$0.2<id<0.5$	1	1
C100	SHL-2	0.32	3.8	0.28	0.50	0.00	0.33	0.42	0.00	LS	$0.5<id<1.5$	1-2	2
C200	SHL-3	0.54	9.7	0.40	1.19	0.04	0.56	0.94	0.03	LS	$0.5<id<1.5$	1-2	2
C300*	SHL-4	-	-	-	4.08	-	-	4.03	-	C	>2.5	$>0.33^{V_i}/_{P_i}$	>4
C300	SHL-4	-	-	-	7.57	2.60		8.09	4.09	C	>2.5	$>0.33^{V_i}/_{P_i}$	>4

*At instant of collapse; V_i, total lateral shear force at story i; $P_i$total gravity load at story i;

Table 2.1.: Overall response parameters

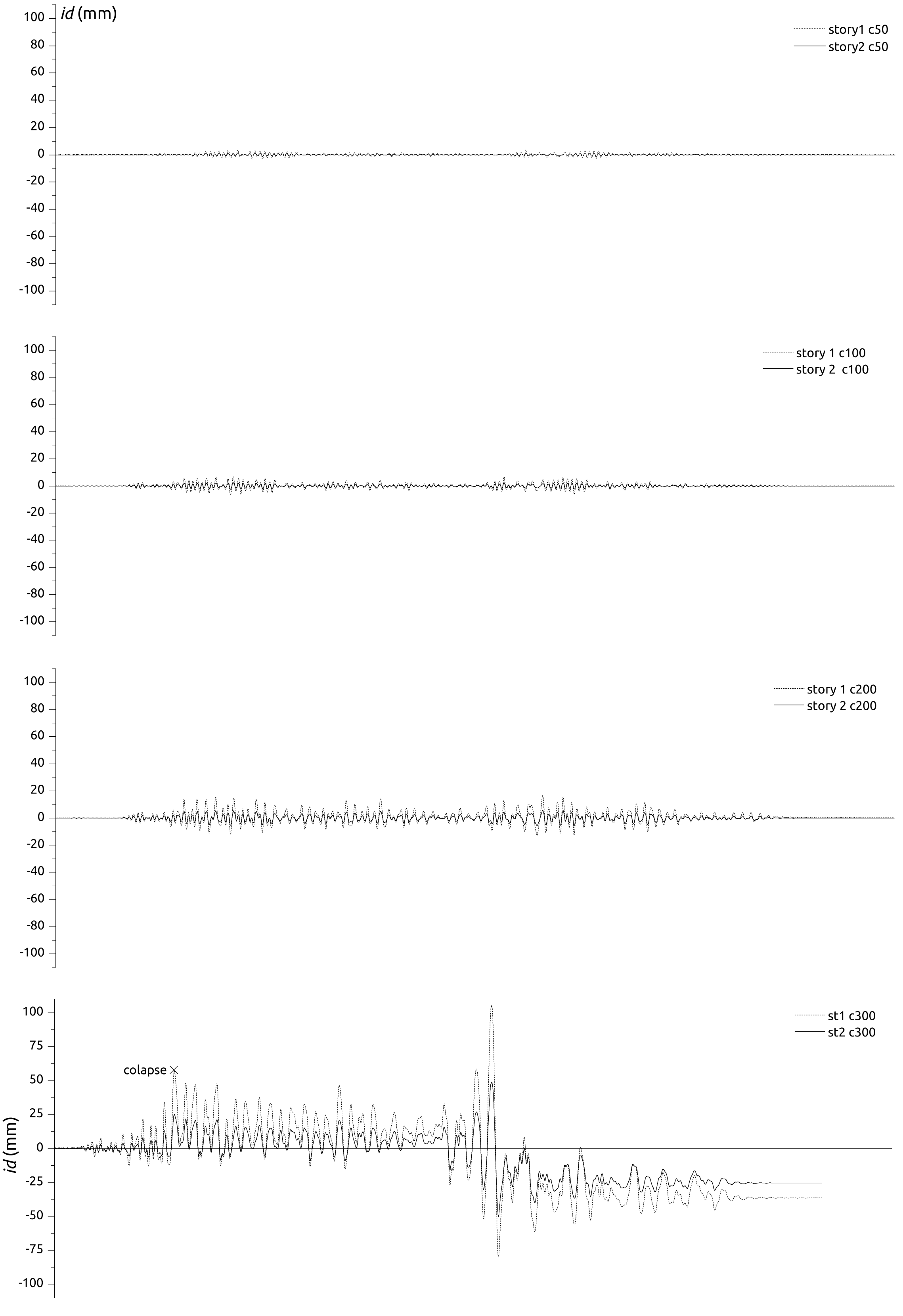

Figure 2.14.: Interstory drift time histories

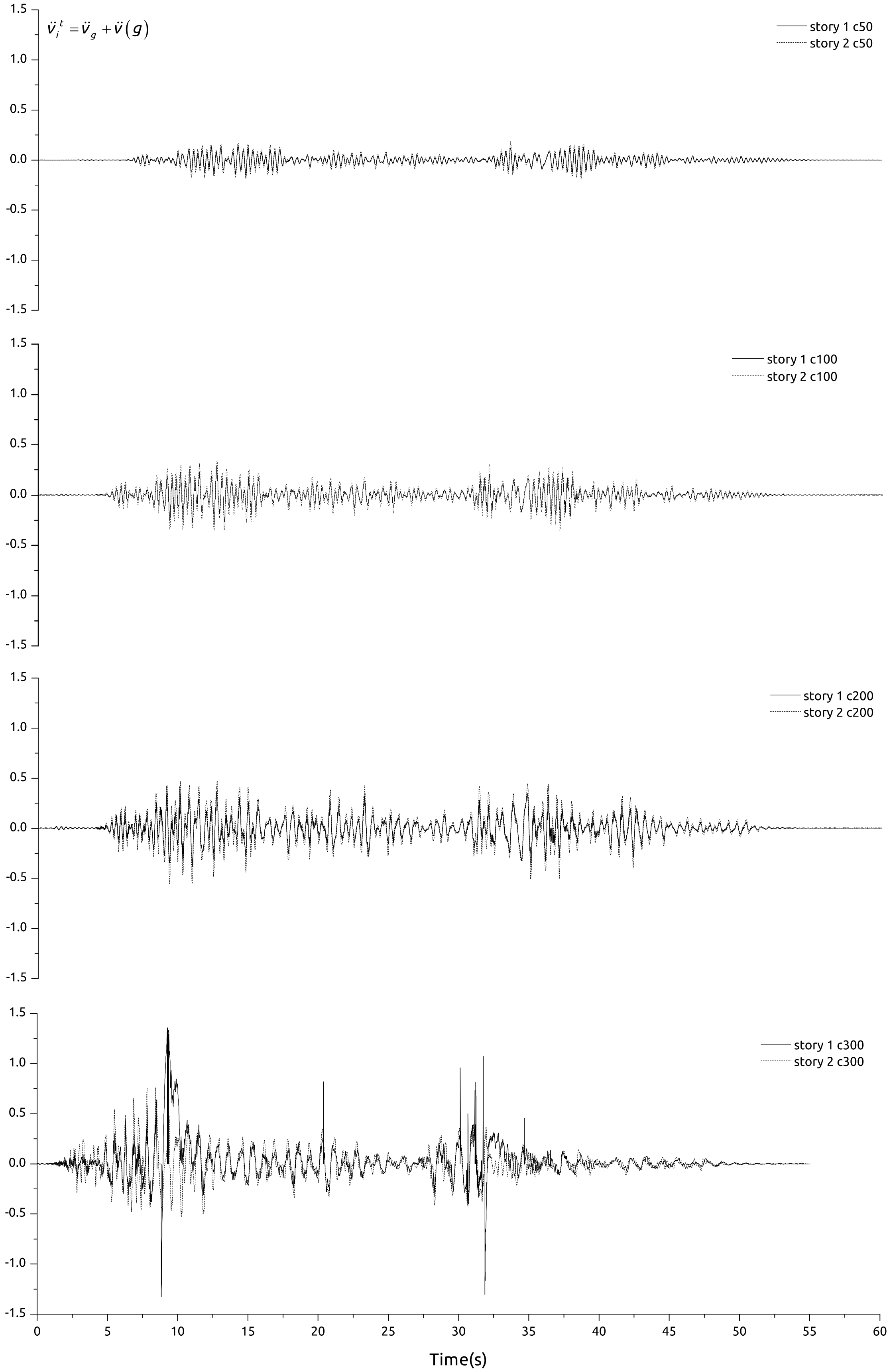

Figure 2.15.: Absolute response accelerations time histories

For convenience in the forthcoming discussions figure 2.16 shows an schematic idealization of the main frames. Columns and beams are considered as elastic elements conecting two plastic hinges at the ends, where the strain gauges are placed and the inelastic flexural deformation are expected. Each plastic hinge is labeled with an identification number n.

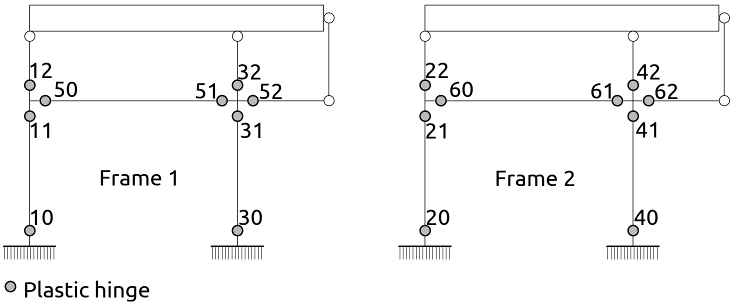

Figure 2.16.: RC main frames idealization

Table 2.2 summarizes the maximum strains measured in the longitudinal bars located at the member end sections of the two RC frames. Each member end section is a potential plastic hinge under lateral loadings, and it is identified with the number shown in Fig. 2.16. In Table 2.2 the member end sections are grouped according to their position in the frames (base, interior beam-column connection, and exterior beam-column connection). Several longitudinal reinforcing bars were instrumented at each member end section (see Figs. 2.3 to 2.9); Table 2.2 shows the maximum ϵ_{max} , $\bar{\epsilon}$, and the standard deviation σ of the strains measured at each section. The strains corresponding to the seismic simulation C300 area not included because during this simulation most gages reached their maximum measurable strain and stop functioning. The yield strain of the steel ϵ_y was 2625 μm/m.

The overall response of the tested structure is characterized by the formation of the expected strong column-weak beam mechanism, as indicated by the measurements of the strain gages, and by the fact that, for all seismic simulations, the interstory drift id reached very similar values in both stories. Plastic hinges developed basically at column bases and at beam ends, although some unexpected plastic strains (up to $1.4\epsilon_y$) were measured in one of the columns (sections 41 and 42 in figure 2.16) when the structure was on the verge of collapse. The members exhibited ductile flexural failures; shear or axial failures were not observed. A detailed description of the performance under each SHL is presented next.

The seismic simulation C50 represented a low SHL for the building site, that is, a "frequent" earthquake expected to take place during the conventional working life of the building, therefore having a mean return period shorter than 50 years. After this level of seismic action, referred to as SHL-1, the specimen showed no visible damage. The strains in the reinforcing bars at the base of the columns remained below $0.7\epsilon_y$, and those at beams ends below $0.5\epsilon_y$. The minor increase of 0.01s in T_1 shown in Table 2.1 can be attributed to the concrete micro cracking. There were no residual interstory drifts or other permanent structural deformations. The overall damage in qualitative terms was therefore very light. The maximum inter-story drift *id* reached 0.24% of story height. This *id* is within the range $0.2<id<0.5$ that the SEAOC [85] associates with the SPL of "Immediate Occupancy" (IO). The SPL of IO corresponds to the SPL of "Damage Limitation" (DL) in Eurocode-8 [39], which limits also the *id* to 0.5% if the story has brittle non-structural elements attached to the structure. For structures of ordinary importance, Eurocode-8 recommends pursuing the SPL of DL for a seismic action of $P_r = 95$ years.

The seismic simulation C100 corresponds to a moderate level earthquake, that is, an "occasional" earthquake with a mean return period between 75 and 200 years. During this level of seismic action, referred to as SHL-2, the longitudinal reinforcement at the base of the columns yielded reaching strains up to about $2\epsilon_y$. The sections at the ends of the beams were on the brim of yielding, exhibiting strains on the longitudinal reinforcement very close or slightly above ϵ_y. The longitudinal reinforcement of the columns at sections other than the base approached the yield strain (up to $0.75\epsilon_y$). This was accompanied by some cracking. The permanent deformations were negligible. The structure was basically undamaged and retained its integrity, full vertical load-bearing capacity, and sufficient residual lateral strength and stiffness to sustain additional shakings. The maximum*id* was 0.5% of story height. According to the SEAOC [85], this *id* is the boundary between the SPL of IO ($0.2<id<0.5$) and "life safety" (LS) ($0.5<id<1.5$). The value of P_r for the seismic simulation C100 (97 years) is very close to the mean return period of seismic action (95 years) under which Eurocode-8 recommends that the structure should respond in the SPL of DL, which is characterized by $id<0.5\%$. From this point of view, it can be said that the specimen behaved on the limit of what Eurocode-8 recommends.

The seismic simulation C200 represents a strong ground motion (the "design earthquake") at the building site, that is, a "rare" earthquake with a mean return period of about 500 years, and is referred to as SHL-3. A visual inspection of the specimen after this test revealed significant damage (extensive flexural cracks at the base of the columns and at beam ends), although the gravity-load bearing system kept functioning. Plastic hinges with ductile flexural yielding developed at the base of the columns and at beam ends. The maximum strains of the longitudinal reinforcement at the base of the columns ranged between $5\epsilon_y$ and $7\epsilon_y$, and those located at beam ends oscillated between $1.7\epsilon_y$ and $6.3\epsilon_y$. Concrete crushing was observed at the base of the columns. The frame developed a complete strong column-weak beam mechanism. Excepting in the sections at the base, columns remained basically elastic, although some slight inelastic excursion was measured in one column at hinges number 41 and 42 (see figure 2.16), where ϵ, exceeded the yield strain up to $1.4\epsilon_y$. Permanent deformation was very small (0.04% of story height). The maximum *id* was 1.19% of story height. According to the SEAOC, this *id* is close to the boundary between the SPLs of LS ($0.5 < id < 1.5$) and "collapse prevention" (CP) . The SPL of LS and CP are the counterparts of the SPLs denominated "significant damage" (SD) and "Near collapse" (NC) by Eurocode-8.

The seismic simulation C300 represents a "very rare" or the "maximum considered" earthquake, with quoted values of the mean return period in the order of 1000–2500 years. Under this seismic action, referred to as SHL-4, the structure was very heavily damaged. The records of a video camera that focused one of the beam ends showed that about 8 seconds after the onset of the movement of the shaking table, a flexural crack opened abruptly at the beam end reaching a maximum width of about 3mm, which was accompanied by a sudden vertical slide of approximately 10mm between the two sides of the flexural crack as shown in figure 2.17. Simultaneously, the interstory drifts reached about four times the maximum values attained in previous simulations. This vertical slide and the fact that the gages attached to the longitudinal reinforcement of this beam experienced a sudden increase of strain and stopped measuring, suggest the exhaustion of the beam's "ultimate" capacity. In this instant, the lateral drift at the top of the specimen (i.e. at the center of the pinned ends of the columns of the second story) was the 4.06% of the total height (2020mm). This instant is taken hereafter as the instant of collapse. In this same instant, severe concrete crashing was also observed at column bases as shown in figure 2.18. The test continued after this instant, and the lateral drift reached about the 8% of story height and the permanent deformations amounted about 4%. This SPL clearly corresponds to a situation of collapse.

Seismic Test		c50			c100			c200			
	Hinge number	ϵ_{max}	$\bar{\epsilon}$ $\left(\frac{\mu\text{m}}{\text{m}}\right)$	σ	ϵ_{max}	$\bar{\epsilon}$ $\left(\frac{\mu\text{m}}{\text{m}}\right)$	σ	ϵ_{max}	$\bar{\epsilon}$ $\left(\frac{\mu\text{m}}{\text{m}}\right)$	σ	$\frac{\sum M_{u,c}}{\sum M_{u,}}$
BASE COLUMN SECTIONS	10	1278	921	234	2598	2005	354	16683	11093	3756	
	20	1674	1234	273	5111	3128	1182	13005	7475	2823	
	30	1461	1200	153	2957	2480	262	18495	9926	5076	
	40	1827	1464	191	3799	2974	475	16185	12079	3398	
EXTERIOR CONECTION FRAME 1	12	591	341	151	1183	738	278	1637	1109	295	5.53
	11	366	213	88	701	421	187	1166	643	322	
	50	900	704	115	2090	1485	389	7500	4270	1757	
EXTERIOR CONECTION FRAME 2	22	656	402	136	1201	818	217	1570	1150	262	5.53
	21	568	349	139	1087	611	233	1454	738	314	
	60	1392	1002	194	2635	2018	315	16500	12148	4986	
INTERIOR CONECTION FRAME 1	32	672	456	86	1297	999	163	1998	1550	297	2.09
	31	568	310	147	1129	694	287	2189	1164	576	
	51	770	576	119	1853	1481	225	8697	4296	2804	
	52	686	485	161	1477	1308	131	4369	2737	809	
INTERIOR CONECTION FRAME 2	42	896	513	211	1702	1119	346	3253	1620	756	2.09
	41	978	519	300	1948	930	610	3313	1334	954	
	61	1024	740	150	2084	1725	289	5489	3190	1343	
	62	1069	538	433	1751	1247	323	6421	2678	1577	

Table 2.2.: Deformation of longitudinal reinforcement

(a) Hinge 50 (b) Hin 51

(c) Hin 60 (d) Hin 61

Figure 2.17.: Damage at beams after c300 test

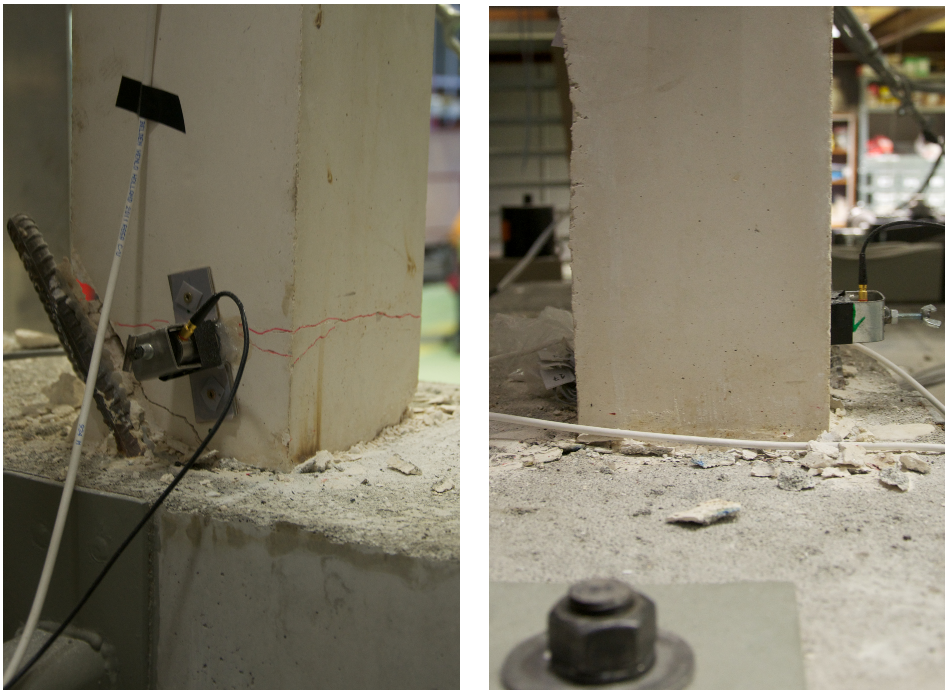

(a) Hin 10 (b) Hin 20

(c) Hin 30 (d) Hin 40

Figure 2.18.: Damage at colums after c300

The floor diaphragm with the added weight, and the added weight on the top of the columns can be assumed to behave as two rigid blocks, and they are idealized as two concentrated masses m_i of 5910 and 4160 kg, respectively. A degree of freedom consisting on the horizontal translation in the direction of shaking is assigned to each concentrated mass. With this model, the equation of dynamic equilibrium of the specimen is as follows:

$$\mathbf{m}\ddot{\mathbf{v}}^{\mathbf{t}} + \mathbf{c}\dot{\mathbf{v}} + \mathbf{F}_s = 0 \tag{2.1}$$

where $\mathbf{m}$ is the diagonal mass matrix, $\ddot{\mathbf{v}}^{\mathbf{t}}$ is the vector of absolute accelerations, $\mathbf{c}$ is damping matrix, $\dot{\mathbf{v}}$ is the vector of relative velocities and $\mathbf{F_S}$ the vector of restoring forces exerted by the structure. Since $\mathbf{m}$ is known and $\ddot{\mathbf{v}}^{\mathbf{t}}$ were measured with the accelerometers, the total shear force $F_{I,B}$ exerted by the inertial forces $\mathbf{F_I} = \mathbf{m}\ddot{\mathbf{u}}^{\mathbf{t}} = -\left(\mathbf{c}\dot{\mathbf{u}} + \mathbf{F_S}\right)$ at the base of the structure can be readily calculated as $F_{I,B} = \mathbf{F_i^T 1}$, where $\mathbf{1}$ is the unit vector. $F_{I,B}$ is plotted in figure 2.19 against the displacement of the top of the structure δ_t, for each seismic simulation. The results of simulation C300 are drawn until the instant of collapse; after this instant many channel of the data acquisition system overflow. The $F_{I,B} - \delta_t$ curve shown in figure 2.19 indicates that up to collapse, the overall response of the specimen was characterized by a stable energy dissipation behavior with minor pinching in the loops.

At the instants of maximum lateral displacement the velocity is zero and therefore the damping forces $\mathbf{c}\dot{\mathbf{v}}$ are null. At these instants $F_{I,B}$ coincides with the base shear force carried by the structure Q_B. Values of $F_{I,B}$ when the velocity is zero and thus $F_{I,B} = Q_B$ were calculated for each seismic simulation and they are plotted in figure 2.19 with open circles. These points define a polygonal curve that is drawn with bold line, which can be interpreted as a "capacity curve" of the structure. From this capacity curve, a yield base shear force, Q_{By}, and a yield top displacement δ_{ty} are defined for each domain of loading, giving $Q^+_{By} = 36.4\,\mathrm{kN}$, $\delta^+_{ty} = 11.7\,\mathrm{mm}$, $Q^-_{By} = 43.7\,\mathrm{kN}$, $\delta^-_{ty} = 13mm$. This capacity curve allows to calculate the averaged base shear force coefficient, $Q_B = 0.5(36.4 + 43.7)/100.7 = 0.4$, and initial stiffness $K_e = (36.4 + 43.7)/(11.7 + 13) = 3.24\,\mathrm{kN/mm}$. Comparing Q_B with the base shear force coefficient used in the design (0.22) it is concluded that the structure has an over strength of 0.4/0.22=1.8. This value is about 40% larger than the over strength specified by Eurocode 8. The initial fundamental period estimated with K_e and the total mass of the specimen (5910+4160=10070 kg) is 0.35s, which is close to that obtained from vibration tests (see Table 2.1).

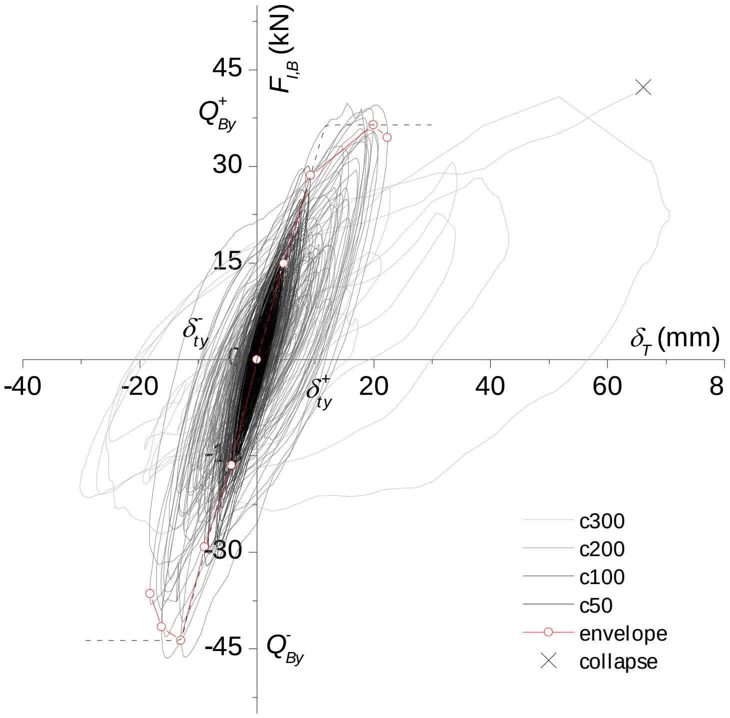

Figure 2.19.: Base shear due to inertial forces vs top displacement.

2.3.3. Gobal damage evaluation.

The energy balance of the structure at any instant t when it is subjected to a horizontal translational component of the ground motion is given by equation 2.2. Here, E_I is the (relative)[94] energy input by the earthquake, W_ξ is the energy dissipated by the inherent damping mechanism, W_p the hysteretic (plastic strain) energy, W_{es} the elastic strain energy and W_k is the kinetic energy. The energy E_I input in each seismic simulation can be easily calculated by equation 2.3 from the masses m_i, their relative velocity $\dot{v}_i$ and the acceleration on the shake-table $\ddot{v}_g$ measured during the tests. W_ξ can be estimated from the damping ratios measured experimentally (Table 2.1) assuming a Rayleigh damping matrix $\mathbf{C}$ as indicated by equation 2.4. The kinetic energy W_k is given by equation 2.5.

$$W_k + W_\xi + W_{es} + W_k = E_I \tag{2.2}$$

$$E_I = \sum_{i=1}^{2} \int_0^t m_i \ddot{v}_g \dot{v}_i dt \tag{2.3}$$

$$W_\xi = \int_0^t \dot{\mathbf{v}}^{\mathbf{T}} \mathbf{C} \dot{\mathbf{v}} dt \tag{2.4}$$

$$W_k = \frac{1}{2}\sum_{i=1}^{2} m_i \dot{u}^2 dt \tag{2.5}$$

The elastic and plastic strain energy absorbed/dissipated by a given plastic hinge n of the structure during the cyclic loading, is the sum of the energy dissipated by the concrete, $W_{C,k}$, and the energy dissipated by the longitudinal reinforcement, $W_{S,k}$ [69]. $W_{S,k}$ was estimated from the data measured during the seismic simulations as follows. The history of strain in a given longitudinal rebar r, $\epsilon_{sr}(t)$ was measured directly by the strain gauges, while the corresponding stress $\sigma_{sr}(t)$ can be approximated from $\epsilon_{sr}(t)$ using an energy conservative steel model that incorporates strain-hardening and Bauschinger effects [53, 4] . Calling A_{sr} the area of rebar r and assuming a length l_p for the plastic hinge, $W_{S,k}$ is:

$$W_{S,k} = \sum_{r=1}^{R} l_p A_{sr} \sigma_{sr} d\epsilon_{sr} \tag{2.6}$$

Where the summation is extended to the R steel longitudinal rebars of the cross section of the plastic hinge n. On the other hand, the energy dissipated by the concrete $W_{C,k}$ in a given plastic hinge n is computed by applying the following procedure: (i) the depth h of the cross section of the RC member is divided in N parts (referred to as fibers), each fiber j having a width b and an area $b(h/N)$; (ii) the plane-remaining-plane assumption is made and the strain $\epsilon_{Cj}(t)$ at a given fiber j is estimated from the curvature measured with the strain gages on the steel rebars; (iii) the corresponding stress $\epsilon_{Cj}(t)$ is approximated from $\epsilon_{Cj}(t)$ using a modified Kent and Park material model with linear loading and reloading paths and no tensile strength; and (iv) the energy $W_{C,k}$ is calculated by:

$$W_{C,k} = \sum_{j=1}^{N} l_p b \frac{h}{N} \sigma_{Cj} d\epsilon_{Cj} \tag{2.7}$$

The elastic and plastic strain energy absorbed/dissipated by a given plastic hinge n is thus:

$$W_{es,n} + W_{p,n} = W_{Sn} + W_{Cn} \tag{2.8}$$

The total elastic and plastic strain energy absorbed/dissipated by the structure is the sum of the contributions of the p plastic hinges, that is:

$$W_{es} + W_p = \sum_{n=1}^{p} \left(W_{es,n} + W_{p,n}\right) \tag{2.9}$$

Figure 2.20a shows the histories of E_I, W_k, $W_k + W_\xi$, $W_k + W_\xi + W_{es} + W_p$ accumulated in the successive seismic simulations from the beginning of simulation C50 until collapse. The amounts of energy input during seismic simulations C50 and C100 are much smaller than that of simulation C200; the energies for C50 are about one-fifth of those of C100, and the latter about one-fifth of

C200. To better view the history of energies for simulation C50 and C100, a zoom of Fig. 2.20a in the temporal range of these simulations is shown in Figs. 2.20b to 2.20d. In the case of simulation C300 it was not possible to calculate the energies beyond collapse due to the large displacements and deformations experienced by the structure, which caused overflow in the measurements of many channels of the data acquisition system. It can be seen in the figures that the bold solid line representing the last member of equation 2.2, E_I, and the thin solid line representing the second member 2.2 are in general very close. This supports the validity of the approximation explained above to estimate $W_{es} + W_p$, and the use of a Rayleigh approach for representing the damping. It is also seen in the figures that in all simulations the kinetic energy W_k is very small in comparison to the other energies. The difference between E_I and W_ξ is what Housner [51] called the energy that contributes to damage E_D, and neglecting W_k it is given by:

$$E_D = E_I - W_\xi \cong W_{es} + W_p \tag{2.10}$$

E_D at any instant t is represented in figure 2.20a by the difference between the dotted line and the solid line, as indicated with arrows. It is observed that E_D increases over time. E_D can be interpreted as a quantitative measure of the global damage imparted to the structure. For convenience, E_I and E_D can be normalized with respect to the total mass ($m1 + m2$) and expressed by equivalent velocities V_E and V_D defined by:

$$V_E = \sqrt{\frac{2E_I}{\sum_{i=1}^{2} m_i}} \tag{2.11}$$

$$V_D = \sqrt{\frac{2E_D}{\sum_{i=1}^{2} m_i}} \tag{2.12}$$

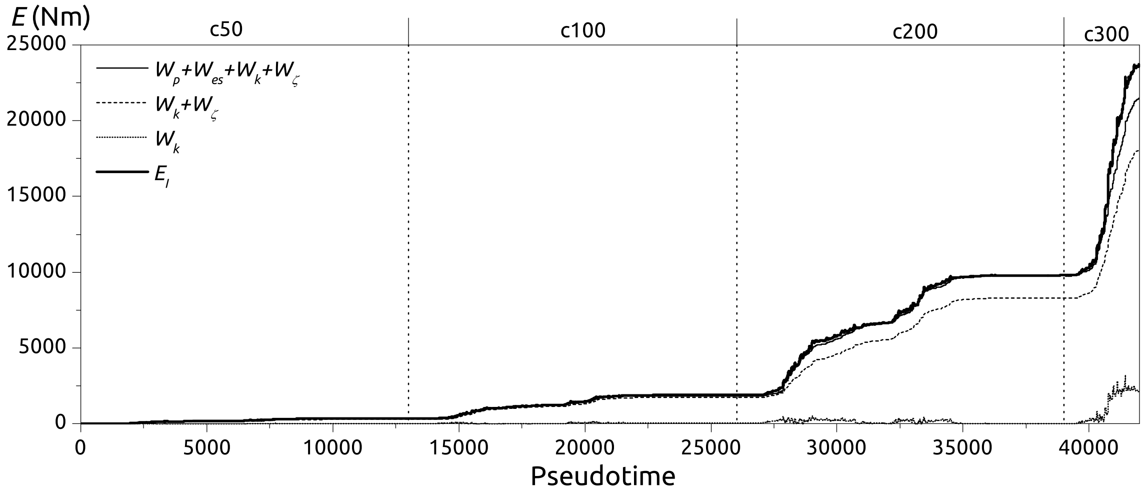

(a) Accumulated energy up to collapse

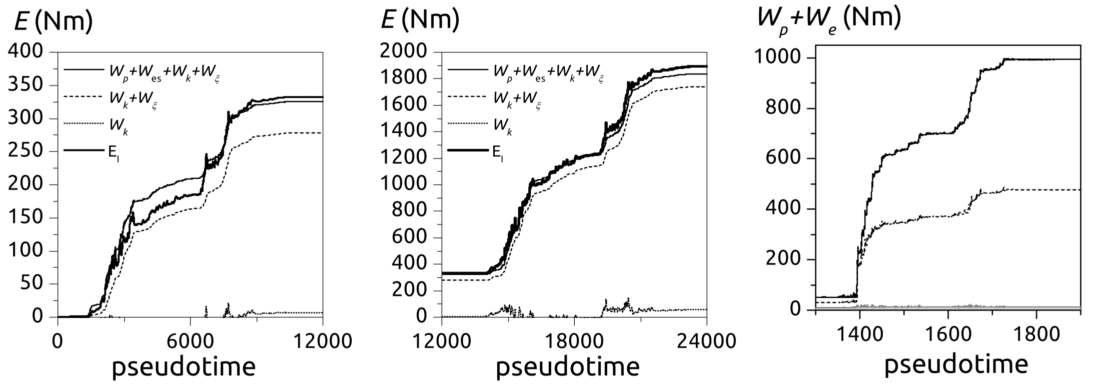

(b) c50 (c) c100 (d) c200

Figure 2.20.: Histories of accumulated energy

Table 2.3 summarizes the (cumulated) input energy V_E, and the corresponding (cumulated) damage imparted to the specimen in terms of V_D from the onset of the tests up to the end of a given seismic simulation or to collapse. It is worth noting that the values V_E and V_D of Table 3 are calculated for the specimen from the test results and that the specimen was scaled by the factors indicated in subsection 2.1. To obtain the corresponding energies in the prototype (real) structure, $V_{E,p}$ and $V_{D,p}$, the values must be divided by the scaling factor for velocity $\lambda_v = {}^{\lambda_L}/_{\lambda_t} = 0.63$. V_D provides a quantitative evaluation of the overall damage expected in a conventional RC frame structure designed following modern codes in a moderate seismicity region (characterized by ab=0.23g for the "design earthquake" associated with Pr=475 years, assuming a ductility factor of 3 and damping ratio 5%, for three typical SHLs characterized in terms of V_E. Table 2.3 indicates that for the design earthquake SHL-3, the expected damage to the structure in terms of equivalent velocity V_D is about 40% of the total input V_E. Expressed directly in terms of energy and taking into account equation 2.12, the expected energy contributing to damage E_D represents approximately 15% of the total energy input by the earthquake E_I.

	Specimen		Prototype	
Energy cumulated values after test	V_E cm/s	V_D cm/s	$V_{E,p}$ cm/s	$V_{D,p}$ cm/s
c50	26	10	41	16
c100	62	17	98	27
c200	140	55	222	87
c300	216	106	343	168

Table 2.3.: Energies in terms of equivalent velocity

2.3.4. Damage at plastic hinges

The energy $W_{es,k} + W_{p,k}$ absorbed/dissipated by the plastic hinges during each seismic simulation, as calculated with equations 2.6 and 2.7, was grouped and summed as follows: energy absorbed/dissipated at the base of the columns (i.e. hinges number 10, 20, 30 and 40 in figure 2.16), energy absorbed/dissipated at beam ends (i.e. hinges number 50, 51, 52, 60, 61, 62 in figure 2.16), energy absorbed/dissipated at the upper ends of the columns of the first story (hinges number 11, 31, 21, 41 in figure 2.16), and energy absorbed/dissipated at lower ends of the columns of the second story (hinges number 12, 32, 22, 42 in figure 2.16). The total energy absorbed/dissipated by the hinges of each group is plotted in figure 2.21a. These energies have been accumulated in the successive seismic simulations, from the onset of simulation C50 until collapse during simulation C300. Since the amounts of energy input during seismic simulations C50 and C100 are much smaller than that of simulation C300 up to collapse, a zoom of figure 2.21a in the temporal range of simulations C50 , C100 and C200 is shown in figures 2.21b,2.21c and 2.21d, respectively. Since the specimen developed a "strong column-weak beam" mechanism, the energy absorbed/dissipated by the upper ends of the columns of the first story and by the lower ends of the columns of the second story is small in comparison to that dissipated at the base of the columns and at beam ends. Until the end of seismic simulation C200, the energy absorbed/dissipated at the base of the columns is from 1.5 to 2 times larger than that dissipated by the beams. However, when the specimen is on the brim of collapse (at the beginning of simulation C300), there is an abrupt increase of about four times of the energy dissipated at beam ends while that dissipated at column bases increases only 1.6 times. The curves do not increase monotonically due to the presence of elastic strain energy (absorbed energy); this effect is negligible in the seismic simulation C200 because the amount of absorbed energy is very small in comparison with the energy dissipated through plastic deformations. During seismic simulation C50, the main source of energy dissipation was the plastic deformation of concrete, since the longitudinal reinforcement did not yield. During the seismic simulation C100, both concrete and longitudinal reinforcement dissipated energy by means of inelastic strains. Conversely, during the seismic simulation C200 energy dissipated by concrete is negligible in comparison to that by the steel.

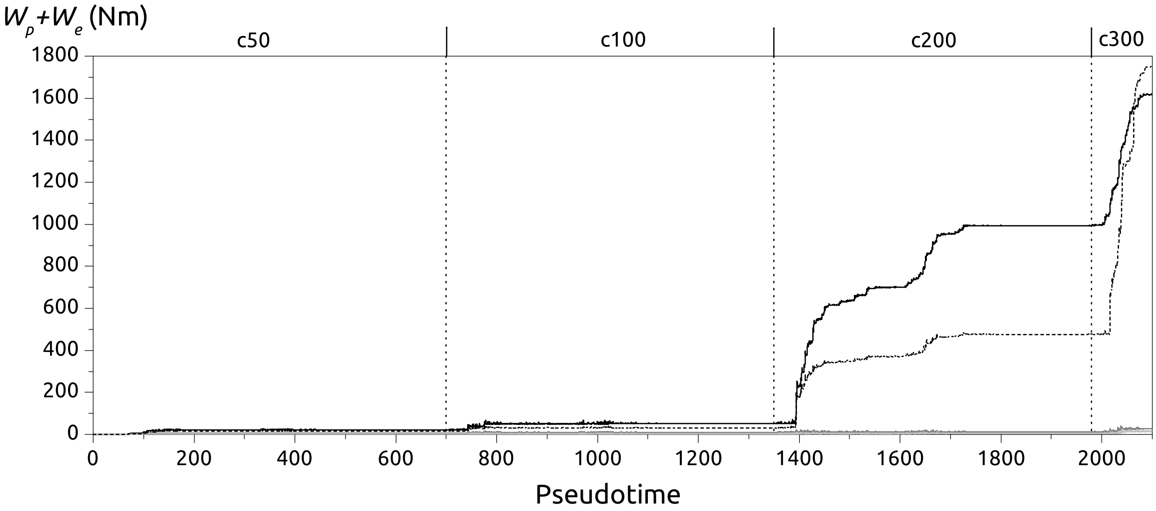

(a) Up to collapse

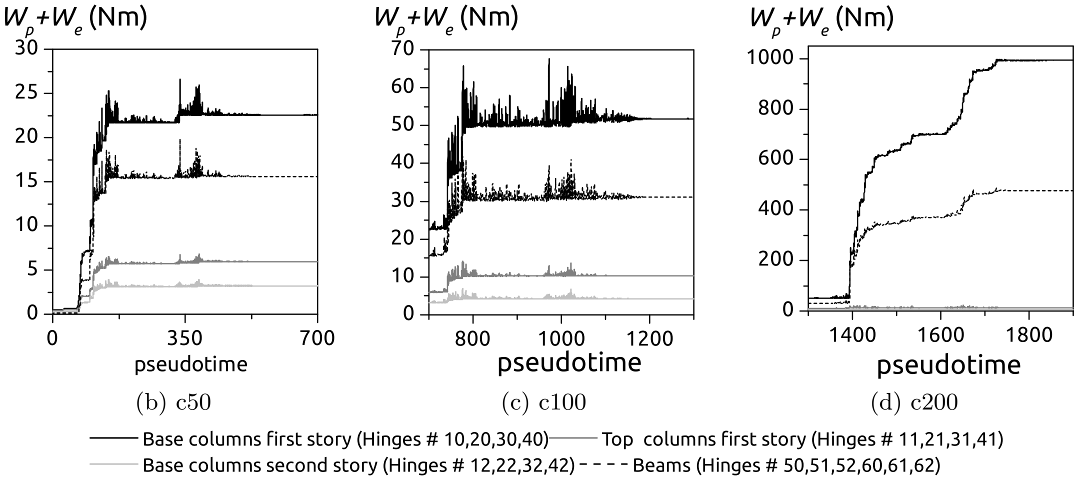

(b) c50 (c) c100 (d) c200

Figure 2.21.: Energy dissipated by plastic hinges

The damage at the level of each individual hinge n was estimated in terms of maximum chord rotation demand θ_m in relation chord rotation capacity at ultimate θ_u, i.e. $\theta_m/\theta_u = max\left(|\theta_m^+/\theta_u^+|, |\theta_m^-/\theta_u^-|\right)$, the energy-based damage index D_i proposed by Darwing and Nmai [33], and the well-known index of damage DI_{PA} developed by Park and Ang [33] considering parameter $\beta = 1$. The results are shown in table 2.4. The damage index D_i, and the Park and Angindex of damage DI_{PA} at a given hinge n were calculated with the following equations:

$$D_i = \frac{W_{p,n}}{0.5\left(M_y^+\theta_y^+ + |M_y^-\theta_y^-|\right)} \tag{2.13}$$

$$DI_{PA} = 0.5\left(\frac{\theta_m^+ - \theta_y^+}{\theta_u^+ - \theta_y^+} + \frac{|\theta_m^- - \theta_y^-|}{|\theta_u^- - \theta_y^-}\right) + \beta\frac{W_{p,n}}{0.5\left(M_y^+\theta_u^+ + |M_y^-\theta_u^-|\right)} \tag{2.14}$$

The chord rotation demand θ_m was estimated from the measurements provided by displacement transducers during the tests. The chord rotation capacities at yielding θ_y and ultimate θ_u states were predicted with the equation recommended by Eurocode 8 Part 3 (Annex A)[39]:

$$\theta_y = \phi_y \frac{L_V + \alpha_V z}{3} + 0.00135\left(1 + 1.5\frac{h}{L_v}\right) + \frac{\epsilon_y}{d - d'}\frac{d_{bL} f_y}{6\sqrt{f_c}} \tag{2.15}$$

Where, ϕ_y is the yielding curvature obtained with Response 2000 software [18], $L_V = {}^{M}/_{V}$ is the ratio moment shear at the end section, α_v equals 1 if shear cracking is expected to precede flexural yielding at the end of the section otherwise 0, h is the depth of the member, $\epsilon_y = {}^{f_y}/_{E_s}$is the yielding strain for steel reinforcement, d and d' are the depths to the tension and compression reinforcement, respectivelly and d_{bL} is the mean diameter of the tension reinforcement.

$$\theta_u = \frac{1}{\gamma_{el}} 0.0016 \cdot (0.3^{\nu}) \left[\frac{max\,(0.01;\omega')}{max\,(0.01;\omega)} f_c\right]^{0.225} \left(\frac{L_V}{h}\right)^{0.35} 25^{\left(\alpha\rho_{SX}\frac{f_{yw}}{f_c}\right)} \left(1.25^{100\rho_d}\right) \tag{2.16}$$

Where γ_{el} is equal to 1.5 for primary elements and 1.0 for secondary elements, $\nu = {}^{N}/_{bhf_c}$(b width of compression zone, N axial force positive for compression), $\omega; \omega'$ are the mechanical reinforcement ratio of the tension and compresion longitudinal reinforcement respectively, f_c is the concrese compressive strength, f_{yw} is the stirrup yield strength, $\rho_{SX} = {}^{A_{SX}}/_{b_w s_h}$ is the ratio of transverse steel parallel to the direction x of loading ($s_h$is the stirrup spacing), ρ_d is the ratio of diagonal reinforcement and α is the confinement effectiveness factor estimated by means of equation 2.17:

$$\alpha = \left(1 - \frac{s_h}{2b_0}\right)\left(1 - \frac{s_h}{2h_0}\right)\left(1 - \frac{\Sigma b_i^2}{6h_0 b_0}\right) \tag{2.17}$$

where $h_0$and b_0 is the dimension of the core to the center line of the hoop and b_i is the centerline spacing oflongitudinal bars laterally restrained by a stirrup corner or a cross-tie along the perimeter of the cross-section.

The yielding moment under positive and negative bending, $M_y^{\pm}$were estimated with the following expressions for beams:

$$M_y = 0.9hA_t f_y \tag{2.18}$$

and for columns:

$$\begin{cases} \text{if } N_{max} > N > 0.4bhf_c & M_y = \dfrac{\left(0.8A_t f_y h + 0.12bh^2 f_c\right)\left(N_{max} - N\right)}{N_{max} - (0.4bhf_c)} \\ \text{if } 0.4bhf_c > N > 0 & M_y = (0.8A_t f_y h) + 0.5Nh\left(1 - ({}^{N}/_{bhf_c})\right) \\ \text{if } 0 > N > N_{min} & M_y = 0.8A_t f_y h + 0.4Nh \end{cases} \tag{2.19}$$

where N is the axial force in the column (positive in compression); $N_{max} = bhf_c + A_g f_y$; $N_{min} = A_g f_y$; A_t is the area of longitudinal reinforcement in tension; A_g is the total area of longitudinal reinforcement in the section; and b, h are the base and depth of the section.

The damage in the plastic hinges was basically null for the seismic simulations C50 and C100. At the end of this simulation C200, the specimen experienced significant damage, attaining chord rotations of about one-fourth of the capacity at ultimate; the damage index D_i reached 7.38, and the index of damage by Park and Ang DI_{PA} reached 0.22. In general, damage was larger in the plastic hinges at the base of the columns than at beam ends. At the instant of collapse, during seismic simulation C300, the chord rotation demand reached the ultimate capacity with ratios θ_m/θ_u very close to $\theta_m/\theta_u = 1$; the damage index D_i reached 22.32 and the damage index DI_{PA} was about 1. The pattern of larger damage at column bases than at beam end observed during simulation C200 remained at collapse. The following considerations must be made to interpret these results. First, the fact that the collapse of the hinges at column bases and at beam ends occurred for values of θ_m/θ_u very close to 1 indicates that the formula recommended by Eurocode 8-Part 3 for assessing chord rotation capacities at ultimate of RC beams and columns subjected to cyclic loading produces very good estimates. Second, on the basis of extensive experimental studies, Darwin and Nmai [33] concluded that the range of D_i for well-behaving RC beams was between 17 and 142; further, these authors recommended $D_i = 35$ to provide adequate performance under cyclic loading. The RC beams tested in the shake-table sustained values of D_i larger than 17 (i.e. 22.32) and can thus be classified as "well behaving beams"; but the values are lower than the one recommended by these authors (35). Third, the results of the shake-table test indicate that the use of ultimate chord rotation capacities θ_u estimated with Eurocode 8-Part 3, using the factor $\beta = 0.1$ (as suggested by Park et al. for nominal strength deterioration) to calculate the index DI_{PA} with equation 2.14, provides a very good estimate of the level of damage in the range $DI_{PA} = 0$ (no damage) to $DI_{PA} = 1$ (collapse).

		c50			c100			c200			c300*		
	hinge number	$\frac{\theta_m}{\theta_y}$	D_i	DI_{PA}	$\frac{\theta_m}{\theta_y}$	D_i	DI_{PA}	$\frac{\theta_m}{\theta_y}$	D_i	DI_{PA}	$\frac{\theta_m}{\theta_y}$	D_i	DI_{PA}
Frame 1	10	0.06	0.04	0.00	0.11	0.07	0.00	0.28	4.83	0.22	1.05	5.81	1.09
	20	0.06	0.18	0.00	0.11	0.51	0.01	0.28	4.75	0.21	1.05	8.52	1.14
	11	0.00	0.02	0.00	0.00	0.05	0.01	0.00	0.05	0.00	0.00	0.06	0.00
	21	0.00	0.002	0.00	0.00	0.005	0.00	0.00	0.07	0.00	0.00	0.08	0.00
	12	0.00	0.01	0.00	0.00	0.01	0.00	0.00	0.01	0.00	0.00	0.1	0.00
	22	0.00	0.02	0.00	0.00	0.02	0.00	0.00	0.003	0.00	0.00	0.06	0.00
	50	0.05	0.003	0.00	0.11	0.06	0.00	0.26	0.40	0.14	0.97	22.32	1.28
	51	0.05	0.05	0.00	0.11	0.06	0.00	0.26	0.40	0.14	0.97	2.49	1.00
	52	0.05	0.04	0.00	0.11	0.06	0.00	0.26	0.13	0.14	0.97	1.66	1.00
Frame 2	30	0.06	0.03	0.00	0.11	0.06	0.00	0.28	1.28	0.16	1.05	2.01	1.03
	40	0.06	0.16	0.00	0.11	0.31	0.01	0.28	7.38	0.26	1.05	13.37	1.22
	31	0.00	0.02	0.00	0.00	0.04	0.00	0.00	0.05	0.00	0.00	0.09	0.00
	41	0.00	0.05	0.00	0.00	0.07	0.00	0.00	0.07	0.00	0.00	0.29	0.00
	32	0.00	0.01	0.00	0.00	0.02	0.00	0.00	0.02	0.00	0.00	0.04	0.00
	42	0.00	0.02	0.00	0.00	0.02	0.00	0.00	0.03	0.00	0.00	0.13	0.00
	60	0.05	0.03	0.00	0.11	0.06	0.00	0.26	5.98	0.22	0.97	5.97	1.05
	61	0.05	0.04	0.00	0.11	0.06	0.00	0.26	0.16	0.14	0.97	2.83	1.01
	62	0.05	0.18	0.00	0.11	0.43	0.01	0.26	4.04	0.19	0.97	5.53	1.95

Table 2.4.: Rotation demand and damage indexes

2.3.5. Beam to column strength ratio.

In order to assure the formation of a strong column-weak beam mechanism and reduce the likelihood of yielding in columns, seismic codes typically require that the sum of flexural strengths of columns framing into a joint be larger than the sum of flexural strengths of the beams framing to the same joint. The amount by which the strength of the columns must exceed that of the beam varies depending on the code. ACI-318-08 [5] requires$\sum M_{nc} \geq 1.2 \sum M_{nb}$ and Eurocode 8 [39] $\sum M_{Rc} \geq 1.3 \sum M_{Rb}$. Here, M_{nc} and M_{nb} are the nominal flexural strengths of columns and beams, while M_{Rc} and M_{Rb} are the corresponding design values. In both cases, the bending moments M_{nc}, M_{nb}, M_{Rc} , M_{Rb} must be evaluated at the faces of the joint. The last column of Table 2.1 shows the beam to column ultimate strength ratios evaluated at the faces of the joints for the specimen tested. $M_{u,c}$ and $M_{u,b}$ were computed from nominal dimensions and the material strengths described in section 2.1, in accordance with code definitions, provisions and assumptions of the strength design methods of ACI-318-08,the corresponding steel reinforcement for beams, and the corresponding steel reinforcement and axial load for columns. The ratios $\sum M_{u,c}/\sum M_{u,b}$ obtained are high due to the overstrength provided in columns at the design stage. In the case of interior joints, the ratio$\sum M_{u,c}/\sum M_{u,b} = 2.09$ is clearly above the minimum required by ACI-318-08 and Eurocode 8, but this fact did not prevent some plastic deformation from taking place in the longitudinal reinforcement of one of the columns (up to 1.4 times the yield strain).

2.4. Summary and conclusions.

Shake-table tests resulting in collapse were conducted on a 2/5-scale reinforced concrete frame structure designed according to current building seismic codes that follow the strong column-weak beam philosophy and capacity design criteria. The specimen was subjected to four seismic simulations representative of "very frequent", "frequent", "rare" and "very rare" earthquakes associated with return periods of 17, 97, 500 and 1435 years, respectively, in the Mediterranean area. The results of the tests lead us to put forth the following conclusions that are transferable to similar structures:

- For the "frequent earthquake", the specimen remained basically undamaged, with maximum interstory drifts of 0.5%, Park and Ang's index of damage in the plastic hinges below 0.01, and maximum chord rotations below 11% of their ultimate capacity. The specimen performed on the boundary of the "immediate occupancy" and "life safety" seismic levels, that is, on the limit of what Eurocode 8 recommends.
- For the "rare earthquake" (design earthquake), the specimen developed a strong column-weak beam mechanism and experienced significant damage. Maximum strains of longitudinal reinforcement in column bases and at beam ends reached about 7 times the yield strain, the maximum interstory drift was 1.19%, and the maximum chord rotations reached 28% of their ultimate capacity. The seismic performance approached the upper bound of the "life safety" level.

- The specimen collapsed at the beginning of the seismic simulation that represented the “very rare” event (maximum considered earthquake). Collapse was characterized by the opening of large flexural cracks of about 3mm, and simultaneous severe vertical sliding (of about 10mm) between the two sides of the crack. At this instant, the lateral drift exceeded 4%, Park and Ang’s index of damage in the plastic hinges was above 1 in all hinges (reaching 1.28 in one of them), and maximum chord rotations reached the ultimate rotation capacity. In general, the structure designed according to modern codes performed adequately (yet on the limit) for the seismic hazard levels corresponding to a "frequent earthquake" and to a "design earthquake", but the performance was not satisfactory for the "very rare" or “maximum considered” earthquake.
- The test data when the specimen reached the point of collapse were compared with the formula recommended by Eurocode 8 (Part 3, informative Annex A). Comparison suggests that Eurocode 8 produces very good estimates on ultimate chord rotation capacities of RC beams and columns under cyclic loading.
- Park and Ang’s damage index with $\beta = 0.1$ was calculated at the instant of collapse for each plastic hinge, giving values very close to 1. This corroborates that the Park and Ang index with $\beta = 0.1$ is a good indicator of the level of damage on RC elements subjected to bending, in a range between 0 (no damage) and 1 (collapse).

3. Quasi-static cyclic tests on ductile walls

Within the conventional seismic resistant structures, the RC frames with RC ductile walls are an alternative to the bare frames dealt with in Chapter 2. Structural walls have been commonly used during the past decades as a lateral-load resisting system. But field observations made by Prof. Pujol after the Maule, Chile, Earthquake of 2010 have shown that structural walls can be vulnerable to rather modest displacement demands. The RC frames with RC walls combine in parallel two systems of very diferent lateral stiffness: the RC frame and the RC wall. The former can be understood as the "flexible part" and the latter as the "stiff part" of a mixed flexible-stiff structure [3]. From this point of view, the RC walls play the same role than the energy dissipating devices in innovative systems consisting on RC frames with hysteretic dampers. The seismic behavior of conventional RC frames was investigated in Chapter 2 through dynamic shaking table tests. This Chaper 3 is devoted to investigate experimentally the conventional RC ductile walls through quasi-static cyclic tests. The final aim is to compare quantitatively the cyclic response of RC ductile walls with that of the hysteretic dampers. In this comparison, two commonly used reinforcing patters of the RC wall are considered. The experimentall results conducted on RC ductile walls provides also new contributions on: (i) unit curvature and unit strain distribution that allow to better understanding of the plastic hinge length in structural walls; and (ii) the influence of the existence of confinement reinforcement at the boundary elements on the hysteretic behavior and ultimate capacity of the RC wall. It is found that that the seismic performance of the hysteretic damper is superior to that of the RC ductile wall. As a result, this thesis goes for the use of RC frames with hysteretioc dampers, instead of RC frames with RC walls. Accordingly, the following chapters of this thesis are focused on the soluciton of RC frames with hysteretic dampers, and adress the seismic response of the combined system taking into account the interaction between the frame and the dampers.

The response of slender walls with height to length ratios larger or equal to two was studied in several experimental tests [72, 73, 74, 34, 78, 1, 93] probing that the inelastic response of the walls is controlled by a desirable flexural mode of failure. These flxural inelastic deformations are mainly located at the base of the wall in what is referred to as plastic hinges, where the response of the wall (i.e. strength, deformation and energy dissipation) is governed. The most common assumptions in the characterization of the plastic hinges are that: i) the normal strain distribution along the wall cross section, used to compute the inelastic curvatures φ_i , is linear. ii) the inelastic curvatures are constant over the length of the idealized plastic hinge, L_p. Based in this simplified assumptions the force-displacement relationship of structural walls can be easily obtained for seismic design and assessment purposes [[98, 42]. This method has been become very popular among design engineers and has been incorporated in the latest codes as [39, 6, 45, 5] because of it simplicity. The most common formulations of this method consider that the displacement of the wall Δ_i, is the sum of an elastic displacement, Δ_y and a plastic displacement Δ_p as can be seen in figure 3.1. In structural walls where displacement is dominated by flexural deformations, the wall displacement can be obtained by integrating the unit curvature distributions over the wall height by means of equation 3.1:

$$\Delta_i = \Delta_y + \Delta_p = \varphi_y \frac{H^2}{3} + (\varphi_i - \varphi_y)\, L_p \left(H - \frac{L_p}{2}\right) \tag{3.1}$$

Where φ_y is the yielding curvature and H is the total height of the wall

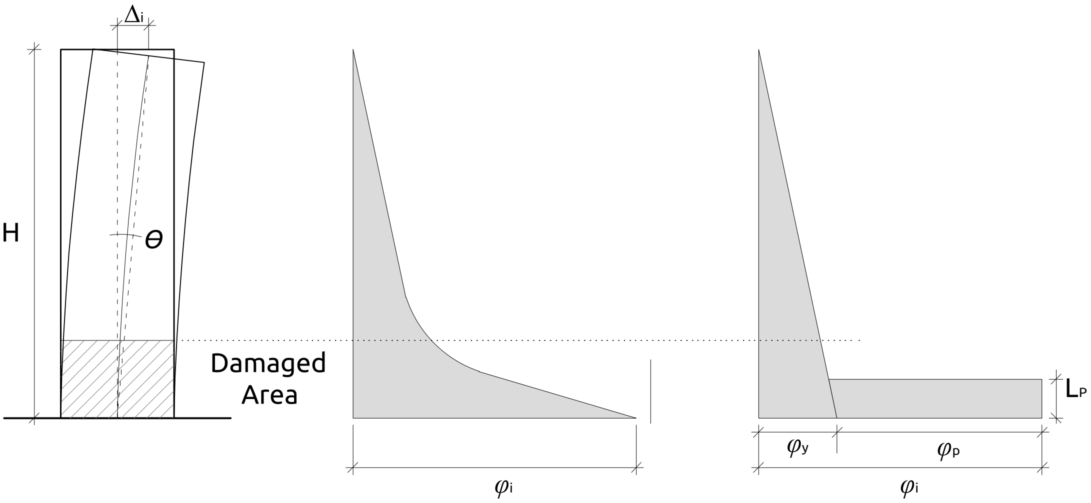

a) Deflections a) Curvature distribution c) Equivalent curvature distribution

Figure 3.1.: Displacements and curvature distribution.

But this simplicity comes at a price: how is one to estimate (or even measure) a quantity as abstract as the length of the idealized hinge? And even if one did so, what is the maximum curvature reached before failure which we can call limiting curvature? The traditional strain limits for concrete of 0.003 and 0.004 are certainly stringent, but being stringent is not always required or necessary. In the case of the length of the idealized hinge, researchers have proposed a plethora of expressions during the last decades for RC columns and beams starting with work at Portland Cement Association and University of Illinois [99, 22, 61] and continuing more recently by several researchers [9, 10, 77, 79]. But we have found less information about the case of structural walls. Wallace & Mohele [97] suggested that the length of the idealized hinge can be assumed to be half the wall length . Adebar et al. [1] proposed plastic hinge lengths based on the results of non-linear finite element analyses validated by tests results . Dazio[34] et al. suggested several strain limits based on the curvature measured at the base of six shear walls during a cyclic loading test .

As pointed out in the beguining of this section, fhe reinforcement detailing of the RC wall can have a great influence on its seismic response. More precisselly, the inclusion or not of confinement reinforcement at the boundary elements of the wall can have a great influcence the hysteretic behavior. This chapter presents the results from two large-scale reinforced concrete structural wall tests that were conducted at Purdue University. One of the specimens differs from the other in the inclusion of confinement reinforcement at the boundary elements. The author of this thesis participated in these tests through two research stays of three months each. The tests conducted at Purdue Universy were led by Santiago Pujol, who is an associate professor of Purdue University that belongs to the reseach group of the project MEC BIA2008 00050 (funded by the Spanish Governement). The author did this thesis with a scholarship (FPI) linked to this research project.

3.1. Structural wall design and description of tests specimens.

Two large-scale reinforced concrete structural walls in full scale were tested under cyclic loads of increasing amplitude at Purdue University. One of the specimens (W-MC-C) had confinement reinforcement in the boundary elements while the other (W-MC-N) did not have any confinement reinforcement. The height to length aspect ratio both was $h_w/l_w = 2.4$ in both specimens.

Specimen W-MC-C (figure 3.2) was designed to meet ACI-318-11 [5] confinement reinforcement requirements. The longitudinal reinforcement was 4 ϕ25.4mm bars in each boundary element and 6 ϕ12.7mm bars in the web. The confinement reinforcement was ϕ6.3mm hoops spaced at 63 mm in center to center in the lower 1.5 m of the wall. Ties were cut from ϕ9.52mm bars and were spaced at 127 mm. They had 135 degree hooks. Specimen W-MC-N (figure 3.3) had the same layout except that is had no confinement reinforcement. The total longitudinal reinforcement ratio was $\rho = 1.2\%$. Both specimens had mechanical couplers at the base of the wall to splice all longitudinal bars from the wall and bars anchored in the footing. Measure values of the yield stress, f_y, and ultimate stress, f_u , of the reinforcement, as well as the compressive strength, f_c , tensile strength from splitting cylinder tests, f_{ct} , and module of elasticity, E_c , of the concrete are listed in table 3.1.

Steel			Concrete						
				W-MC-C			W-MC-N		
ϕ	fy	fsu	Lift	f'c	fct	Ec	f'c	fct	Ec
mm	(MPa)	(MPa)		(MPa)	(MPa)	(MPa)	(MPa)	(MPa)	(MPa)
6.3	475	550	Footing 1	35	3.1	25131	34.8	2.7	25131
9.5	480	675	Footing 2	31.7	3.2	22228	31.5	2.7	24848
12.7	427	620	0-1.95 m	30.7	3.2	25076	30.8	2.8	17712
25.4	461	648	1.95-3.3 m	34.7	2.9	26703	35.37	2.9	25786
28.6	427	675	3.3-3.6 m	33	2.9	27647	34.9	3	27510

Table 3.1.: Mechanical properties of materials

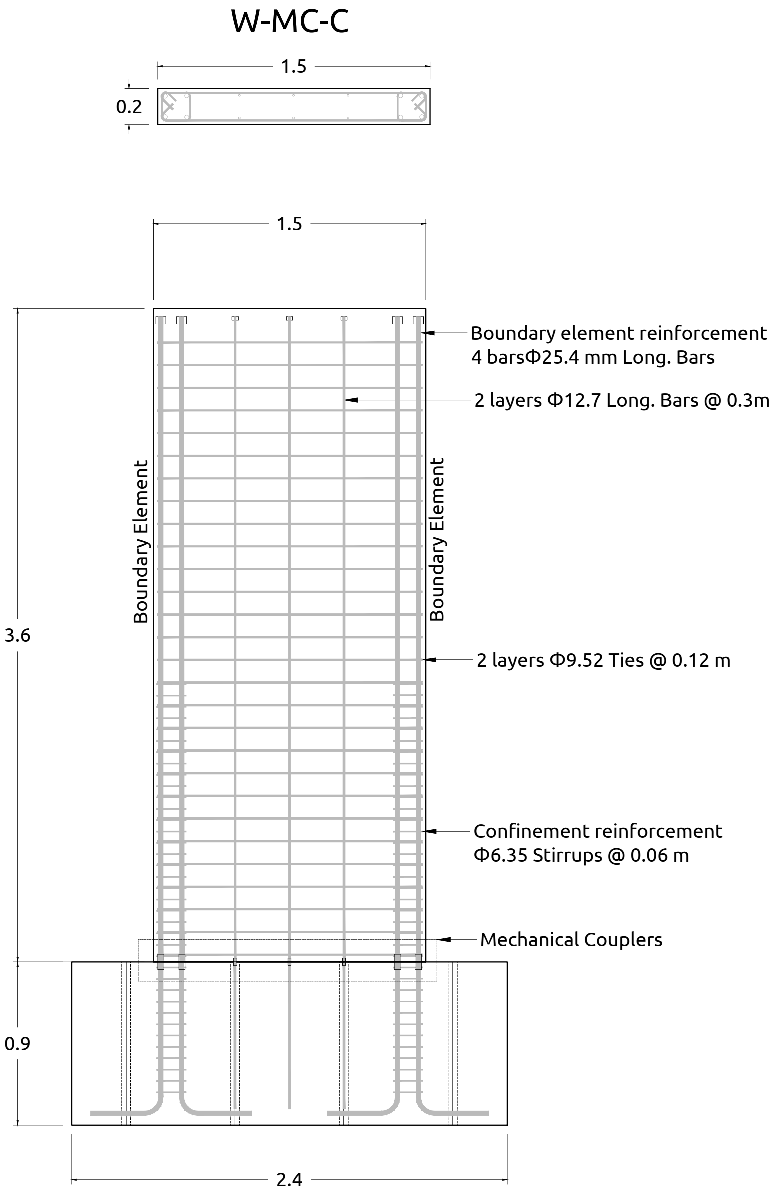

Figure 3.2.: Geometry and reinforcement details W-MC-C

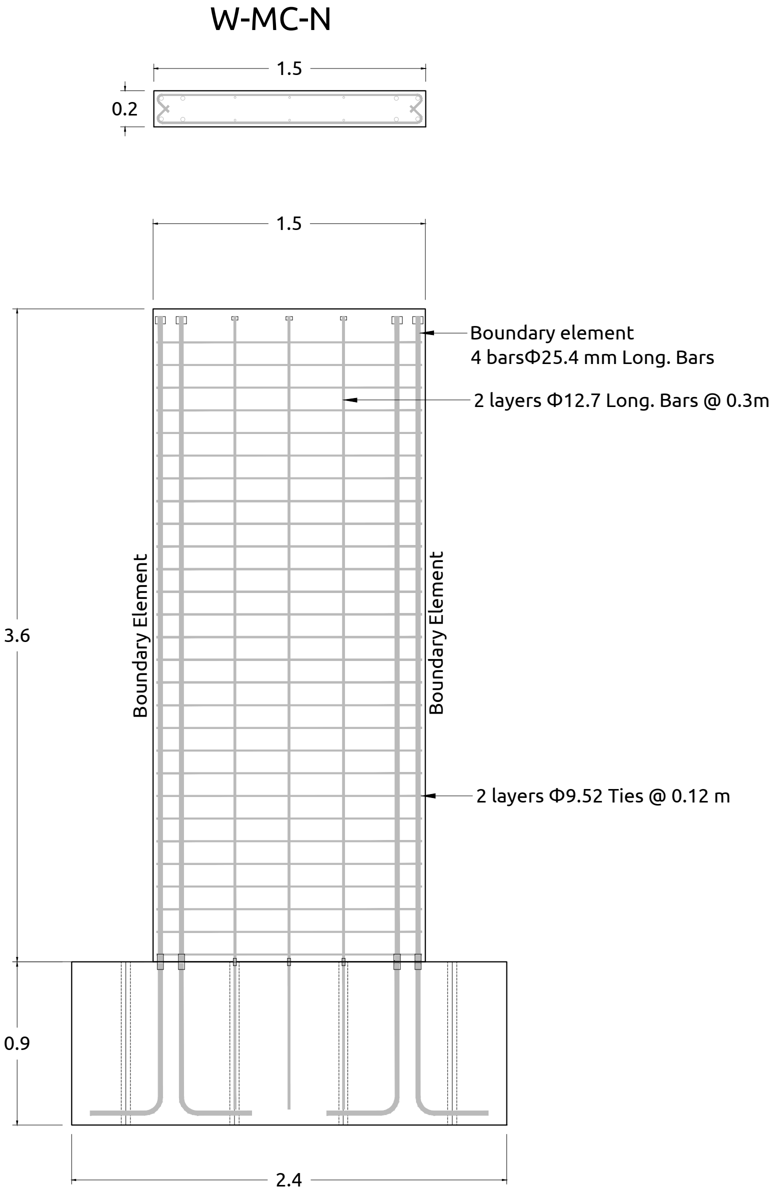

Figure 3.3.: Geometry and reinforcement details W-MC-N

3.2. Set-up, instrumentation and loading history.

The structural walls were fixed to the strong floor using 8 ϕ3cm diameter post-tensioning bars with a total clamping force of 4270 kN providing a fix-end restraint. The walls were loaded using two hydraulic actuators, supported by the strong wall, with hinges at both ends. The resultant from the actuator forces acted at approximately 3.31 m. from the top of the foundation block. The axial load was applied using four post-tensioning bars connected to foundation. The bars were post-tensioned by 4 jacks placed at the top of the walls. The pressure in the jacks was controlled to keep the axial load nearly constant through the tests. Two load cells (LC1 and LC2 in Fig. 3) were used to monitor the axial load. Steel tubes were placed on either side of the wall, 3m from the top of the foundation block and parallel to the loading direction, to prevent the out of plane movement of the walls exceeding approximately 5 mm. figure 3.4 shows the experimental set up.

3.2.1. Instrumentation.

Figure 3.5 shows the labels and positions of instruments. During each cycle loads and displacements, was measured with the following sensors :

- Load cells LC1 and LC2 measured the applied load.
- Load cells LC3 and LC4 measured the axial load.
- Optical encoders, ENC 1 to 8 and 12, measured the displacements in the direction of the loading.
- The coordinates of 62 non contact coordinate-tracking targets forming a 0.3 by 0.3 m grid were also measured at of the peak of each cycle using an Optotrack Pro system.

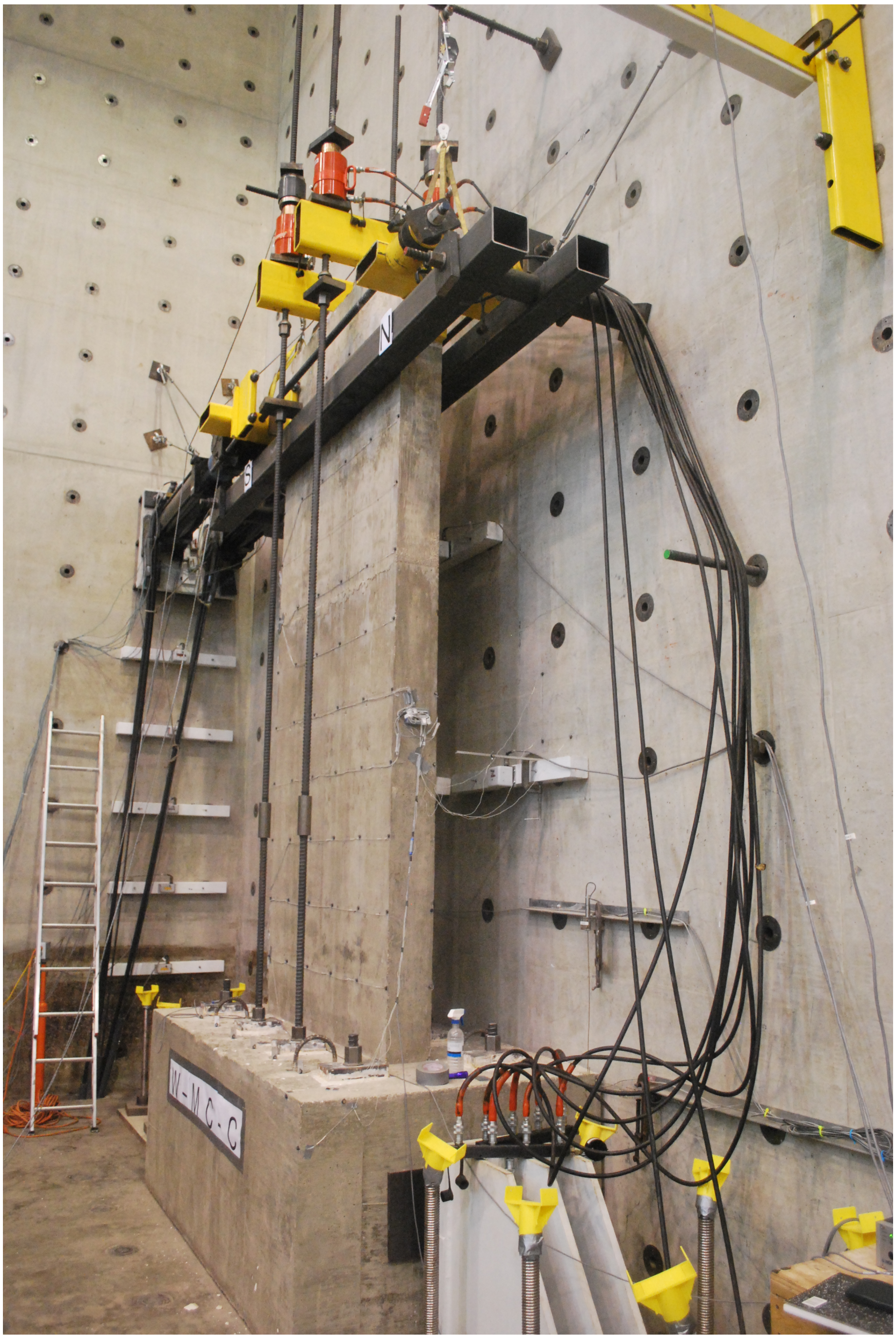

Figure 3.4.: Set-up

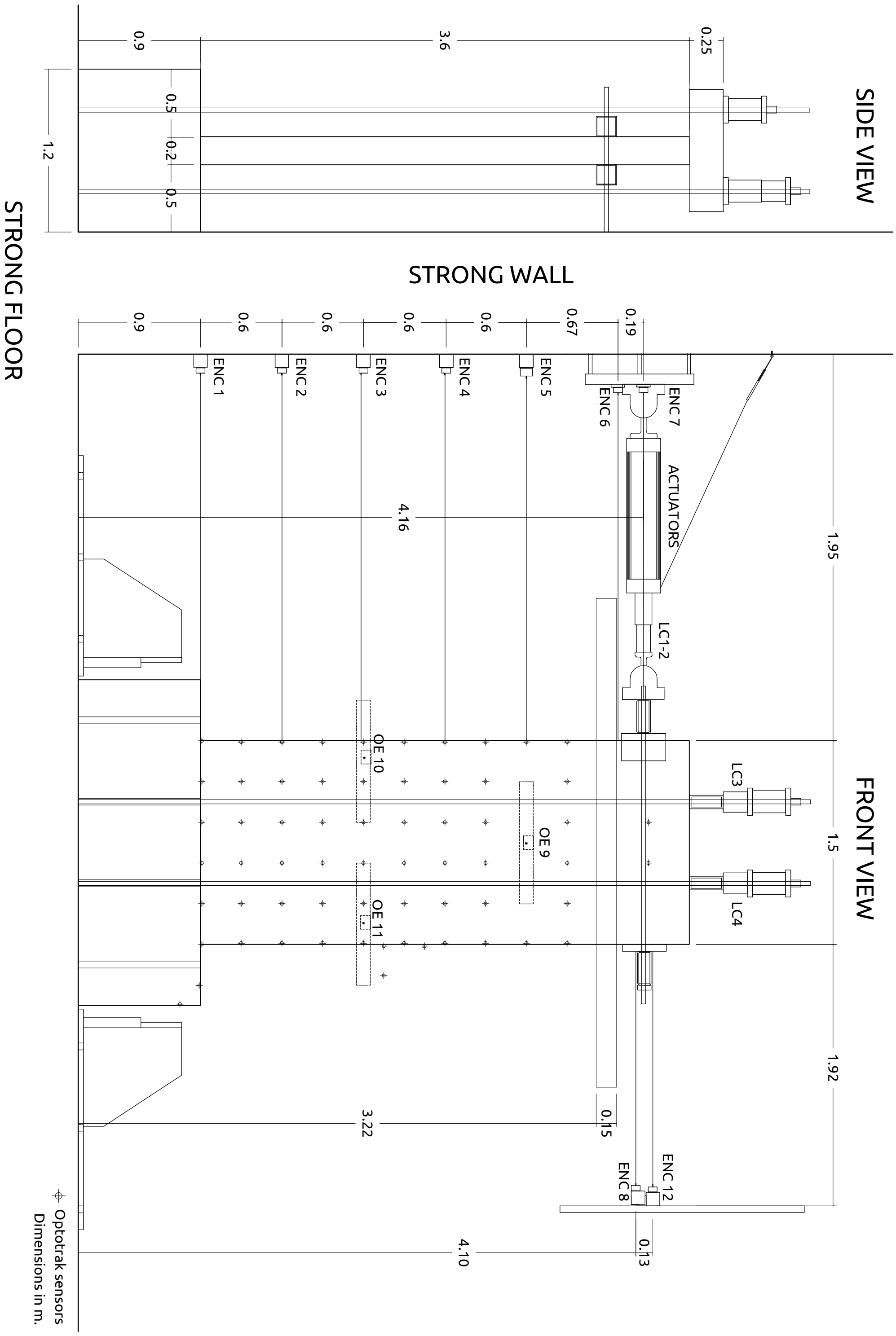

Figure 3.5.: Experimental set-up

3.2.2. Loading history.

The axial load was 888 kN and was kept approximately constant during the tests. The imposed horizontal displacement history at the top of the walls (4.15m), computed as the average displacement measured by encoders 8 and 12, is shown in Fig. 3.6. Three cycles were applied at each drift level. The drift ratio targets were 0.12, 0.25, 0.5, 0.75, 1.0, 1.50, 2, 2.5 and 3.0% (expressed as percentage of the wall height). Because of a failure in the control system, only one cycle at 0.75% and no cycles at 1% were applied to wall W-MC-N.

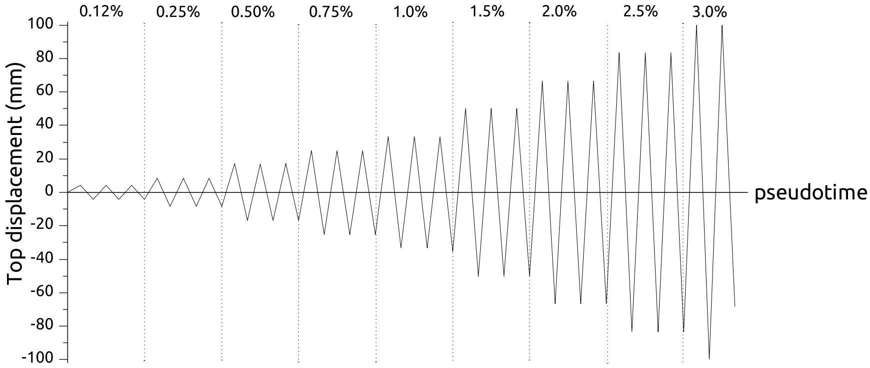

Figure 3.6.: Loading history

3.3. Test results and discussion.

3.3.1. Limit states

Table 3.2 summarizes the values of displacement and force for i) flexural cracking (Δ_{cr} and V_{cr}) ii) First yield $\Delta_y$and V_y, and iii) (first peak at) limiting displacement Δ_u and V_u. The flexural cracking was determined as the displacement in which the first crack appeared. The first yield was defined as the displacement in which a degradation of the lateral stiffness to a value of 2% of the elastic stiffness was observed. The limiting displacement was selected as the maximum displacement reached before failure due to buckling out of plane of the reinforcement of the boundary elements . The numbers in Table 3.2 and the envelopes in figure 3.7 show that the the inclusion of confinement reinforcement at the boundary elements affected the ductility more than on the moment capacity similarly to previous studies [73]. As expected, the response of the two walls was nearly identical up to first yield. The limiting displacement for the wall with confinement (W-MC-C) was larger that that of the wall without confinement (W-MC-N). But it is interesting that the difference between these two displacements did not exceed 0.5% of the height of the walls.

Specimen	Δ_{cr} (mm)	$drift$ (%)	V_{cr} (kN)	Δ_y (mm)	$drift$ (%)	V_y (kN)	Δ_u (mm)	$drift$ (%)	V_u (kN)
W-MC-C	4.06	0.12	257.5	24.9	0.75	626	99.8	3.0	708.4
W-MC-N	4.06	0.12	250	24.9	0.75	607	80.8	2.5	697.1

Table 3.2.: Limit States

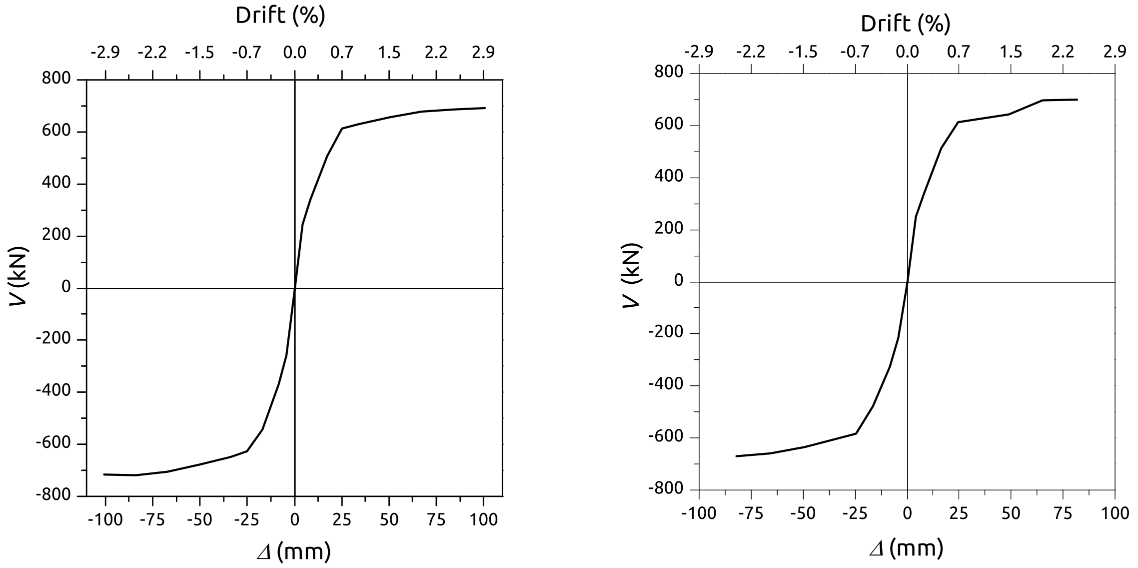

(a) W-MC-C

(b) W-MC-N

Figure 3.7.: Load versus top displacement envelope curves

3.3.2. Overall response.

After the tests for W-MC-C specimen the following observations are remarkable: First cracking was observed in cycle #1 at a load of 204 kN and a displacement of 4.31 mm (0.12%). First yield occurred in cycle #10 at a load of 608 kN kips and a displacement of nearly 25.4 mm (0.75%). Splitting cracks and spalling at the base of the boundary elements was first observed in cycle #11. The peak lateral load (723.7 kN) was reached in cycle #25 at 99 mm (3%) of displacement. The wall collapsed in cycle #26 when the boundary element failed in compression. During the failure all the boundary reinforcement buckled in the same direction (out of plane). Figure 3.8a shows the load-top displacement hysteresis curve measured. Figure 3.9 shows photographs of the crack patterns at the base for key response states. The maximum crack widths measured during the tests were 0.12, 0.76 and 3.81 mm. at first cracking (0.12%), first yield (0.75%) , and limiting displacement. (3%).

In the case of the W-MC-N specimen the following observations are remarkable after the tests: First cracking was observed in cycle #1 at a load of 186 kN and a displacement of 4 mm (0.12%). First yield occurred in cycle #10 at a load of 608 kN and a displacement of nearly 25.4 mm (0.75%)

. Splitting cracks and spalling at the base of the boundary elements was first observed in cycle #9. The peak lateral load (688 kN) was reached in cycle #14 at 66.04 mm (2%) of displacement. The wall failed in cycle #19 as the bars in one of the boundary elements buckled (away from the center of the wall). During the failure all the boundary reinforcement buckled in the same direction (out of plane). Figure 3.8b shows the load-top displacement hysteresis curve measured. Figure 3.10 shows photographs of the crack patterns at the base for key response states. The maximum crack widths measured during the tests were 0.12, 0.63 and 3.81 mm at first cracking (0.12%), first yield (0.75%), and limiting displacement (2.5%).

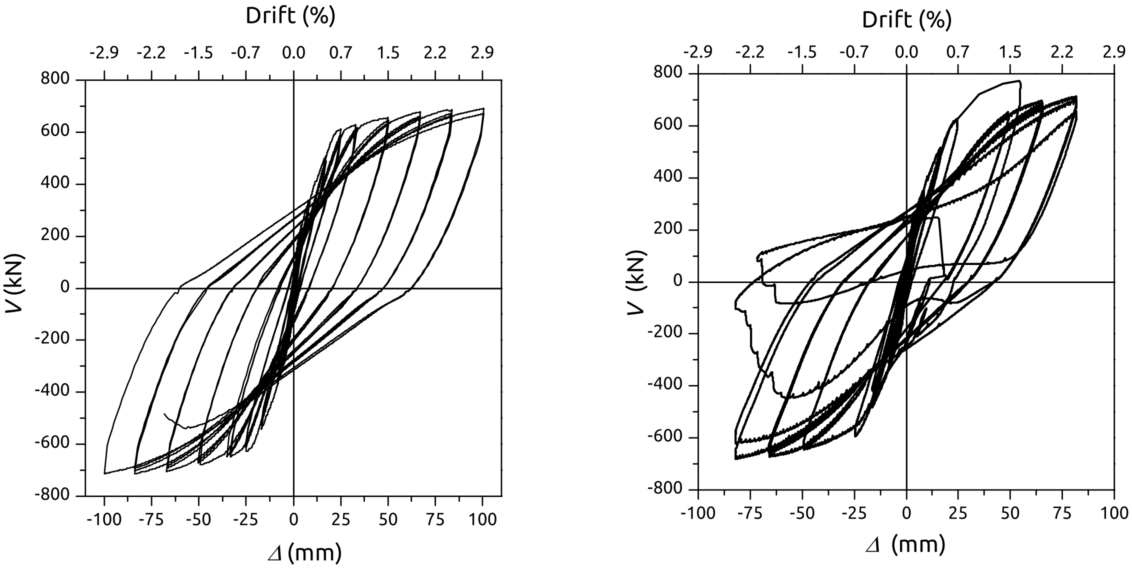

(a) W-MC-C

(b) W-MC-N

Figure 3.8.: Load versus top displacement hysteresis curve

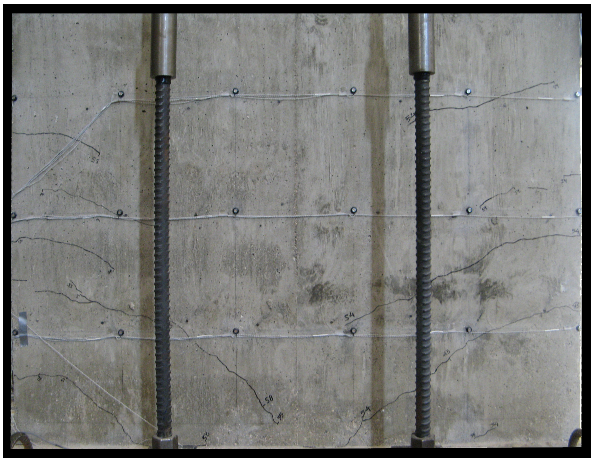

(a) Flexural cracking (0.12%)

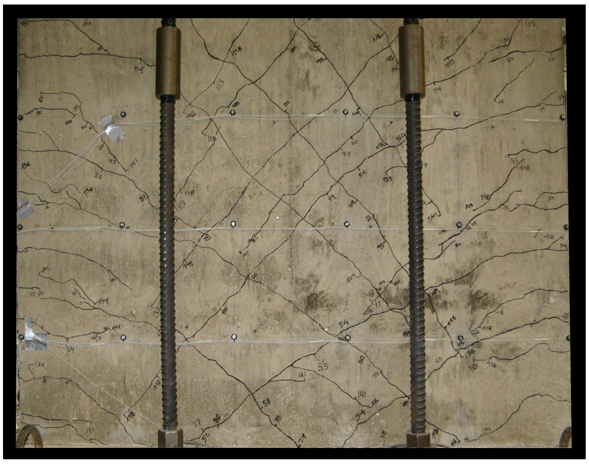

(b) First yield (0.75%)

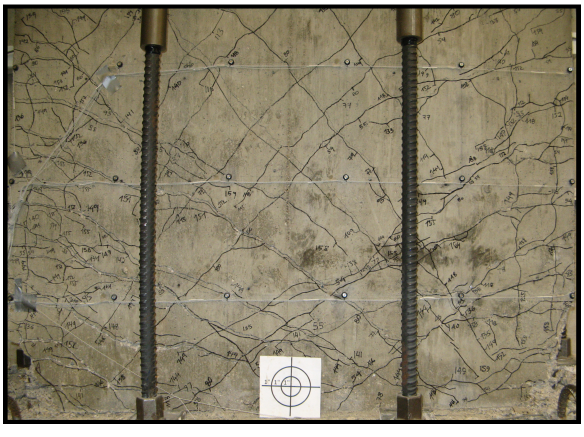

(c) Limit displacement (3%)

Figure 3.9.: Cracks patterns for limit states. W-MC-C specimen.

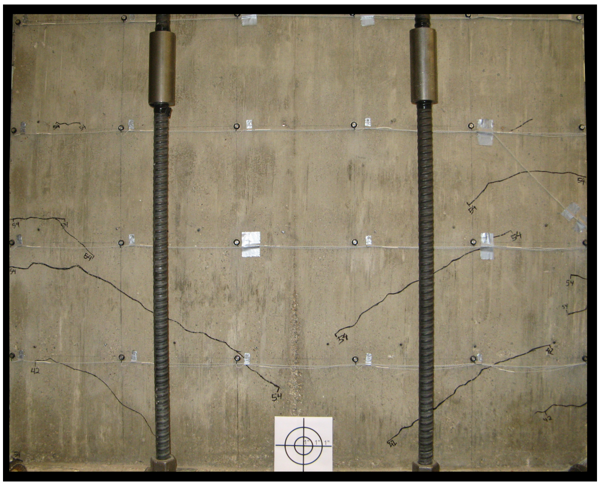

(a) Flexural cracking (0.12%)

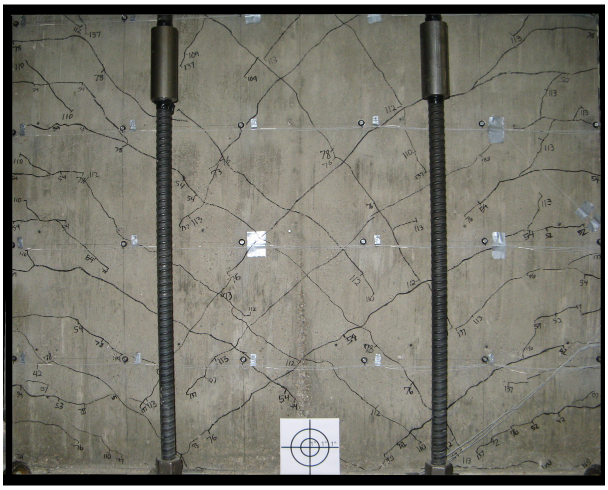

(b) First yield (0.75%)

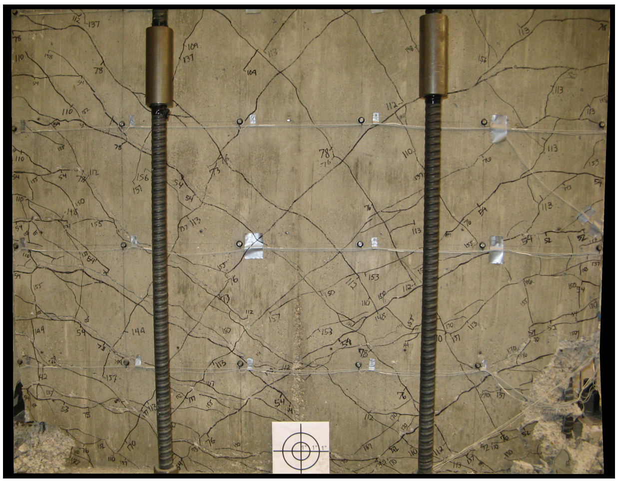

(c) Limit displacement (2.5%)

Figure 3.10.: Cracks patterns for limit states. W-MC-N specimen.

3.3.3. Normal strain distribution.

To speak of strain (or rather unit strain) in reinforced concrete and after cracking requires making the following considerations. Strictly, we should speak of average deformation per unit length. But we keep with the norm and call these unit deformation strains here to keep things brief. Figure 3.11 shows contours of the strains measured using the infrared targets in the lower 1.5 m of wall shown in Figure 3.4. The strains were computed dividing the length increment experimented by two correlative targets at each cycle i by the original span length $\epsilon = {}^{(L_i - L_0)}/_{L}$.

Overall, the distribution of strain appears to have been remarkably similar in both walls. Of course there are differences. But more interestingly, in both walls the strains in the boundary in compression seem to have concentrated within approximately 0.45m from the base (approximately twice the wall thickness [90] and 1.5 times the neutral axis depth) both at a drift ratio of 0.75% and at a drift ratio of 2%. In the boundary in tension the strains spread over a region at least twice as tall (with a height nearly equal to half the wall length).

Figure 3.12 show the distributions of maximum normal unit strains due to flexural deformations measured on the edges of the walls at each drift ratios. These figures show clearly that the “spread of plasticity” –as it is often called- it is very different on the side of the wall in tension and the side of the wall in compression. The concepts of curvature and plastic hinge do not help explain these observations.

Figure 3.13 show the distribution of the maximum normal unit strains due to flexure deformations measured along the wall base at each drift ratio. As can be seen in these figures the distribution of the normal strains along the wall cross section only can be assumed as linear before the yielding point. After yielding the common plane section assumption is inaccurate, being greater as inelastic deformations grow.

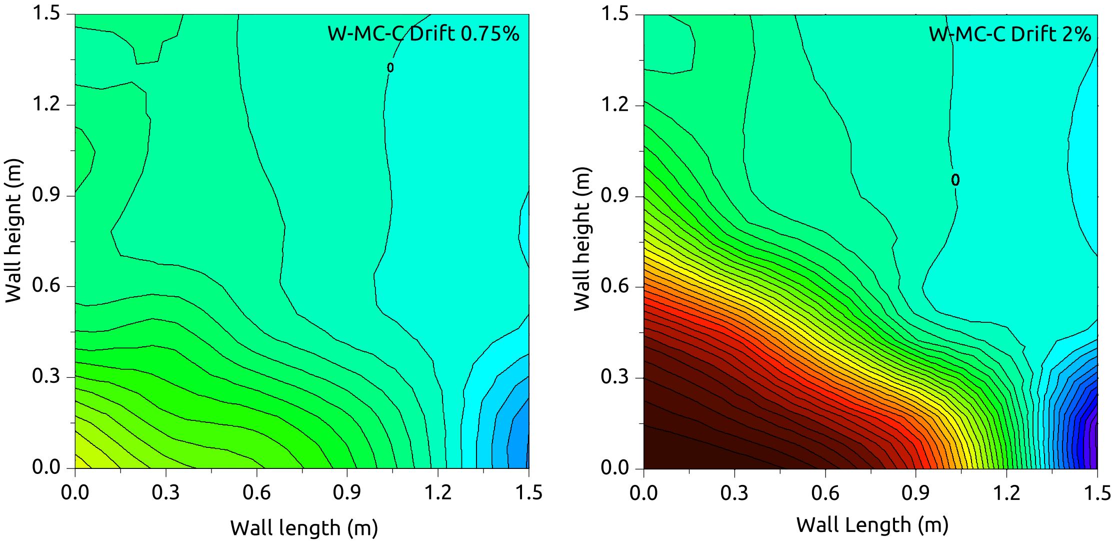

(a) W-MC-C

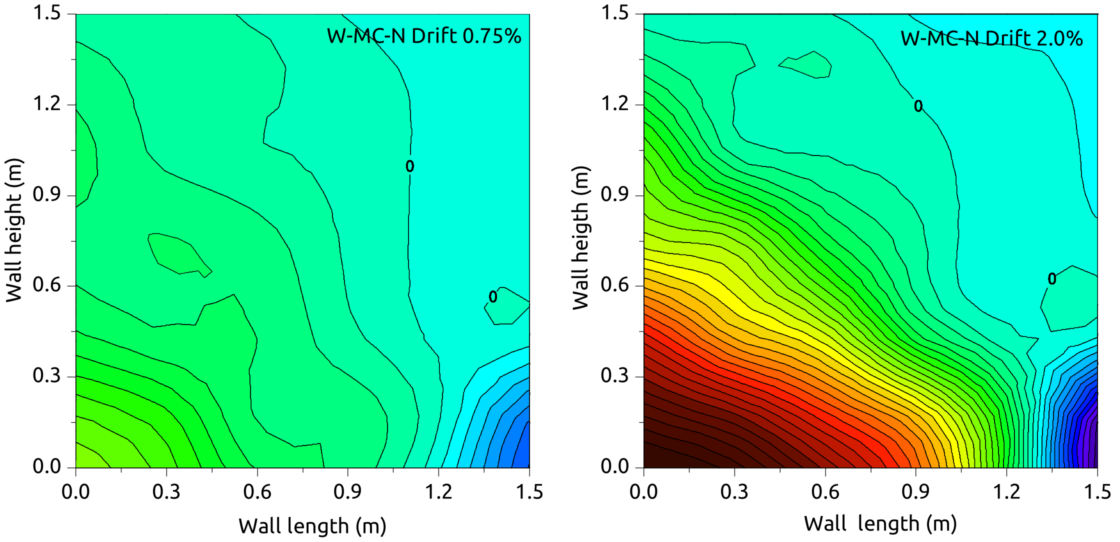

(b) W-MC-N

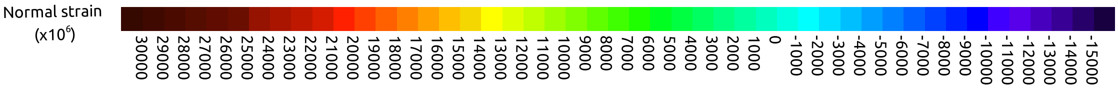

Figure 3.11.: Normal strain distribution

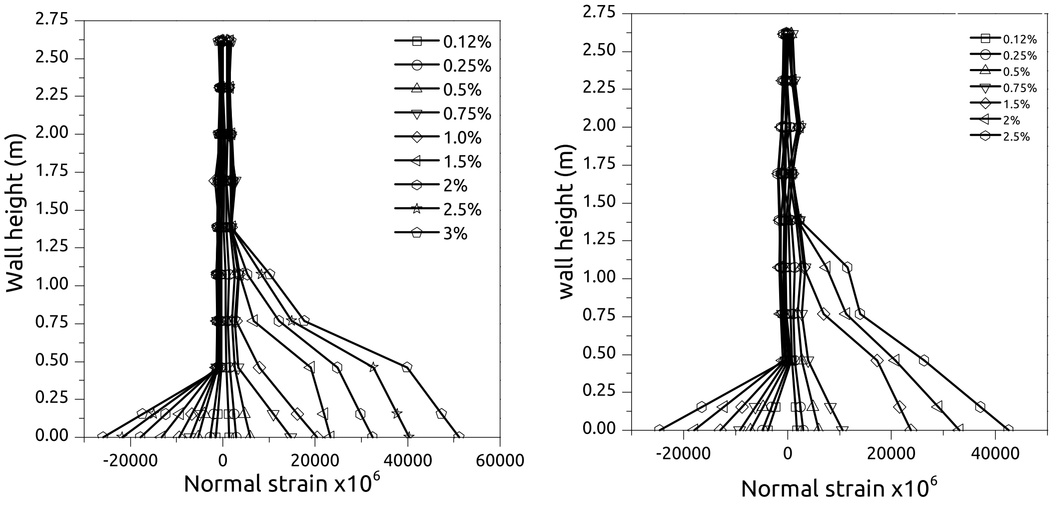

(a) W-MC-C (b) W-MC-N

Figure 3.12.: Normal strain distribution at wall edges over the height at different drift ratios

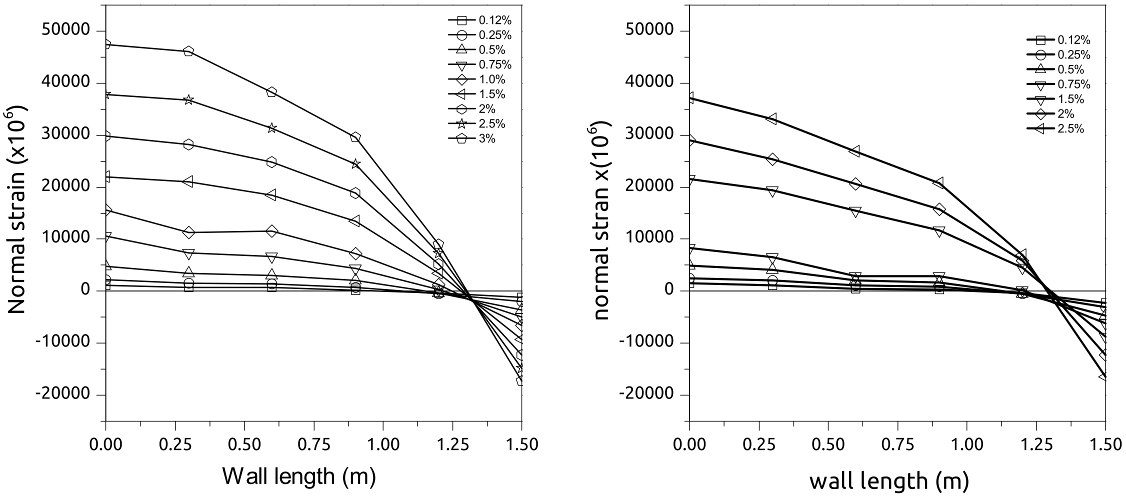

(a) W-MC-C (b) W-MC-N

Figure 3.13.: Normal Strain distribution at the base at different drift ratios

3.3.4. Curvature Distribution.

Unit curvature was computed, by means of equation 3.2, as the ratio of change in angle to height difference using the outer targets in the non-contact sensor grid shown in figure 3.5. Figure 3.14 shows the distribution of unit curvature along the wall height computed as the mean values of the unit curvatures obtained for the 3 cycles at each drift level. The unit curvatures at the base were linearly extrapolated from the values obtained at 0.15 and 0.45m. The maximum curvature observed at a given drift was almost equal for both specimens. Near the base of the wall, the curvature profile approaches a triangle of height equal to $0.5L_w$ (0.76 m.).

$$\varphi_i = \frac{\left(\dfrac{\Delta L_{t,i}}{L_t} - \dfrac{\Delta L_{c,i}}{L_c}\right)}{L_w} \tag{3.2}$$

Where $\Delta L_{t,i}$ and $\Delta L_{c,i}$ is the length increment between to targets at tension and compression edges respectively, L_t and L_c is the original length between to targets at tension and compression edges respectively and L_w is the wall length.

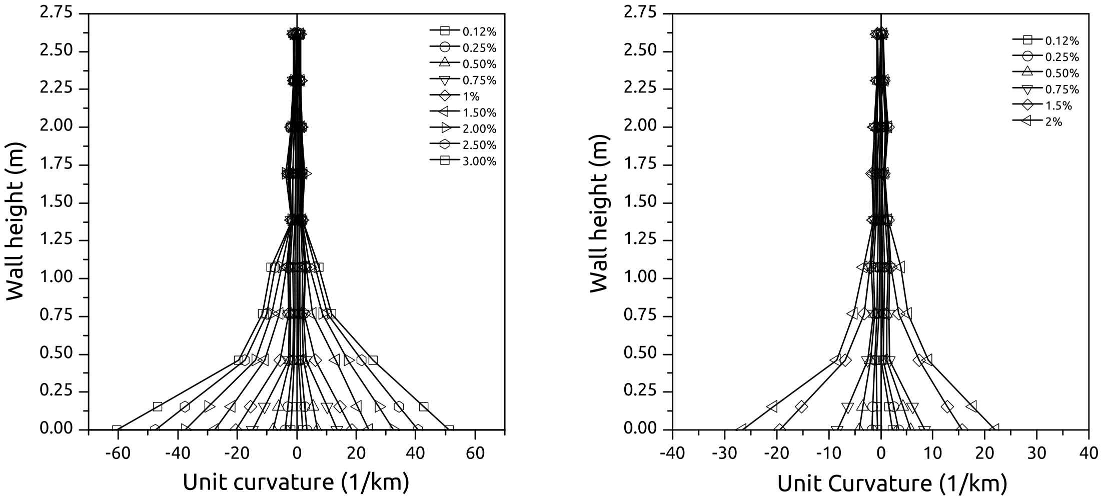

(a) W-MC-C

(b) W-MC-N

Figure 3.14.: Unit curvature distribution over the height at different drift ratios

3.3.5. Energy dissipation

The cumulative plastic energy dissipated by both walls was computed integrating the experimental load-top displacement hysteresis curves shown in figure 3.8. Figure 3.15 compares the plastic energy dissipated throughout time for both specimens. As can be seen the energy dissipation was identical until yielding, when problems with the control system occurred as described in subsection 3.2.2. Despite this problems during the tests the maximum energy dissipated by the wall with inclusion of confinement reinforcement at the boundary elements was 3.2 times higher than the energy dissipated by the structure without confinement reinforcement.

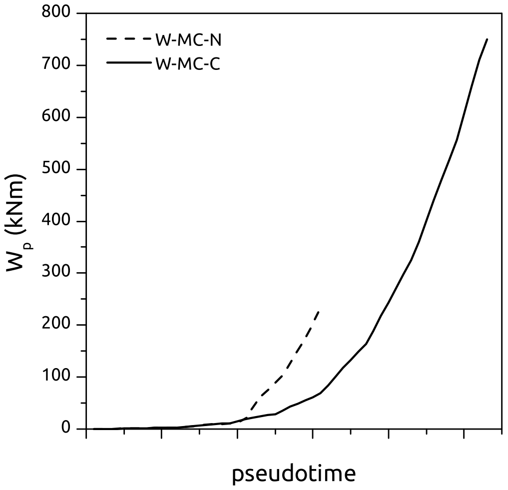

Figure 3.15.: Cumulative plastic energy

3.4. Wall vs Damper.

Figure 3.16 compares the experimental hysteresis curves obtained for the RC wall, with the hysteretic curves of a WPD-type hysteretic damper [15] with the same initial stiffness and strength that the RC wall, subjected to the same history of cyclic loading. The histeretic curves of the WPD-type damper were obtained by using the numericla model developped by Benavent-Climent et al. [15]. It was based in the studies from Kato et al. [53] and calibrated with several experimental tests. Figure 3.17 compares the results of the cumulative energy dissipated at each cycle for both structural elements. As can be seen, for the same amplitude of the cycles, the energy dissipated by the hysteretic damper is up to 2.3 times greater than by the RC wall with confinement reinforcement.

This difference is attributable to the lack of pinching effect in the Q-delta loops exhibited by the WPD type damper, which contrast with the severe pinching effect exhibited by the RC wall. In addition, the total amount of plastic strain energy W_p dissiapted by the RC wall (specimen W-MC-C) up to failure, normalizad by V_y and δ_y and expressed in terms of the ratio $\eta = {W_p}/{V_y \delta_y}$ is

$\eta = 48$. This value is far below the range of values of η that can be exhibited by a WPD-type damper (between 200 and 1100) [15]. Further, the WPD-type hysteretic damper can sustain lateral deformations up to about 50 times the displacement at yielding [15], while the ultimate deformation og the RC wall was about 4 times the yield deformation. The maximum lateral drif that can be sustained by a WPD-type damepr is far beyond the approximately maximum 2% drift exhibited by the RC wall when failure occurred. Another important advantage of the hysteretic damper in comparison to the RC wall is that it can easily sustituted after the earthquake.

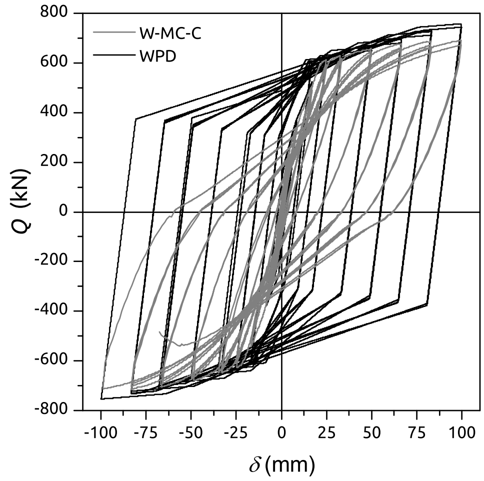

Figure 3.16.: hysteresis curves. W-MC-C vs WPD damper

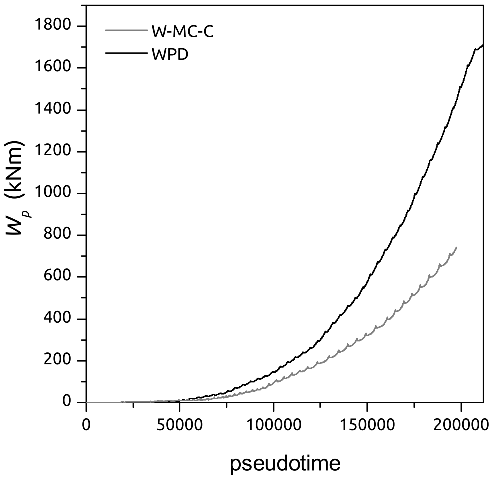

Figure 3.17.: Cumulative plastic energy. W-MC-C vs WPD damper

3.5. Summary and conclusions.

This chapter addressed the conventional seismic resistant structure consisting of RC frames with RC walls. This structure combines in parallel two systems of very diferent lateral stiffness: the RC frame and the RC wall. The seismic behavior of conventional RC frames was investigated in chapter 2 through dynamic shaking table tests. In this chaper 3 the seismic behavior of conventional RC ductile walls was studied through quasi-static cyclic tests. Two large-scale reinforced concrete structural walls were tested. The walls had height-to-length ratios of approximately 2.2. One of the walls had confinement reinforcement in the boundary elements meeting ACI-318-11 requirements while the other wall did not have any confinement reinforcement. As expected, the confinement reinforcement didn't affect the strength of the wall but it increased its lateral displacement capacity. The increase in displacement capacity was 0.5% of the wall height (the wall with confinement failing at a displacement equal to 3% of its height). Another important effect of the inclusion of confinement reinforcement is that the maximum energy dissipated by the wall with confinement reinforcement at the boundary elements was 3.2 times higher than that of the wall without confinement reinforcement.

Measurements made with a dense array of non-contact sensors indicated that inelastic unit curvatures had a nearly linear distribution near the wall base. The height of the region in which these curvatures concentrated was nearly half the wall length. The concepts of curvature and plastic hinge, nevertheless, do not help explain measurements indicating that the lengths of the regions in which inelastic compressive and tensile strains concentrate (on opposite sides of the wall) are radically different from one another. Tensile strains concentrated in a length approximately equal to half the wall length (0.75 m) while compressive strains concentrated in a length approximately equal to twice the wall thickness and 1.5 times the neutral axis depth (approximately 0.45m). The distribution of the normal strains along the wall cross section cannot be assumed as linear after the yielding point.

A comparison between the energy dissipated by the RC wall with reinforcement confinement, and the energy that would dissipate a WPD-type hysteretic damper with the same initial stiffness and strength, subjected to the same history of loading, was done. It was found that the energy dissipated by the WPD-type hysteretic damper is 2.3 times greater than the energy dissipated by the structural wall. In addition, the total amount of plastic strain energy W_p dissiapted by the RC wall up to collapse was far below (between the ultimate energy dissipation capacity exhibited by the WPD-type damper range of values of η that can be exhibited by a WPD-type damper (between 200 and 1100)[15]. Further, the maximum displacement that can be sustained by a hysteretic damper, such as the WPD-type damper, is more than 10 times larger than that of the RC wall.

The better performance of the hysteretic dampers compared to the RC ductile wall in terms of energy dissipation capacity and deformation capacity, among other advantages (such as the easy to repair/substitute after the earthquake), makes the hysteretic dampers a better choice. Consequently Chapter 4 of this Thesis is focussed on the seismic response of frames with hysteretic dampers.

4. Performance assessment and comparison of conventional RC frames and innovative RC frames with hysteretic dampers based on non-linear dynamic analysis

4.1. Objectives

This chapter compares the dynamic response of two different seismic resistant systems based on the results of nonlinear dynamic analyses with finite element's numerical models. Two prototypes of 3 and 6 storeys are considered in this study. In each case two different seismic resistant designs are examined. On one hand, the traditional seismic resistant reinforced concrete frame with strong column weak beam collapse mechanism. On the other hand, an innovative seismic resistant design, as the reinforced concrete frame (designed basically for gravitational forces without imposing the formation of a strong column weak beam mechanism) equipped with hysteretic dampers. To make them comparable, both prototypes were designed to meet the same reference base shear Q_{y1}. The reference base shear selected, is that required by a conventional RC framed seismic resistant structure with strong column weak beam collapse mechanism, designed to resist the 500 year return period earthquake expected at the city of Granada according to the current seismic code NSCE-02 [35].

Each prototype was modeled with the finite element software "Engineer's Studio" [59]. Nonlinear Time History Analysis (NTH) were carried out for each prototype using eight historical accelerograms shown in appendix A. The maximum response values were compared within the framework of the Performance Based Engineering, using probabilistic structural response functions for the different structural types. The main reference values used to compare the performance of the prototypes are those ratios associated with structural damage as the inter-story drift, id, the maximum inelastic deformation ratio μ, the cumulative inelastic deformation ratio η, or the chord rotation demand and other well-known damage indexes as D_i by Darwin and Nmai [33] and $DI_{P\&A}$ by Park and Ang [71] estimated at global and local level.

The results of this study suggest that the inclusion of hysteretic damper enhance the seismic behaviour of RC framed structures reducing the damage in the primary vertical load resisting system.

4.2. Definition of the prototype structures

4.2.1. Bare Frame Strong Column Weak Beam prototypes (BF-SCWB). Design parameters and criteria

Two RC seismic-resistant framed structures were designed using the commercial software “Tricalc”. These structures are prototypes of a typical housing building in Spain with three and six storeys. Both structures were designed to resist the vertical gravitational loads defined by the Spanish building technical code [36] (Codigo Técnico de la Edificación (CTE)) and the lateral seismic loads defined by the Spanish building seismic-resistant code [35] (Norma de Construcción Sismorresistente Española (NSCE-02). The structural elements were designed for the ultimate limit state based on the results of a modal spectral analysis.

Table 4.1 shows the permanent and live gravitational loads considered in the analysis, according to the specifications of the CTE-DB-SE

Permanent Loads		Live Loads	
Concrete	24.5 kN/m^3	Floor	2.0 kN/m^2
Floor	2.15 kN/m^2	Roof	1.0 kN/m^2
Partitions	1.0 kN/m^2		
Flooring	1.0 kN/m^2		
Deck	3.0 kN/m^2		
Cladding	7.0 kN/m		

Table 4.1.: gravitational loads considered

The load combination for an accidental seismic situation is defined in the CTE by means of equation 4.1

$$\sum_{j>1} G_{k,j} + A_d + \sum_{i>1} \psi_{2,i} Q_{k,i} \tag{4.1}$$

Where $G_{k,j}$ is each permanent j load, A_d is the seismic action and $Q_{k,i}$ is each i live load multiplied by a simultaneity factor $\psi_{2,i}$.

The masses to consider in the dynamic analysis are defined in the combination of the NCSE-02 by means of equation 4.2:

$$\sum_{j>1} G_{k,j} + 0.5 \sum_{i>1} Q_{k,i} \tag{4.2}$$

The total mass of the building determined by equation 4.2 is distributed among the rigid elements that define the structural joints (lumped masses). Table 4.2 shows the values of the masses considered in the representative joints of the structure.

Roof		Floor	
Exterior joint	Interior joint	Exterior joint	Interior joint
8.83 kNs^2/m	16.41 kNs^2/m	12.35 kNs^2/m	15.88 kNs^2/m

Table 4.2.: Reactive masses concentrated at the structural joints

Table 4.3 summarizes the parameters that define the seismic action according to the seismic resistant code NSCE-02. Where C is the soil type coefficient, in our case type III, a_b is the basic ground acceleration for the city of Granada, ρ is the building risk coefficient and μ is the ductility performance factor. Our structure has a strong column weak beam collapse mechanism hence the ductility factor is considered as high ductility. Figure 4.1 shows the acceleration elastic response spectrum used for the seismic design in the city of Granada, obtained from the parameters in table 4.3.

C	a_b	ρ	μ
1.6	0.23g	1	3

Table 4.3.: NSCE-02 parameters

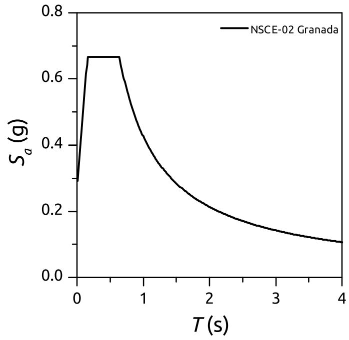

Figure 4.1.: NSCE-02 Acceleration elastic response spectrum

To ensure that the collapse mechanism is the strong column weak beam required by the NSCE-02 code, a global capacity assessment of the structure is done. To this end we consider that the inelastic strains, due to the seismic action, are concentrated in the plastic hinges at the ends of the beams and the base of the columns. Figure 4.2 shows the deformation of the entire frame once the collapse mechanism is developed. It also shows a detail of the rotation at the plastic hinges for a top displacement equal to δ_t. The moment-rotation relationship of the plastic hinges is assumed to be of the rigid-perfeclty plastic type.

Considering that the structural response is governed by the first vibration mode, the distribution of the maximum lateral forces will follow a pattern close to the inverted triangular distribution shown in figure 4.2. The value of the lateral forces at each i-storey can be determined by equation 4.3. Herein the lateral forces, $\mathbf{F}_i$ are normalized by the value of the force acting in the top storey, f_t .

$$\mathbf{F}_i = f_t \left[\frac{h_i}{H} \right] \tag{4.3}$$

Where h_i is the height of the i-storey measured from the ground level and H is the total height of the structure.

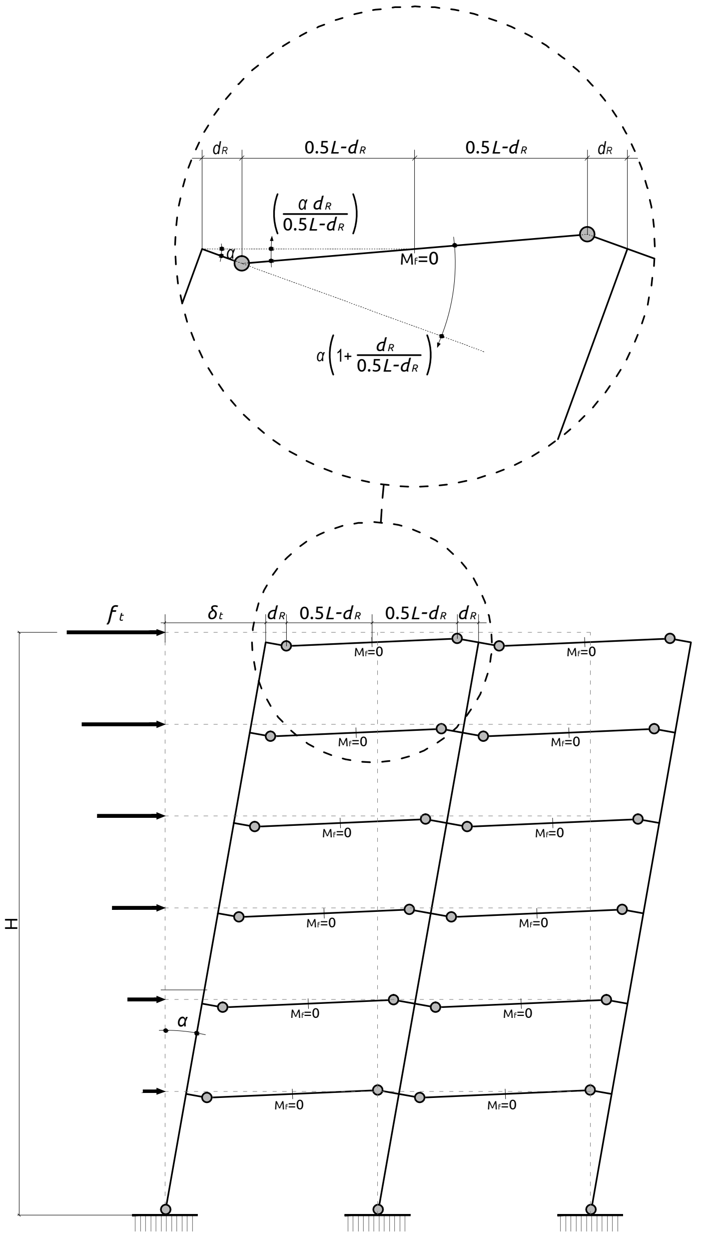

Figure 4.2.: Weak beam strong column collapse mechanism.

Assuming that the bending moment is zero in the middle of the spans, we can divide the structure and analyze each part separately as show in figure 4.3.

At the instant in which all the plastic hinges are developed f_t gets its maximum value $f_{t,max}$. Taking into account the geometric relationships at that moment, the external work done by the lateral forces has to be equal to the internal work done by the plastic hinges as is expressed in the work balance equation 4.4.

$$f_{t,max}\left[\left(\frac{h_i}{H}\right)^2\right]\alpha H=\alpha\sum M_{u,c}+\alpha\left(1+\frac{d_R}{0.5L-d_R}\right)\sum M_{u,b} \tag{4.4}$$

Where α is the rotation at the column bases, $M_{u,c}$ is the maximum bending moment at the column bases, $M_{u,b}$ is the maximum bending moment at the beams ends and d_R is the distance to the plastic hinge center.

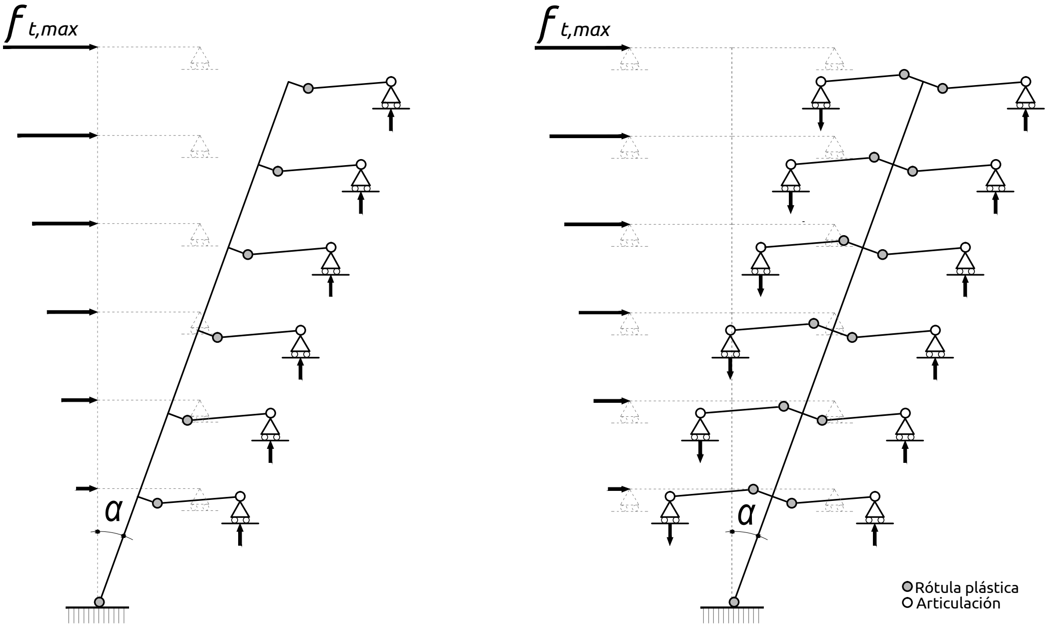

Figure 4.3.: Isolated column collapse mechanism

The position of the plastic hinge center is a key point and it depends on the plastic hinge length considered, L_p. There are several formulations in the literature to determine L_p nowadays [37, 9, 20, 10, 77]. A plastic hinge length of 0.5 to 1 times the element depth is commonly assumed. In our case for design purposes we consider a plastic hinge length equal to the depth of the beam $L_p = h_b$. The center of the plastic hinge is hence located at a distance from the column center $d_R = 0.5\,h_c + h_b$ where h_c is the column depth.

Once the maximum bending resistance at beam ends and at bottom ends of the columns of the first storey are known, it is possible to derive the maximum lateral force $f_{t,max}$ with equation 4.4. Once $f_{t,max}$ is determined, the strength required in the columns to guarantee the formations of a strong column weak beam mechanism was calculated, by solving the equilibrium equations.

4.2.2. Frame Damper Gravity Load prototypes (FD-GL). Design parameters and criteria

A Flexible-Stiff mixed structure as described in section 1.1 was designed to meet the base shear Q_{y1} given by the conventional seismic resistant structure BF-SCWB studied in section 4.2.1. The flexible part of the mixed structure is determined by a framed RC structure designed to resist gravitational loads exclusively. The rigid part of the mixed structure is constituted by the hysteretic dampers at each level and its main function will be to resist the lateral loads due to the seismic action. Figure 4.4 shows a schematic example of the shear versus displacement curve of the mixed system and the main parameters that define this structural type: (i) yield strength , ${}_fQ_y$, and yield displacement,${}_f\delta_y$, of the flexible part (frame). (ii) yield strength, ${}_sQ_y$, and yield displacement, ${}_s\delta_y$, of the rigid part (dampers).

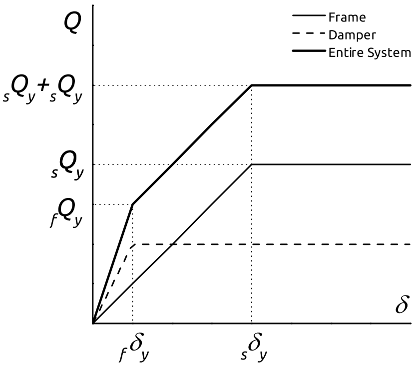

Figure 4.4.: Capacity curve of the flexible-stiff structural system

4.2.2.1. Flexible part design criteria. RC Bare frame Gravity Load (BF-GL)

Two RC seismic-resistant framed structures prototypes were designed with the commercial software Tricalc. The prototypes are the typical housing structure in Spain with three and six storeys. Both structures were designed to resist gravitational loads exclusively at the ultimate limit state. Table 4.4 summarizes the permanent and live gravitational loads considered in the analysis, according to the specifications of the CTE-DB-AE [36]

Permanent Loads		Live Loads	
Concrete	24.5 kN/m^3	Floor	2.0 kN/m^2
Floor	2.15 kN/m^2	Roof	1.0 kN/m^2
Partitions	1.0 kN/m^2		
Flooring	1.0 kN/m^2		
Deck	3.0 kN/m^2		
Cladding	7.0 kN/m		

Table 4.4.: gravitational loads

The load combination for a permanent load situation is defined in the CTE by means of equation 4.5.

$$\sum_{j>1}\gamma_{G,j}G_{k,j}+\gamma_{Q,1}\psi_{1,1}Q_{k,1}+\sum_{i>1}\gamma_{Q,i}\psi_{2,i}Q_{k,i} \tag{4.5}$$

Where $G_{k,j}$ is the permanent action, $\gamma_{G,j}$ is the load factor for permanent loads, $Q_{k,1}$ is one permanent load acting as primary load multiplied by the $\gamma_{Q,1}$ load factor and $\psi_{1,1}$ simultaneity factor and $Q_{k,i}$ are the rest of the live loads multiplied by the load factor $\gamma_{Q,i}$ and a simultaneity factor $\psi_{2,i}$.

The total mass of the building determined according to equation 4.2, is distributed among the rigid elements that define the structural joints (lumped masses). Table 4.5 shows the values of the masses considered at the representative joints of the structure.

Roof		Floor	
Exterior joint	Interior joint	Exterior joint	Interior joint
8.83 kNs^2/m	16.41 kNs^2/m	12.35 kNs^2/m	15.88 kNs^2/m

Table 4.5.: Reactive masses concentrated at the joints

4.2.2.2. Stiff part design criteria. Hysteretic Damper

The hysteretic dampers constitute the "stiff part" of the mixed structure, and their lateral stiffness and strength were determined on the basis of the following assumptions:

1. The total yield strength of the mixed system at each i-th level Q_{yi} follows the optimum distribution of shear force coefficient defined by Akiyama [3].
2. The damper to frame strength ratio at each i-th level β_i , is made equal to the optimum strength ratio, β_{opt}, proposed by Inoue and Kuwahara [52].

Optimal distribution of the yield shear coefficient

The yield-shear force coefficient, α_i, of any i-th storey in a structure is defined by the following equation:

$$\alpha_i=\frac{Q_{yi}}{\sum_{j=i}^{n}m_j g} \tag{4.6}$$

Where Q_{yi} is the the lateral yield shear force of the i-th storey, m_j the mass of the j-th storey, and n is the number of storeys of the building.

The distribution of the yield shear force coefficient between the storeys can be expressed in terms of the ratio α_i/α_1, where α_1 is the base shear force coefficient. There are infinite different possibilities to distribute α_1 but it is desirable to find a distribution that leads to an equal value of the cumulative inelastic deformation ratio η_i at each i level. This means that the energy is equally distributed between all storeys, avoiding damage concentration. Among the infinite possible distributions α_i/α_1 the one proposed by Akiyama,[3] that makes the cumulative inelastic deformation ratio η approximately equal in all storeys, was adopted. This distribution is referred to hereafter as "optimum distribution" of shear force coefficients and it is expressed by equation 4.7:

$$\bar{\alpha}_i = \frac{\alpha_{i,opt}}{\alpha_1} \tag{4.7}$$

Based on the results of several NTH analyses of framed structures from 3 to 9 storeys Akiyama proposed a base shear coefficient distribution law defined by equation 4.8:

$$\begin{cases} \bar{\alpha} = 1 + 1.5927x' - 11.8519x'^2 + 42.5833x'^3 - 59.4827x'^4 + 30.1586x'^5 & x' > 0.2 \\ \bar{\alpha} = 1 + 0.5x' & x' \leq 0.2 \end{cases} \tag{4.8}$$

Where $x' = x/H = (i-1)/N$, H is the height of the building, N is the number of storeys of the building and i is the considered storey.

Taking into account the relationships of equations 4.6 to 4.8 the damper yield strength at each level ${}_sQ_{yi}$ can be determined by means of equation 4.9:

$${}_sQ_{yi} = \alpha_1 \bar{\alpha}_i \sum_{j=i}^{n} m_j g -_f Q_{yi} \tag{4.9}$$

In equation 4.9 the yield strength of the flexible part ${}_fQ_{yi}$, at each level is known since it is given by the strength of the RC members that constitute the bare frame, as defined in section 4.2.2.1. The base shear coefficient α_1 of the prototype under study is also known as it is made equal to the base shear coefficient of the BF-SCWB prototype from section 4.2.1 which is the reference structure.

Optimum strength ratio of hysteretic dampers

Inoue and Kuwahara conducted a parametric study to investigate the ratio of the lateral strength of the damper to the total strength of the structure, at each level, β , which leads to a minimum damage in the frame. The results of their research concluded that the optimum value of the ratio beta, β_{opt} is defined by equation 4.10.

$$\beta_{opt} = 1 - \frac{1}{\sqrt{k+1}} \tag{4.10}$$

Where k is the ratio of the lateral stiffness of the dampers, ${}_sk$, to the lateral stiffness of the bare frame, ${}_fk$, that is:

$$k = \frac{{}_sk}{{}_fk} \tag{4.11}$$

The ratio β has been defined as the ratio between the damper strength ${}_sQ_y$, and the entire system $Q_{yi} = {}_sQ_y + {}_fQ_y$ as seen in equation 4.12:

$$\beta = \frac{{}_sQ_y}{{}_sQ_y + {}_fQ_y} \tag{4.12}$$

As can be seen in equation 4.10 the optimum ratio depends on the k ratio exclusively. Hence equation 4.10 can be rewritten to obtain the ratio k necessary for a β_{opt} ratio as follows:

$$k = \frac{1 - (\beta_{opt} - 1)^2}{(\beta_{opt} - 1)^2} \tag{4.13}$$

In our case the strength and stiffness of the flexible part is determined by the RC bare frame defined in section 4.2.2.1. The strength of the rigid part was obtained previously to meet the Akiyama's optimum distribution. Hence we can obtain the strength ratio β at each level i. Taking into account equation 4.13, the value of the ratio k that makes $\beta = \beta_{opt}$ can be readily determined. As we know the stiffness of the flexible part, the stiffness of the rigid part can be obtained with equation 4.11 to meet the previous conditions.

Damper configuration.

A arrangement consisting of two hysteretic dampers at each level i-th is considered in the design. Both dampers are installed as diagonals within the RC frame with a cross shape configuration as shown in figure 4.5. This damper installation compared to that with a single diagonal at each level diminishes the axial load on the RC beams as shown in detail on figure 4.5.

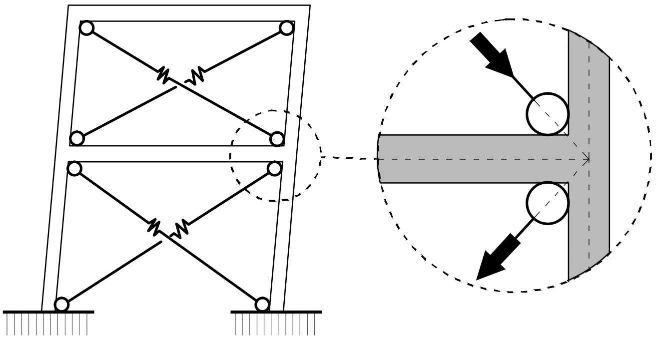

Figure 4.5.: Damper installation

4.3. Development of numerical models.

A representative frame of each prototype was modeled with nonlinear uni-dimensional finite elements (FE) with 'Engineer's Studio' software. Figure 4.6 shows the discretization of two typical uni-dimensional frame members intersecting at an exterior beam-column connection. In this figure L is the span and H is the heigth of the storey. The end portions of the frame members within the joint are assumed rigid; therefore shear deformation of the joint panel are neglected. Each frame member (column or beam) is divided in several portions along its length, L. The central part of the frame member (of length $L/3$) is assumed to remain elastic, and non-linearity are assumed to occur in the end portions, where fibre elements [84, 83] with nonlinear behaviour and a more dense mesh of FE is used. Figure 4.6 shows the FE discretization.

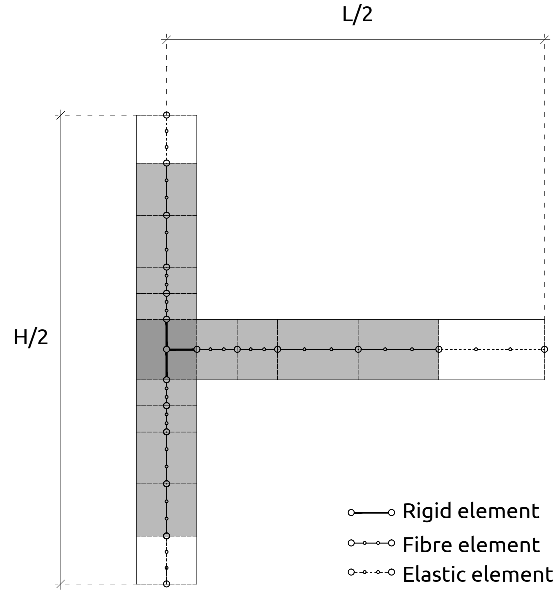

Figure 4.6.: FE discretization

Fibre element definition

The RC cross section of each fibre element is divided into a $h/30 \times b/30$ rectangular mesh as shown in figure 4.7. As a result of the in-plane Euler-Kirchoff assumption, uni-axial strains are distributed linearly across the cross-section as shown in figure 4.7. The uni-axial normal strain of each fibre can be expressed with equation 4.14

$$\epsilon_{zij} = \epsilon_{z0} + y_{ij}\phi_x + x_{ij}\phi_y e \tag{4.14}$$

Where ϵ_{ij} is the normal strain of cell ij, x_{ij} and y_{ij} are the coordinates from the centroid of the cross section to the centroid of cell ij in x and y directions respectively, $\epsilon_{z0}$is the mean axial strain at the centroid of the cross section, and ϕ_x, ϕ_y are the curvatures around x and y axes.

After uni-axial strain is computed, the uni-axial normal stress in each cell is computed using a one-dimensional tension-compression constitutive law. Assuming a constant strain over a cell the internal normal forces including bending (M_x, M_y) and the axial force N can be obtained by integrating the internal normal stresses over the cross section as:

$$P = \int_A \sigma dA \quad M_x = \int_A \sigma y dA \quad M_y = \int_A \sigma x dA \tag{4.15}$$

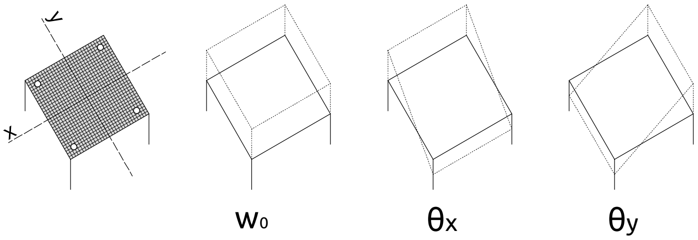

Figure 4.7.: fibre Element Section Subdivision

Figure 4.8 shows the one-dimensional tension-compression constitutive law used in the definition of concrete cells. Table 4.6 summarizes the numerical values used in the FE model for the definition of the constitutive law parameters. This constitutive law was developed at the University of Tokyo concrete laboratory [59].

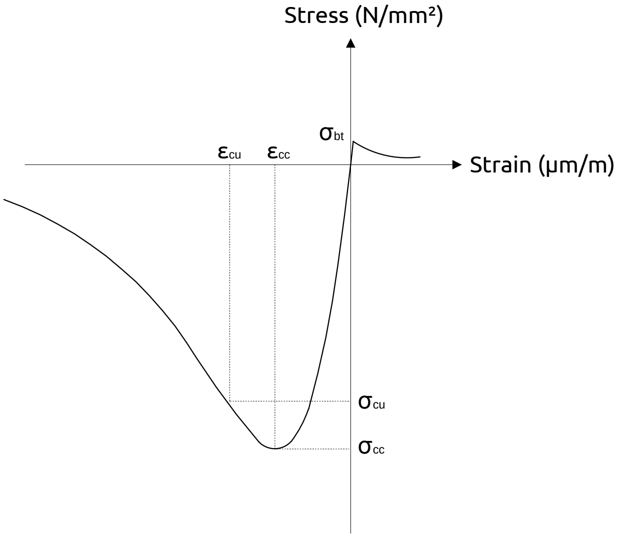

Figure 4.8.: HA-25 concrete constitutive law

ϵ_{cc} (μm/m)	σ_{cc} (N/mm^2)	ϵ_{cu} (μm/m)	σ_{cu} (N/mm^2)	ϵ_{tu} (μm/m)	σ_{bt} (N/mm^2)	E_c (N/mm^2)
-1.79E-3	25.0	-3.57E-3	-18.82	1.40E-2	1.966	28000

Table 4.6.: HA-25 concrete properties

Figure 4.9 shows the one-dimensional tension-compression constitutive law used in the definition of steel reinforcement. Table 4.7 summarizes the numerical values used in the FE model for the definition of the constitutive law parameters. The constitutive law was developed at the University of Tokyo concrete laboratory. The model considers the Bauschinger effect using the Giuffre-Menegotto-Pinto model [62].

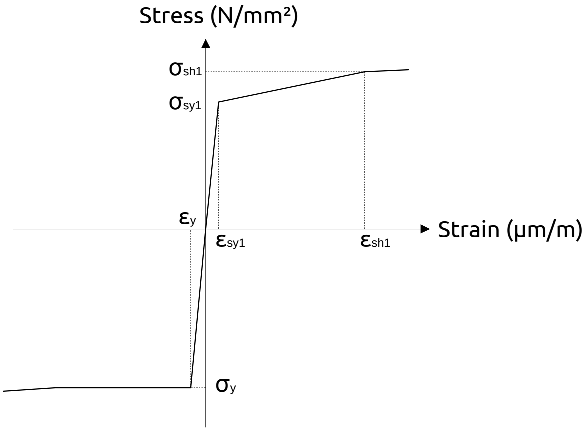

Figure 4.9.: B-500S steel reinforcement constitutive law

ϵ_{sy} (μm/m)	σ_{sy} (N/mm^2)	ϵ_{sh} (μm/m)	σ_{sh} (N/mm^2)	ϵ_y (μm/m)	σ_{int} (N/mm^2)	E_{sr} (N/mm^2)
0.0025	500	0.056	550	-0.0025	-500	200000

Table 4.7.: B-500S reinforcement steel properties

Damping model

The classic damping Rayleigh model is chosen to define the damping of the structures [28]. In this model the damping matrix **C** in equation 4.16, is assumed to be a linear combination of a mass-proportional damping term $a_0\mathbf{M}$ and a stiffness-proportional damping term $a_1\mathbf{K}$.

$$\mathbf{C} = a_0\mathbf{M} + a_1\mathbf{K} \tag{4.16}$$

Given coefficients a_0 and a_1 the damping ratio in mode i can be determined from equation 4.17

$$\xi_i = \frac{a_0}{2\omega_i} + \frac{a_1\omega_i}{2} \tag{4.17}$$

The coefficients a_0 and a_1 can be determined by specifying damping ratios in any two modes, say k and n. Expressing equation 4.17 for these two modes in matrix form leads to equation 4.18:

$$\left\{ \begin{array}{c} \xi_k \\ \xi_n \end{array} \right\} = \frac{1}{2} \left[\begin{array}{cc} 1/\omega_k & \omega_k \\ 1/\omega_n & \omega_n \end{array} \right] \left\{ \begin{array}{c} a_0 \\ a_1 \end{array} \right\} \tag{4.18}$$

Considering that both modes k and n have the same damping ratio ξ and solving equation 4.18 the coefficients a_0 and a_1 can be obtained as follow:

$$a_0 = \xi \frac{2\omega_k\omega_n}{\omega_k + \omega_n} \quad a_1 = \xi \frac{2}{\omega_k + \omega_n} \tag{4.19}$$

The damping coefficient ratio for any other i mode, ξ_i are defined by equation 4.17.

The use of the Rayleigh damping model for non-linear analysis of structures has some limitations that can lead to errors during the calculations. These issues are well described in the literature: the use of the initial stiffness in the definition of the damping model leads to unrealistic damping forces [19, 49]. Unrealistic damping forces lead to an underestimation of the displacements and to an overestimation of the internal forces [25, 102]. If the damping matrix remains constant as the structure yields resulting in a decrease in the stiffness and the natural frequencies then the fractions of critical damping increase [24]. Inappropriate modeling of structural damping may cause underestimation of the collapse potential of buildings [102].

One solution to avoid the problems of using the Rayleigh damping model is to update the damping matrix after each step [27]. But the limitations of the software used for the analysis makes this solution impossible. An alternative to the above mentioned solution consists of using reduced frequencies in the estimation of the Rayleigh coefficients [27]. This solution limits the damping in the lower modes of vibration after yielding avoiding considering an overestimation of the damping as the structures suffers inelastic displacements. In our case a reduced first frequency ω_1 is considered. To estimate the values of ω_1, an effective period of vibration T_{eff} is considered. Based on the push over capacity curve of the structure T_{eff} can be estimated with equation 4.20:

$$T_{eff} = 2\pi\sqrt{\frac{M\delta_y}{Q_y}} \tag{4.20}$$

Where Q_y and δ_y are the yield displacement an strength of the idealized bi-linear curve according to FEMA-356 [45].

4.3.1. Prototypes BF-SCWB.

4.3.1.1. Prototype 3S-BF-SCWB.

Geometric definition

The building is a 3 × 3 spans and 3 storeys RC structure with a total height of 9.7 m above the basement. The dimensions of the typical floor are 15 × 14.4 m. The height of the first storey is 3.5 m, whereas the height of the other storeys is 3.1 m. The elevation of the building and one typical floor are shown in figures 4.11 and 4.10. The reinforcement details of the RC sections are shown in table 4.8. Where h is the section depth, b is the section width and Top and bottom Reinf. are the top and bottom bars sizes. The bending mechanical properties of the RC sections are also summarized in table 4.8, where φ_c is the cracking curvature, M_c is the cracking bending moment, φ_y is the yielding curvature, M_y is the yielding bending moment, φ_u is the ultimate curvature and M_u is the ultimate bending moment. The section types and the potential plastic hinge locations are labelled in figure 4.11 with the letter H followed by numbers.

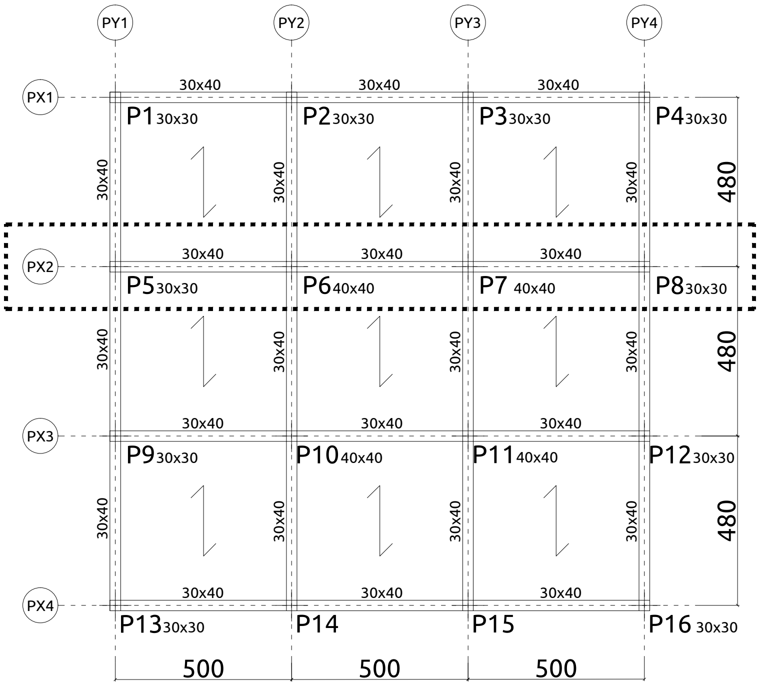

Figure 4.10.: 3S-BF-SCWB Prototype. Plan

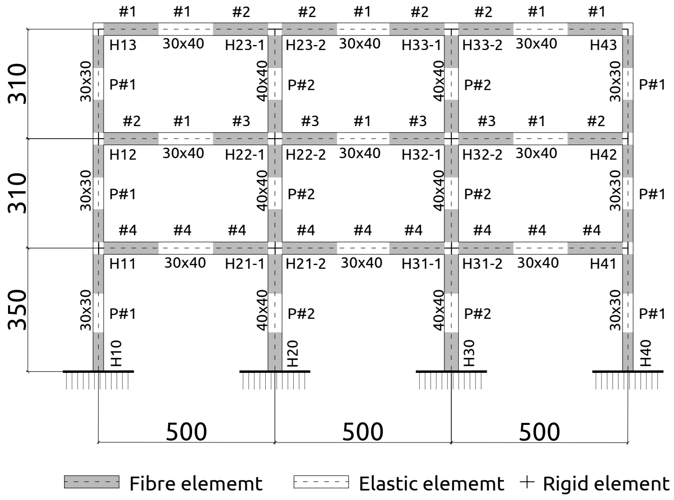

Figure 4.11.: 3S-BF-SCWB Prototype. Elevation

Section	bxh (cm)	Top Reinf.	Bottom Reinf.	φ_C^+ (1/m)	M_C^+ (kNm)	φ_y^+ (1/m)	M_y^+ (kNm)	φ_u^+ (1/m)	M_u^+ (kNm)	φ_C^- (1/m)	M_C^- (kNm)	φ_y^- (1/m)	M_y^- (kNm)	φ_u^- (1/m)	M_u^- (kNm)
#1	30X40	$4\phi12$	$5\phi12$	4.9E-4	24.6	1.0E-2	106.1	6.1E-2	110.5	-4.9E-4	-24.4	-9.7E-3	-88.9	-6.9E-2	-92.6
#2	30X40	$4\phi12 + 1\phi16$	$5\phi12$	3.5E-4	17.6	9.4E-3	91.4	7.5E-2	94.69	-3.5E-4	-17.42	-9.7E-3	-104.5	-6.9E-2	-108.4
#3	30X40	$4\phi12 + 2\phi16$	$5\phi12$	4.8E-4	25.0	9.8E-3	106.4	6.7E-2	110.3	-4.9E-4	-25.6	-1.1E-2	-149.6	-4.9E-2	-155.6
#4	30X40	$4\phi12 + 2\phi20$	$5\phi12$	3.4E-4	18.1	9.2E-3	91.3	7.4E-2	94.6	-3.6E-4	-18.9	-1.1E-2	-166.1	-4.8E-2	-173.8
P#1	30X30	$5\phi16$ x cara		6.8E-4	16.2	1.7E-2	142.1	3.4E-2	164.1	-6.7E-4	-16.24	-1.8E-2	-142.1	-3.4E-2	-164.1
P#2	40X40	$6\phi16$ x cara		4.4E-4	34.8	1.2E-2	369.1	2.7E-2	441.7	-4.4E-4	-34.8	-1.2E-2	-369.1	-2.7E-2	-441.9

Table 4.8.: Section reinforcement details 3S-BF-SCWB

Dynamic properties.

The results of an elastic modal analysis, considering gross sections, for the first three modes of vibration are shown in table 4.9, where T_n is the vibration period, $\mathit{\Gamma}_n$ is the modal participation factor and ϕ_n are the shape vectors for each n-mode of vibration considered.

	Mode 1	Mode 2	Mode 3
T_n(s)	0.54	0.16	0.09
$\mathit{\Gamma}_n$	1.24	0.35	-0.13
Modal shape	ϕ_1	ϕ_2	ϕ_3
3	1	-0.88	-0.47
2	0.78	0.46	1
1	0.42	1	-0.84

Table 4.9.: Dynamic characterization 3S-BF-SCWB

Capacity curve.

The base shear versus top displacement relationship (overall capacity curve) obtained by a force-controlled push over analysis is shown in bold line in figure 4.12. The push over analysis was performed using the first vibration mode lateral force pattern. The dash line in figure 4.12 shows the idealization of the capacity curve according to the FEMA-356. Based on the idealized capacity curve, the global yield displacement δ_y and yield strength Q_y parameters shown in table 4.10 can be determined. Table 4.11 summarizes the values of δ_{yi} and Q_{yi} at each i-storey obtained from the lateral shear force vs. inter-storey drift curves obtained from the push over analysis, and shown in figure 4.13.

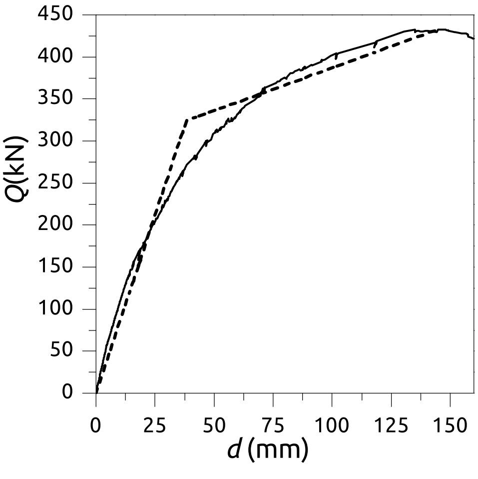

Figure 4.12.: Capacity curve 3S-BF-SCWB

δ_y (mm)	Q_y (kN)
38.4	324

Table 4.10.: Global parameters 3S-BF-SCWB

storey	δ_{yi} (mm)	Q_{yi} (kN)
3	8.58	152.24
2	11.32	233.6
1	11.57	291.0

Table 4.11.: Mechanical properties at i-th storey 3S-BF-SCWB

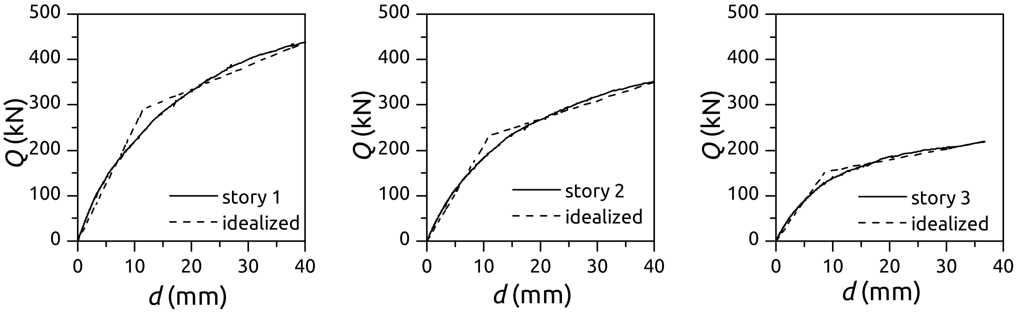

(a) storey 1 (b) storey 2 (c) storey 3

Figure 4.13.: Capacity curve at i-th storey 3S-BF-SCWB

4.3.1.2. Prototype 6S-BF-SCWB.

Geometrical definition.

The prototype building is a 3 × 4 spans and 6 storeys RC structure with a total height of 19 m above the basement. The dimensions of the typical floor are 20 × 14.4 m. The height of the first storey is 3.5 m, whereas the height of the other storeys is 3.1 m. The elevation of the building and one typical floor plan are shown in figures 4.15 and 4.14. The reinforcement details of the typical RC sections are shown in table 4.12. Where h is the section depth, b is the section width and Top and bottom Reinf. are the top and bottom bars sizes. The bending mechanical properties of the RC sections are also summarized in table 4.12, where φ_c is the cracking curvature, M_c is the cracking bending moment, φ_y is the yielding curvature, M_y is the yielding bending moment, φ_u is the ultimate curvature and M_u is the ultimate bending moment. The section types and the potential plastic hinge locations are labelled in figure 4.15 with the letter H followed by numbers.

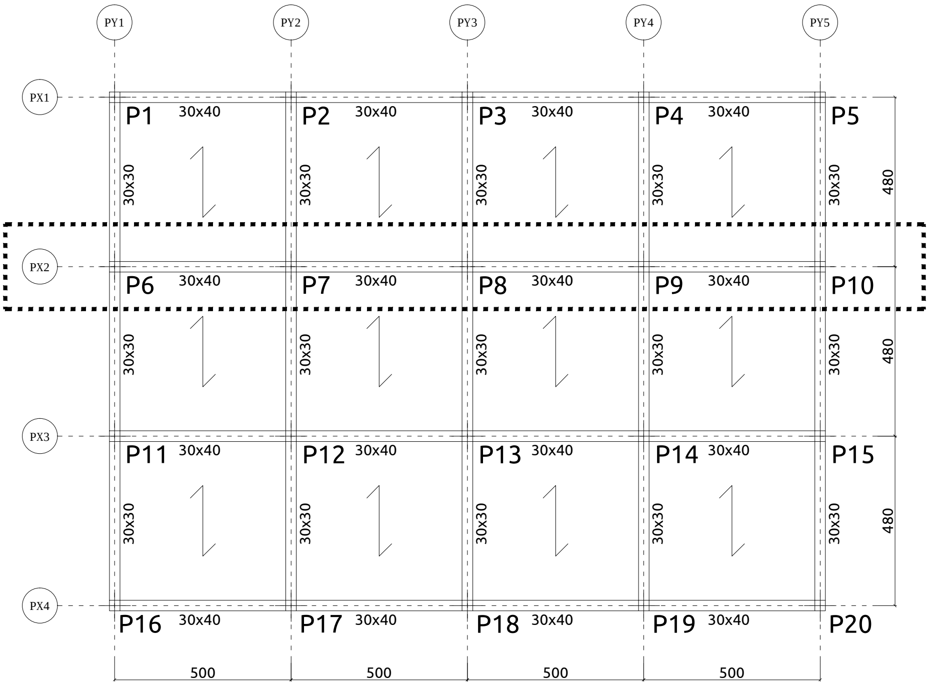

Figure 4.14.: 6S-BF-SCWB Prototype elevation

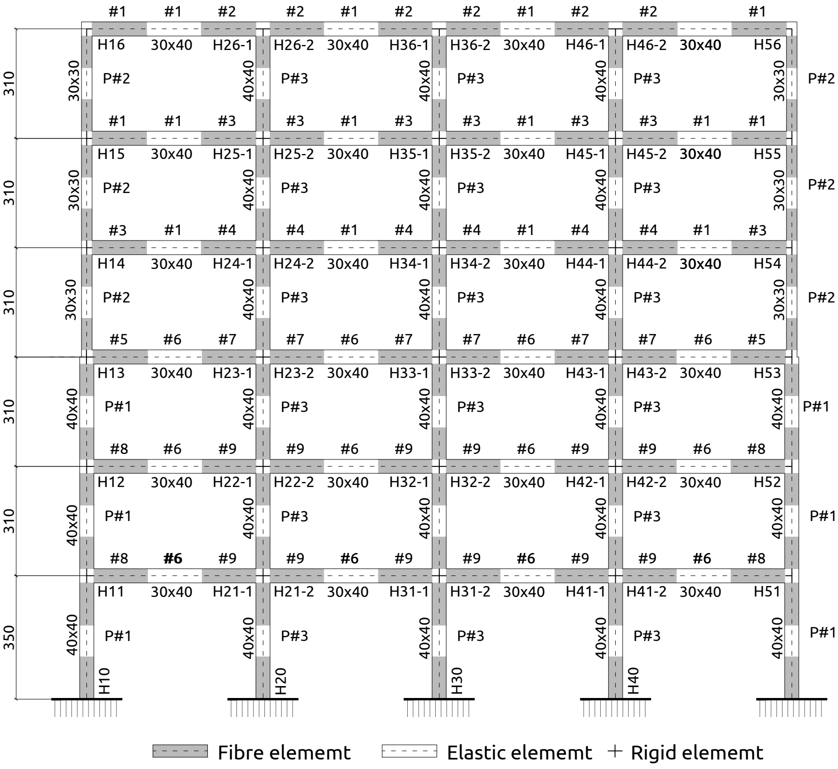

Figure 4.15.: 6S-BF-SCWB Prototype elevation

Section	bxh (cm)	Top Reinf	Bottom Reinf	φ_C^+ (1/m)	M_C^+ (kNm)	φ_y^+ (1/m)	M_y^+ (kNm)	φ_u^+ (1/m)	M_u^+ (kNm)	φ_C^- (1/m)	M_C^- (kNm)	φ_y^- (1/m)	M_y^- (kNm)	φ_u^- (1/m)	M_u^- (kNm)
#1	30X40	2ϕ20	2ϕ20	3.9E-4	17.8	9.5E-3	101.9	7.4E-2	105.4	-3.9E-4	-17.8	-9.5E-3	-101.9	-7.4E-2	-105.4
#2	30X40	3ϕ20	2ϕ20	5.4E-3	24.4	9.8E-3	117.3	6.8E-2	121.4	-5.4E-3	-24.4	-1.1E-2	-163.7	-4.9E-2	-170.4
#3	30X40	2ϕ20 + 1ϕ16	2ϕ20	5.4E-3	24.4	9.9E-3	117.1	6.6E-2	121.4	-5.4E-2	-24.4	-1.0E-2	-147.0	-5.3E-2	-152.9
#4	30X40	2ϕ20 + 2ϕ16	2ϕ20	3.9E-4	17.7	9.3E-3	102.2	7.8E-2	105.4	-3.9E-4	-17.8	-1.0E-2	-163.1	-5.3E-2	-169.0
#5	40X40	3ϕ20	3ϕ20	5.1E-4	30.3	1.0E-2	167.0	6.3E-2	173.1	-5.1E-4	-30.3	-1.0E-2	-167.0	-6.3E-2	-173.2
#6	40X40	2ϕ20	3ϕ20	5.1E-4	30.3	1.0E-2	167.0	5.7E-2	172.8	-5.1E-4	-30.3	-9.4E-3	-118.5	-7.5E-2	-123.1
#7	40X40	4ϕ20	3ϕ20	3.9E-4	23.7	9.5E-2	152.6	7.3E-2	157.3	-3.9E-4	-23.6	-1.0E-2	-200.2	-5.8E-2	-207.2
#8	40X40	2ϕ20 + 2ϕ16	3ϕ20	5.1E-4	30.3	1.0E-2	167.1	6.4E-2	173.2	-5.1E-4	-30.3	-1.0E-2	-180.3	-5.9E-2	-187.9
#9	40X40	2ϕ20 + 3ϕ16	3ϕ20	5.1E-4	30.3	9.9E-3	167.5	-5.6E-2	173.3	-5.1E-4	-30.3	-1.0E-2	-210.5	-5.3E-2	-218.6
P#1	40X40	5ϕ20 por cara		3.9E-4	23.7	1.1E-2	303.4	3.2E-2	375.8	-3.9E-4	-23.7	-1.1E-2	-303.4	-3.2E-2	-375.8
P#2	30X30	5ϕ16 por cara		7.9E-4	15.0	1.7E-2	146.0	3.5E-2	171.9	-7.9E-4	-15.0	-1.7E-2	-146.0	-3.5E-2	-171.9
P#3	40X40	6ϕ20 por cara		5.1E-4	30.35	1.2E-2	381.2	2.8E-2	463.1	-5.1E-4	-30.3	-1.2E-2	-381.2	-2.8E-2	-463.1

Table 4.12.: 6S-BF-SCWB Section reinforcement details

Dynamic properties. The results of an elastic modal analysis, considering gross sections, for the first three modes of vibration are shown in table 4.13, where T_n is the vibration period, $\mathit{\Gamma}_n$ is the modal participation factor and ϕ_n are the shape vectors for each n-mode of vibration considered.

	Mode 1	Mode 2	Mode 3
T_n(s)	0.97	0.33	0.18
$\mathit{\Gamma}_n$	1.24	0.42	-0.24
Modal shape	ϕ_1	ϕ_2	ϕ_3
6	1	-1	-0.86
5	0.92	-0.43	0.37
4	0.77	0.34	1
3	0.59	0.88	0.23
2	0.41	0.92	-0.72
1	0.2	0.56	-0.82

Table 4.13.: Dynamic characterization 6S-BF-SCWB.

Capacity curve. The base shear versus top displacement relationship (overall capacity curve) obtained by a force-controlled push over analysis is shown in bold line in figure 4.16. The push over analysis was performed using the first vibration mode lateral force pattern. The dash line in figure 4.16 shows the idealization of the capacity curve according to the FEMA-356. Based on the idealized capacity curve the global yield displacement δ_y and yield strength Q_y parameter shown in table 4.14 can be determined. Table 4.15 summarizes the values of δ_{yi} and Q_{yi} at each i-storey obtained from the lateral shear force vs. inter-storey drift curves obtained from the push over analysis, and shown in figure 4.17.

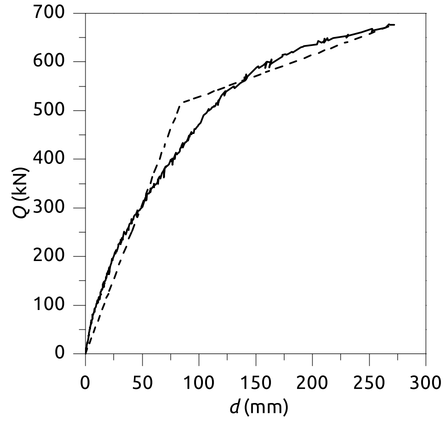

Figure 4.16.: Capacity curve 6S-BF-SCWB

δ_y (mm)	Q_y (kN)
85.7	516

Table 4.14.: Global parameters 6S-BF-SCWB

storey	δ_y	Q_y
6	10.3	206.3
5	12.4	287.1
4	10.9	310.0
3	10.4	346.8
2	10.9	383.6
1	12.4	473.1

Table 4.15.: Mechanical properties at *i*-th storey 6S-BF-SCWB

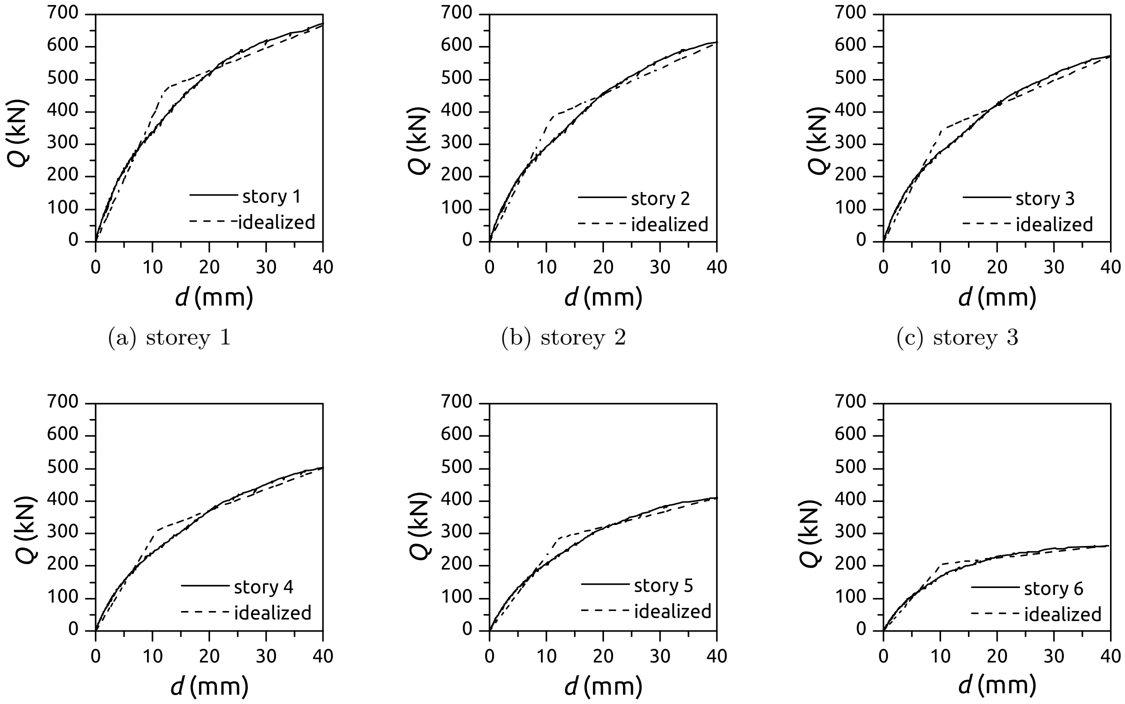

(a) storey 1 (b) storey 2 (c) storey 3

(d) storey 4 (e) storey 5 (f) storey 6

Figure 4.17.: storey capacity curve 6S-BF-SCWB prototype

4.3.1.3. Prototype 3S-FD-GL.

Geometrical definition The prototype building is a 3 × 3 spans and 3 storeys RC structure with a total height of 9.7 m above the basement. The dimensions of the type floor are 15 × 14.4 m. The height of the first storey is 3.5 m, whereas the height of the other storeys is 3.1 m. At each level two hysteretic dampers are included. The connection of the damper with the beam-column joint is solved with pin joints to ensure that only axial loads are transmitted to the main frame. The elevation of the building and one floor type plan are shown in figures 4.19 and 4.18. The dampers are represented by the spring elements in figure 4.19. The reinforcement details of the type RC sections are shown in table 4.16. The section types and the potential plastic hinge locations are labelled in figure 4.19 with the letter H followed by numbers.

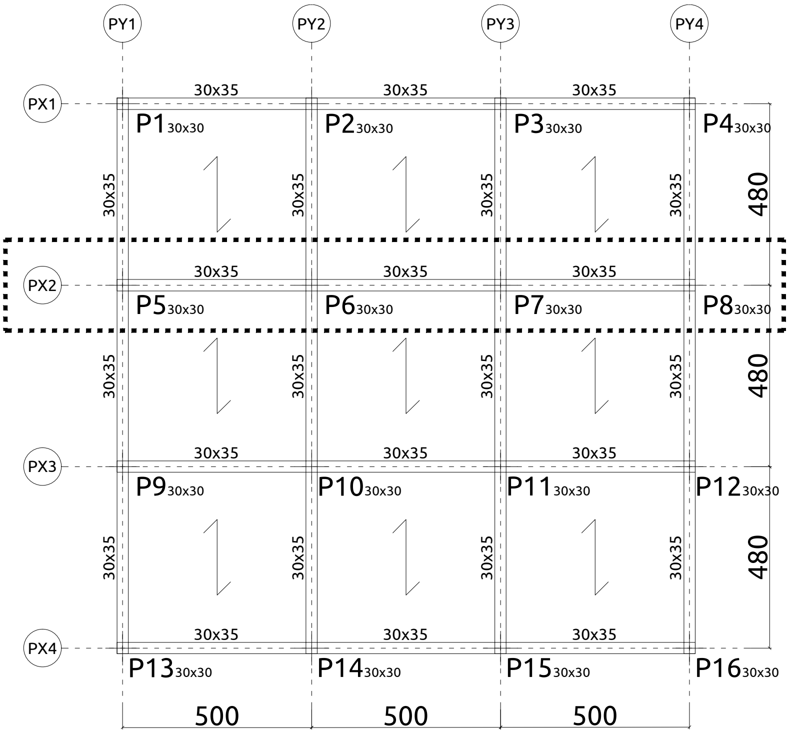

Figure 4.18.: 3S-FD-GL prototype plan

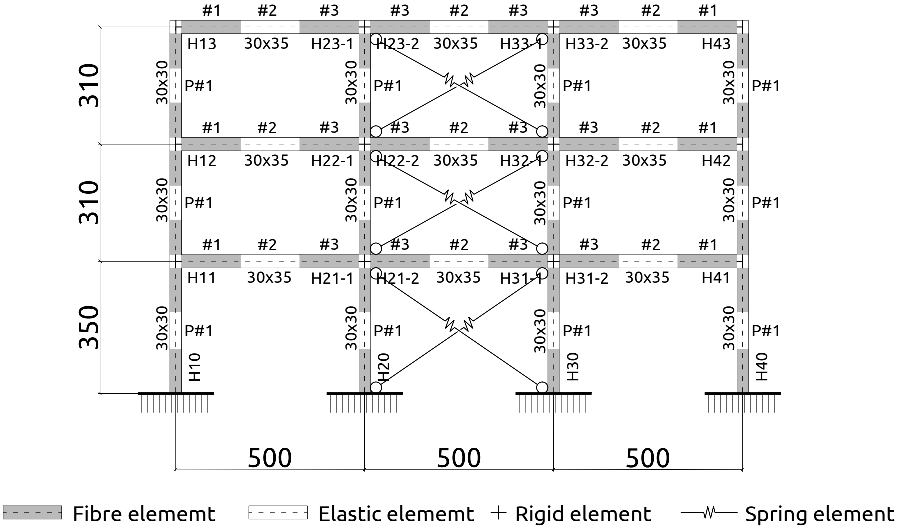

Figure 4.19.: 3S-FD-GL prototype elevation

Section	bxh (cm)	Arm sup	Arm inf	φ_C^+ (1/m)	M_C^+ (kNm)	φ_y^+ (1/m)	M_y^+ (kNm)	φ_u^+ (1/m)	M_u^+ (kNm)	φ_C^- (1/m)	M_C^- (kNm)	φ_y^- (1/m)	M_y^- (kNm)	φ_u^- (1/m)	M_u^- (kNm)
#1	30X35	5ϕ12	4ϕ12	6.5E-4	19.4	1.1E-2	79.5	8.4E-2	82.7	-6.5E-4	-19.4	-1.1E-2	-94.5	-7.0E-2	-98.8
#2	30X35	2ϕ12	7ϕ12	4.5E-4	13.6	1.1E-2	96.5	6.7E-2	100.5	-4.5E-4	-13.6	-9.41E-3	-33.7	-1.24E-1	-35.4
#3	30X35	7ϕ12	4ϕ12	6.5E-4	19.4	1.1E-2	79.8	9.1E-2	82.8	-6.5E-4	-19.43	-1.2E-2	-124.5	-5.5E-2	-130.3
P#1	30X30	4ϕ12 esquina		7.9E-4	15.0	1.3E-2	39.1	8.9E-2	41.1	-7.9E-4	-15.0	-1.3E-2	-39.1	-8.9E-2	-41.1

Table 4.16.: Section reinforcement details 3S-BF-GL

Capacity curve flexible part. The base shear versus top displacement relationship obtained by a force-controlled push over analysis of the RC bare frame without dampers is shown in bold line in figure 4.20. The push over analysis was performed using the first vibration mode lateral force pattern. The dash line in figure 4.20 shows the idealization of the capacity curve according to the FEMA- 356. Based on the idealized capacity curve the global yield displacement ${}_f\delta_y$ and yield strength ${}_fQ_y$ shown in table 4.17 can be determined. Table 4.18 summarizes the values of ${}_f\delta_{yi}$ and ${}_fQ_{yi}$ at each i-storey obtained from the storey capacity curves from figure 4.21.

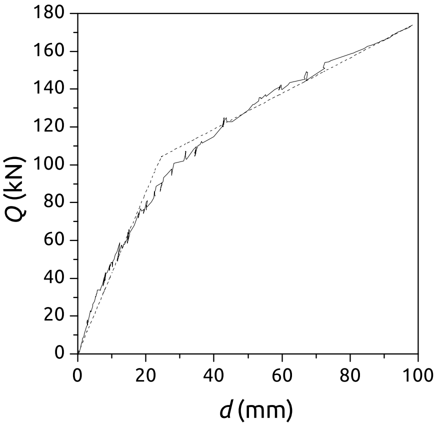

Figure 4.20.: RC Frame capacity curve. 3S-FD-GL

δ_y(mm)	Q_y (kN)
24.3	104.1

Table 4.17.: RC Frame global mechanical properties. 3S-FD-GL

storey	δ_y(mm)	Q_y (kN)
3	5.8	57.9
2	7.4	80.2
1	7.3	91.2

Table 4.18.: RC Frame mechanical properties at i-th storey. 3S-FD-GL

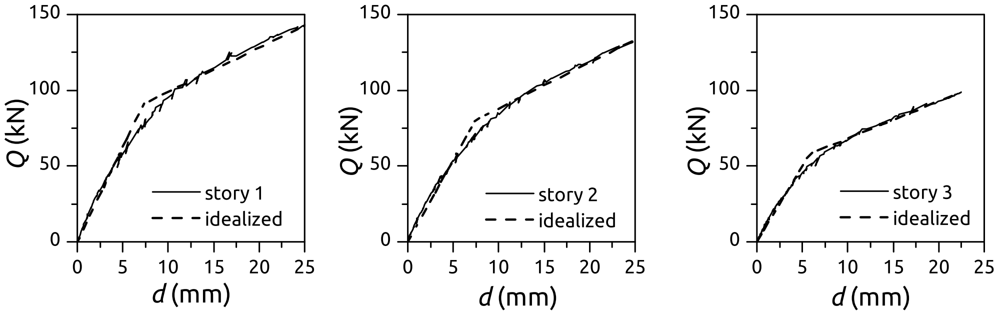

(a) storey 1 (b) storey 2 (c) storey 3

Figure 4.21.: RC Frame capacity curve at i-th storey 3S-FD-GL

Damper design.

Table 4.19 summarizes the design parameters of the mixed system at each level according to the procedure describe in subsection 4.2.2.2. The design lateral yield force and lateral displacement of the stiff part is related with the axial yield force and axial displacement of the dampers through the cosine of the angle that the axis of the damper form with the horizontal. Taking this fact into account ${}_sF_{yi}$ and ${}_s\Delta_{yi}$ in table 4.19 are the axial yield force and displacement of the dampers in their axial direction.

storey	$\bar{\alpha}_i$	α_i	β_i	k	${}_sQ_{yi} + {}_fQ_{yi}$ (kN)	${}_sQ_{yi}$ (kN)	${}_s\delta_{yi}$ (mm)	${}_sF_{yi}$ (kN)	${}_s\Delta_{yi}$ (mm)
3	1.63	0.43	0.73	13.18	218	160	1.2	188.7	1.4
2	1.18	0.31	0.76	16.35	334	254	1.4	298.6	1.7
1	1.00	0.26	0.79	21.44	432	341	1.3	400.9	1.5

Table 4.19.: Damper design at each level 3S-FD-GL.

Dynamic definition.

The results of an elastic modal analysis, using the gross section properties, for the first three modes of vibration are shown in table 4.20 , where T_n is the vibration period, Γ_n is the modal participation factor and $\phi_n$are the shape vectors for each n-mode of vibration considered.

	Mode 1	Mode 2	Mode 3
T_n(s)	0.22	0.08	0.059
Γ_n	1.27	0.44	-0.21
Modal shape	ϕ_1	ϕ_2	ϕ_3
3	1	0.94	-0.32
2	0.72	-0.78	0.88
1	0.34	1	-1

Table 4.20.: Dynamic characterization 3S-FD-GL.

Capacity curve mix system.

The base shear versus top displacement relationship (capacity curve) obtained by a force-controlled push over analysis of the RC frame equipped with the hysteretic dampers designed above is shown in bold line in figure 4.22 (FD). The push over analysis was performed using the first vibration mode lateral force pattern. For comparison the capacity curve obtained from the push over analysis of the RC bare frame (BF) was included with the dash line in figure 4.22. Table 4.21 shows the global parameters of the 3S-FD-GL prototype based on the idealization of the capacity curve.

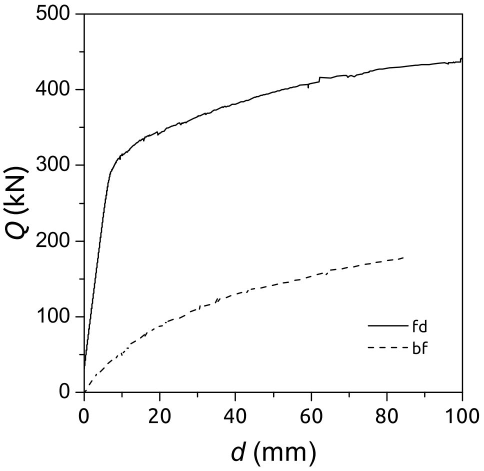

Figure 4.22.: Capacity curve 3S-BF-GL vs 3S-FD-GL.

δ_y(mm)	Q_y (kN)
7.1	291

Table 4.21.: Global parameters. 3S-FD-GL

4.3.1.4. Prototype 6S-FD-GL

Geometrical definition.

The building is a 3 × 4 spans and 6 storeys RC structure with a total height of 19 m above the basement. The dimensions of the type floor are 20 × 14.4m. The height of the first storey is 3.5 m, whereas the height of the other storeys is 3.1 m. At each level two hysteretic dampers are included. The connection with the RC frame is solved with pin joints to ensure that only axial loads are transmitted to the main frame. The elevation of the building and one floor type plan are shown in figures 4.23 and 4.19. The reinforcement details of the type RC sections are shown in table 4.22. , where φ_c is the cracking curvature, M_c is the cracking bending moment, φ_y is the yielding curvature, M_y is the yielding bending moment, φ_u is the ultimate curvature and M_u is the ultimate bending moment. The section types and the potential plastic hinge locations are labelled in figure 4.24with the letter H followed by numbers.

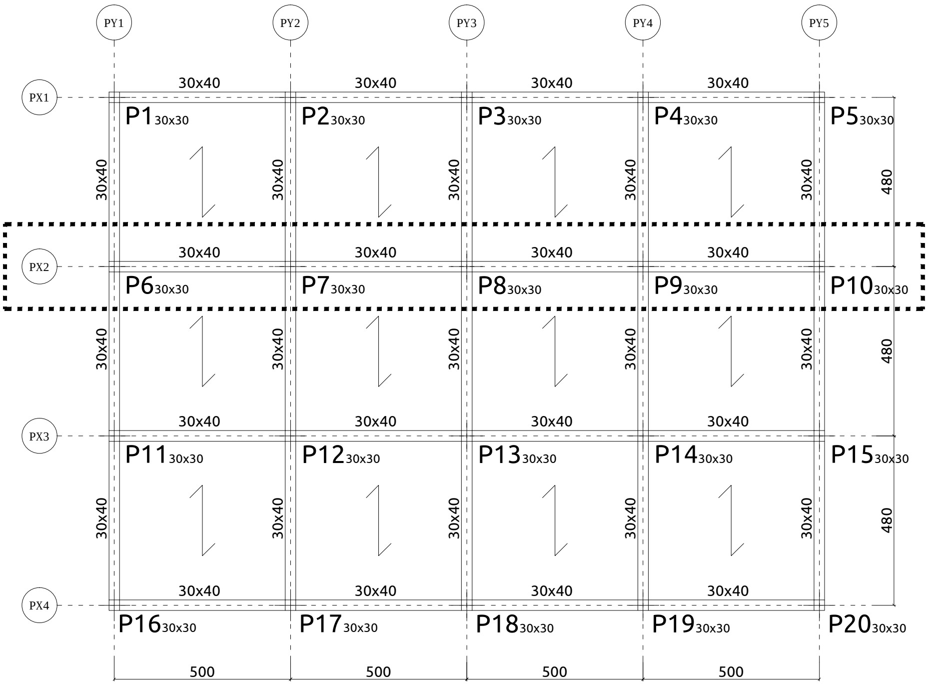

Figure 4.23.: Prototype 6S-FD-GL plan

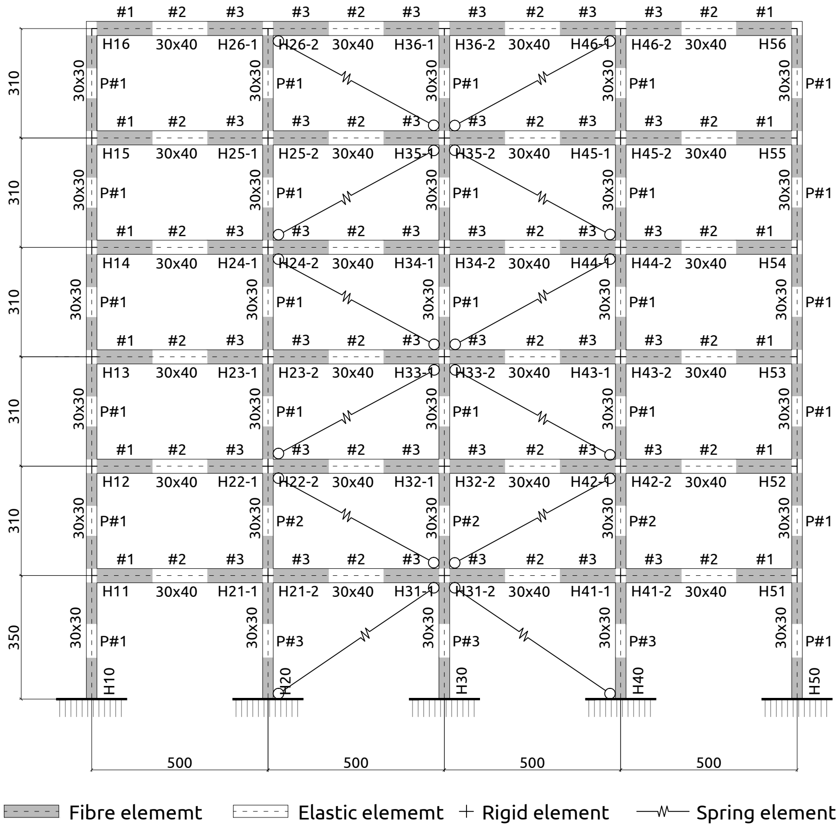

Figure 4.24.: Prototype 6S-FD-GL elevation

Section	bxh (cm)	Arm sup	Arm inf	φ_C^+ (1/m)	M_C^+ (kNm)	φ_y^+ (1/m)	M_y^+ (kNm)	φ_u^+ (1/m)	M_u^+ (kNm)	φ_C^- (1/m)	M_C^- (kNm)	φ_y^- (1/m)	M_y^- (kNm)	φ_u^- (1/m)	M_u^- (kNm)
#1	30X40	4ϕ12	4ϕ12	5.4E-4	24.4	9.7E-3	89.4	6.9E-2	93.27	-5.4E-4	-24.4	-9.7E-3	-89.4	-6.9E-2	-93.2
#2	30X40	2ϕ12	5ϕ12	3.9E-4	17.8	9.6E-3	91.8	7.4E-2	95.5	-3.9E-4	-17.8	-8.3E-3	-38.3	-1.0E-1	-41.2
#3	30X40	6ϕ12	4ϕ12	5.4E-4	24.4	9.5E-3	89.7	7.3E-2	93.28	-5.4E-4	-24.4	-1.0E-2	-123.8	-5.6E-2	-128.9
P#1	30X30	4ϕ12 esquina		7.4E-4	15.0	1.3E-2	39.1	9.0E-2	41.14	-7.4E-4	-15.0	-1.3E-2	-39.1	-9.0E-2	-41.14
P#2	30X30	4ϕ16 esquina		5.3E-4	10.0	1.3E-2	47.8	9.4E-2	49.7	-5.3E-4	-10.0	-1.3E-2	-47.8	-9.4E-2	-49.7
P#3	30X30	4ϕ20 esquina		7.9E-4	15.0	1.4E-2	83.8	6.6E-2	86.8	-7.9E-4	-15.0	-1.4E-2	-83.8	-6.6E-2	-86.8

Table 4.22.: Section reinforcement details 6S-FD-GL

Capacity curve flexible part.

The base shear versus top displacement relationship obtained by a force-controlled push over analysis of the RC bare frame without dampers is shown in bold line in figure 4.25. The push over analysis was performed using the first vibration mode lateral force pattern. The dash line in figure 4.25 shows the idealization of the capacity curve according to the FEMA- 356. Based on the idealized capacity curve the global yield displacement ${}_f\delta_y$ and yield strength ${}_fQ_y$ shown in table 4.23 can be determined. Table 4.24 summarizes the values of ${}_f\delta_{yi}$ and ${}_fQ_{yi}$ at each i-storey obtained from the storey capacity curves from figure 4.26.

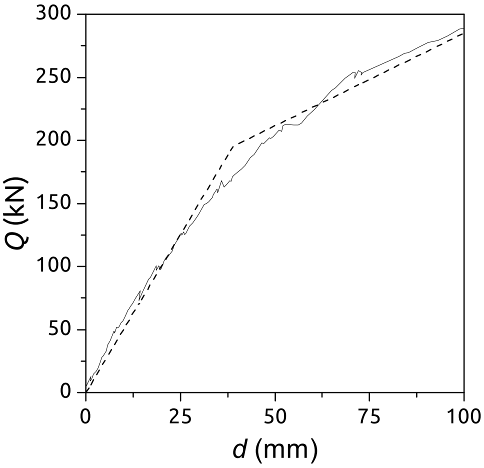

Figure 4.25.: RC frame capacity curve 6S-FD-GL

δ_y(mm)	Q_y (kN)
73.7	292

Table 4.23.: RC frame global parameters 6S-FD-GL

storey	δ_y(cm)	Q_y (kN)
6	6.4	131
5	7.4	151
4	7.5	152
3	8.7	170
2	9.2	176
1	9.6	190

Table 4.24.: RC frame mechanical properties at i-th storey 6S-FD-GL

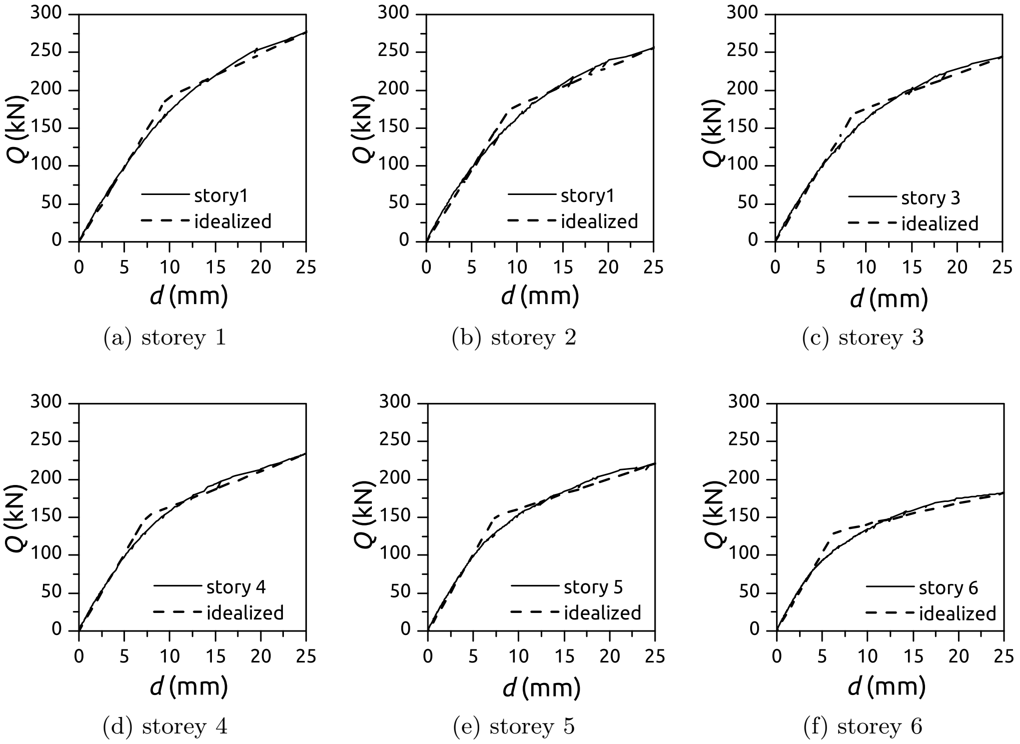
(a) storey 1 (b) storey 2 (c) storey 3

(d) storey 4 (e) storey 5 (f) storey 6

Figure 4.26.: RC frame capacity curve at i-th storey 6S-FD-GL

Damper design.

Table 4.25 summarizes the design parameters of the mixed system at each level according to the procedure describe above 4.2.2.2. The design lateral yield force and lateral displacement of the stiff part is related with the axial yield force and axial displacement of the dampers through the cosine of the angle that the axis of the damper form with the horizontal. Taking this fact into account ${}_sF_{yi}$ and ${}_s\Delta_{yi}$ in table 4.25 are the axial yield force and displacement of the dampers in their axial direction.

storey	$\bar{\alpha}_i$	α_i	β_i	k	${}_sQ_{yi} + {}_fQ_{yi}$ kN	${}_sQ_{yi}$ kN	${}_s\delta_{yi}$ mm	${}_sF_{yi}$ kN	${}_s\Delta_{yi}$ mm
6	2.17	0.38	0.48	2.67	251	120	2.2	140.9	2.6
5	1.63	0.28	0.62	5.79	393	242	2.1	285.2	2.4
4	1.38	0.24	0.70	10.08	506	354	1.7	416.5	2.0
3	1.18	0.20	0.71	10.68	581	411	2.0	483.5	2.3
2	1.08	0.19	0.74	13.45	669	493	1.9	579.9	2.3
1	1.00	0.17	0.74	14.29	743	553	2.0	650.6	2.3

Table 4.25.: Damper design at each level 6S-FD-GL

Dynamic definition.

The results of an elastic modal analysis, using the gross section properties, for the first three modes of vibration are shown in table 4.26 , where T_n is the vibration period, $\varGamma_n$ is the modal participation factor and ϕ_n are the shape vectors for each n-mode of vibration considered.

	Mode 1	Mode 2	Mode 3
T_n(s)	0.47	0.19	0.12
Γ_n	1.38	0.54	0.17
Modal shape	ϕ_1	ϕ_2	ϕ_3
6	1	-1	-0.79
5	0.84	-0.09	1
4	0.67	0.52	0.64
3	0.52	0.74	-0.25
2	0.33	0.63	-0.84
1	0.16	0.37	0.76

Table 4.26.: Dynamic characterization. 6S-FD-GL

Capacity curve analysis mix system.

The base shear versus top displacement relationship (capacity curve) obtained by a force-controlled push over analysis of the RC frame equipped with hysteretic damper designed above is shown in bold line in figure 4.27. The push over analysis was performed using the first vibration mode lateral force pattern. For comparison the capacity curve obtained from the push over analysis of the RC bare frame was included with the dash line in figure 4.27. Table 4.27 shows the global parameters of the 6S-FD-GL prototype based on the idealization of the capacity curve.

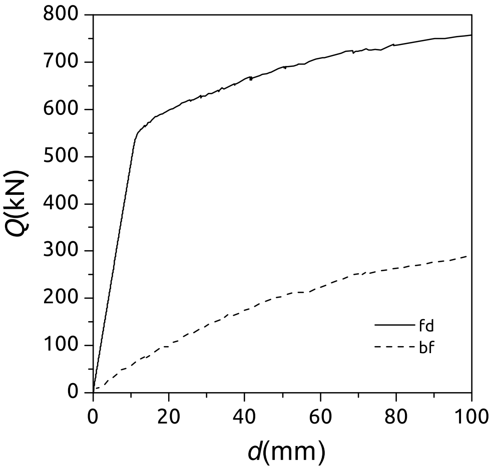

Figure 4.27.: Capacity curve 6S-FD-GL vs 6S-BF-GL.

δ_y(mm)	Q_y (kN)
11.5	545

Table 4.27.: Global parameters. 6S-FD-GL

4.4. Non linear time history analysis.

Eight historical accelerograms shown in Appendix A are used to perform the NTH analyses. Each accelerogram was scaled in amplitude by multiplying the PGA by the required factor to ensure that the total energy input in terms of equivalent velocity V_E was the same in every analysis. Matsumura [60] proved that V_E is a stable parameter to measure the intensity of the ground motions. The V_E reference value considered in this study corresponds to the 500 years return period earthquake expected in the highest prone area in Spain, which is the city of Granada. Benavent et al. [16] defined the energy input spectrum in terms of the equivalent velocity V_E and the maximum expected value in this area is 112.7 cm/s. Figure 4.28 shows the reference energy input spectra according to Benavent et al. [16] . Table 4.28 shows the scale factor used to modify the original accelerogram of the historical earthquakes in Appendix A to introduce the reference energy input at each analysis with a error lower than a ±10% after a trial and error procedure. Figure 4.29 shows the energy input response spectra in terms of equivalent velocity V_E and the velocity elastic response spectra S_v of the scaled ground motions for a 0.05 damping ratio . The dash line in the equivalent velocity spectrum shows the design earthquake reference value. The dot line in the spectra show the value of the effective period, T_{eff} considered during the analysis according to equation 4.20.

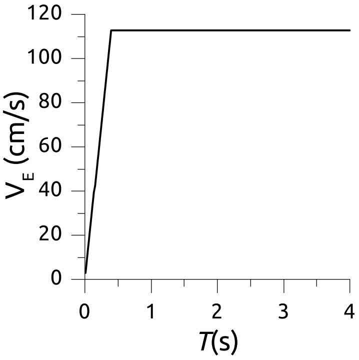

Figure 4.28.: Reference energy input spectra [16]

	3S-BF-SCWB	6S-BF-SCWB	3S-FD-GL	6S-FD-GL
Alkion (Korinthos)	1.63	1.45	1.85	1.47
Friuli (Tolmezzo)	2.40	3.0	1.90	2.08
El centro	1.27	1.30	1.47	1.3
Kobe	0.39	0.53	0.46	0.43
Montenegro (Petrovac)	0.72	0.96	0.72	0.6
Taft	1.90	2.12	2.02	2.1
Campano-Lucano (Calitri)	1.05	1.16	2.12	1.38
Montebello (Northridge)	3.65	4.27	3.10	2.97

Table 4.28.: Ground motion acceleration scale factors

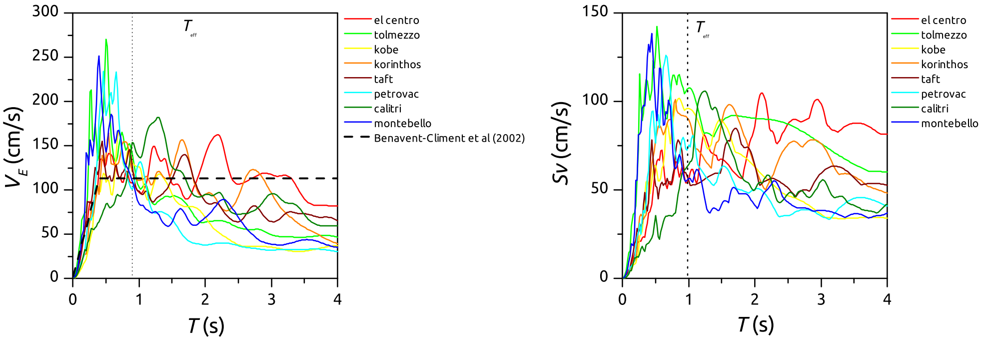

(a) 3S-BF-SCWB

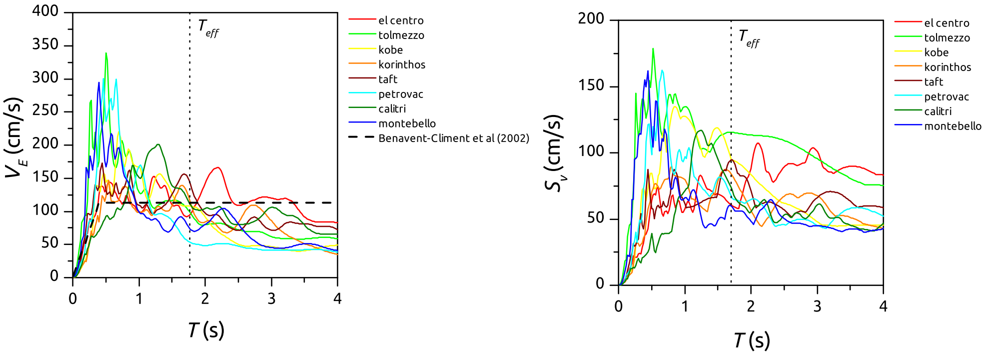

(b) 6S-BF-SCWB

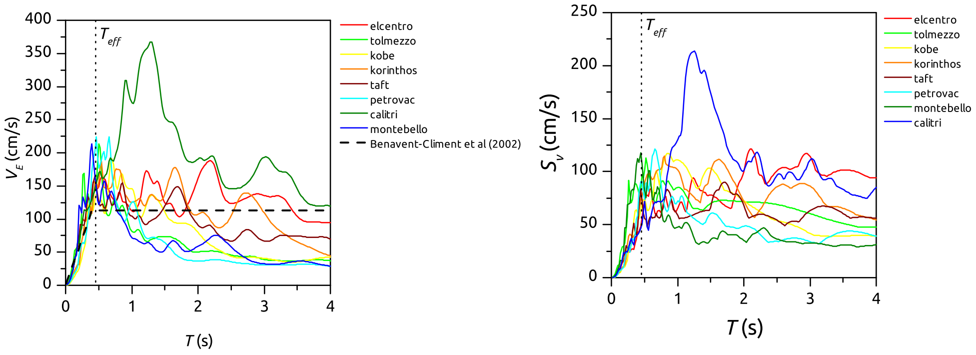

(c) 3S-FD-GL

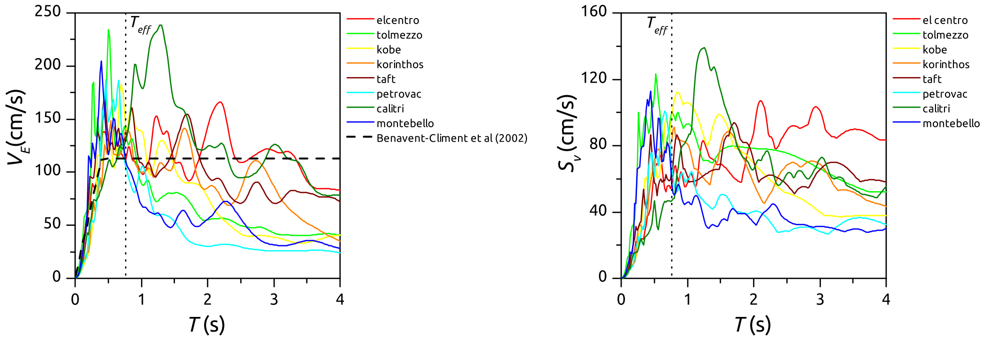

(d) 6S-FD-GL

Figure 4.29.: Energy inputV_E and Velocity S_v , elastic response spectra

4.5. Seismic response.

4.5.1. Global seismic response.

Based on the results of the NTH analyses the maximum global response values for each seismic analysis and prototype are evaluated in terms of the inter-storey drift ratio, id, cumulative inelastic deformation ratio, η, maximum plastic deformation ratio, μ and structural efficiency (cumulative to maximum plastic deformation ratios η/μ).

Maximum inter-storey drift ratio.

The id ratio was obtained using the absolute value of the maximum inter-storey displacement at the i-storey in the positive and negative domain $\delta^{\pm}_{max,i}$ divided by the storey height h_i as expressed in equation 4.21.

$$id = \frac{max\left(|\delta^{+}_{max,i}|, |\delta^{-}_{max,i}|\right)}{h_i} \times 100 \tag{4.21}$$

Cumulative inelastic deformation ratio.

η_i is defined as the ratio between the plastic energy dissipated at the i-th storey $W^{\pm}_{pi}$ and the yield force and displacement, in the positive and negative domain as expressed in equation 4.22.

$$\eta_i = \eta^{+}_i + \eta^{-}_i = \frac{W^{+}_{pi}}{Q^{+}_{yi}\delta^{+}_{yi}} + \frac{W^{-}_{pi}}{Q^{-}_{yi}\delta^{-}_{yi}} \tag{4.22}$$

Maximum plastic deformation ratio.

μ_i was obtained as the ratio between the absolute value of the maximum inter-storey displacement $\delta^{\pm}_{max,i}$ minus the storey yield displacement δ_{yi}, and the yield displacement at the i-storey in the positive and negative domain as expressed in equation 4.23

$$\mu_i = max\left(\frac{|\delta^{+}_{max,i}| - \delta^{+}_{yi}}{\delta^{+}_{yi}}; \frac{|\delta^{-}_{max,i}| - \delta^{-}_{yi}}{\delta^{-}_{yi}}\right) \tag{4.23}$$

4.5.2. Local seismic response.

A study of the seismic response of the prototype structures at the potential plastic hinges have been done. The results obtained by the NTH analyses have been also compared with the experimental results explained in chapter 2. As can be seen below a good agreement between experimental and numerical results was found for the same seismic hazard scenario.

4.5.2.1. Energy dissipated at plastic hinges

In fibre element models the non-linearity of structural elements are determined by the constitutive laws of the materials which define the mechanical properties and its hysteretic behaviour as seen in section 4.3. In constrast to lumped plasticity models, where the expected non lineal deformations are concentrated in clearly located springs defined by moment-rotation ($M - \theta$) laws, in fibre element models the non linear deformations are spread among different finite elements that define the model. Figure 4.30 shows the curvature distribution along a beam due to the seismic action lateral loads. Analyzing half beam from figure 4.30 in detail the curvature distribution law can be simplified considering that the value of the curvature φ_i at each Gauss point of the finite element mesh is constant for each half finite element.

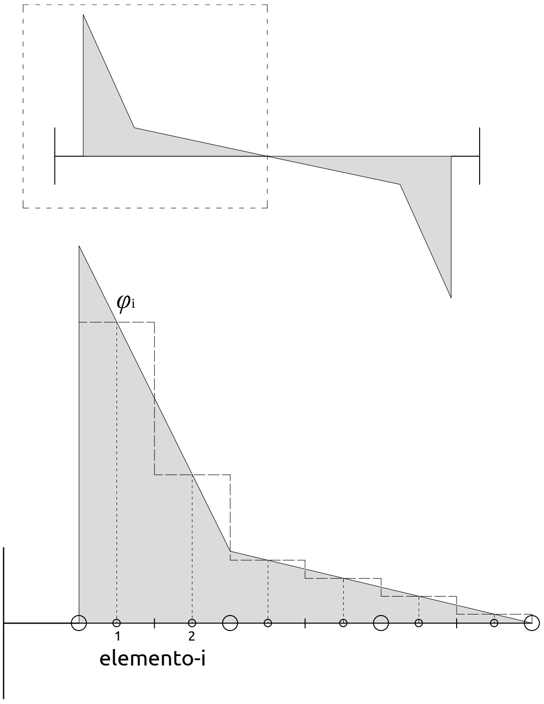

Figure 4.30.: Curvature distribution

Based on this curvature distribution, the rotation at each half finite element , θ_i can be obtained by multiplying the curvature φ_i by half the length of the element, L_i as can be seen in figure 4.31

$$\theta_i = \varphi_i \frac{L_i}{2} \tag{4.24}$$

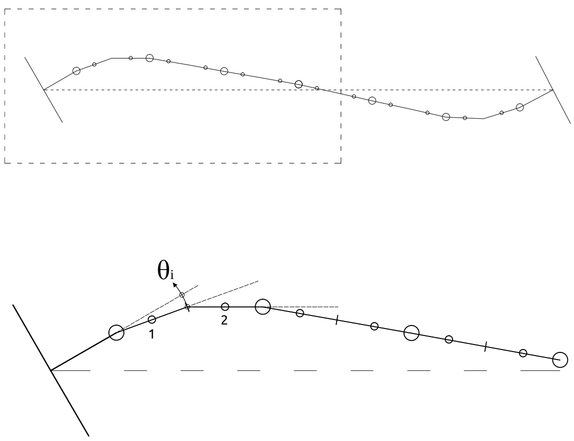

Figure 4.31.: Rotation at beams due to seismic action

Multiplying the rotation at each half finite element by the bending moment at each Gauss point of the elements that configure the beam an integrating along the duration of the earthquake we can obtain the energy dissipated by bending at each half element as expressed in equation 4.25:

$$W_{\theta i} = \int M_i d\theta_i \tag{4.25}$$

The energy dissipated at the structural elements hence can be estimated as the sum of the energy dissipated by each half finite element i that configure them.

$$W_e + W_p = \sum_{i=1}^{n} W_{\theta i} \tag{4.26}$$

4.5.2.2. Damage at plastic hinges.

The damage at idealized plastic hinges is characterized in terms of chord rotation demand θ_{max}/θ_u, and two different damage indexes: D_i index from Darwing & Nmai and DI_{PA} index from Park & Ang. A summary of this response parameters definition is done below.

Chord rotation demand

The chord rotation demands at plastic hinge level were obtained with the absolute values of the ratio between the maximum rotation at the plastic hinge, θ_{max}, and the ultimate rotation capacity of the plastic hinge, θ_u, estimated by the expression 2.16 from Eurocode 8 Part 3 [39] It was shown in chaper 2 from the dynamic test conducted in this Thesis, that these equations can predict accurately the ultimate rotation capacity of the plastic hinges.

$$\frac{\theta_m}{\theta_u} = max\left(\left|\frac{\theta_m^+}{\theta_u^+}\right|, \left|\frac{\theta_m^-}{\theta_u^-}\right|\right) \tag{4.27}$$

D_i Damage Index

The energy based damage index D_i proposed by Darwin and Nmai [33] is defined as the ratio between the plastic energy dissipated at the plastic hinge n and the average of the yield bending moment M_y and rotation θ_y in the positive and negative domain.

$$D_i = \frac{W_{p,n}}{0.5\left(M_y^+\theta_y^+ + |M_y^-\theta_y^-|\right)} \tag{4.28}$$

$DI_{P\&A}$ Damage Index

A modified version of the Park & Ang damage index for bending elements has been used [95]. The yield rotations of the plastic hinges were obtained from the results of a monotonic pushover analysis of the whole structure. The ultimate rotation capacities were obtained from EC8 expressions 2.16. A value of $\beta = 0.1$ was considered as suggested by Park & Ang [70] for strength deterioration systems.

$$DI_{PA} = 0.5\left(\frac{\theta_m^+ - \theta_y^+}{\theta_u^+ - \theta_y^+} + \frac{|\theta_m^- - \theta_y^-|}{|\theta_u^- - \theta_y^-}\right) + \beta\frac{W_{p,n}}{0.5\left(M_y^+\theta_u^+ + |M_y^-\theta_u^-|\right)} \tag{4.29}$$

4.5.3. Seismic response of conventional RC frame systems: BF-SCWB prototype.

4.5.3.1. Maximum inter-storey drift.

Figures 4.32a and 4.32b show the maximum inter-storey drift, id, for the 3S-BF-SCWB and 6S-BF-SCWB prototypes respectively.

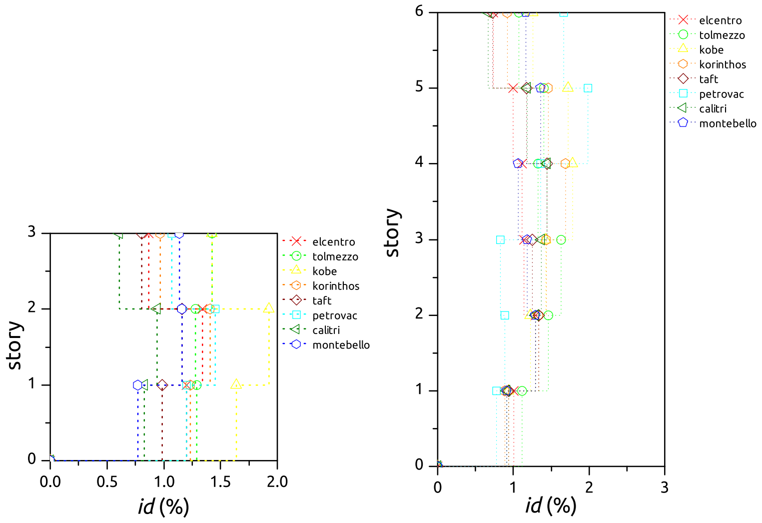

(a) 3S-BF-SCWB (b) 6S-BF-SCWB

Figure 4.32.: Maximum inter-storey drift, id , at i-th storey

4.5.3.2. Cumulative inelastic deformation ratio.

Figures 4.33a and 4.33b show the non-dimensional cumulative inelastic deformation ratio at i-th storey, η_i, for the 3S-BF-SCWB and 6S-BF-SCWB prototypes respectively.

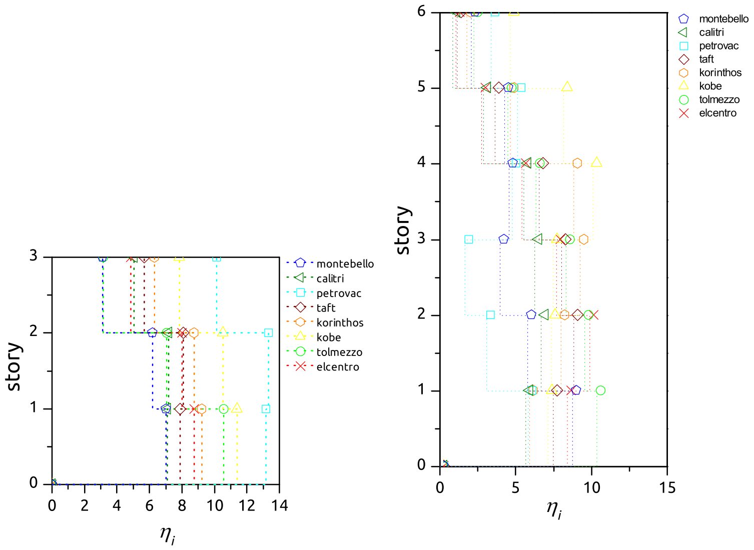

(a) 3S-BF-SCWB (b) 6S-BF-SCWB

Figure 4.33.: Cumulative inelastic deformation ratio, η_i , at i-th storey

4.5.3.3. Maximum plastic deformation ratio.

Figures 4.34a and 4.34b show the maximum plastic deformation ratio μ_i at the i-th storey for the 3S-BF-SCWB and 6S-BF-SCWB prototypes respectively.

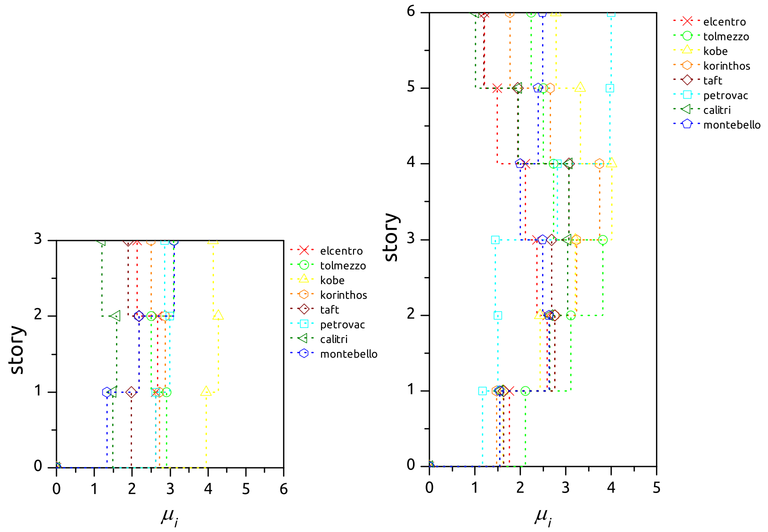

(a) 3S-BF-SCWB (b) 6S-BF-SCWB

Figure 4.34.: Maximum plastic deformation ratio μ_i

4.5.3.4. Structural efficiency: Cumulative to maximum plastic deformation ratios.

Figure 4.35 shows the relation between the cumulative inelastic deformation ratio η_i and the maximum plastic deformation ratio μ_i at i-th storey. The squares and circles represents the pairs of values (μ_i, η_i) at any i-th storey for the 6S-BF-SCWB and 3S-BF-SCWB prototypes respectively. The bold line in figure 4.35 is the linear regression of the scatter data, which is also compared with the limiting values proposed by Akiyama for an structure characterized with a Clough type hysteretic behaviour [3], represented with dash lines in the same figure. It can be seen in the figure that the design value of $^{\eta}/_{\mu}$ proposed by Akiyama (3.75) is greater (and thus on the unsafe side) than the value obtained from a regresion analysis of the resutls of this study (2.5). Therefore, a desgin value of 2.5 would be more appropriate.

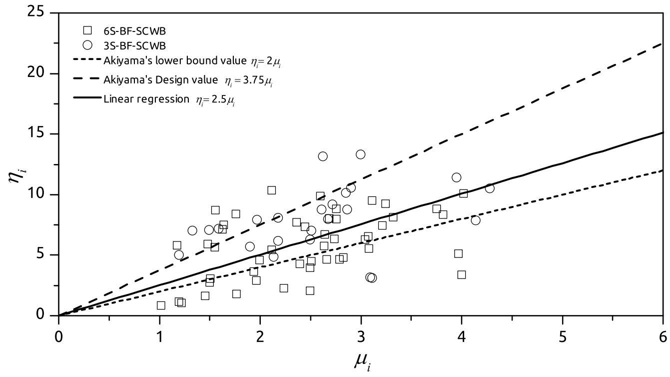

Figure 4.35.: η_i/μ_{mi}

4.5.3.5. Chord rotation demand

Figures 4.36a 4.36b show the results of the average chord rotations demand (θ_{max} normalized by the ultimate rotation capacity θ_u estimated with the equation of EC8-Part 3) for the plastic hinges (labelled at figures 4.11 and 4.15) at the same storey for the 3S-BF-SCWB and 6S-BF-SCWB prototypes respectively. Comparing the results obtained in the numerical analysis with the experimental results from table 2.4in chapter 2 it can be seen that the average maximum chord rotation demand at hinge level (0.26 for the 3S-BF-SCWB and 0.40 for the 6S-BF-SCWB) is consistent with the maximum chord rotation demand measured experimentally during the test for the same structural hazard level (0.28 for the c200 test).

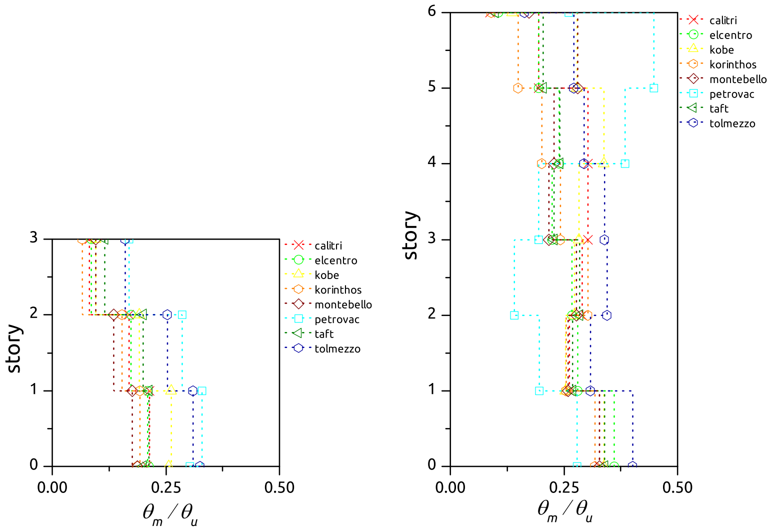

(a) 3S-BF-SCWB (b) 6S-BF-SCWB

Figure 4.36.: Chord rotation demand $^{\theta_{max}}/_{\theta_u}$ BF-SCWB

4.5.3.6. D_i damage index

Figures 4.37b and 4.37a show the average values of the D_i damage index for the plastic hinges (labelled at figures 4.11 and 4.15) at the same storey for the 3S-BF-SCWB and 6S-BF-SCWB prototypes respectively. The average maximum D_i index obtained with the NTH analysis (7.63 for 3S-BF-SCWB and 3.93 for the 6S-BF-SCWB) compared to those measured in the experimental test for the same seismic hazard level (7.38 for the c200 test) shows a similar range of values.

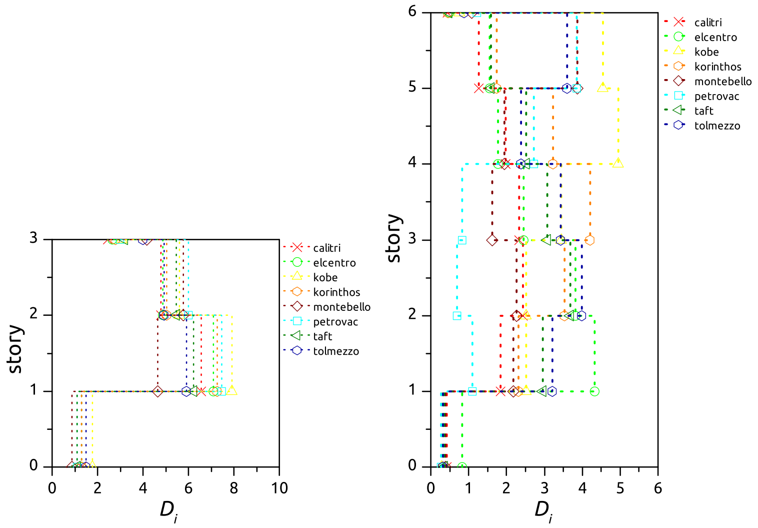

(a) 3S-BF-SCWB (b) 6S-BF-SCWB

Figure 4.37.: D_i index BF-SCWB

4.5.3.7. $DI_{P\&A}$ damage index

Figures 4.38b and 4.38a show the average values of the $DI_{P\&A}$ Park & Ang damage index for the plastic hinges (labelled at figures 4.11 and 4.15) at the same storey for the 3S-BF-SCWB and 6S-BF-SCWB prototypes respectively. The maximum average $DI_{P\&A}$ index at the plastic hinge level (0.18 for the 6S-BF-SCWB and 0.27 for the 3S-BF-SCWB) compared to the maximum $DI_{P\&A}$ index measured during the experimental test at the same seismic hazard level (0.26 for the c200 test) shows that there is a very good correlation between the results obtained with the NTH analysis and the test, which validates the accuracy of the FEM model.

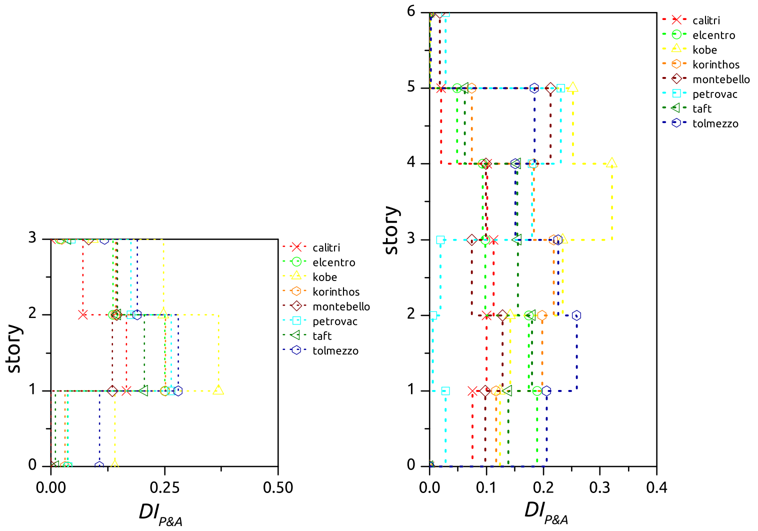

(a) $DI_{P\&A}$ 3S-BF-SCWB (b) $DI_{P\&A}$ 6S-BF-SCWB

Figure 4.38.: $DI_{P\&A}$ BF-SCWB

4.5.4. Seismic response innovative seismic resistant systems: FD-GL prototypes

4.5.4.1. Maximum inter-storey drift

Figures 4.39a and 4.39b show the maximum inter-storey drift, *id*, for the 3S-FD-GL and 6S-FD-GL prototypes respectively.

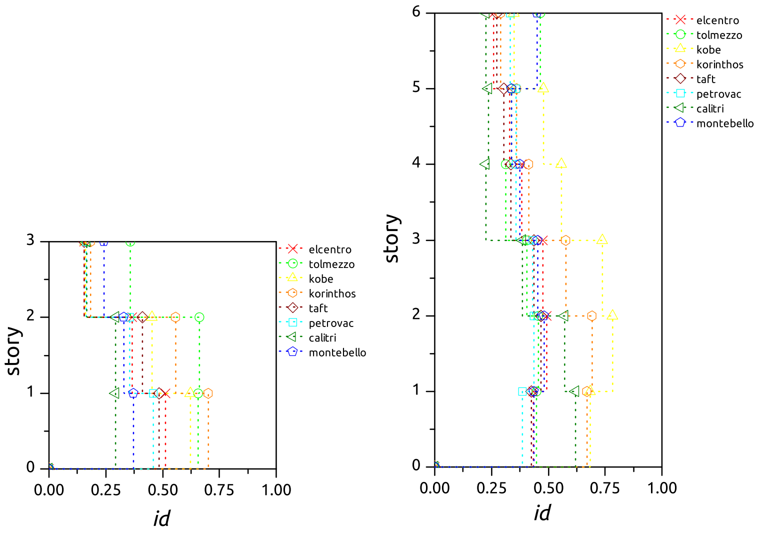

(a) 3S-FD-GL (b) 6S-FD-GL

Figure 4.39.: Maximum inter-storey drift, id , at i-th storey

4.5.4.2. Cumulative inelastic deformation ratio: RC frame

Figures 4.40a and 4.40b show the non-dimensional cumulative inelastic deformation ratio of the flexible part at i-th storey, ${}_f\eta_i$, for the 3S-FD-GL and 6S-FD-GL prototypes respectively.

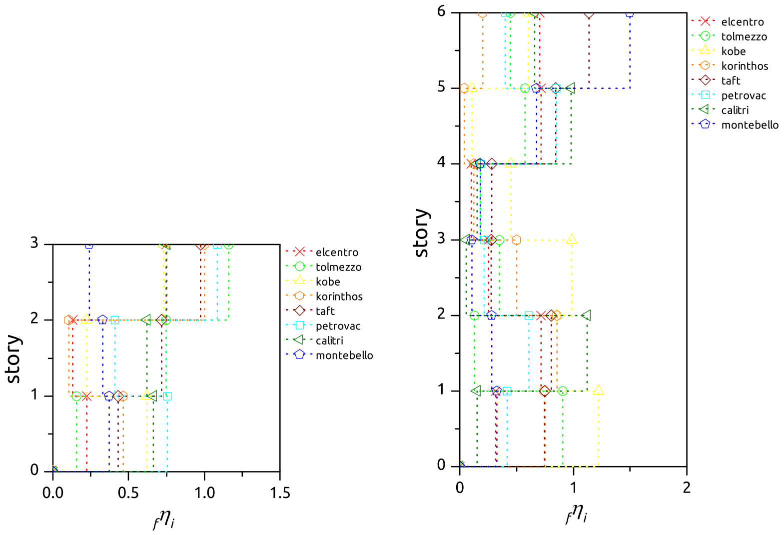

(a) 3S-FD-GL (b) 6S-FD-GL

Figure 4.40.: Cumulative inelastic deformation ratio of the flexible part, ${}_f\eta_i$, at i-th storey

4.5.4.3. Maximum plastic deformation ratio: RC frame

Figures 4.41a and 4.41b show the maximum plastic deformation ratio of the flexible part ${}_f\mu_i$ at the i-th storey for the 3S-FD-GL and 6S-FD-GL prototypes respectively.

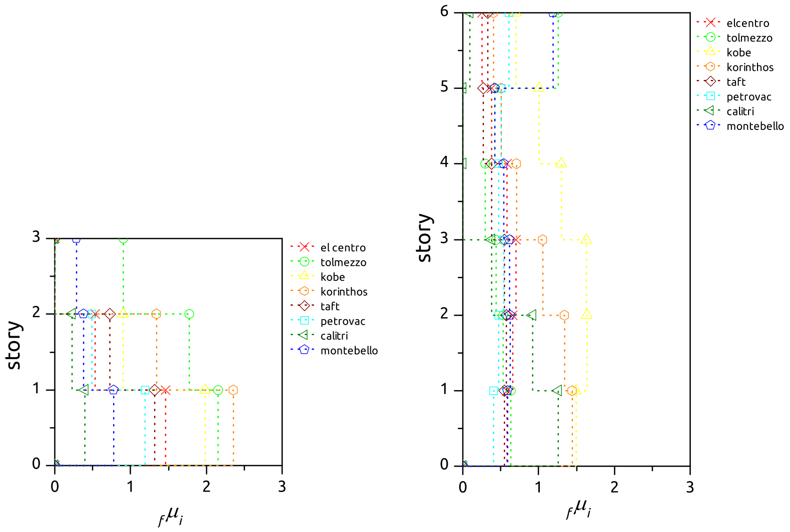

(a) 3S-FD-GL

(b) 6S-FD-GL

Figure 4.41.: Maximum plastic deformation ratio of the flexible part ${}_f\mu_i$ storey i^{th}

4.5.4.4. Cumulative inelastic deformation ratio: Dampers

Figures 4.43a and 4.42b show the non-dimensional cumulative inelastic deformation ratio of the stiff part at i-th storey, ${}_f\eta_i$, for the 3S-FD-GL and 6S-FD-GL prototypes respectively.

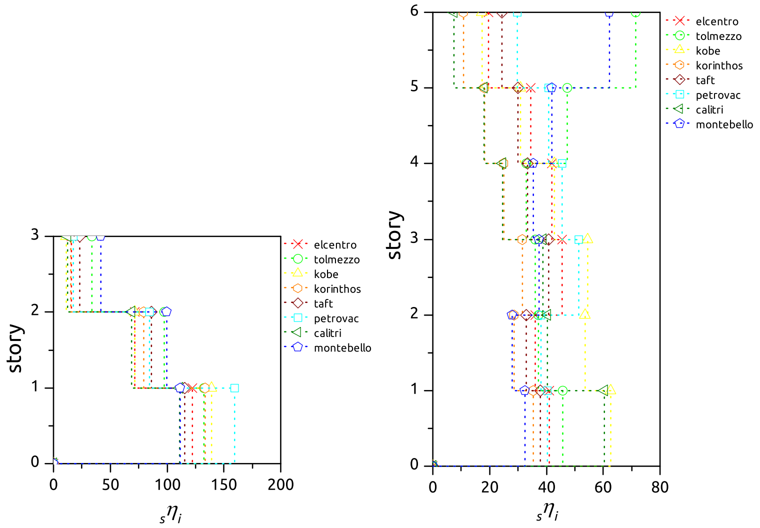

(a) 3S-FD-GL

(b) 6S-FD-GL

Figure 4.42.: Maximum plastic deformation ratio of the stiff part${}_s\eta_i$ storey i^{th}

4.5.4.5. Maximum plastic deformation ratio: Dampers

Figures 4.43a and 4.43b show the maximum plastic deformation ratio of the flexible part ${}_s\mu_i$ at the i-th storey for the 3S-FD-GL and 6S-FD-GL prototypes respectively.

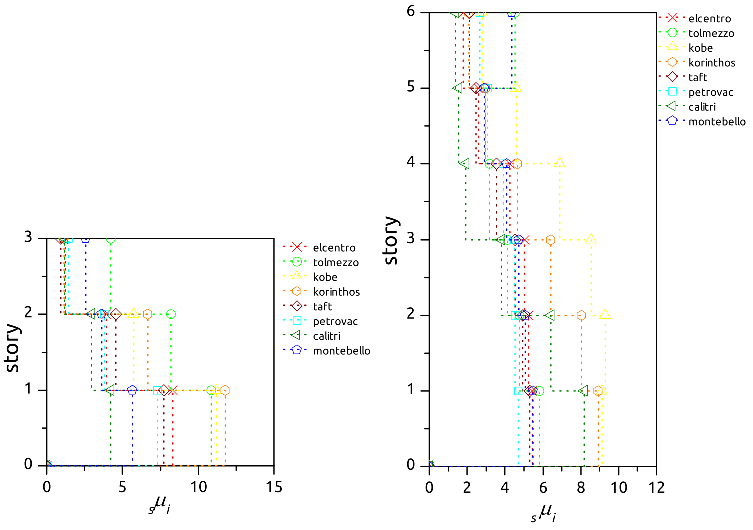

(a) 3S-FD-GL (b) 6S-FD-GL

Figure 4.43.: Maximum plastic deformation ratio of the stiff part ${}_s\mu_{mi}$ storey i^{th}

4.5.4.6. Structural efficiency: Cumulative to maximum plastic deformation ratios

Figure 4.44 shows the relation between the maximum plastic deformation ratio ${}_s\mu_i$ and the cumulative inelastic deformation ratio ${}_S\eta_i$ for the hysteretic dampers. The squares and circles represents the pairs of values $({}_s\mu_i, {}_s\eta_i)$ at any i-th storey for the 6S-FD-GL and 3S-FD-GL prototypes respectively. The bold line in figure 4.44 is the linear regression of the scatter data. The dashed lines in figure 4.44 are the lower bound and the design values of η/μ proposed by Akiyama [3] for flexible-stiff mixed structures with elastic-perfectly plastic restoring force characteristics and a value of the ratio $r_q = {}_fQ_y/{}_sQ_y$ greater than 1.

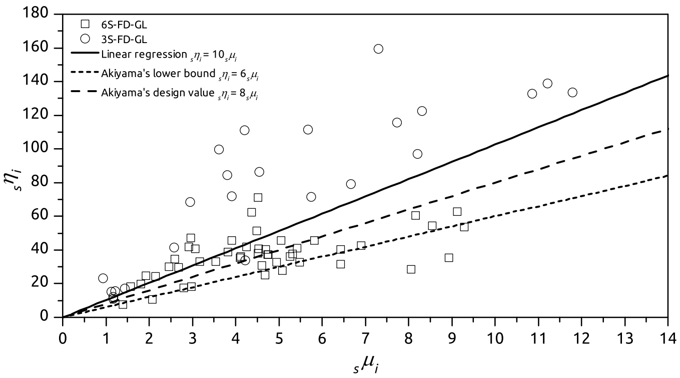

Figure 4.44.: $\eta_{s\,i}/\mu_{s\,i}$

4.5.4.7. Chord rotation demand

Tables 4.45b and 4.45a show the average chord rotation demand for the plastic hinges (labelled in figures 4.19 and 4.24) at the same storey for the 3S-FD-GL and 6S-FD-GL prototypes respectively.

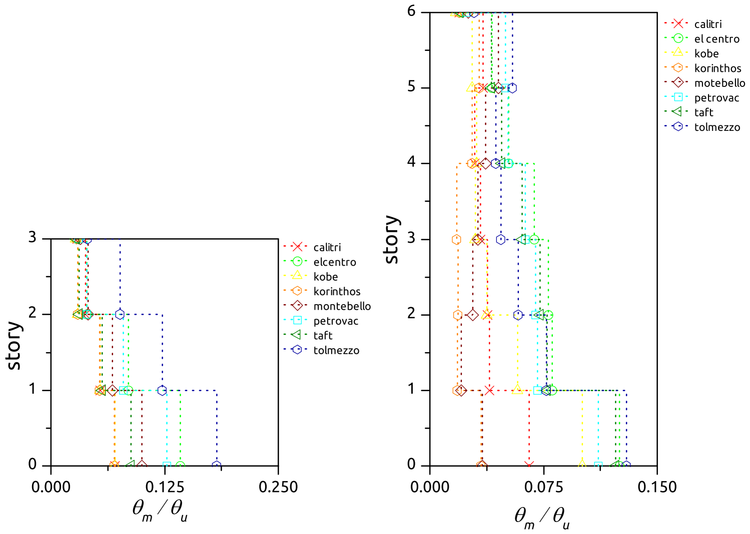

(a) 6S-FD-GL (b) 6S-FD-GL

Figure 4.45.: Average chord rotation demand at i^{th} storey FD-GL prototypes

4.5.4.8. D_i damage index

Tables 4.46b and 4.46ashow the average D_i damage index for the plastic hinges (labelled in figures 4.19 and 4.24) at the same storey for the 3S-FD-GL and 6S-FD-GL prototypes respectively.

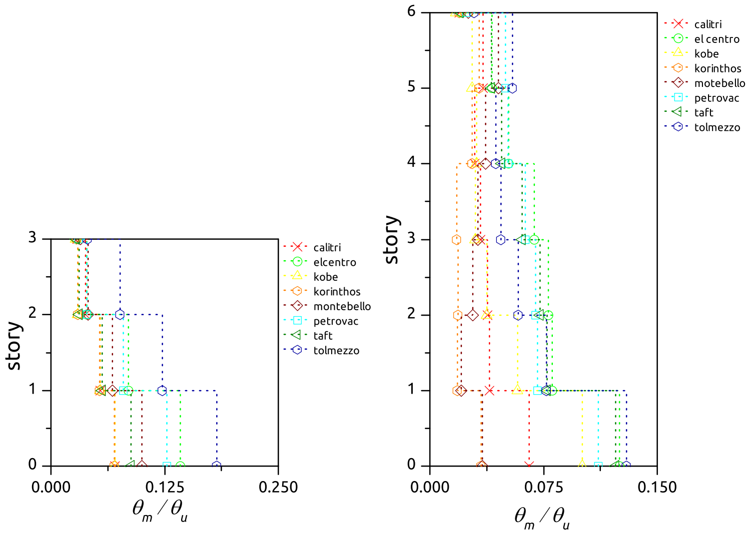

(a) 3S-FD-GL (b) 6S-FD-GL

Figure 4.46.: Average D_i at i^{th} storey FD-GL prototypes

4.5.4.9. $DI_{P\&A}$ damage index

The results of the $DI_{P\&A}$ at the plastic hinges (labelled in figures 4.19 and 4.24) were zero in all the plastic hinges except for the bases of the 3S-FD-GL where the average value $DI_{P\&A}$ was 0.12.

4.6. Comparison of seismic responses of models BF-SCWB and FD-GL

In order to compare the results obtained from the non-linear time history analysis of BF-SCWB and FD-GL prototypes, the seismic performance assessment within the framework of the Performance-Based Seismic Design is used herein [101, 100]. The performance-based seismic design process evaluates how a building is likely to perform, given the potential hazard it is likely to experience, considering uncertainties inherent in the quantification of potential hazard and uncertainties in assessment of the actual building response [8]. The performance assessment procedure considered is based in the following steps [65]:

1. Characterization of the ground shaking hazard.
   It is necessary to define a specific intensity of ground motion that the building will be designed to resist. The parameter used to describe the ground motion intensity is termed as intensity measure, im. In our case the energy input in terms of equivalent velocity V_E is adopted as im. Although several im levels should be considered to correctly define a risk scenario for a specific site, only the im level corresponding to the 500 years return period earthquake is considered herein.

2. Structural Analysis and Structural Response Functions.
   The response of the structural components of the structure to the seismic excitation is obtained using non-linear finite element models of the BF-SCWB and FD-GL prototype structures. The ground motions from apendix A are scaled to the im representative of the seismic hazard. The structural response quantities, including inter-storey drifts and cumulative inelastic deformation ratio, predicted in the NTH analysis are used as damage indicators. These response quantities are termed Engineering Demand Parameter (EDP). These EDP depend on diverse factors as the ground motion or the structural characteristic, and are likely to be different in each NTH analysis. If a large number of representative NTH are done, the results of these NTH analysis will define a random distribution of the EDP that can result for this particular ground motion im. In the cases where the structure didn't reach the collapse state, it can be assumed that the data of the peak engineering demand parameters can be fitted with a log-normal distribution [81] from equation 4.30 which is the probability density function. The probability density function can also be presented as a cumulative distribution function (CDF), which indicates the probability that an EDP will be less than or equal to a given value.

Figure 4.30 shows probability density function representing the log-normal distribution from equation 4.30. Figure 4.48 shows the cumulative distribution function for the log-normal distribution of figure 4.47

$$f\left(x;\mu,\sigma\right)=\frac{1}{x\sigma\sqrt{2\pi}}e^{-\frac{1}{2}\left(\frac{lnx-\mu}{\sigma}\right)^2} \tag{4.30}$$

Where μ is the median and σ is the standard deviation of the logarithm of the data from peak EDP.

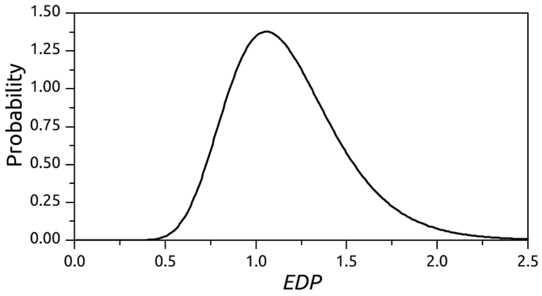

Figure 4.47.: Probability Distribution Function

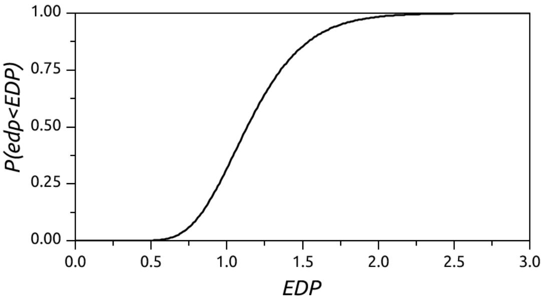

Figure 4.48.: Cumulative Distribution Function

In order to assign a structural performance level to the structures, the seismic codes propose several limiting values for the reference damage indexes nowadays. The most common damage index for RC framed structures is the inter-storey drift index, however there are few reference values for energy based damage indexes. Darwing and Nmai proposed values for several RC beams and Akiyama proposed several η design values for RC buildings. Based on the results from subsection 4.5.3.4 and previous results from Akiyama, it can be considered that the η/μ relationship for a lower bound value can be estimated by equation 4.31.

$$\eta=2\,\mu_m \tag{4.31}$$

Introducing in equation 4.32 the limiting values proposed by the SEAOC, which had been proved experimentally accurate for RC frames in the previous Chapter 2, it can be obtained the expected maximum values of η correspondent to different limiting values of the maximum inter-storey drift

id_m, at each performance level. Table 4.29 summarizes the limiting values of η given by equation 4.32 for the representative id_m at different performance levels.

$$\eta = 2\frac{id_m - id_y}{id_y} \tag{4.32}$$

Where id_y is the yielding inter-storey drift. An stringent value of $id_y = 0.2\%$ considered, that is the limiting value for the Operational Structural Performance level in which minor yielding in some elements are expected.

	Fully Operational	Operational	Life Safe	Near Collapse
Permissible id_m	<0.2%	<0.5%	<1.5%	<2.5%
Permissible η	0	<3	<13	<23

Table 4.29.: Limiting Damage values by Performance levels

4.6.1. Global *id*.

Figure 4.49 shows the CDF estimated with the results of peak *id* obtained in the NTH analyses at any i-th level. The dash line and the bold line correspond to the 3S-BF-SCWB and 3S-FD-GL prototypes respectively. The vertical dot lines also represent the *id* limiting values for the different structural performance levels defined by the SEAOC. As can be seen the seismic performance of the RC frame equipped with hysteretic dampers is significantly better than the conventional seismic resistant frame. Based on the FD-GL structural response function, the probability of non-excedence for a 0.5% (IO), 1.5% (LS) and 2.5% (NC) drifts are 78%, 100% and 100% respectively which means that the structure performance level will probably be IO. In the case of the BF-SCWB structural response function, the probability of non-excendence for a 0.5% (IO), 1.5% (LS) and 3% (NC) drift are 0%, 85% and 100% respectively which means that the structure performance level probably will exceed IO and will be between LS and NC for the *im* considered.

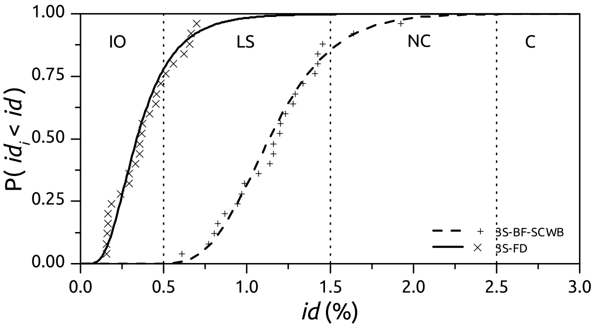

Figure 4.49.: CDF of global peak *id*

Similar trends are found in the 6 storeys prototypes. Figure 4.50 shows the CDF estimated with the results of peak *id* obtained in the NTH analyses at any i-th level. The dash line and the bold line correspond to the 6S-BF-SCWB and 6S-FD-GL prototypes respectively. The vertical dot lines also represent the *id* limiting values for the different structural performance levels defined by the SEAOC. As can be seen the seismic performance of the RC frame equipped with hysteretic dampers is significantly better than the conventional seismic resistant frame. Based on the 6S-FD-GL structural response function, the probability of non-excedence for a 0.5% (IO), 1.5% (LS) and 2.5% (NC) drifts are 72%, 100% and 100% respectively which means that the structure performance level will probably be IO. In the case of the 6S-BF-SCWB structural response function, the probability of non-excendence for a 0.5% (IO), 1.5% (LS) and 3% (NC) drift are 0%, 82% and 100% respectively which means that the structure performance level probably will exceed IO and will be between LS and NC for the *im* considered.

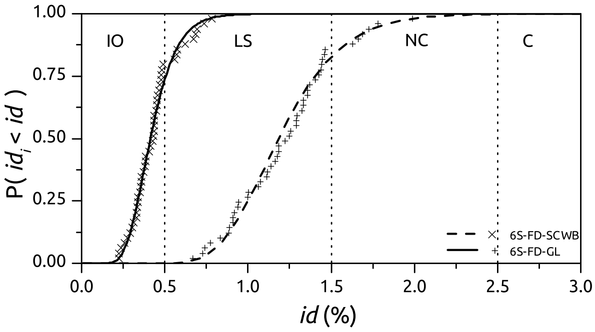

Figure 4.50.: CDF of global peak *id*

4.6.2. *id* at storey *i*-th.

Figure 4.51 shows the CDF estimated with the results of peak *id* obtained in the NTH analyses at each *i*-th level. The dash line and the bold line correspond to the 3S-BF-SCWB and 3S-FD-GL prototypes respectively. The vertical dot lines also represent the *id* limiting values for the different structural performance levels defined by the SEAOC. A comparison of the structural response functions of the different storeys for the FD-GL prototype shows that the first storey is the most vulnerable with a 50% of probability of non-excedence of the 0.5% *id* which means a structural performance level between IO and LS. For the second and third storey the probability that a *id* of 0.5% is not exceed is a 75% and 100% respectively which means that both storeys mainly behaved with a IO structural performance level. In the case of the BF-SCWB prototype all storeys had a similar behaviour. All storeys exceed the 0.5% *id* therefore all storeys behaved over the IO structural performance level. For the 1.5% *id* limit all storeys had a similar behaviour with a probability of non-excedence of 88%, 74% and 90% for first, second and third storeys respectively, it van be said that all storeys mainly behaved with a LS structural performance level.

Figure 4.52 shows the CDF estimated with the results of peak *id* obtained in the NTH analysis at each *i*-th level. The dash line and the bold line correspond to the 6S-BF-SCWB and 6S-FD-GL prototypes respectively. The vertical dot lines also represents the *id* limiting values for the different structural performance levels defined by the SEAOC. A comparison of the structural response functions of the different storeys for the FD-GL prototype shows that the three lower storeys are the most vulnerable with a 47%, 35% and a 55% probability of non-excedence of the 0.5% *id* for the first, second and third storey. The expected structural performance level could be considered between IO and LS. In the case of the upper storeys the probability that a *id* of 0.5% is not exceed is a 90%, 97% and 95% for the fourth, fifth and sixth storeys, that correspond with a IO structural performance level. For the BF-SCWB prototype all storeys exceed the 0.5% *id* therefore all storeys behaved over the IO structural performance level. For the 1.5% *id* limit the storeys had different behaviors with a probability of non-excedence of 100%, 89%, 80%, 67%, 64% and 90% for first to sixth floor, A LS structural performance level can be assigned to first, second and sixth storeys while a structural performance level between LS and NC can be considered for the rest of the stores.

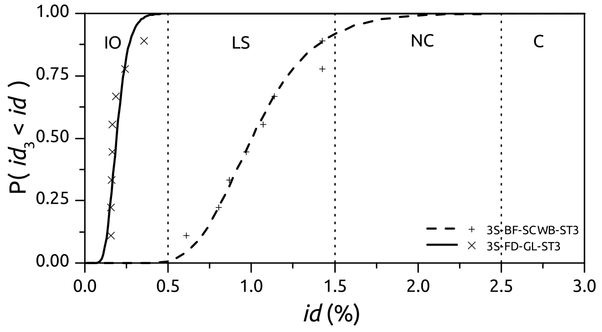

(a) CDF of peak *id* at storey 3

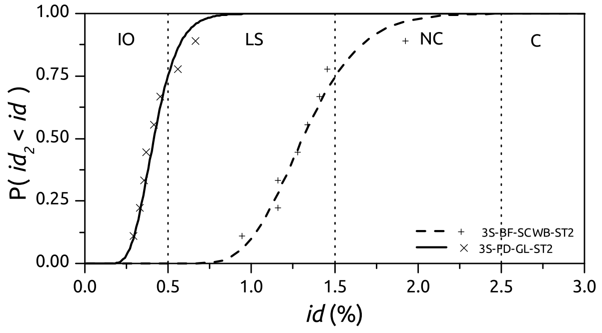

(b) CDF of peak *id* at storey 2

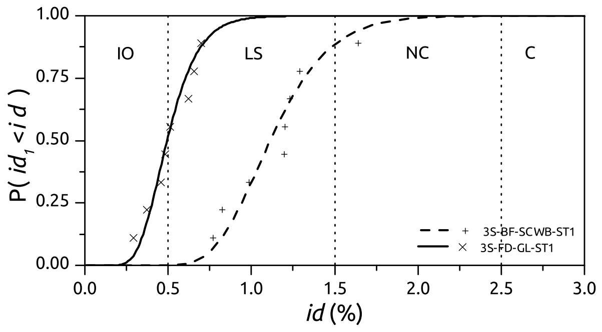

(c) CDF of peak *id* at storey 1

Figure 4.51.: CDF of peak *id* at storey i^{th}

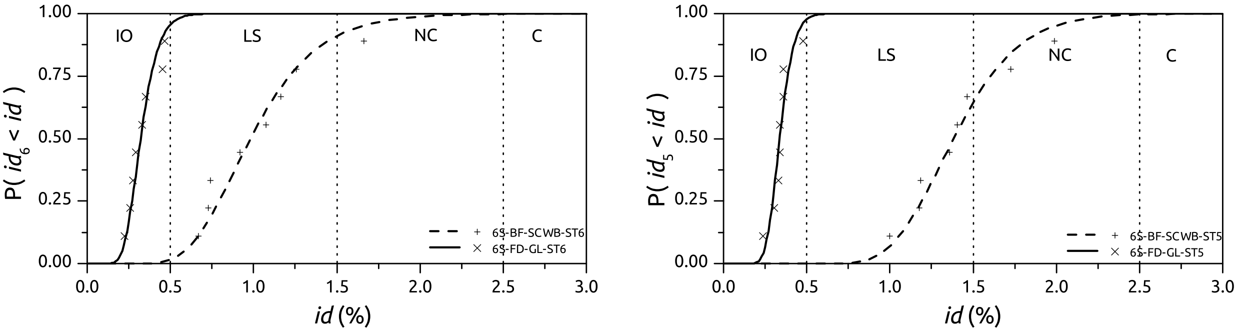

(a) CDF of peak *id* at storey 6 (b) CDF of peak *id* at storey 5

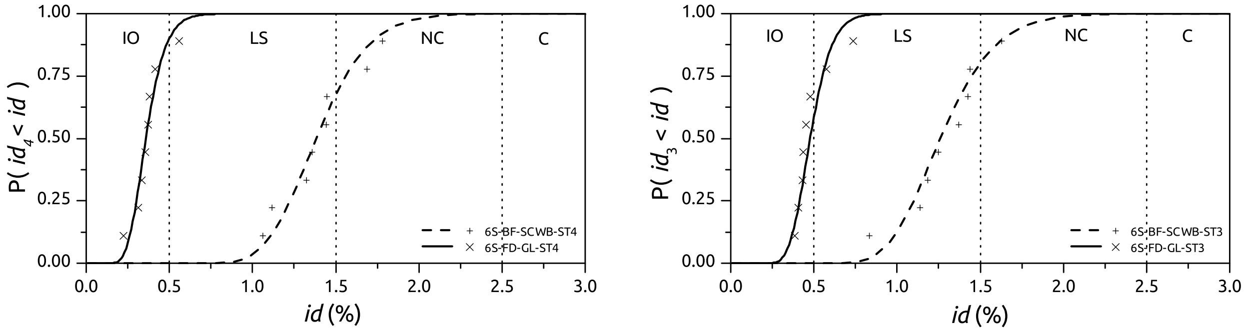

(c) CDF of peak *id* at storey 4 (d) CDF peak *id* at storey 3

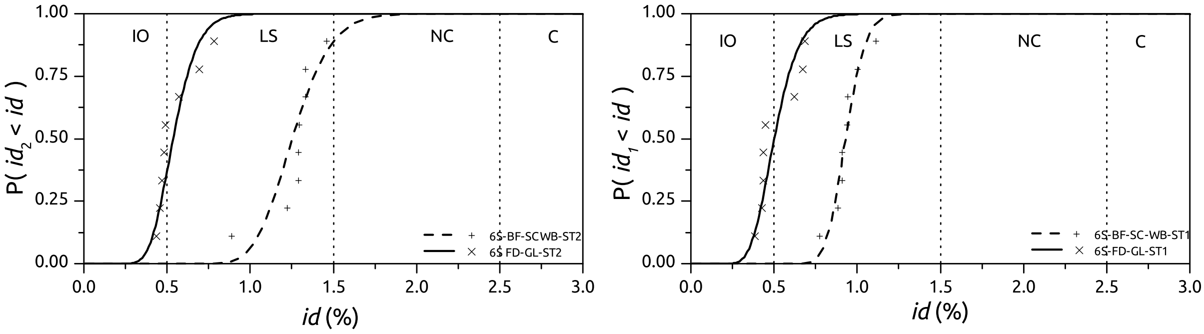

(e) CDF of peak *id* at storey 2 (f) CDF of peak *id* at storey 1

Figure 4.52.: CDF of peak storey i^{th} *id*

4.6.3. Global inelastic cumulative deformation ratio : RC frame.

Figure 4.53 shows the CDF estimated with the results of the cumulative deformation ratio η for the RC frames, obtained in the NTH analysis at any level. The dash line and the bold line correspond to the 3S-BF-SCWB and 3S-FD-GL prototypes respectively. The comparison of the structural response functions shows that the energy dissipated by the RC frame equipped with hysteretic dampers was much lower than the seismic resistant RC frame. The vertical dot lines also represents the η limiting values for the different structural performance levels defined in table 4.29 for the limit values defined by the SEAOC. Based on the FD-GL structural response function the probability that a value of $\eta = 3$ is not exceed is 100% therefore the main structure will behave with a IO structural performance level. In the case of the BF-SCWB structural response function, the probability of non-excendence of 3 (IO), 13(LS) and 23 (NC) drift are 0%, 85% and 100% hence the structural performance level of the structure will be LS.

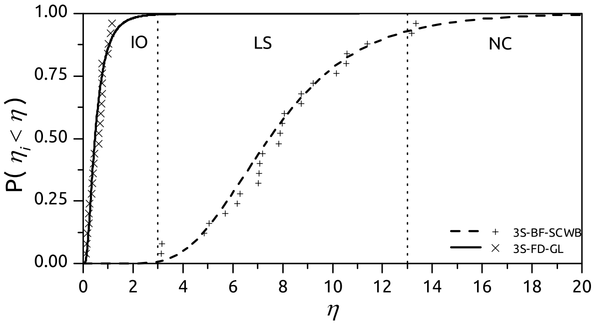

Figure 4.53.: CDF of global$_f\eta$

Figure 4.54 shows the CDF estimated with the results of peak η for the RC frames, obtained in the NTH analyses at any level. The dash line and the bold line correspond to the 6S-BF-SCWB and 6S-FD-GL prototypes respectively. The comparison of the structural response functions shows that the energy dissipated by the RC frame equipped with hysteretic dampers was much lower than the seismic resistant frame. The vertical dot lines also represent the η limiting values for the different structural performance levels defined in table 4.29 for the limit values defined by the SEAOC. Based on the FD-GL structural response function the probability that a value of $\eta = 3$ is not exceed is 100% therefore the main structure will behave with a IO structural performance level. In the case of the BF-SCWB structural response function, the probability of non-excendence of $\eta = 3$ (IO), $\eta = 13$ (LS) and $\eta = 23$ (NC) are 25%, 90% and 100% hence the structural performance level of the structure will be LS.

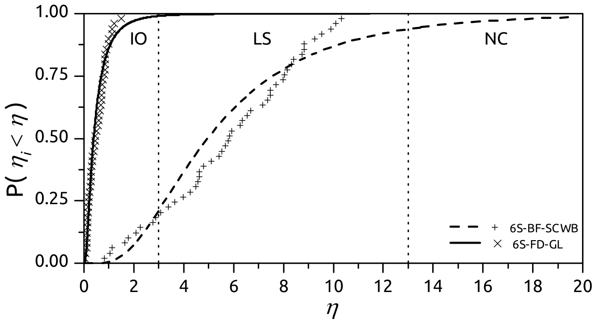

Figure 4.54.: CDF of global $_f\eta$

4.6.4. Cumulative inelastic deformation ratio at storey *i*-th: RC frame

Figure 4.55 shows the CDF estimated with the results of the cumulative inelastic deformation ratio η for the RC frame, obtained in the NTH analyses at each i-th level. The dash line and the bold line correspond to the 3S-BF-SCWB and 3S-FD-GL prototypes respectively. The vertical dot lines also represent the η limiting values for the different structural performance levels defined in table 4.29. Based on the structural response functions of the different stores for the FD-GL prototype shows that tall stores behaved with a IO structural performance level. In the case of the BF-SCWB prototype all stores had a similar behaviour. All stores exceed the $\eta = 3$ therefore all storeys behaved over the IO structural performance level. For the $\eta = 13$ limit all storeys had a similar behaviour with a probability of non-excedence of 85%, 95% and 99% for first, second and third storeys respectively, it can be said that all storeys mainly behaved with a LS structural performance level.

Figure 4.56 shows the CDF estimated with the results of cumulative inelastic deformation ratio η for the RC frame obtained in the NTH analyses at each i-th level. The dash line and the bold line correspond to the 6S-BF-SCWB and 6S-FD-GL prototypes respectively. The vertical dot lines also represent the η limiting values for the different structural performance levels defined in table 4.29. Based on the structural response functions of the different stores for the FD-GL prototype shows that tall stores behaved with a IO structural performance level. In the case of the BF-SCWB prototype all stores had a similar behaviour except the sixth storey. All stores exceed the $\eta = 3$ therefore all storeys behaved over the IO structural performance level. For the $\eta = 13$ limit the probability of non-excedence was 100%, 95% 90%,100%, 100% and 100% for first to sixth stores respectively, it can be said that all storeys mainly behaved with a LS structural performance level, except the sixth storey that behaved with a IO structural performance level.

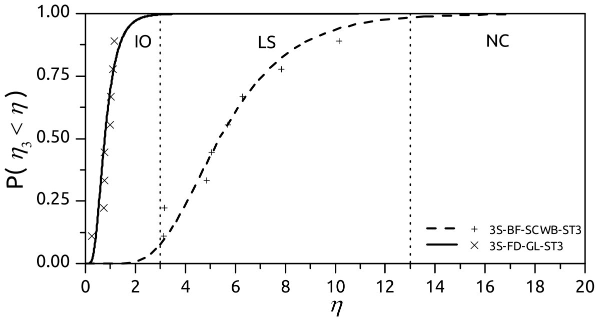

(a) CDF η at storey 3

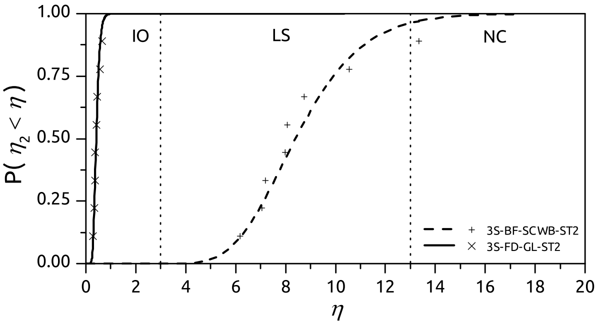

(b) CDF η at storey 2

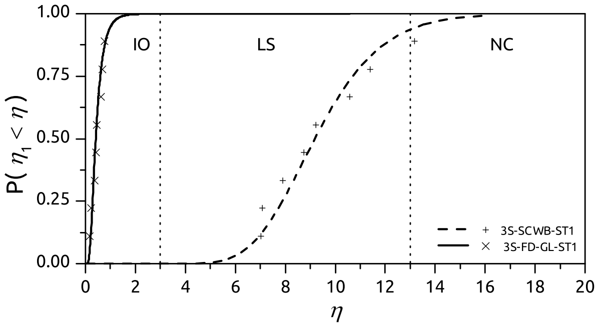

(c) CDF of η at storey 1

Figure 4.55.: CDF of η storey at i^{th}

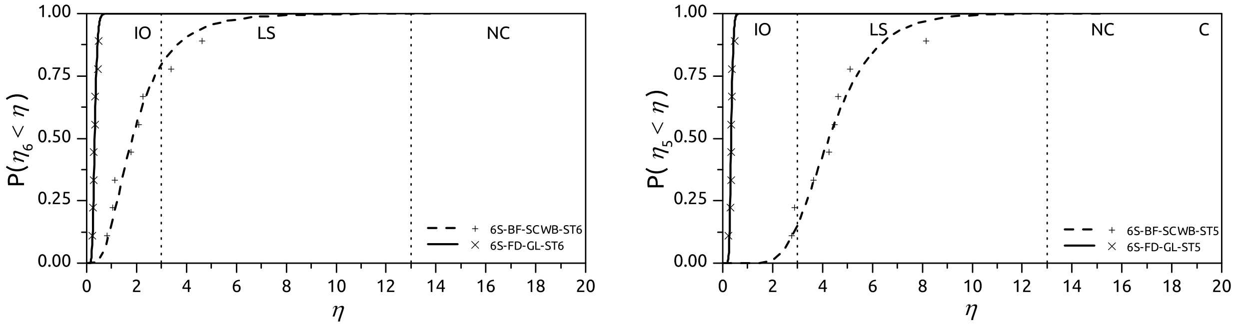

(a) CDF of η at storey 6

(b) CDF of η at storey 5

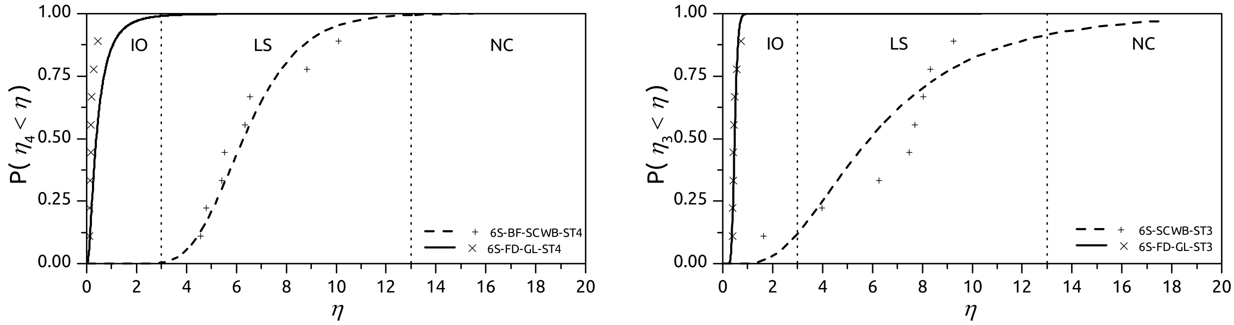

(c) CDF of η at storey 4

(d) CDF of η at storey 3

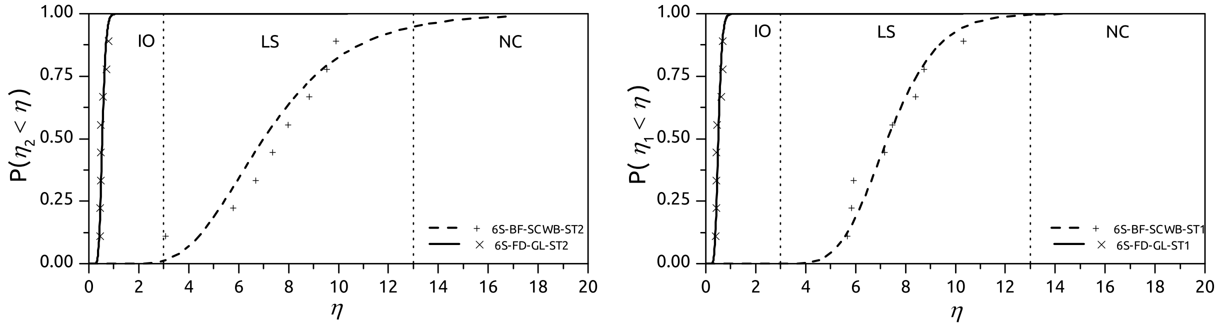

(e) CDF of η at storey 2

(f) CDF of peak storey 1 η

Figure 4.56.: CDF of η at storey i^{th}

4.6.5. Chord rotation at storey *i*-th plastic hinges: RC frame

Figure 4.57 shows the CDF estimated with the results of the chord rotation demand at the idealized plastic hinges at each i-th level. The dash line and the bold line correspond to the 3S-BF-SCWB and 3S-FD-GL prototypes respectively. The vertical dot lines also represent the limiting values for the different structural performance levels defined in table Eurocode 8 Part3 [39]. Based on the structural response functions of the different storeys for the FD-GL prototype, it can be seen that the plastic hinges at all storeys mainly behaved below the damage limitation structural performance level. Only the first storey exceed the limiting value with a probability of non-excedence of 90%. In the case of the BF-SCWB prototype a different behaviour was observed at the hinges of each storey. The maximum chord rotation demand was observed at the first and second level with a structural performance level of damage limitation, while the ground and third storey had a performance between no damage and damage limitation with a probability of non-excedence of 70 and 60 % respectively.

Figure 4.58 shows the CDF estimated with the results of the chord rotation demand at the idealized plastic hinges at each i-th level. The dash line and the bold line correspond to the 6S-BF-SCWB and 6S-FD-GL prototypes respectively. The vertical dot lines also represents the limiting values of the different structural performance levels defined in table Eurocode 8 Part3 [39]. Based on the structural response functions of the different storeys for the FD-GL prototype, it can be seen that the plastic hinges at storeys mainly behaved below the damage limitation structural performance level. In the case of the BF-SCWB prototype the plastic hinges at storeys one to five had a damage limitation structural behaviour. The plastic hinges at ground floor behaved below the damage limitation level while the sixth floor behaved between no damage and damage limitation with a probability of non-excendence of 50%.

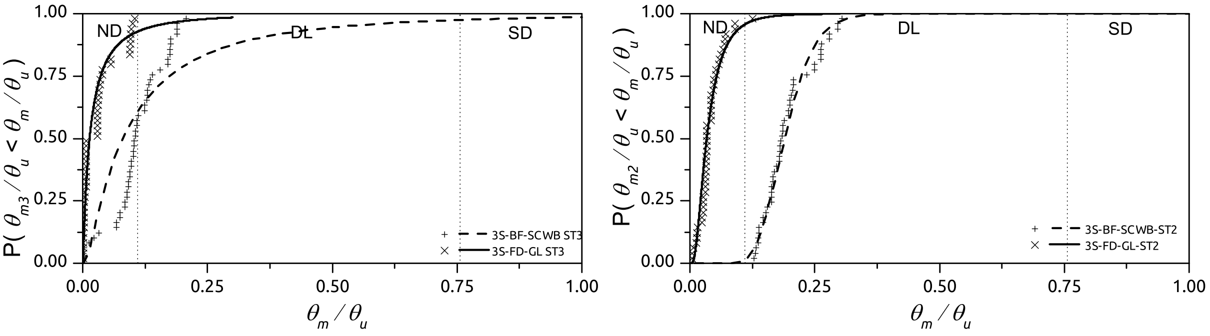

(a) CDF of chord rotation demand at storey 3

(b) CDF of chord rotation demand at storey 2

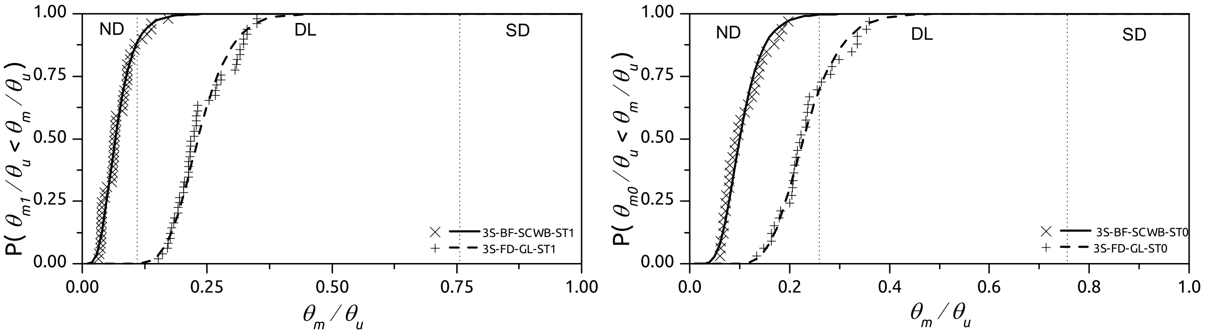

(c) CDF of chord rotation demand at storey 1

(d) CDF of chord rotation demand at storey 0

Figure 4.57.: CDF of chord rotation demand at plastic hinges of storey i^{th}

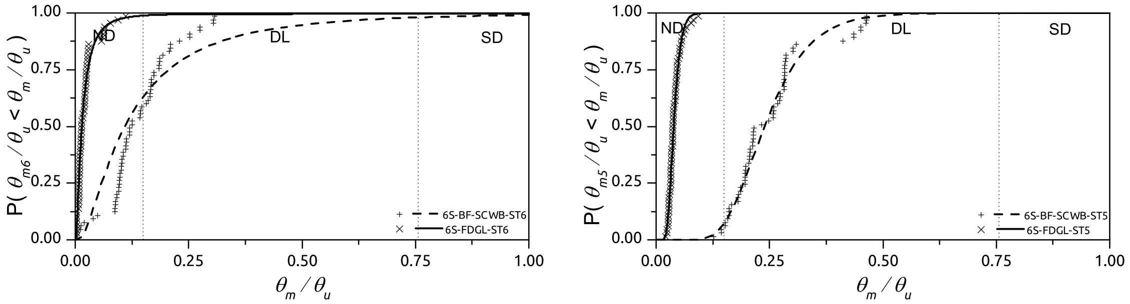

(a) CDF of chord rotation demand at storey 6 (b) CDF of chord rotation demand at plastic hinges at storey 5

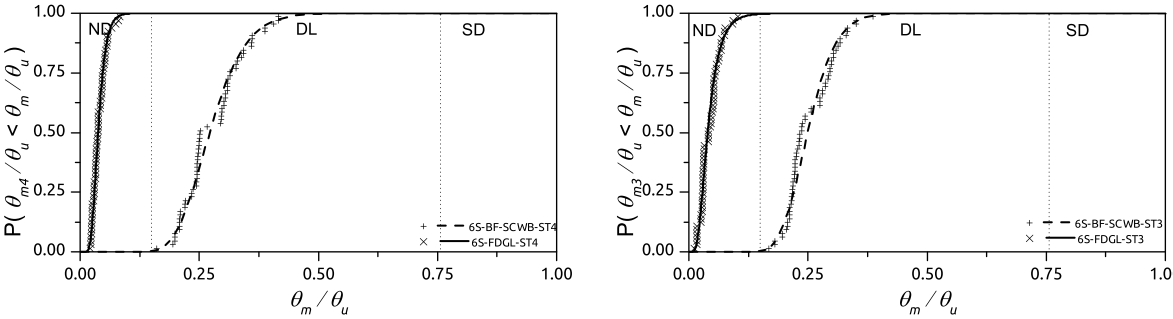

(c) CDF of of chord rotation demand at storey 4 (d) CDF of peak of chord rotation demand at storey 3

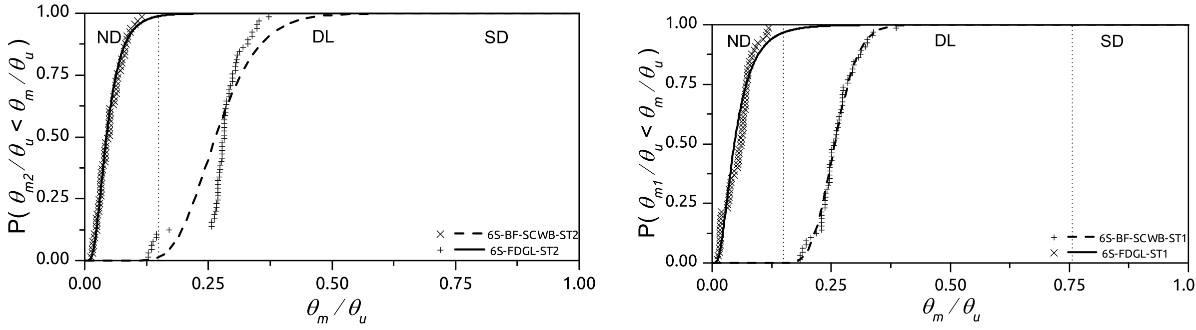

(e) CDF of of chord rotation demand at storey 2 (f) CDF of chord rotation demand at storey 1

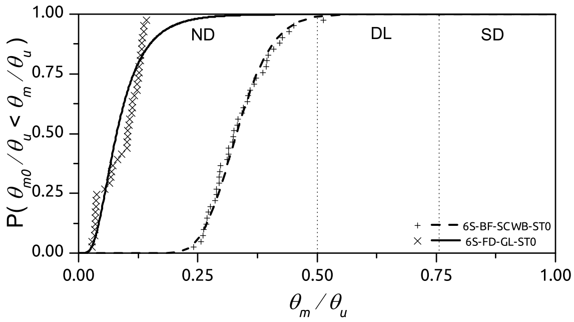

(g) CDF of chord rotation demand at storey 0

Figure 4.58.: CDF of chord rotation demand at plastic hinges of storey i^{th}

4.6.6. *Di* index at storey *i*-th plastic hinges: RC frame

Figure 4.59 show the CDF obtained from the results of D_i damage index at the idealized plastic hinges at each i-th level. The dash line and the bold line correspond to the 3S-BF-SCWB and 3S-FD-GL prototypes respectively. A comparison between both prototypes show that the damage at the plastic hinges at all levels was much greater in the 3S-BF-SCWB prototype than the 3S-FD-GL prototype. The D_i values for the 3S-FD-GL prototype show that the damage is almost neglible in all storeys being much greater in the ground storey. In the case of the 3S-BF-SCWB the damage was mainly concentrated at the first level plastic hinges with values ranging from 4-12.

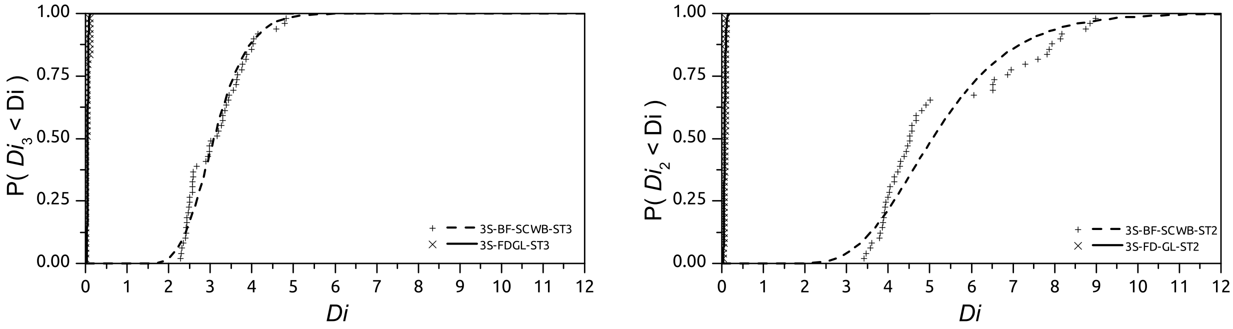

(a) CDF of *Di* index at storey 3 (b) CDF of *Di* index at storey 2

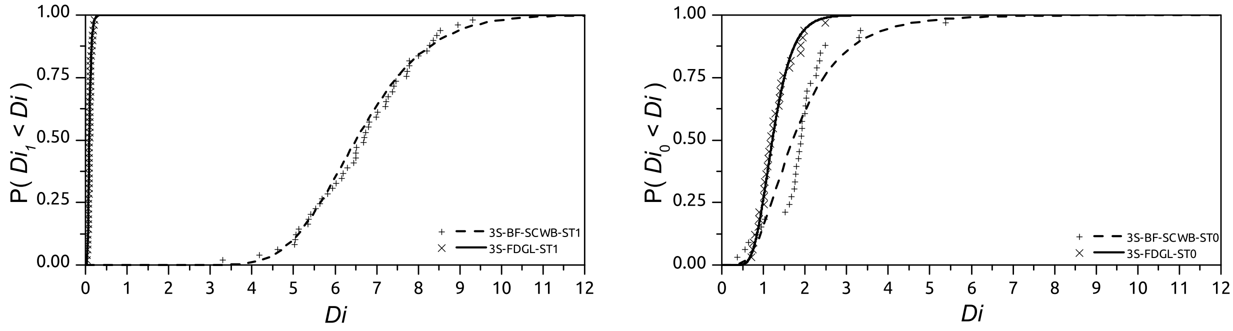

(c) CDF of *Di* index at storey 1 (d) CDF of *Di* index at storey 0

Figure 4.59.: CDF of *Di* index at plastic hinges of storey i^{th}

Figure 4.60 show the CDF obtained from the results of D_i damage index at the idealized plastic hinges at each i-th level. The dash line and the bold line correspond to the 6S-BF-SCWB and 6S-FD-GL prototypes respectively. A comparison between both prototypes show that the damage at the plastic hinges at all levels was much greater in the 6S-BF-SCWB prototype than the 6S-FD-GL prototype. The D_i values for the 6S-FD-GL prototype show that the damage is almost null in all storeys being much greater in the ground storey. For the 6S-BF-SCWB the damage at different storeys was almost the same for first to sixth storey while the ground floor had D_i values significantly lower compared to those from the other storeys.

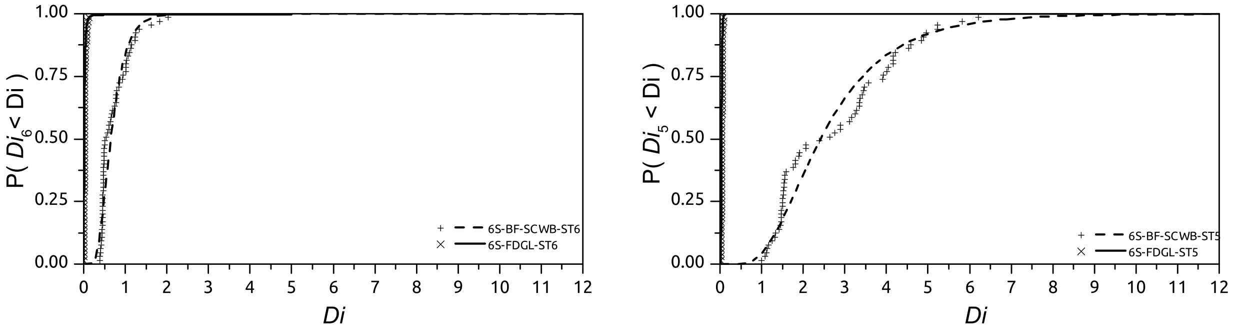

(a) CDF of Di index at storey 6 (b) CDF of Di index at storey 5

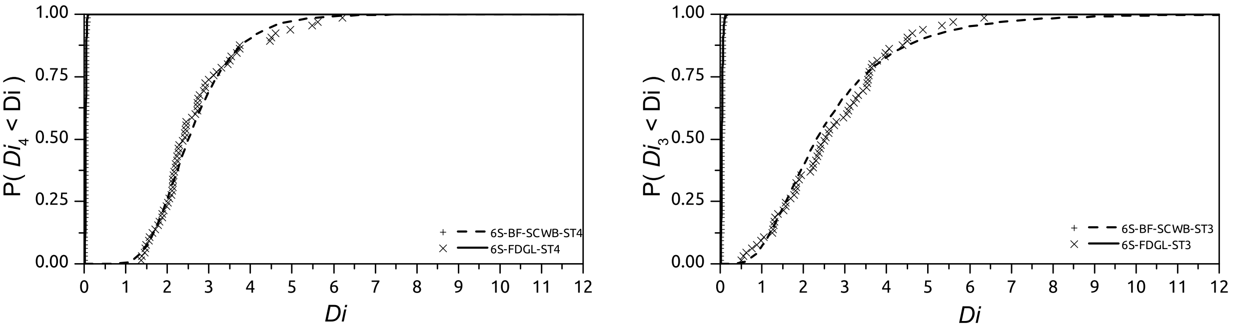

(c) CDF of Di index at storey 4 (d) CDF of Di index at storey 3

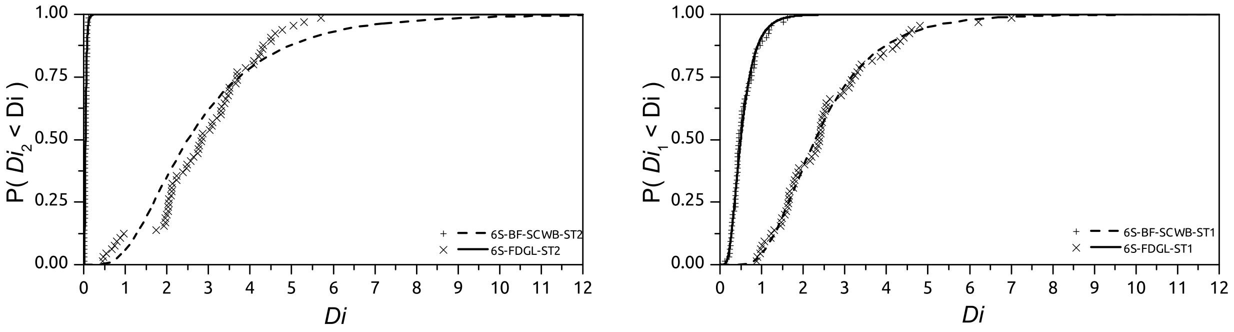

(e) CDF of Di index at storey 2 (f) CDF of Di index at storey 1

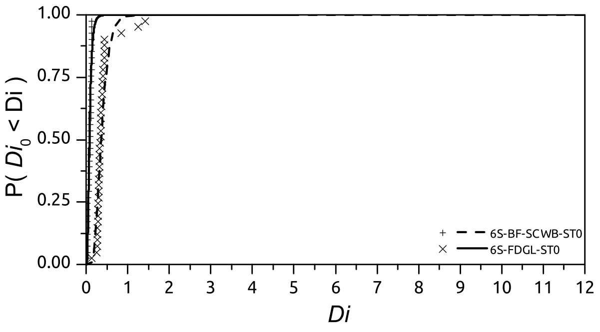

(g) CDF of Di index at storey 0

Figure 4.60.: CDF of Di index at plastic hinges of storey i^{th}

4.6.7. $DI_{P\&A}$ index at storey i-th plastic hinges: RC frame

Figure 4.61 and 4.62 shows the CDF obtained from the results of $DI_{P\&A}$ damage index at the idealized plastic hinges at each i-th level for the 3S-BF-SCWB and 6S-BF-SCWB prototype respectively. As indicated in subsection 4.5.4.9 the value of the index $DI_{P\&A}$ for the RC frames of the prototypes with dampers FD-GL was zero or very small, therefore it is not plot in the following figures. The ground and sixth storey for the 6S-BF-SCWB prototype are omitted because no damage was measured with the $DI_{P\&A}$ index at the plastic hinges of this levels. This results are also coincidental with the results of the chord rotation demand and the D_i damage index as can be seen in figures 4.60g,4.60a,4.58a and 4.58g.

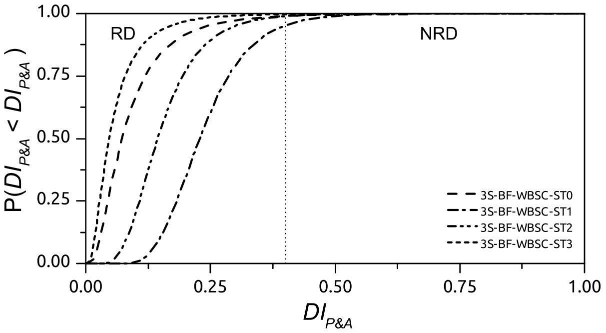

Figure 4.61.: CDF of $DI_{P\&A}$ index at plastic hinges of storey i^{th} 3S-BF-SCWB prototype

The vertical line with dots in both graphics represents the limiting value $DI_{P\&A} = 0.4$ defined by Park & Ang [70] as the boundary between reparable and non-reparable damages while values above 1 comprises the collapse of the element. Based in this assumption and the results from the NTH analysis from both prototypes, as all the plastic hinges had values bellow 0.4 with a probability of non-excedence around 90%, the damage expected at the plastic hinges can be considered as repairable. This level of damage was also observed in the tests from chapter 2 after the same hazard level test.

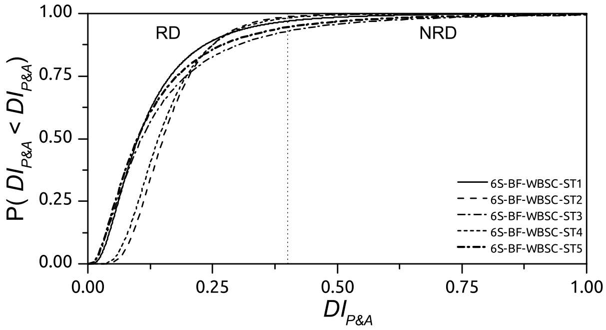

Figure 4.62.: CDF of $DI_{P\&A}$ index at plastic hinges of storey i^{th} 6S-BF-SCWB prototype

4.7. Summary and conclusions

The seismic response of conventional RC framed seismic resistant structures with weak beam strong column collapse mechanism (BF-SCWB) was compared with the response of innovative seismic resistant RC structures equipped with hysteretic dampers (FD-GL). This comparison is done in terms of the inter-storey drift id and the cumulative inelastic deformation ratio η at global structural level. A comparison at local plastic hinge level was also made in terms of the chord rotation demand, the Darwin and Nmai Di energy based damage index and the well known-Park and Ang $DI_{P\&A}$ damage index. The following results are worth noting in the comparison of both structural types:

1. The cumulative inelastic ratios, η, in the RC frames of the for the FD-GL prototypes were below 1 in all cases and for all storeys while, in the BF-SCWB prototypes the values of η ranged between 4 to 12. This means that the damage in the RC frames of the strcutures with dampers was negligible, while the damage in the conventional RC frames (without dampers) was significant, being at least from 4 to 12 times larger than in the frames with dampers.

2. The values of the maximum inter-storey drifts, id, for the FD-GL prototypes ranged between 0.5-0.75 which are typically related to first yielding state in RC frames, while for the BF-SCWB prototypes the values of id ranged between 0.5-2 which are representative values of moderate to severe damage.

3. The chord rotation demand at plastic hinge level for the FD-GL prototypes was bellow the limits defined by EC8 part 3 for the damage limitation structural performance level. In the case of the BF-SCWB prototypes the chord rotation demand was included in the damage limitation structural performance level. The results of the maximum chord rotation demand values were consistent with the chord rotation demand measured during the experimental test in chapter 2for the same seismic hazard level.

4. The Park & Ang Damage index at the plastic hinge level were neglible for the FD-GL prototypes. In contrast, in the case of the conventional RC frames, prototypes 3S-BF-SCWB and the 6S-BF-SCWB, the $DI_{P\&A}$ reached the value of 0.4 which implies a reparable damage in the elements. A comparison of the average values at each plastic hinge obtained in the numerical simulations with the maximum $DI_{P\&A}$ index measured during dynamic shaking table tests reported in chapter 2 at the same seismic hazard level shows a very good correlation between the numerical and the experimental results.

5. The installation of dampers (prototypes FD-GL) reduced the structural Performance Level expected for this seismic hazard Level from Life Safety to Immediate Occupancy. In addition to the benefit of this reduction, it is worth emphasizing that in general the cross section of the members and the amount of the reinforcing steel in the RC frames of the structures with dampers, were smaller that those of the conventional RC frames. This is because the former were designed only for gravitational loads (without forcing the formation of a strong-column weak beam mechanism), while the later were dimensioned for gravitational and seismic forces imposing the formation of a beam-sway mechanism.

6. The design value of the ratio η/μ proposed by Akiyama (3.75) for conventional RC frames is larger than the obtained in this study. In the light of the results of this study, a conservative value of $\eta/\mu = 2.5$ would be more appropiate.
7. The innovative structures consisting on RC frame designed for gravitational loads and hysteretic dampers (prototypes FD-GL) present an structural efficiency in terms of the ratio η/μ that is four times larger than conventional RC frames with beam-sway collapse mechanisms.

On the basis of the previous outcomes it can be concluded that the inclusion of hysteretic dampers improves the seismic performance of the RC frames reducing the damage in the gravitational load resisting system in terms of energy dissipation and ductility demand. Apart from the comparison done for the structural types the following results are also worth mentioning:

The observation of the structural response functions of the 6S-BF-SCWB prototype and different damage ratios reveals that the damage in terms of interstory drift tends to concentrate in the upper levels of the framed structures. In contrast, if the damage is evaluated in terms of the cumulative inelastic deformation ratio the results are completely opposite showing that damage tends to concentrate in the lower storeys. This contradictory results reveal that estimating damage based exclusively on drift demand or energy demand can lead to an underestimation of the damage in the structure. In this sense, it is more appropiate to evaluate the damage in terms of the Park and Ang index that takes into account both contributions (maximum plastic deformation and cumulativa plastic deformation) to damage.

The results of the distribution of the cumulative inelastic deformation ratio for the FD-GL prototypes show that the damper design based on the optimum strength distribution of Akiyama tends to reduce the damage in the dampers of the upper storeys, especially for the 3S-FD-GL prototype. This tendency is not observed in the 6 storey frames, where the mean value of η for the ground motions considered is similar in the upper and lower storeys. This can be explained because Akiyama's optimum strength distribution tends to overestimate the effect of higher modes of vibration in the lower structures.

5. Non-Linear Static Procedures

In recent decades the research community has recognized a need for change in seismic design methodology, towards new Performance Based Design (PBD) procedures that can account for the non-linear behaviour of structures during earthquakes in a simple manner. Clearly, non-linear time history analyses are the most reliable tool for estimating the inelastic response to a given accelerogram. But difficulties in correctly modelling the characteristics of cyclic load deformation of structural members, and the need of a set of ground motions that would properly define the seismic input at a given site, among other hindrances, make this method impractical for general use. The force-based methods currently implemented in seismic codes take into account the non-linear behaviour of structures during ground motions, using a behaviour factor to reduce the lateral forces of a modal response spectrum analysis. This approach focuses on determining the strength of the structure, providing a very rough estimation of the non-linear structural behaviour[21]. Consequently, there is a lack of a displacement-based methodology able to estimate the inelastic behaviour of structures without great computational efforts. Non-linear Static Procedures (NSP) have thus become a common tool under present standards Eurocode 8 [38] and guidelines like FEMA-440 [46] to this end.

The most important NSP are: (i) the Capacity Spectrum Method (CSM) proposed by Freeman [48] included in ATC-40 [6] and improved in FEMA-440; (ii) the Displacement Coefficient Method (DCM) firstly presented in FEMA-273, FEMA-274 [43, 44] and FEMA-356 [46] and recently improved in FEMA-440; and (iii) the N2 method developed by Fajfar[41, 40] and adopted by Eurocode 8. The main goal of all NSPs is to characterize the structural response induced by a design earthquake in terms of maximum displacement. All these methods are based on a process that involves two basic steps. The first step lies in determining an equivalent single-degree-of-freedom (SDOF) system, by means of the capacity curve obtained in a static push over (SPO) non-linear analysis. The second step is the characterisation of the seismic demand in terms of an over-damped elastic response spectrum (in the case of the CSM) or in terms of an inelastic design spectrum (in the case of the DCM and N2 methods). The maximum displacement is determined by the so-called ‘performance point’ or ‘target displacement’, as an indicator of the level of damage imparted to the structure. Although such methods fill the gap between current force-based methods and non-linear time history analysis, the background of all these procedures presents some limitations well reported in the literature [55, 47, 54].

Past research has studied the application of previous versions of the CSM from ATC-40 and DCM from FEMA-356 and the N2 method in conventional structures [23, 26, 58]. However, there is a lack of experimental evidence of how NSPs apply to structures with hysteretic dampers. In this paper, the seismic response of a structure equipped with hysteretic dampers predicted with the latest versions of the CSM and DCM methods and the N2 method is compared with the experimental results obtained in shaking table tests.

5.1. Test models and experimental Results.

A prototype one-bay and one-story structure with 2.8 m height and 4.8 x 4.8m^2 plan and a 0.25m deep reinforced concrete (RC) slab supported by four box-type steel columns was designed according to Spanish codes for a Peak Ground Acceleration (PGA) of 0.34g (here g is the acceleration of gravity).

5.1.1. Description of the test models.

From the prototype structure, a reduced-scale test model satisfying the similitude laws was designed. The test model was derived applying the following scaling factors for geometry, acceleration and stress, respectively: $\lambda_l = 1/2$, $\lambda_a = 1$ and $\lambda_\sigma = 1$. To ensure the consistency with the scaling factors used for the model, the accelerograms were scaled down in time by the factor $\lambda_l = \sqrt{\lambda_l} = \sqrt{1/2}$. Two identical test models were built in the Structural Engineering Laboratory at the University of Granada. In one of the models —referred to as FSD hereafter— two hysteretic dampers were installed. The other model —referred to as FS hereafter—did not have dampers.

Figures 5.1 and 5.2 show the geometry and reinforcing details of the test model FSD. The slab is 125 mm deep and it is reinforced with two steel meshes; one on the top with 6 mm diameter bars at 100 mm, and another on the bottom consisting of 6 mm diameter bars at 75 mm. The slab was reinforced at the corners by shear-heads consisting of 60 mm deep steel C-shapes, in order to prevent punching shear failure. The shape of the slab was a parallelepiped in which each pair of adjacent sides was perpendicular. The dimensions of the plate were $2700 \times 2700 \times 125\,\mathrm{mm}^3$. In plan, the plate (including the steel meshes used as bending reinforcement and the deep C-shapes used as punching shear reinforcement at the corners) formed a $2700 \times 2700\,\mathrm{mm}^2$ parallelogram with two lines of symmetry parallel to each side and passing through its centroid. Figure 5.3 shows a detail of the slab. The average yield stress, f_s, of the reinforcing steel was 467 MPa, and the average concrete strength, $f_c$was 23.5 MPa. The columns were built with an $80 \times 80 \times 4\,\mathrm{mm}$ hollow-steel section. The average yield stress f_y of the columns steel was 216 MPa and the maximum stress 329 MPa.

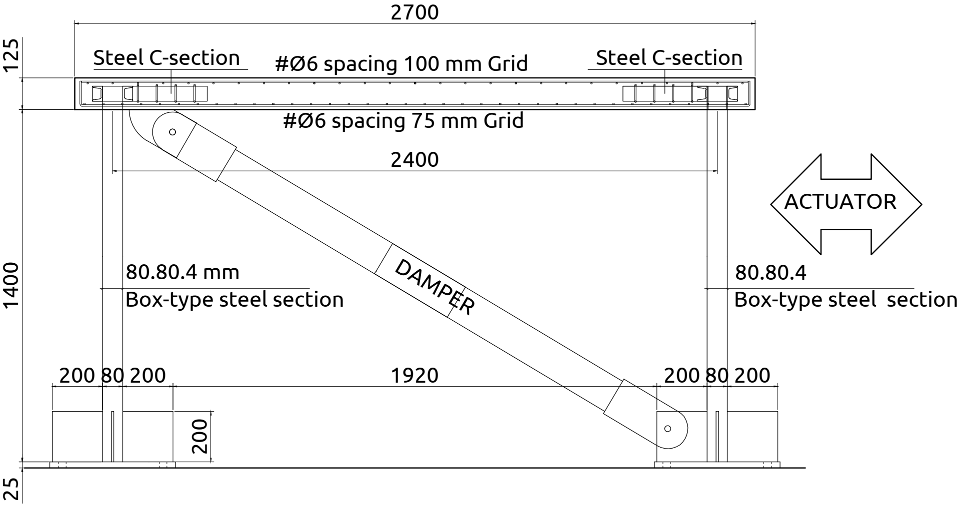

Figure 5.1.: Test model geometry (elevation)

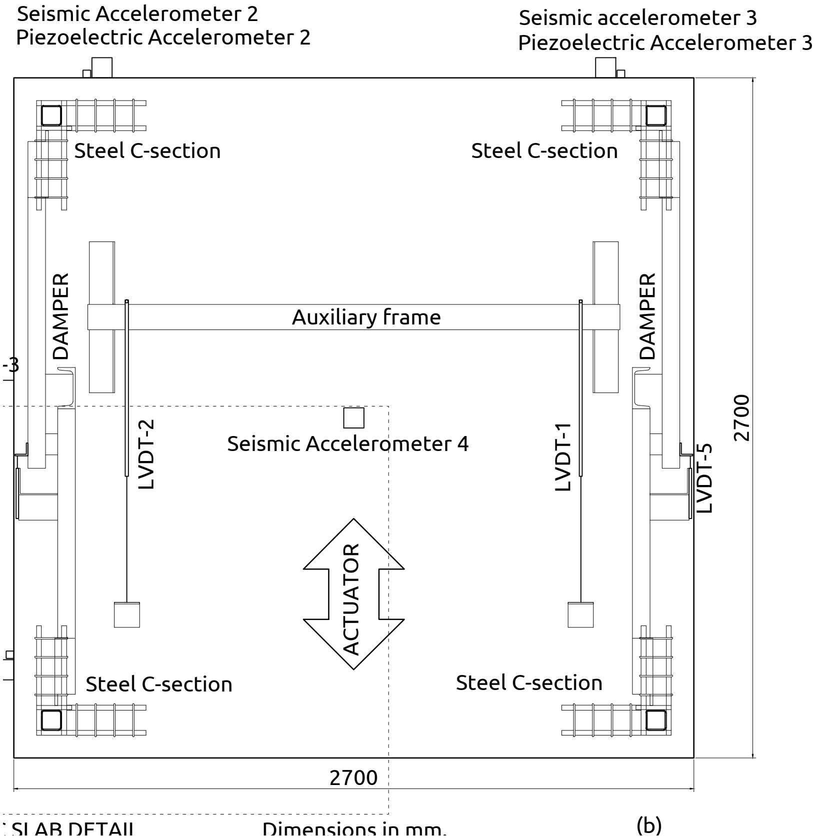

Figure 5.2.: Test model geometry (Plan) (bottom view)

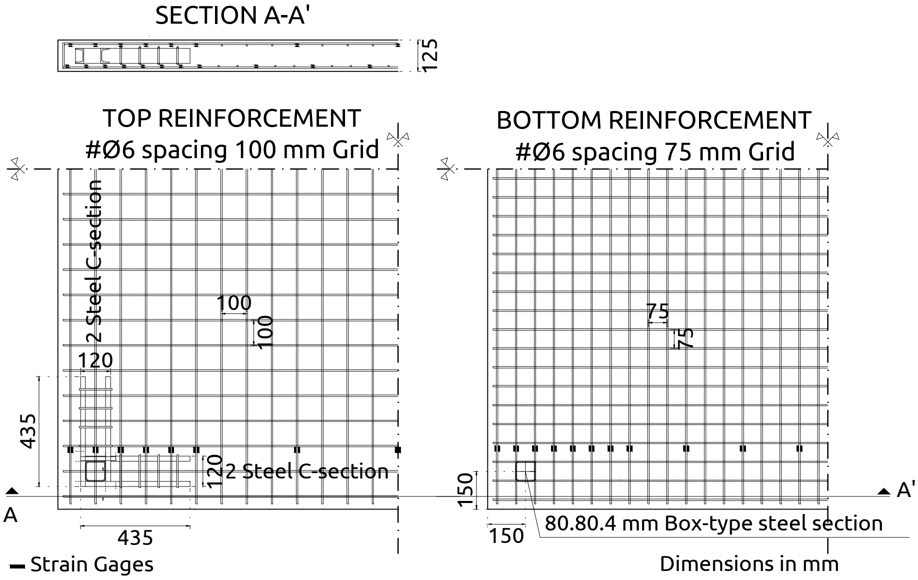

Figure 5.3.: Detail of the RC slab

The hysteretic damper used in the tests has the form of a conventional brace and it is installed in the main structure as a standard diagonal bar. Each hysteretic damper is constructed by assembling five short length segments of I-shaped steel sections which constitute the energy dissipating device, and two U-shaped steel bars that function as auxiliary elements. The seismic damper dissipates the energy through plastic strains on the web of the I-shaped sections under out-of-plane flexure. The auxiliary elements are designed to remain elastic. A detailed description of the hysteretic damper can be found in [15].

Figure 5.4 shows the hysteretic dampers installed in specimen FSD, which were connected to the main structure as shown in Fig 5.1. The procedure considered to design the hysteretic dampers is an energy-based method that is rooted in establishing the energy balance of the structure. Energy-based design procedures are particularly appropriate for designing structures incorporating passive damping mechanisms [82] and have recently been included in the Japanese seismic code [63]. A detailed development of the procedure and the equations required to design the dampers in this case can be found in [13]. Using these equations, the hysteretic dampers were designed as follows. First, the lateral stiffness of the main structure ${}_fk$ (i.e. without dampers), the mass M and the corresponding period ${}_fT$ were estimated as ${}_fk = 37.2\,\mathrm{kN/cm}$, $M = 0.0739\,\mathrm{kNs^2/cm}$ and ${}_fT = 0.28\,\mathrm{s}$. Second, a stiffness ratio $K =_s k/_f k = 2$ was discretionally adopted so that the damper yields far before the main structure reaches its elastic deformation capacity. Here ${}_sk$ is the lateral stiffness provided by the dampers; ${}_sk$ and lateral strength of the dampers ${}_sQ_y$ were determined, so that the maximum lateral displacement of the structure v_{max} for a design earthquake of far-field type characterized by $I_d = 18.5$, $T_{NH} = 0.9\,\mathrm{s}$ and $V_D = 70\,\mathrm{cm}/s$ was $v_{max} = 12\,\mathrm{mm}$. The value adopted for v_{max} corresponds to a drift of 1% of story height. I_d is a seismological parameter proposed by Cosenza and Manfredi[32], T_{NH} is the initial period of medium period region in the Newmark and Hall representation of the design earthquake, and V_D is the energy input that contributes to damage expressed in terms of equivalent velocity. The values adopted for Id and T_{NH} correspond to the Calitri 1980 NS earthquake, and the value adopted for V_D is representative of the seismic hazard in Granada, Spain [16]. I_d, T_{NH} and V_D were scaled by the corresponding factors to ensure consistency.

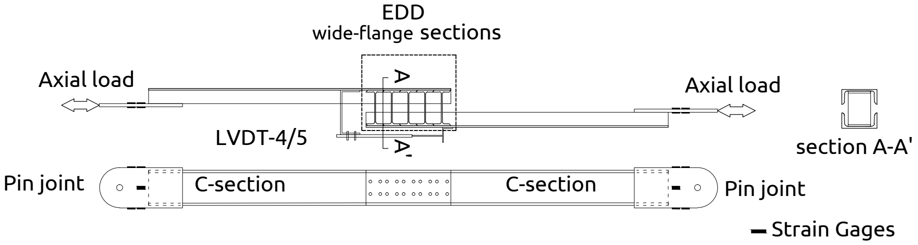

Figure 5.4.: Hystertic damper installed in FSD specimen

5.1.2. Experimental set-up, instrumentation and load history.

The dynamic tests were carried out on the uniaxial MTS 3×3 m shaking table of the University of Granada. The test models were bolted to the shaking table as seen in Figures 5.5 and 5.6. In order to satisfy the similitude laws between prototype and test model, additional mass was added to the top of the RC slab; the total mass including the steel blocks was $M = 7.39\,Ns^2/mm$. The MTS shaking table has a digital controller which provides for closed loop control of the system using three high-level control techniques: TVC (Three Variable Control) for high fidelity reproduction across a wide band width; DPS (Delta Pressure Stabilization) for effectively damping oil column compliance to allow for higher gain settings across a wider bandwidth; and SFL (Servovalve Flow Linearization) for effectively removing the inherent non-linearities present in the servohydraulic system. To track the acceleration performance of the table and improve the table response, the MTS shaking table includes two adaptative control techniques: the AIC (Adaptive Inverse Control) and the OLI (On-line Iteration). AIC is a control compensation technique that augments a fixed-gain controller to correct for closed loop gain and phase irregularities in order to improve control fidelity. It measures control system dynamics directly and modifies the control compensation accordingly in real time, making it possible to adapt to changing system dynamics. OLI is a control technique that repeatedly modifies the command input to a control system on an individual sample-by-sample basis until the control system response is an almost perfect replica of the desired command. OLI requires knowledge of transfer function of the equipment in order to compute a drive correction. The calibration of the system was conducted by moving the shaking table with the specimen mounted on it under acceleration control, as follows. First, a flat-shape random signal of root mean square (RMS) amplitude of about $0.05g$ was applied to the table, and several parameters that govern the TVC system (dynamic force gain, displacement lead, velocity lead, acceleration jerk lead, acceleration gain, etc.) were adjusted so that the coherence of the transfer function (ratio between the reference acceleration and the feedback acceleration) was close to one in the bandwidth of 0-50Hz. Second, the AIC controller was trained in two consecutive phases. In the first phase, the forward transfer function was trained by moving the shaking table with a random signal with an RMS amplitude of about $0.05g$. The second phase consisted of training the inverse transfer function. Third, the controller OLI was trained through an iterative process in which the shaking table was subjected to the desired accelerogram scaled to a low intensity of $0.1g$. The gain was progressively reduced in each iteration until the errors between the desired acceleration and the actual acceleration measured on the table were reduced to acceptable values.

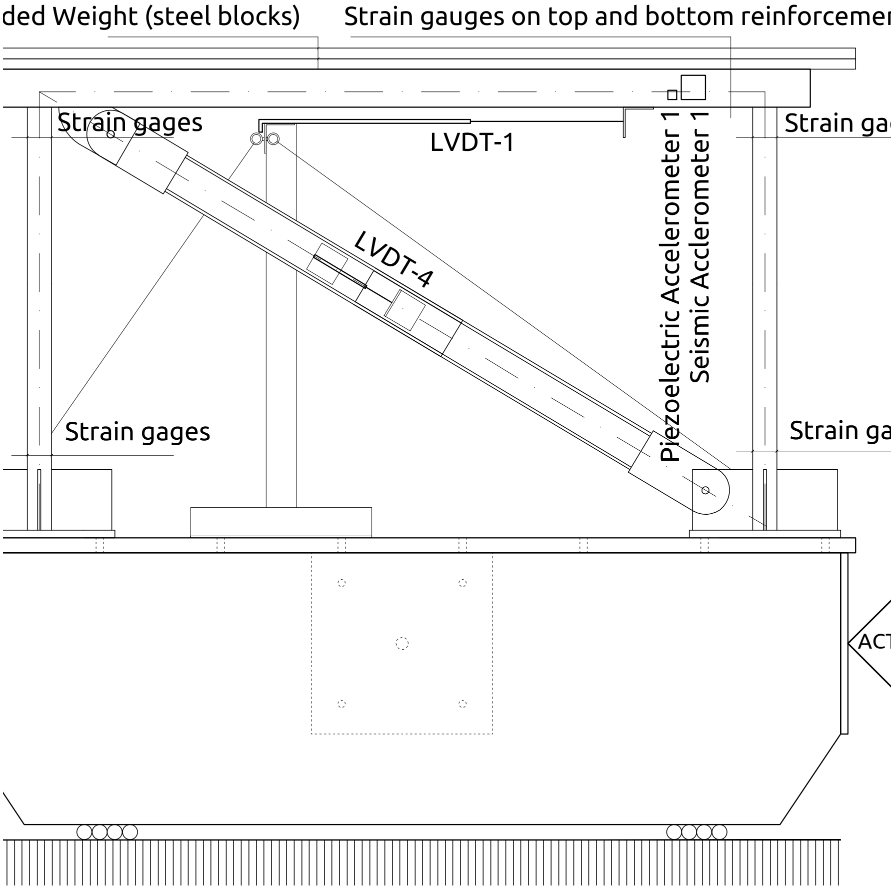

Figure 5.5.: Experimental set-up

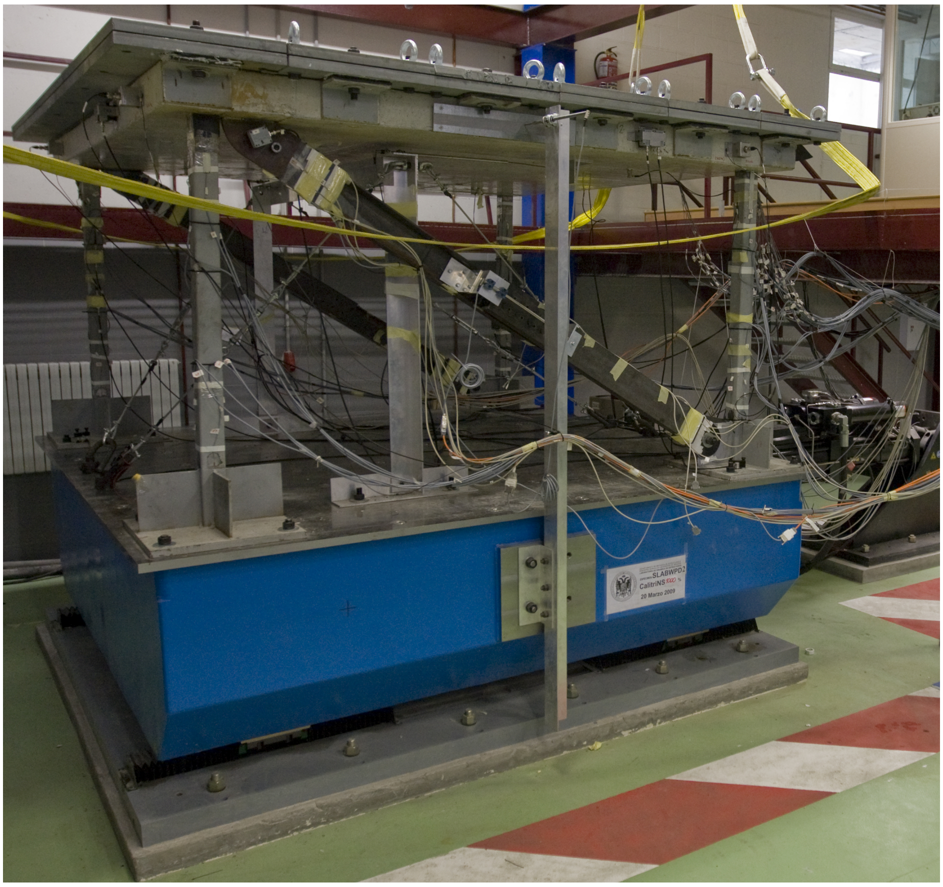

Figure 5.6.: Set-up overview

The models were tested applying to the shake table the Calitri 1980 NS earthquake signal (Campano-Lucano, Italy). Figures 5.7a and 5.7b show the time history of ground acceleration and the 5% damped elastic response spectra in terms of absolute response acceleration S_a normalized by PGA, corresponding to the original (unscaled) earthquake. Figure 5.7c shows the corresponding elastic response spectra for the earthquake signal scaled in time by the scaling factor $\lambda_t = \sqrt{1/2}$. Each specimen was subjected to a series of consecutive seismic simulations. In each seismic simulation the acceleration of the original record measured at Calitri during the Campano-Lucano earthquake was scaled by multiplying it by the factors of 1, 2, 3, 4, 5, 6, 7 and 14. The PGA of the earthquake signals obtained in this way were 0.16g, 0.31g, 0.47g, 0.62g, 0.78g, 0.94g, 1.10g and 2.23g, respectively. Model FS was subjected to seven seismic simulations with the following PGA: 0.16g, 0.31g, 0.47g, 0.62g, 0.78g, 0.94g, and 1.10g. In turn, model FSD was subjected to eight shaking simulations with PGA equal to 0.16g, 0.31g, 0.47g, 0.62g, 0.78g, 0.94g, 1.10g, and 2.23g.

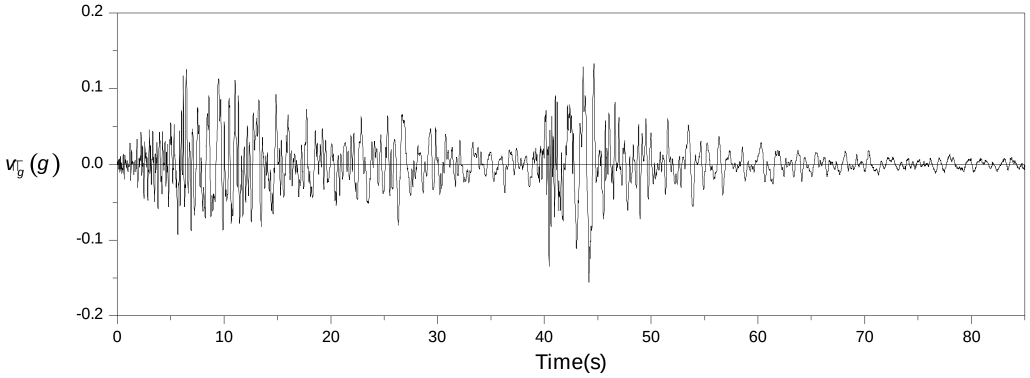

(a) Unscaled history of acceleration

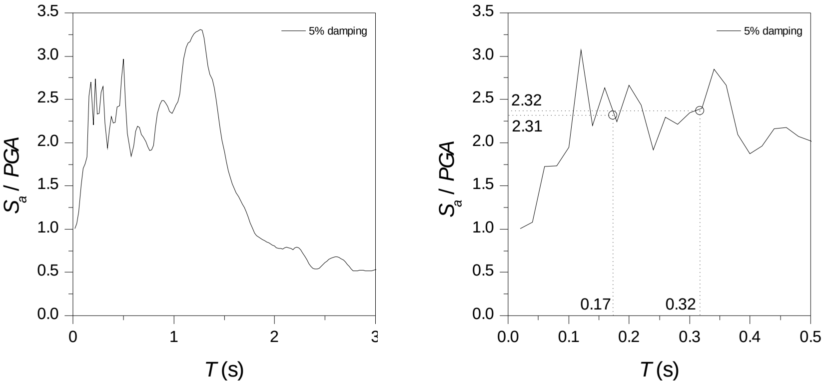

(b) Unscaled elastic response spectrum (c) Scaled elastic response spectrum

Figure 5.7.: Calitri 1980 NS earthquake acceleration record used in the seismic simulations

During each seismic simulation, displacements, strains and accelerations were acquired simultaneously. Data was continuously collected by a HBM MGC Plus data acquisition system using a sampling rate of 200 Hz. Both FS and FSD models were instrumented with the following sensors:

1. Two HBM inductive displacement transducers model WA-500, indicated as LVDT-1 and LVDT-2 in figure 5.2. These sensors measured the relative horizontal displacement, v, between the shake table and the slab in the direction of the seismic loading;
2. One HBM inductive displacement transducer model WA-100, indicated as LVDT-3 in figure 5.2, that measured the relative displacement between the shake table and the slab in the direction perpendicular to the seismic loading.
3. Three pairs of Bruel & Kjaer piezoelectric and seismic accelerometers. The piezoelectric accelerometer was a miniature deltatron type 4507. The seismic accelerometer was a deltatron type 8340. They were fixed to the slab to measure its absolute response acceleration, $\ddot{v}^t$ as indicated in figure5.1. The pair formed by the piezoelectric accelerometer 2 and the seismic accelerometer 2, and the pair formed by piezoelectric accelerometer 3 and seismic accelerometer 3, measured accelerations in the direction of the seismic loading. The pair formed by the piezoelectric accelerometer 1 and the seismic accelerometer 1 measured the

acceleration in the direction perpendicular to the seismic loading.

4. An accelerometer labelled “Accelerometer MTS” in figure 5.1 was fixed to the shake table to measure the absolute table acceleration $\ddot{v}_g$ in the direction of the seismic loading.
5. Seventy-eight Tokyo Sokki Kenkyujo 120Ω electrical resistance strain gauges were attached to top and bottom longitudinal reinforcing bars prior to casting the concrete as shown in Fig.5.3, and to the upper and lower ends of the columns as shown in Fig. 5.5

Each damper installed in specimen FSD was instrumented with the following sensors:

1. One HBM inductive displacement transducer modelWA-100 indicated as LVDT-4 and LVDT-5 in Fig. 5.2. Each sensor measured the axial deformation in one diagonal brace.
2. Four Tokyo Sokki Kenkyujo 120 electrical resistance strain gauges were attached to both ends of the diagonal braces as shown in Fig. 5.4.

5.1.3. Overall test results

Figure 5.8 shows the time histories of the relative displacement v of the slab with respect to the shaking table, in the direction of the shaking, for several seismic simulations. It was obtained by averaging the measurement provided by the displacements transducers LVDT-1 and LVDT-2 (see Figs. 5.2, 5.5).

Figure 5.9 shows the corresponding time histories of absolute response acceleration $\ddot{v}^t$ of the slab in the direction of the shaking. It is clear in the figures that the presence of hysteretic dampers significantly reduces the relative displacement of the structure while increasing the absolute response acceleration.

Figure 5.10 shows the overall response of models FS and FSD during the seismic simulations with PGA equal to 0.16, 0.31, 0.47, 0.62, 0.78, 0.94 and 1.1 g. In the figures, the abscissa shows the relative displacement v of the slab with respect to the shaking table. The ordinate shows the absolute response acceleration of the slab $\ddot{v}^t(=\ddot{v}+\ddot{v}_g)$ multiplied by the mass of the system (inertial force). In the seismic simulations with PGA=0.94 g the hysteretic dampers reduced the lateral displacement to approximately one half. In the seismic simulations with PGA 0.78g the hysteretic dampers increased the maximum inertial force up to about 45%; this increase reached 57% in the seismic simulation with PGA=0.94 g and 97% in the seismic simulation with PGA=1.1 g. The maximum lateral force that can be sustained by each specimen is limited by its lateral strength. Since the lateral strength of the specimen with hysteretic dampers FSD is larger than that of the specimen without dampers FS, the maximum force of the former may increase with respect to the latter while the PGA input to the shaking table is the same. The specimen FS reached its limit lateral strength and yielded for PGA=0.47 g, and consequently the maximum absolute response acceleration (and hence the maximum lateral force) remained almost constant in the seismic simulations with PGA>0.47 g. In contrast, in specimen FSD the plastification of the steel columns started during the seismic simulation corresponding to PGA=0.94 g.

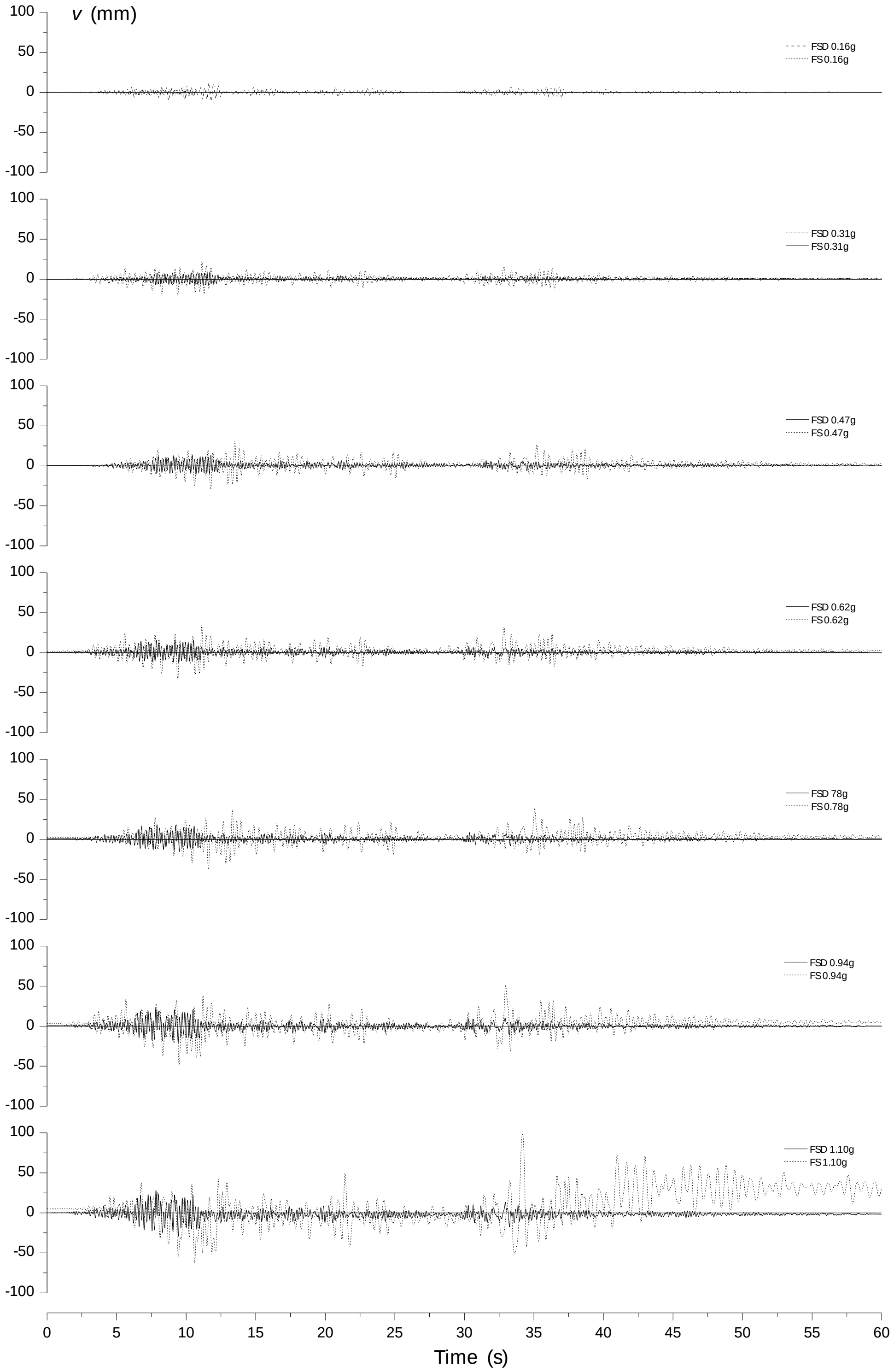

Figure 5.8.: Time histories of relative displacements of the slab for specimens FD and FSD.

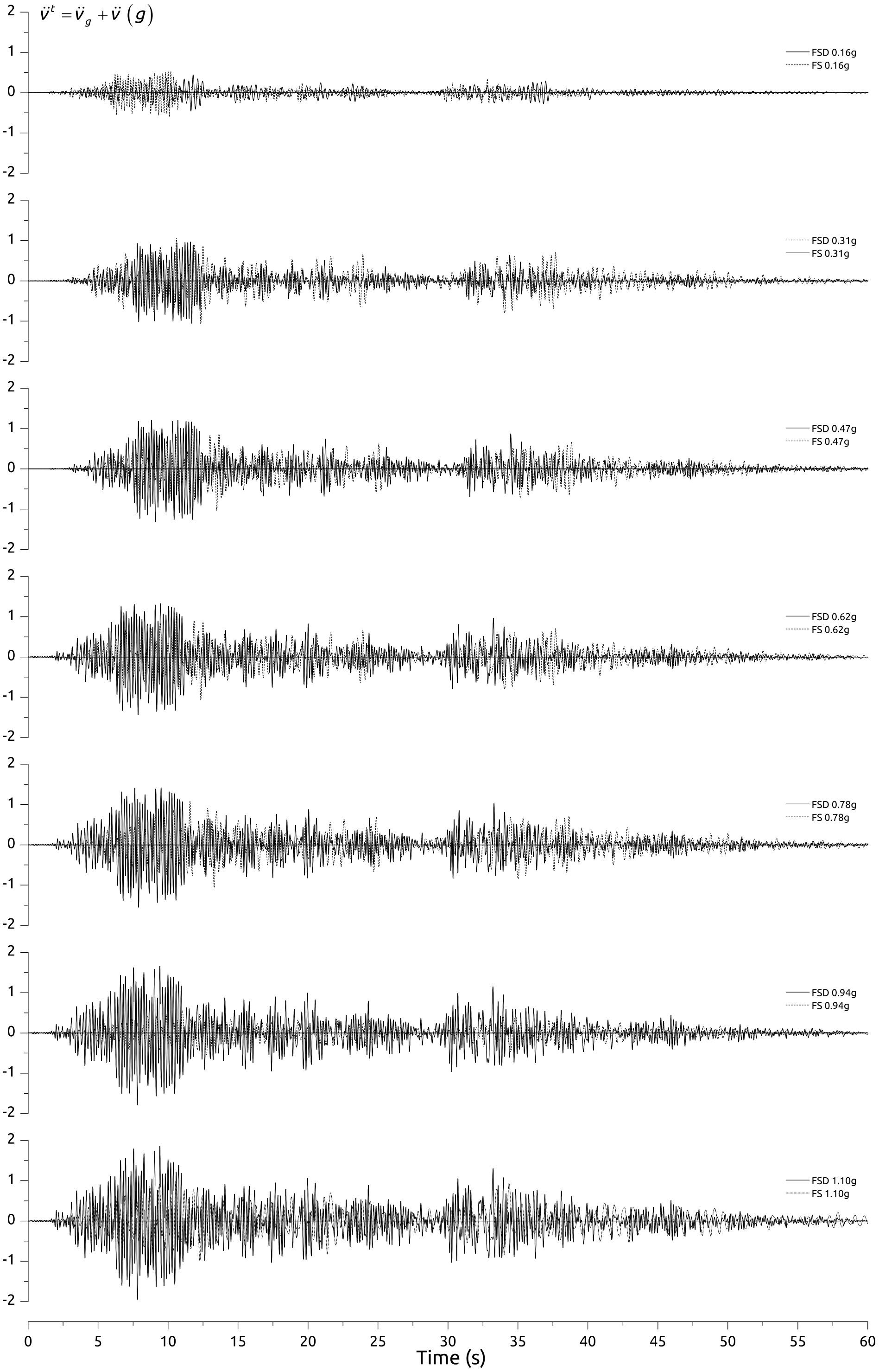

Figure 5.9.: Time histories of absolute response acceleration of the slab for specimens FD and FSD.

Table 5.1 summarizes the parameters that characterized the dynamic response of models FS and FSD during the different seismic simulations. In this table, T is the period of vibration, ξ is the damping ratio, id is the maximum drift expressed as percentage of the story height, v_{max} is the maximum relative displacement, $\ddot{v}^t_{max}$ is the maximum absolute response acceleration, v_r is the residual displacement after each test, V_E is the total energy E input by the earthquake expressed in terms of an equivalent velocity by $VE = \sqrt{2E/M}$, and SPL is the Structural Performance Level according to the limiting values of id defined in Table C1-3 of FEMA-356. T and ξ were calculated from the time history of response displacements v measured during free vibration tests conducted after each seismic simulation. More precisely, the damping ratio was obtained considering two response peaks which are r cycles apart, v_n and v_{n+r}, by $\xi = Ln\left(v_n/v_{n+r}\right)/2\pi r$; $\ddot{v}^t_{max}$was obtained experimentally by averaging the accelerations measured by the accelerometers 2 and 3 in the direction of the shaking. For relating the $SPLs$ with the values of id according to Table C1-3, the test model FS was considered as a steel moment frame, whereas model FSD was treated as a Braced Steel Frame. The discrete $SPLs$ established by FEMA-356 are: Immediate Occupancy level (S1), Damage Control Range (S2), Life Safety (S3), Limited Safety Range (S4), Collapse prevention (S5) and Not Considered (S6). Specimen FS collapsed in the seismic simulation corresponding to 1.1 g, and specimen FSD in the seismic simulation corresponding to 2.23 g. It is worth noting that in specimen FSD, the dampers broke completely (splitting in two parts) before the end of the seismic simulation corresponding to 2.23 g, and from this instant the system behaved as a bare structure (i.e. without hysteretic dampers). The values of v_r at the end of each seismic simulation before the one that caused the collapse of the structure were below 0.39% in specimen FS and below 0.13% in specimen FSD. These residual displacements at the end of a given seismic simulation are negligible on the structural global response in the following test. In both test models and for all seismic simulations, the reinforcement steel of the slab remained elastic.

The plastic mechanism of both test models was characterized by the formation of plastic hinges at both ends of the columns. In test model FS, the formation of plastic hinges in the columns occurred during the seismic simulation in which PGA=0.47 g. In test model FSD, the onset of yielding of the dampers occurred in the seismic simulation corresponding to PGA=0.31 g, prior to plastification of the columns. The columns started to plastify during the seismic simulation corresponding to PGA=0.94 g. Figures 5.11a and 5.11b show, with open circles, discrete pairs of values for the displacement, v, and the restoring force, F_S, recorded at the instants in which the velocity was zero (i.e. $\dot{v} = 0$). The equation of dynamic equilibrium of the slab is:

$$m\ddot{v}^t + c\dot{v} + F_S = 0 \tag{5.1}$$

where c is the damping coefficient ($c = 4m/T$). At the instants of $\dot{v} = 0$ the damping force $c\dot{v}$ is null, and therefore the inertial force is equilibrated entirely by the restoring force, i.e. $F_S = -m\ddot{v}^t$. Consequently, F_S was computed at the instants when the velocity was zero by multiplying the absolute acceleration $\ddot{v}^t$ by the mass of the system m.

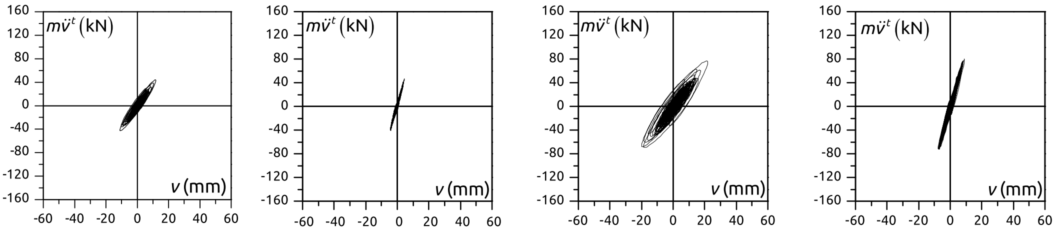

(a) FS 0.16g test (b) FSD 0.16g test (c) FS 0.31g test (d) FSD 0.31g

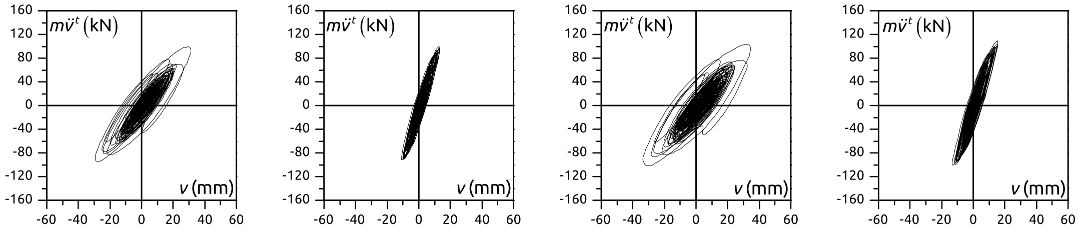

(e) FS 0.47g test (f) FSD 0.47g test (g) FS 0.62g test (h) FSD 0.62g

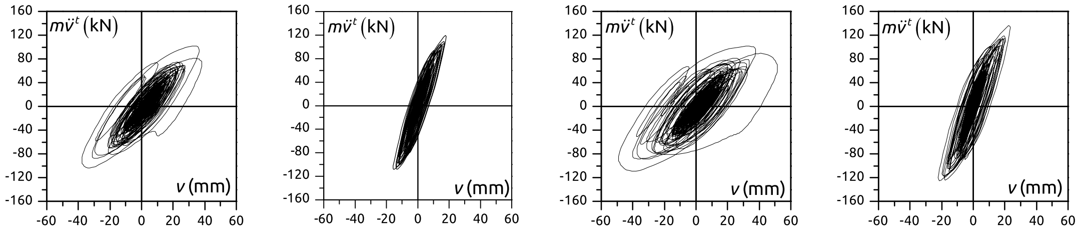

(i) FD 0.78g test (j) FSD 0.78g test (k) FS 0.94g test (l) FSD 0.94g test

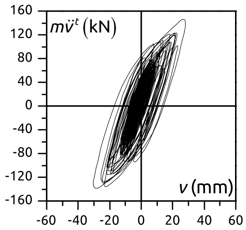

(m) FSD 1.10g

Figure 5.10.: Inertial force $m\ddot{v}^t$ versus lateral displacement v obtained for the tests for specimens FS and FSD

	Model FS								Model FSD							
PGA (g)	T (s)	ξ (%)	id (%)	v_{max} (mm)	$\ddot{v}^t_{max}$ (g)	v_r (mm)	V_E (cm/s)	SPL	T (s)	ξ (%)	id (%)	v_{max} (mm)	$\ddot{v}^t_{max}$ (g)	v_r (mm)	V_E (cm/s)	SPL
0.16	0.32	1.6	0.9	11.9	0.46	0	38	S1	0.16	1.6	0.34	4.3	0.60	0	30	S1
0.31	0.32	2.1	1.7	21.8	0.79	0.3	90	S2	0.16	2.1	0.70	8.8	1.05	0.3	68	S1
0.47	0.32	2.5	2.4	31.2	1.03	1.9	152	S3	0.16	2.5	1.04	13.1	1.3	0.8	142	S2
0.62	0.32	3.1	2.7	34.6	1.06	2.6	187	S3	0.16	3.1	1.22	15.4	1.44	0.7	181	S3
0.78	0.32	3.2	2.9	37.8	1.07	3.2	222	S4	0.17	3.2	1.42	17.9	1.55	0.6	220	S3
0.94	0.32	3.5	4.0	51.5	1.13	4.9	303	S5	0.17	3.5	1.84	23.3	1.78	0.23	304	S4
1.10	0.32	3.5	7.7	98.2	1.01	31.2	428	*	0.17	3.5	2.33	29.4	1.94	1.6	393	S5
2.23									0.17	3.5	4.17	52.6	2.07	17	445	*

*collapse

Table 5.1.: Response parameters obtained from the experiments

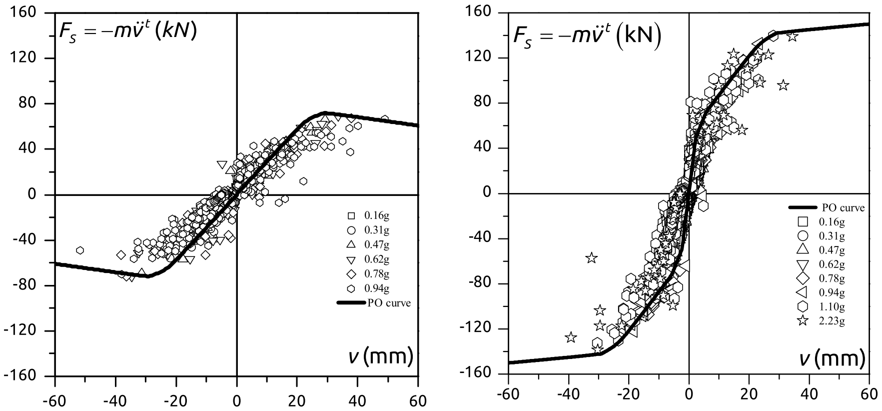

(a) FS model

(b) FSD model

Figure 5.11.: Pairs of values (v, F_S) and numerical PO curve.

5.2. Estimation of capacity curves with numerical models and comparison with test results

In order to estimate the capacity curves of the FS and FSD models, two non-linear 3D finite element models were developed using Engineer's Studio software [59]. Both models were subjected to a displacement-controlled SPO analysis including second order ($P-\Delta$) effects. Figure 5.12 shows the finite element mesh of the models. The RC slab was modeled with non-linear rectangular isoparametric plate elements. In the vicinity of the columns, the plate elements had 4 nodes and their size in plan was $87.5 \times 87.5\,\mathrm{mm}^2$. For the rest of the slab, plate elements with 8 nodes and $175 \times 175\,\mathrm{mm}^2$ were used. Each plate element was internally subdivided into six layers. The top and the bottom layers included the longitudinal reinforcement of the slab. The constitutive relationships of the materials were formulated using the non-linear mechanics of reinforced concrete proposed by Maekawa [59]. The C-shape steel sections that form the shearheads were modeled with elastic frame elements connected to the nodes of the plate element. The columns were modeled with 84 mm-long fiber frame elements. The base of the column was modeled with a momentcurvature, $M-\varphi$, element in order to simulate a semi-rigid union. The FSD model was defined attaching two diagonal bars that represented the hysteretic dampers to the FS numerical model. Each diagonal bar consisted of two elastic elements and one non-linear spring connected in series.

The base shear versus top displacement relationship (capacity curve) obtained from the SPO analysis is shown in bold lines in Fig. 5.11. To better compare the capacity curve obtained numerically with the experimental results, the pairs of values (v, F_s) corresponding to the maximum absolute acceleration attained by the slab in each seismic simulation were selected from Fig. 5.11a and 5.11b, and they are drawn in Figures 5.13a and 5.13b, respectively. It can be seen that there is a good agreement between the test results and the curve obtained with the finite element models.

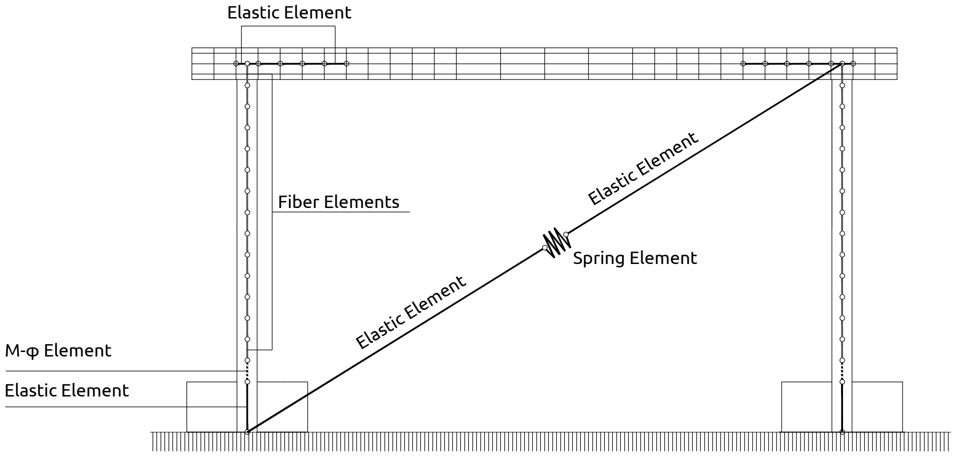

(a) Elevation

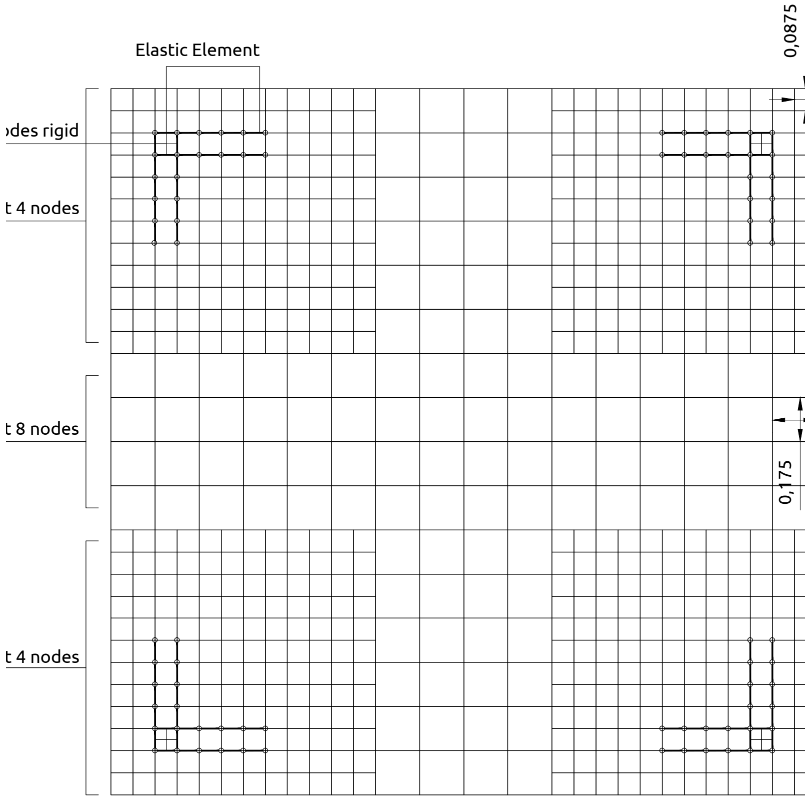

(b) Plan

Figure 5.12.: Definition of the finite element model

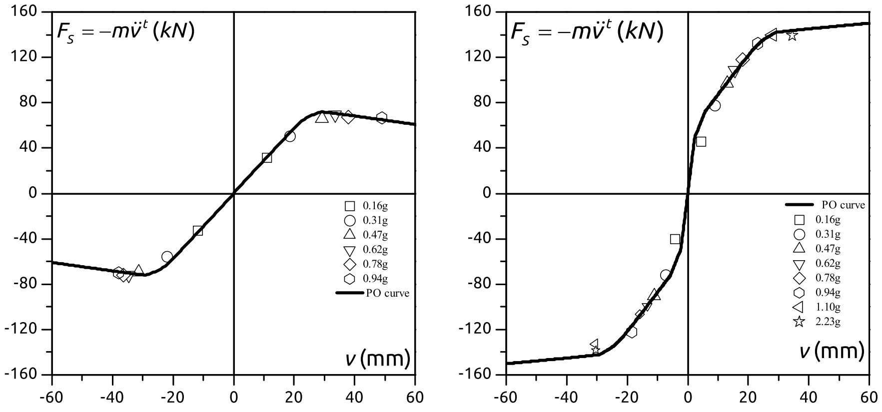

(a) FS model

(b) FSD model

Figure 5.13.: Maximum experimental values (v, F_S) at instant of $\dot{v} = 0$ and numerical PO curve.

5.3. Comparison between prediction with NSPs and experimental results for specimen FSD.

In this section, the maximum response of the structure with hysteretic dampers, FSD, is predicted with current NSPs for four levels of ground motion corresponding to the seismic simulations with PGA=0.31 g, PGA=0.62 g, PGA=0.94 g and PGA=1.1 g reported in Section 5.1. Each simulation produced a different level of damage on the structure. Similar to previous studies [23, 26], the prediction with NSPs was calculated using a smoothed spectrum S_a—T . The smoothed spectrum for each level of PGA was obtained from the elastic response spectrum calculated with the inherent damping measured during the tests, by applying the rule of equal areas [96]. Figure 5.14 shows with simple lines the unsmoothed spectra, and with bold lines their counterpart smoothed ones. It is worth noting in this figure that the comparison of the elastic acceleration responses depends on the natural periods of the two specimens FS and FSD, $T = 0.17$s and $T = 0.32$s, respectively, which are indicated with a vertical line. As seen in the figure, within the spectral window delimited by about 0.15 and 0.9 s the spectra are approximately flat, and the periods of both specimens FS and FSD are located within this period range.

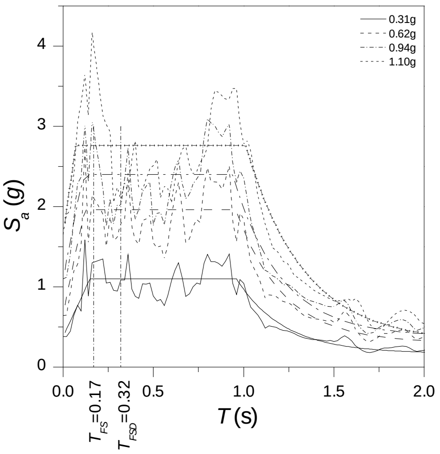

Figure 5.14.: Elastic response spectra for the FSD test model under three different levels of PGA.

5.3.1. Capacity spectrum method

The CSM presented in FEMA 440 is an improved equivalent linearization procedure as a modification to the CSM of ATC-40. The performance point of the structure is obtained in terms of maximum displacement by direct comparison of the capacity and demand curves in an Acceleration Displacement Response Spectra (ADRS) format, in which spectral acceleration, S_a, is plotted against spectral displacement, S_d. The performance point is obtained by the intersection of the capacity curve with the demand curve. The latter is obtained from a 5% damped elastic response spectrum modified by two factors: (1) factor $B(\beta_{eff})$ to adjust the initial response spectrum to the appropriate level of effective damping, β_{eff} ; and (2) factor M to obtain the modified ADRS demand curve (MADRS). Values of B and M can be obtained with the following expressions:

$$B = \frac{4}{5.6 - ln\,(\beta_{eff})} \tag{5.2}$$

$$M = \left(\frac{T_{eff}}{T_0}\right)^2 \frac{1 + \alpha\,(\mu - 1)}{\mu} \tag{5.3}$$

The effective linear parameters (effective period T_{eff} and effective damping β_{eff}) are functions of the capacity curve, the initial period and damping, and the ductility demand. They can be obtained from the following expressions:

$$\begin{aligned} \beta_{eff} &= A\,(\mu-1)^2 - B\,(\mu-1)^3 + \beta_0 \\ T_{eff} &= \Big(G\,(\mu-1)^2 - H\,(\mu-1)^3 + 1\Big)\,T_0 \end{aligned} \quad 1.0 \le \mu \le 4.0 \tag{5.4}$$

$$\begin{aligned} \beta_{eff} &= C + D\,(\mu-1) + \beta_0 \\ T_{eff} &= (T + J\,(\mu-1) + 1)\,T_0 \end{aligned} \quad 4.0 \le \mu \le 6.5 \tag{5.5}$$

$$\begin{aligned} \beta_{eff} &= E\left[\frac{F(\mu-1)-1}{(F(\mu-1))^2}\right]\left(\frac{T_{eff}}{T_0}\right)^2+\beta_0 \\ T_{eff} &= \left(K\left(\sqrt{\frac{(\mu-1)}{1+L(\mu-2)}}-1\right)+1\right)T_0 \end{aligned} \qquad \mu > 6.5 \tag{5.6}$$

Here, μ is the ductility ratio. β_0 and $T_0$are the initial damping and the initial period of vibration of the structure defined by an idealized bi-linear curve as shown in Fig. 5.15. In this bilinear curve, the elastic slope is equal to the initial stiffness in the capacity curve, and the post-yield branch should have a slope such that (1) it passes through the performance point, and (2) the areas below the SPO curve and the idealized curve are the same. Coefficients A to L are defined in Tables 6-1 and 6-2 in FEMA-440. Since all these parameters are functions of ductility, which is the objective of the analysis, the solution must be found using an iterative technique.

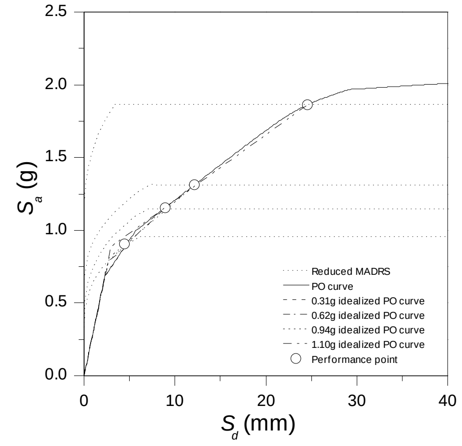

Figure 5.15.: Idealized capacity curve and target displacement ADRS format (specimen FSD)

	PGA 0.31g		PGA 0.62g		PGA 0.94g		PGA 1.10g	
	CSM	Test	CSM	Test	CSM	Test	CSM	Test
T_{eff} (s)	0.13	0.16	0.16	0.16	0.17	0.16	0.28	0.17
PP (mm)	4.5	8.7	9	15.4	11	23.2	24.5	29.4
$F_{S,max}$ (kN)	64.0	79.8	83.0	108.6	91.0	132.8	134.4	139.5

Table 5.2.: CSM Results for specimen FSD

Table 5.2 compares the results of the improved CSM prediction in terms of effective period T_{eff} , displacement corresponding to the performance point PP, and maximum restoring force $F_{S,max}$, with the experimental results for the seismic simulations corresponding to PGA=0.31 g, PGA=0.62 g, PGA=0.94 g and PGA=1.1 g. In turn, Figure 5.15 offers a graphic view of the idealized capacity curve and the target displacement predicted at the last step of the iterative process in ADRS format.

5.3.2. Displacement coefficient method

The improved version of the DCM in FEMA-440 estimates maximum global displacement (target displacement) of the structure at roof level, δ_t, by multiplying the elastic response of an equivalent SDOF system by a series of coefficients—C_0 to C_2—as indicated in Eq. (7):

$$\delta_t = C_0\, C_1\, C_2\, S_a\, \frac{T_e^2}{4\pi^2}\, g \tag{5.7}$$

Here S_a is the maximum response acceleration of the equivalent SDOF system obtained from an elastic response spectrum assuming a 5% damping ratio. T_e is the effective fundamental period of the equivalent SDOF given by $T_e = T_i\sqrt{k_i/k_e}$ where T_i is the elastic fundamental period and K_i is the lateral stiffness of the structure. To determine the dynamic properties of the equivalent SDOF, an iterative graphic method should be applied so that the areas under the capacity and idealized curves are equal. Accordingly, the effective lateral stiffness K_e, is taken as the secant stiffness corresponding to a base shear force equal to 60% of the effective yield strength of the structure, V_y. In Equation 5.7, C_0 relates the spectral displacement of the equivalent SDOF system with the roof displacement of the buildingmulti-degree-of-freedom (MDOF) system. C_1 relates the expected maximum inelastic displacements with respect to those calculated for linear elastic response, as follows:

$$c_1 = 1 + \frac{R-1}{aT_e^2} \tag{5.8}$$

where the constant a is equal to 130, 90 and 60 for site classes B, C and D, respectively, and R is the ratio of required elastic strength to the yield strength defined by means of Equation 5.9:

$$R = \frac{S_a W}{V_y} C_m \tag{5.9}$$

where W is the effective seismic weight and C_m is the effective mass factor. The coefficient C_2 need only to be applied to structures that exhibit significant stiffness and/or strength degradation, and it can be obtained as follows:

$$C_2 = 1 + \frac{1}{800}\left(\frac{R-1}{T}\right)^2 \tag{5.10}$$

Again, an iterative process is necessary if the estimated target displacement and the predicted performance point are much different.

Below, Table 5.3 summarizes the results of the equivalent period, T_e, target displacement, δ_t, and the maximum restoring force, $F_{S,max}$, predicted with the improved DCM from FEMA- 440, and compares them with the experimental results corresponding to the seismic simulations with PGA=0.31 g, PGA=0.62 g, PGA=0.94 g and PGA=1.1 g. Figure 5.16 offers a graphic view of the idealized capacity curve and the target displacement predicted in the last step of the iterative process.

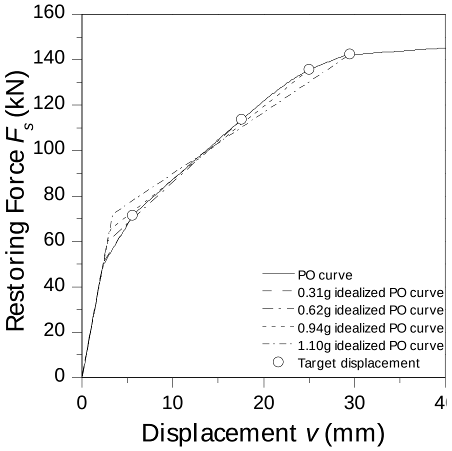

Figure 5.16.: DCM idealized capacity curve and target displacement (specimen FSD)

	PGA 0.31g		PGA 0.62g		PGA 0.94g		PGA 1.10g	
	N2	Test	N2	Test	N2	Test	N2	Test
T_e (s)	0.13	0.16	0.18	0.16	0.19	0.17	0.19	0.17
S_a (m/s2)	10.8	-	19.3	-	23.0	-	27.0	-
δ_t (mm)	6.4	8.7	22.3	15.45	34.5	23.3	55.9	29.4
$F_{S,max}$ (kN)	74.5	79.8	128.8	108.6	143.9	132.8	149.2	139.5

Table 5.3.: DCM results for specimen FSD

5.3.3. N2 method

This method is called N2 because it is non-linear and it uses two mathematical models: the response spectrum method and non-linear SPO analysis [41] . It is based on the inelastic demand spectra of an SDOF system [96] following the equal displacement rule for systems with medium and long periods.

The N2 method assumes that the target displacement d_t of the structure at the control node can be obtained from the elastic displacement d_{et}^* of an equivalent SDOF system. The equivalent SDOF system is defined by an elastic-perfectly plastic bilinear idealization of the SPO curve, imposing that (1) the yield strength $F_y^*$is equal to the strength of the target point, and (2) the yield displacement $d_y^*$is selected so that the areas below both curves are equal, as shown in Figure 5.17. The elastic equivalent period T^* of the idealized bilinear system can be determined as

$$T^* = 2\pi\sqrt{\frac{m^* d_y^*}{F_y^*}} \tag{5.11}$$

where $m^*$is the equivalent mass of the SDOF system. The elastic displacement d_{et}^* of the equivalent SDOF is obtained from the spectral acceleration at the period T^*, $S_a\left(T^*\right)$by Equation 5.12 :

$$d_{et}^{*} = S_a\left(T^{*}\right)\left(\frac{T^{*}}{2\pi}\right)^{2} \tag{5.12}$$

The inelastic displacement d_t^* of the equivalent SDOF system can be derived from the elastic displacement d_{et}^*, applying a simplified version of the equations proposed by Vidic et al. [96] and adopted in Eurocode 8 [38], as follows:

$$\begin{gathered} d_t^{*} = \frac{1}{R_\mu}\left[1 + \left(R_\mu - 1\right)\frac{Tc}{T^{*}}\right] d_{et}^{*} \quad for\, T^{*} < T_c \\ d_t^{*} = d_{et}^{*} \quad for\, T^{*} \geq T_c \end{gathered} \tag{5.13}$$

where T_c is the corner period where the spectrum changes from the constant acceleration segment to the constant velocity segment, and R_μ can be determined as the ratio between the accelerations corresponding to the elastic and inelastic systems.

$$R_\mu = \frac{S_a\left(T^{*}\right)m^{*}}{F_y^{*}} \tag{5.14}$$

As the properties of the equivalent SDOF system depend on the d_t^*selected, an iterative procedure is also required if the d_t^* obtained differs greatly from the value estimated for the determination of the idealized elastic-perfectly plastic capacity curve.

Table 5.4 summarizes the predictions of the N2 method, and compares them with the experimental results obtained for the test with PGA=0.31g, 0.62g, 0.94g and 1.1g. A view of the idealized capacity curve and target displacement predicted in the last step of the iterative process can be seen in Figure 5.17.

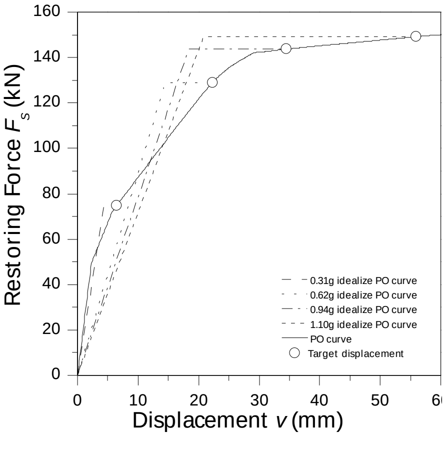

Figure 5.17.: N2 method idealized capacity curve and target displacement (specimen FSD).

	PGA 0.31g		PGA 0.62g		PGA 0.94g		PGA 1.10g	
	N2	Test	N2	Test	N2	Test	N2	Test
T_e (s)	0.13	0.16	0.18	0.16	0.19	0.17	0.19	0.17
S_a (m/s^2)	10.8	-	19.3	-	23.0	-	27.0	-
δ_t (mm)	6.4	8.7	22.3	15.45	34.5	23.3	55.9	29.4
$F_{S,max}$ (kN)	74.5	79.8	128.8	108.6	143.9	132.8	149.2	139.5

Table 5.4.: N2 method results for specimen FSD

5.3.4. Comparison of three NSPs

Figure 5.18 shows the error coefficient C_d (=prediction/test) of each NSP in predicting the maximum displacement (Figure 5.18a), and the maximum base shear (Figure 5.18b). Under the low intensity earthquake corresponding toPGA=0.31 g, the structure with FSD dampers behaved at an “immediate occupancy” structural performance level. For this performance level, the prediction given by all NSPs underestimated the maximum displacement and the maximum base shear. C_d ranged from 0.51 (for CSM) to 0.73 (for N2) in the case of the maximum displacement, and from 0.80 (for CSM) to 0.93 (for N2) for the maximum base shear. The method N2 provided the best approximation and the CSM method the worst.

For the medium intensity earthquake corresponding to PGA=0.62 g, the structural performance level observed was “life safety”. For this performance level, the prediction given by the CSM clearly underestimated the maximum displacement (C_d = 0.58) and the maximum base shear (C_d = 0.76). The prediction of the DCM was very close to the test results (C_d = 1.14 for the maximum displacement and C_d = 1.05 for the maximum shear force), while that provided by the N2 method overestimated the response in terms of maximum displacement (C_d = 1.44) and was close to the test results (C_d = 1.19) for the maximum shear force.

Under the high intensity earthquake corresponding to PGA=0.94 g, the structure exhibited a “limited safety range” performance level. Similarly to the “life safety” level, in this case the CSM underestimated both the maximum displacement (C_d = 0.47) and the maximum base shear (C_d = 0.69), while the DCM predicted both parameters of the experimental response (C_d= 1.07 for the maximum displacement and C_d = 1.02 for the maximum base shear). The N2 method overestimated the response for the maximum displacement (C_d = 1.48), but provided a good approximation for the maximum base shear (C_d = 1.08).

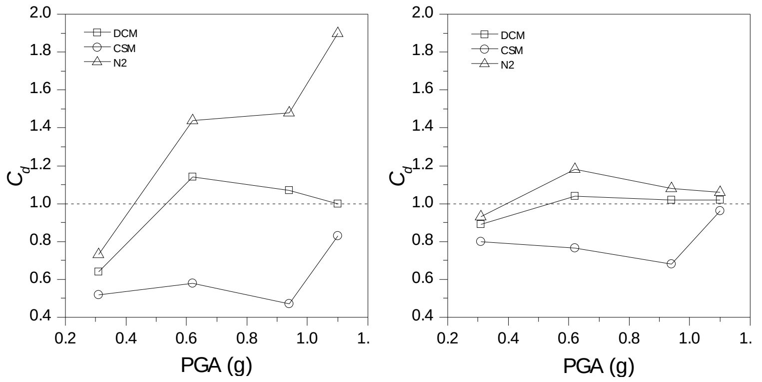

(a) C_d for maximum displacement (b) C_d for maximum base shear

Figure 5.18.: Error coeficients C_d of NSPs

5.4. Summary and conclusions.

In this study, the response in terms of maximum displacement and maximum base shear of a structure equipped with hysteretic dampers was obtained experimentally through shaking table tests. The response was obtained for three levels of structural performance ("immediate occupancy", "life safety" and "limited safety range") associated with earthquakes having peak ground accelerations (PGA) of 0.31, 0.62 and 0.94 g, respectively. The response was compared with the prediction provided by three different Non-linear Static Procedures (NSPs): the improved versions of the Capacity Spectrum Method (CSM) and of the Displacement Coefficient Method (DCM) from FEMA-440, and the N2 Method from Eurocode 8. It was found that for the three levels of structural performance, the CSM provided the worst (underestimated) prediction, with errors ranging from 0.47 to 0.58 for the maximum displacement, and from 0.69 to 0.80 for the maximum base shear. In contrast, the DCM method predicted values close to the experimental results, especially for PGA=0.62 g and PGA=0.94 g, with errors ranging from 0.64 to 1.14 for themaximum displacement, and from 0.89 to 1.05 for the maximum base shear. The N2 method also provided reasonably good results, and proved better in predicting the maximum base shear (errors ranging from 0.93 to 1.19) than in the prediction of maximum displacement (errors ranging from 0.73 to 1.48). Any one of the methods investigated (CSM, DCM and N2) can reproduce with satisfactory accuracy the whole range of responses obtained experimentally for the different seismic simulations. Different adjustments of the parameters involved in each method would have led to other conclusions; in this study the parameters were adjusted as determined by each method, according to the corresponding standards and codes. Finally, it is worth noting that there are further limitations that must be taken into account when using these methods, such as the cumulative damage effects.

6. Summary and conclusions.

The field observations after recent earthquakes and the research during the last two decades in earthquake engineering have led both the scientific and professional community towards a design philosophy based on the performance of the structures against earthquakes rather than on their strength. But there are still some uncertainties to be addressed before it can be trustfully applied as: the knowledge about strength, deformations and energy dissipation capacities of the structural elements under cyclic loading, and particularly when acting in two ortogonal directions simultaneously; the identification and quantification of the engineering demand parameters to define damage in structural elements; and the evaluation of the design and checking methodologies based on the performance of the structures. This thesis contributes to a better understanding of the seismic performance and design of new RC framed structures designed with conventional and innovative solutions. The research carried out for this thesis is based on the results of an experimental approach consisting on shaking table tests and quasi-static tests done at the University of Granada and Purdue University respectively. And the results of a numerical approach consisting of nonlinear static and dynamic time history analyses with refined Finite Element Models.

This thesis was organized in 6 independent chapters aimed for four objetives. Chapter 1 presents the introduction and objectives of the thesis. Chapter 2 investigates the seismic performance of a conventional “strong column-weak beam” RC bare frame structure through shaking table tests. Chapter 3 addresses another type of conventional seismic resistant structure: the RC frames with RC ductile walls. In this type of mixed structures the seismic loading is sustained mainly by the RC ductile wall that governs the seismic response. Consequently chapter 3 is focussed on investigating through quasi-static cyclic tests the hysteretic response of the RC ductile walls isolated from the whole structure (i.e. without considering the interaction between RC frame and RC walls). The hysteretic response of the RC ductile wall is compared with that of the hysteretic dampers, and it is concluded the superiority of the later. Accordingly, this thesis goes on the use of hysteretic dampers instead of RC ductile walls for combining with RC frames. Chapter 4 investigates the seismic performance of RC frames with hysteretic dampers (including the interaction effects) through numerical simulations. Its performance is compared to that of the conventional RC bare frame. It is worth noting that for the RC frame with hysteretic dampers the condition of developing a strong column-weak beam collapse mechanism was not imposed. The consecuence is additional cost savings for the RC frame. To take advantage of the innovative systems consisting on RC frames with hysteretic dampers, and make possible its use in the context of the current average level of knowledge of designer not specialized in seismic desing, it is necessary to address another important aspect: how to design these innovative systems with the conventional design methods and tools nowadays included in many codes. This wholes issue is addressed in chapter 5. Chapter 5 evaluates and compares the accuracy of three common non-linear static procedures already introduced in seismic guidelines and codes in the prediction of the response of structures with hysteretic dampers. The procedures considered are: (1) the improved version of the Capacity Spectrum Method (CSM) from FEMA 440; (2) the improved version of the Displacement Coefficient Method (DCM) from FEMA 440; and (3) the N2 Method implemented in Eurocode 8. Finally, Chapter 6 presents a summary of the main conclussions and future research. The content and main conclusions of this research are outlined below. These conclusions are presented in more detail at the end of each Chapter.

1. Four shake-table tests (refered to as seismic simulations hereafter) were conducted on a 2/5-scale reinforced concrete frame designed with the strong column-weak beam philosophy and capacity design criteria. The structure was designed to meet the requirements of the current building seismic code of Spain, for a building located at the city of Granada. The seismic hazard level of each seismic simulation represented, according to the SEAOC, the "very frequent", "frequent", "rare" and "very rare" ground motions at the city of Granada. The response of the structure evaluated in terms of several engineering demand parameters and damage indexes revealed that the structure behaved with the following structural performance levels: within "immediate occupancy" and "life safety" for the "frequent earthquake"; "life safety" level for the "rare earthquake" and “collapse” for the “very rare” event. The RC bare frame tested performed basically as expected by the seismic code NCSE-02, for the "rare" earthquake (associated with a return period of about 500 years). However, the structure collapsed under the "very rare" or "maximum expected" ground motion. A study of the local response in terms of chord rotations at plastic hinge level of the structural elements suggests that Eurocode 8 formula produces very good estimates on ultimate chord rotation capacities of RC beams and columns under cyclic loading. The Park and Ang’s damage index has proved a very effective damage index to predict the collapse of RC elements subjected to bending.

2. Two large-scale RC ductile structural walls were tested through quasi-static tests to investigate their hysteretic response and compare it to that of hysteretic dampers. Both walls were identical except that one of the walls had confinement reinforcement in the boundary elements. The results of the tests have shown that both walls had almost equal lateral strength, while the wall with confinement reinforcement had a greater displacement and energy dissipation capacity. The analysis of the normal strains distributions reveals that the height in which the inelastic deformations spreaded was very different for the tension and compression sides. The comparison of the hysteretic behaviors of the RC ductile wall with and a hysteretic damper with equal strength and initial stiffness, subjected to the same history of loading, shows that the seismic performance of the hysteretic dampers is better than that of the RC ductile wall. It is found that the hysteretic damper can dissipate an amount of plastic strain energy 4 to 20 times higher than a RC ductile wall. The maximum plastic deformation capacity of the dampers are found to be up to 10 times larger that that of the RC walls.

3. The seismic performance of two different seismic-resistant systems, the conventional RC bare

frame and the RC frame with hysteretic dampers, was investigated through numerical simulations (nonlinear time history analyses NTH). Two sets of prototypes of 3 and 6 storeys were considered. The first group of prototypes were RC bare frames designed to develop a strong column-weak beam collapse mechanism under seismic loading. The second group were RC frames designed only to resist gravitational loads and were eqquiped with hysteretic dampers. Both groups of prototypes were designed to meet the same reference base shear Q_{y1} which value was that required for a conventional RC frame designed according to Spanish seismic code NCSE-02, to resist the 500 year return period earthquake expected at the city of Granada. The results of this nonlinear time history analysis are compared at global storey level and local plastic hinge level. At global level, the comparison was done in terms of the inter-storey drift, id, and the cumulative inelastic deformation ratio, η. At local plastic hinge level the comparison was done in terms of the chord rotation demand, the Darwing and Nmai Di energy based damage index and the well known Park and Ang $DI_{P\&A}$ damage index. On the basis of the outcomes from the non-linear time history analyses it can be concluded that the innovative system consisting on RC frames with hysteretic dampers presented a much better seismic performance in terms of reduction of the damage in the gravitational load resisting system, reduction of lateral drifts, and greater energy dissipation efficiency. The results of the NTH analyses, in terms of chord rotation demand, Di and $DI_{P\&A}$, were also compared with the experimental results of Chapter 2 for the same seismic hazard level. A good correlation was found between the numerical and experimental results.

4. The response in terms of maximum displacement and maximum base shear of a structure equipped with hysteretic dampers tested in a shaking table was predicted using three well known non-linear static procedures included in current seismic guidelines and codes (NSPs): the improved versions of the Capacity Spectrum Method (CSM) and of the Displacement Coefficient Method (DCM) from FEMA-440, and the N2 Method from Eurocode-8. The response was obtained for three levels of structural performance (“immediate occupancy”, “life safety” and “limited safety range”). A comparison between the prediction given by the three methods and the experimental results shows that all of them can give an acceptable prediction of the maximum response of the structure with hysteretic dampers. However the CSM clearly underestimated the maximum response while the DCM and N2 overestimated it.

Future lines of research.

During the development of this thesis the following issues were found worthy of a deeper research:

Investigate energy-based procedures to design RC structures, that could be included in future seismic codes, based on the seismic performance of the structural elements obtained trough static and dynamic tests.

Investigate the diverse components that characterize deformations of structural walls and its relation with the main strains measured experimentally.

Compare the seismic performance of the frame-damper and frame-wall mixed “stiff-flexible” structures.

Compare the prediction given by the three NSPs studied in chapter 5 with the experimental results of the “strong column-weak beam” structure studied in chapter 2.

References

[1] Perry Adebar, Ahmed M M Ibrahim, and Michael Bryson. Test of High-Rise Core Wall : Effective Stiffness for Seismic Analysis. *ACI Structural Journal*, 104(5), 2007.

[2] Hiroshi Akiyama. *Earthquake-Resistant Limit-State Design for Buildings.* University of Tokyo Press, 1980.

[3] Hiroshi Akiyama. *Earthquake-resistant limit-state design for buildings.* University of Tokyo Press, 1985.

[4] Hiroshi Akiyama and Ryosuke Takahashi. Influence of Bauschinger effect on seismic resistance of steel structures. *Journal of Structural and Construction Engineering, Transactions of the Architectural Institute of Japan*, 418:49–57, 1990.

[5] American Concrete Institute. *318-11: Building Code Requirements for Structural Concrete and Commentary.* 2011.

[6] Applied Technology Council. ATC-40 Seismic evaluation and retrofit of concrete buildings. Technical report, 1996.

[7] Applied Technology Council. FEMA P695 Quantification of Building Seismic Performance Factors. Technical Report June, Federal Emergency Management Agency FEMA, Redwood City, 2009.

[8] ATC. *FEMA-445: Next-Generation Performance-Based Seismic Design Guidelines.* Number August. 2006.

[9] Sungjin Bae and Bayrak Oguzhan. Plastic hinge length of reinforced concrete columns. *ACI Structural Journal*, (105), 2008.

[10] O Bayrak. Plastic hinge analysis. *Journal of Structural Engineering*, (September), 2001.

[11] Amadeo Benavent-Climent. An energy-based damage model for seismic response of steel structures. *Earthquake Engineering & Structural Dynamics*, 36:1049–1064, 2007.

[12] Amadeo Benavent-Climent. Reinforced Concrete Exterior Waffle Flat Plate-Column Connections Subjected to Lateral Earthquake Loading. *Journal of Earthquake Engineering*, 13(3):275–292, March 2009.

[13] Amadeo Benavent-Climent. An energy-based method for seismic retrofit of existing frames using hysteretic dampers. *Soil Dynamics and Earthquake Engineering*, 31(10):1385–1396, October 2011.

[14] Amadeo Benavent-Climent, X Cahis, and A Catalan. Seismic behavior of interior connections

in existing waffle-flat-plate structures. *Engineering Structures*, 30(9):2510–2516, September 2008.

[15] Amadeo Benavent-Climent, Leandro Morillas, and Juan M Vico. A study on using wide-flange section web under out-of-plane flexure for passive energy dissipation. *Earthquake Engineering & Structural Dynamics*, 40(July 2010):473–490, 2011.

[16] Amadeo Benavent-Climent, Lluis G. Pujades, and Francisco Lopez-Almansa. Design energy input spectra for moderate-seismicity regions. *Earthquake Engineering & Structural Dynamics*, 31(5):1151–1172, May 2002.

[17] Amadeo Benavent-Climent and R. Zahran. An energy-based procedure for the assessment of seismic capacity of existing frames: Application to RC wide beam systems in Spain. *Soil Dynamics and Earthquake Engineering*, 30(5):354–367, May 2010.

[18] Evan Bentz and Michael P Collins. Response-2000. Technical report, University of Toronto, Toronto, 2001.

[19] Dionisio Bernal. Viscous Damping in Inelastic Structural Response. *Journal of Structural Engineering*, 120(4):1240–1254, 1993.

[20] Alfredo Bohl and Adebar Perry. Plastic hinge lengths in high-rise concrete shear walls. *ACI Structural Journal*, 108(2):148–157, 2011.

[21] Melina Bosco, Aurelio Ghersi, and Edoardo M Marino. On the evaluation of seismic response of structures by nonlinear static methods. *Earthquake Engineering & Structural Dynamics*, 38:1465–1482, 2009.

[22] NH Burns and CP Siess. Load-deformation characteristics of beam-colun connections in Reinforced Concrete. Technical report, University of Illinois, Urbana, Illinois, 1962.

[23] Donatello Cardone. Nonlinear Static Methods vs. Experimental Shaking Table Test Results. *Journal of Earthquake Engineering*, 11(6):847–875, November 2007.

[24] Anthol J Carr. damping models for inelastic analisis. *Asia-Pacific Vibration Conference, Kyongju, Korea*, 1997.

[25] Athol J Carr. *Ruaumoko Manual - Theory*, volume 1. University of Canrtebury, Christchurch, New Zealand, 2007.

[26] Mehmed Causevic and Sasa Mitrovic. Comparison between non-linear dynamic and static seismic analysis of structures according to European and US provisions. *Bulletin of Earthquake Engineering*, 9(2):467–489, July 2010.

[27] Finley A Charney. Unintended Consequences of Modeling Damping in Structures. *Journal of Structural Engineering*, 134(4, April):581–592, 2008.

[28] Anil K Chopra. *Dynamics of Structures Theory and Applications to Earthquake Engineering.* PEARSON Prentice Hall, 2007.

[29] Anil K Chopra and Rakesh K. Goel. Direct Displacement-Based Design: Use of Inelastic vs. Elastic Design Spectra. *Earthquake Spectra*, 17(1):47–64, 2001.

[30] Chung-Che Chou and Chia-Ming Uang. A procedure for evaluating seismic energy demand of framed structures. *Earthquake Engineering & Structural Dynamics*, 32(2):229–244, February 2003.

[31] M C Constantinou and M D Symans. Seismic Response of Structures with Sumplental Damping. *the structural Design of tall and special buildings*, 2(January):77–92, 1993.

[32] Edoardo Cosenza and Gaetano Manfredi. The improvement of the seismic-resistant design for existing and new structures using damage criteria. In Peter Fajfar and Helmut Krawinkler, editors, *Seismic Design Methodologies for the Next Generation of Codes*, pages 119–130. Balkema, Rotterdam, 1997.

[33] David Darwin and Charles K Nmai. Energy dissipation in RC beams under cyclic load. *Journal of Structural Engineering*, 112(8), 1986.

[34] Alessandro Dazio, Katrin Beyer, and Hugo Bachmann. Quasi-static cyclic tests and plastic hinge analysis of RC structural walls. *Engineering Structures*, 31(7):1556–1571, July 2009.

[35] Ministerio de Fomento. *Norma de Construción Sismorresistente: Parte general y edificación (NSCE-02).* 2004.

[36] Ministerio de la Vivienda. *Código Técnico de la Edificación (CTE).* 2009.

[37] Rajesh P Dhakal and Richard C Fenwick. Detailing of Plastic Hinges in Seismic Design of Concrete Structures. *Aci Structural Journal*, (105), 2009.

[38] European Committee for Standardization. *Eurocode 8: Design of structures for earthquake resistance. Part 1: General rules, seismic actions and rules for buildings.* Brussels, 2003.

[39] European Committee for Standardization. Eurocode 8 Design of structures for earthquake resistance - Part 3 : Assessment and retrofitting of buildings European Standard EN 1998-3:2005. Technical report, European Committee for Standardization, Brussels, 2005.

[40] Peter Fajfar. A Nonlinear Analysis Method for Performance Based Seismic Design. *Earthquake Spectra*, 16(3):573–592, 2000.

[41] Peter Fajfar and Peter Gaspersic. The N2 method for the seismic damage Analysis of RC Buildings. *Earthquake Engineering & Structural Dynamics*, 25:31–46, 1996.

[42] Michael N Fardis. Concrete members under cyclic loading. In *Seismic design, Assesment and REtrofitting os Concre Buildings. Based on EN-Eurocode 8*, chapter 2. Springer, 2009.

[43] Federal Emergency Management Agency (FEMA). *FEMA 273: NEHRP GUIDELINES FOR THE SEISMIC REHABILITATION OF BUILDINGS.* 1997.

[44] Federal Emergency Management Agency (FEMA). *FEMA 274: NEHRP COMMENTARY ON THE GUIDELINES FOR THE SEISMIC REHABILITATION OF BUILDINGS.* 1997.

[45] Federal Emergency Management Agency (FEMA). *FEMA 356: Prestandard and commentary for the seismic rehabilitation of buildings.* Number November. Washington DC, 2000.

[46] Federal Emergency Management Agency (FEMA). *FEMA 440: Improvement of Nonlinear Static Seismic Analysis Procedures.* Number June. 2005.

[47] M Fragiacomo, C Amadio, and S Rajgelj. Evaluation of the structural response under seismic actions using non-linear static methods. *Earthquake Engineering & Structural Dynamics*, 35:1511–1531, 2006.

[48] S Freeman. The capacity spectrum method as a tool for seismic design. In *Proceedings of the 11th European Conference on Earthquake Engineering*, Paris.

[49] John F. Hall. Problems encountered from the use (or misuse) of Rayleigh damping. *Earthquake Engineering & Structural Dynamics*, 35(5):525–545, April 2006.

[50] Harry G Harris and Gajanan M Sabnis. *Structural modelling and experimental techniques.* CRC Press, 2nd edition, 1999.

[51] George W. Housner. Limit Design of Structures to Resist Earthquakes. In *First World Conference on Earthquake Engineering*, Berkeley, 1956.

[52] Kazuo Inoue and Susumu Kuwahara. Optimum strength ratio of hysteretic damper. *Earthquake Engineering & Structural Dynamics*, 27(6):577–588, June 1998.

[53] Ben Kato, Hiroshi Akiyama, and H Yamanouchi. *Predictable properties of material under incremental cyclic loading.* IABSE, Preliminary Publication, Lisbon, 1973.

[54] Simon Kim and Enzo D'Amore. Push-over Analysis Procedure in Earthquake Engineering. *Earthquake Spectra*, 15(3):417–434, 1999.

[55] Helmut Krawinkler and G.D.P.K. Seneviratna. Pros and cons of a pushover analysis of seismic performance evaluation. *Engineering Structures*, 20(4-6):452–464, April 1998.

[56] Sutat Leelataviwat, Subhash C Goel, and Bozidar Stojadinovic. Energy-based Seismic Design of Structures using Yield Mechanism and Target Drift. *Journal of Structural Engineering*, (August):1046–1054, 2002.

[57] Sutat Leelataviwat, Winai Saewon, and Subhash C Goel. Application of Energy Balance Concept in Seismic Evaluation of Structures. *Journal of Structural Engineering*, 135(2):113–121, 2009.

[58] Yu-Yuan Lin, Kuo-Chun Chang, and Yuan-Li Wang. Comparison of displacement coefficient method and capacity spectrum method with experimental results of RC columns. *Earthquake Engineering & Structural Dynamics*, 33(1):35–48, January 2004.

[59] K. Maekawa, H. Okamura, and A. Pimanmas. *Non-Linear Mechanics of Reinforced Concrete.* Taylor & Francis, 2003.

[60] K Matsumura. On the intensity measure of strong motions related to structural failures. In *10 World Conference on Earthquake engineering*, Balkema, Rotterdam, 1992.

[61] HM McCollister, CP Siess, and NM Newmark. Load-deformation characteristics of simulated beam column connections in reinforced concrete. Technical report, University of Illinois, Urbana, Illinois, 1954.

[62] M Menegotto and E Pinto. Method of analysis for cyclically loaded reinforced concrete plane frames including changes in geometry and non-elastic behavior of elements under combined normal force and bending. In *IABSE Symposium*, Lisbon,Portugal, 1973.

[63] Ministry of Land Infrastructure Transport Tourism. *BSL 2009 The Building Standard Law of Japan.* Tokyo, 2009.

[64] E Miranda. *Seismic Upgrading and evaluation of existing buildings.* PhD thesis, University os California, Berkeley, 1991.

[65] Jack Moehle and Gregory G Deierlein. A framework Methodology for Performance-Based Eartquake Engineering. In *13 th World Conference on Earthquake Engineering*, number 679, 2004.

[66] Jack P Moehle. Displacement design approach for reinforced concrete structures subjected to earthquakes. *Earthquake Spectra*, 8(3), 1992.

[67] Jack P Moehle. Displacement-based seismic design criteria. In *Eleventh World conference on Earthquake Engineering*, Mexico, 1996. Elsevier Science Ltd.

[68] T. B. Panagiotakos and M. N. Fardis. A displacement-based seismic design procedure for RC buildings and comparison with EC8. *Earthquake Engineering & Structural Dynamics*, 30(10):1439–1462, October 2001.

[69] Honggun Park and Taesung Eom. A simplified Method for Estimating the Amount of Energy Dissipated by Flexure Dominated Reinforced Concrete Members fo Moderate Cyclic Deformations. *Earthquake Spectra*, 22(2):459, 2006.

[70] Young-ji Park and Alfredo H Ang. Seismic Damage analysis and damage limiting design of RC buildings. Technical Report October 1984, University of illinois, Urbana, 1984.

[71] Young-ji Park and Alfredo H Ang. Mechanistic seismic damage model for reinforced concrete. *Journal of Structural Engineering*, 111(4):722–739, 1985.

[72] K Pilakoutas and A S Elnashai. Cyclic Behavior of Reinforced Concrete Cantilever Walls , Part II : Discussions and Theoretical Comparisons. *Aci Structural Journal*, (92):425–433, 1995.

[73] Kypros Pilakoutas and Arm Elnashai. Cyclic Behaviour of Reinforced Concrete Cantilever Walls, PartI: Experimental Results. *Aci Structural Journal*, 92(3):271–281, 1995.

[74] Marco Preti and Ezio Giuriani. Ductility of a Structural Wall with Spread Rebars Tested in Full Scale. *Journal of Earthquake Engineering*, 15(8):1238–1259, December 2011.

[75] M J N Priestley, D N Grant, and C A Blandon. Direct displacement-based seismic design. In *2005 NZSEE Conference*, number 33, 2005.

[76] M.J.N. Priestly, G. M. Calvi, and Mervyn J Kowalsky. *Displacement-Based Design Of Structures.* IUSS Press, Pavia, Italy, 2007.

[77] M.J.N. Priestly and R. Park. Strength and Ductility of Concrete Bridge Columns Under Seismic Loading. *Aci Structural Journal*, January-Fe:61–76, 1987.

[78] Thomas N Salonikios, Andreas J Kappos, Ioannis A Tegos, and Georgios G Penelis. Cyclic Load Behavior of Low-Slenderness Reinforced Concrete Walls : Design Basis and Test Results. (96):649–661, 2000.

[79] S.A. Sheikh and S.S. Khoury. Confined concrete columns with stubs. *ACI Structural Journal*, 90:414–414, 1993.

[80] K Shimazaki and M A Sozen. Seismic Drift of Reinforced Concrete Structures. Technical report, Hazama-Gumi Ltd, Tokyo, Japan, 1984.

[81] Niels Shome. *Probabilistic Seismic Demand Analysis of Nonlinear Structures.* PhD thesis, Stanford University, 1999.

[82] T.T. Soong and G.F. Dargush. *Passive Energy Dissipation Systems in Structural Engineering.* New York, 1997.

[83] Enrico Spacone, Filip C Filippou, and Fabio F Taucer. Fibre Beam-Column Model for Non-Linear Analysis of R/C Frames: Part I. Formulation. *Earthquake Engineering & Structural Dynamics*, 25:727–742, 1996.

[84] Enrico Spacone, Filip C Filippou, and Fabio F Taucer. Fibre Beam-Column Model for Non-Linear Analysis of R/C Frames: Part I. Formulation. *Earthquake Engineering & Structural Dynamics*, 25:771–725, 1996.

[85] Structural Engineers Association of California & Vision 2000 Commitee. Performance Based Seismic Engineering of Buildings. Technical report, California Office of Emergency Services, Sacramento, CA, 1995.

[86] Haluk Sucuoglu and Bora Acun. Energy Dissipation Capacity of Reinforced Concrete Columns under Cyclic Displacements. *Aci Structural Journal*, 109(July-August):531–540, 2012.

[87] Haluk Sucuoglu and Altug Erberik. Energy-based hysteresis and damage models for deteriorating systems. *Earthquake Engineering & Structural Dynamics*, 33(1):69–88, January 2004.

[88] Adang Surahman. Earthquake-resistant structural design through energy demand and capacity. *Earthquake Engineering & Structural Dynamics*, 36:2099–2117, 2007.

[89] M D Symans, A M Asce, F A Charney, F Asce, A S Whittaker, M Asce, M C Constantinou, C A Kircher, M W Johnson, and R J Mcnamara. Energy Dissipation Systems for Seismic Applications : Current Practice and Recent Developments. *Journal of Structural Engineering*, (January):3–21, 2008.

[90] S Takahashi. Flexural drift capacity of reinforced concrete walls which fails in flexural compression failure. In *13th Taiwan-Japan-Korea Joint Seminar on Earthquake Engineering for Building Structures*, 2011.

[91] Amador Teran-Gilmore. *Performance-Based Earthquake-Resistant Design of Framed Buildings Using Energy Concepts.* PhD thesis, University of California at Berkeley, 1996.

[92] Amador Teran-Gilmore, Esmeralda Avila, and Gilberto Rangel. On the use of plastic energy to establish strength requirements in ductile structures. *Engineering Structures*, 25(7):965–980, June 2003.

[93] John H Thomsen and John W Wallace. Displacement-Based Design of Slender Reinforced Concrete Structural Walls - Experimental Verification. *Journal of Structural Engineering*, 130(4), 2004.

[94] Chia-Ming Uang and Vitelmo V Bertero. Evaluation of Seismic Energy in Structures. *Earthquake Engineering & Structural Dynamics*, 19(77), 1990.

[95] RE Valles, AM Reinhorn, Sashi K. Kunnath, C Li, and A Madan. A Program for the Inelastic Damage Analysis of Buildings. Technical report, State University of New York at Buffalo, Buffalo, NY, 1996.

[96] Tomaz Vidic, Peter Fajfar, and Matej Fischinger. Consistent Inelastic Design Spectra: Strength and Displacement.

[97] John W Wallace and Jack P Moehle. Ductility and detailing requirements of bearing w all buildings. *Journal of Structural Engineering*, 118(6):1625–1644, 1992.

[98] John W Wallace and Kutay Orakcal. ACI 318-99 Provisions for Seismic Design of Structural Walls. *Aci Structural Journal*, 4(99):499–508, 2002.

[99] R Yamashiro and C P Siess. Moment-rotation characteristics of ceinforced concrete members subjected to bending shear and axial load. Technical report, University of Illinois, Urbana, Illinois, 1962.

[100] T. Y. Yang, Bozidar Stojadinovic, and Jack Moehle. Demonstration of a Practical Method for Seismic Performance Assessment of Structural Systems. *Earthquake Spectra*, 28(2):811–829, May 2012.

[101] TY Yang, Jack P Moehle, and Bodizar Stojandinovic. Performance Evaluation of Innovative Steel Braced Frames Performance Evaluation of Innovative Steel Braced Frames. Technical Report August, Pacific Earthquale Engineering Research Center, University of California, Berkeley, 2009.

[102] Farzin Zareian and Ricardo a. Medina. A practical method for proper modeling of structural damping in inelastic plane structural systems. *Computers & Structures*, 88:45–53, January 2010.

A. Earthquakes

A.1. El centro.

Earthquake	Station	Magnitud	Epicentral distance (km)	Fault distance (km)
El centro	Imperial Co.	6.6	27.6	-

Table A.1.: Seismological parameters

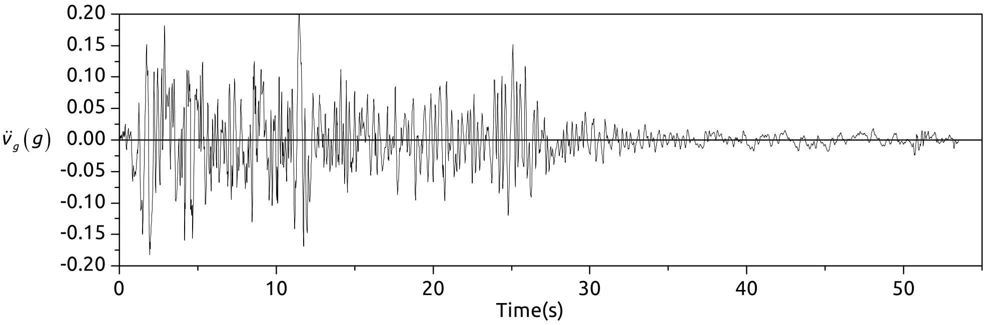

Figure A.1.: History of accelerations

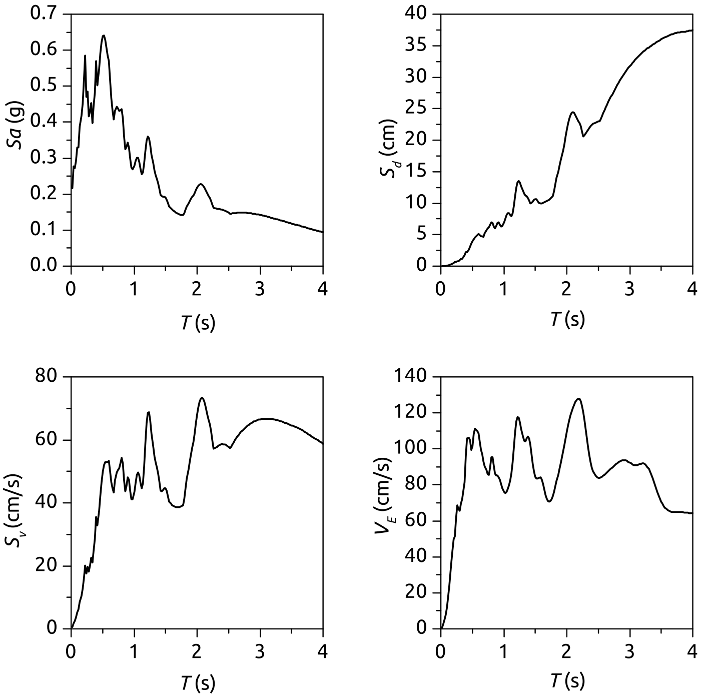

Figure A.2.: Elastic response spectra

A.2. Tolmezzo

Earthquake	Station	Magnitud	Epicentral distance (km)	Fault distance (km)
Friuli	Tolmezzo- Diga Ambiesta	6.5	23	7

Table A.2.: Seismological parameters

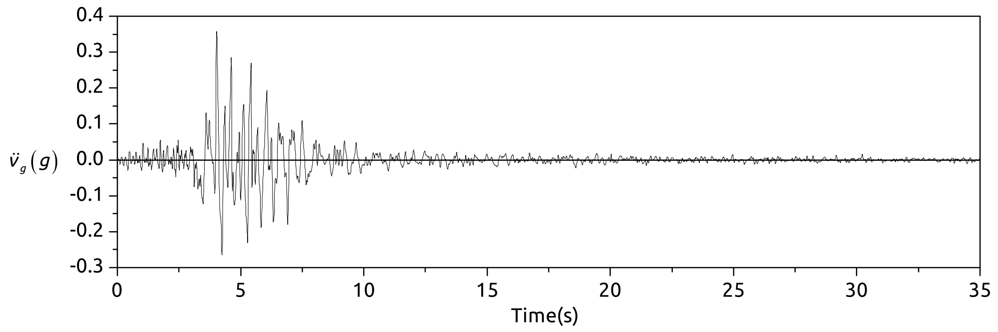

Figure A.3.: History of accelerations

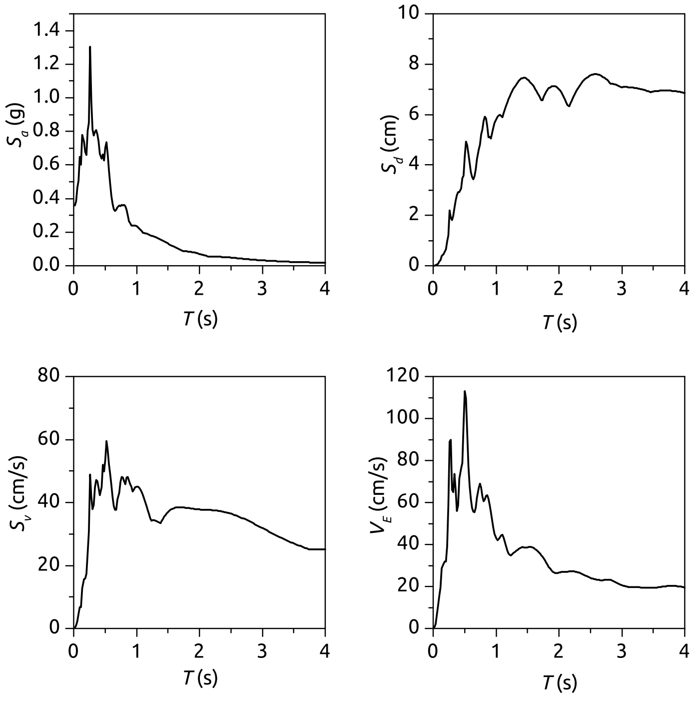

Figure A.4.: Elastic response spectra

A.3. Kobe.

Earthquake	Station	Magnitud	Epicentral distance (km)	Fault distance (km)
Kobe	KJMA	6.9	25.6	1

Table A.3.: Seismological parameters

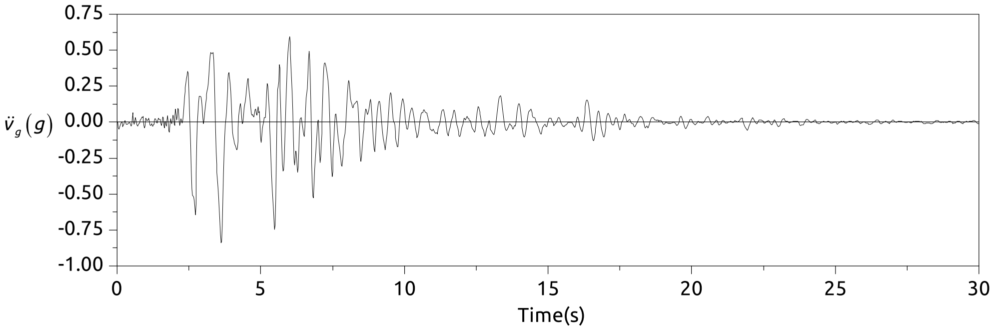

Figure A.5.: History of accelerations

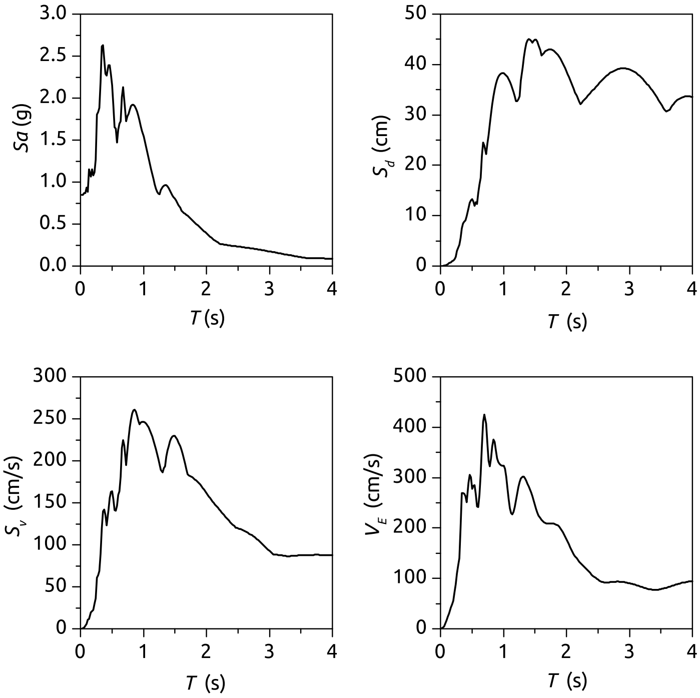

Figure A.6.: Elastic response spectra

A.4. Korinthos.

Earthquake	Station	Magnitud	Epicentral distance (km)	Fault distance (km)
Alkion	Korinthos-OTE Building	6.6	20	10

Table A.4.: Seismological parameters

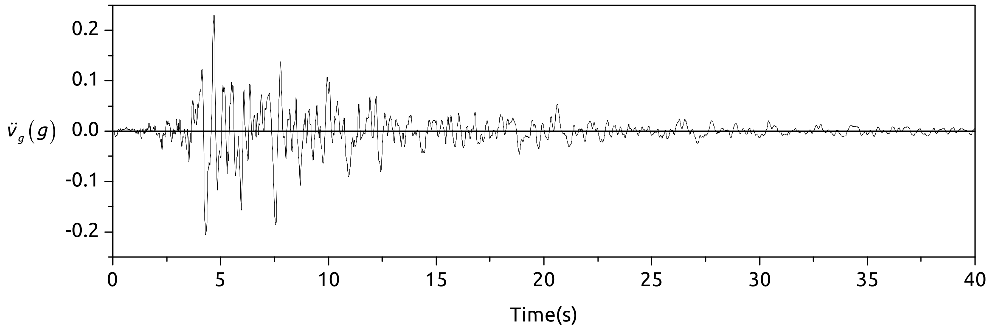

Figure A.7.: History of accelerations

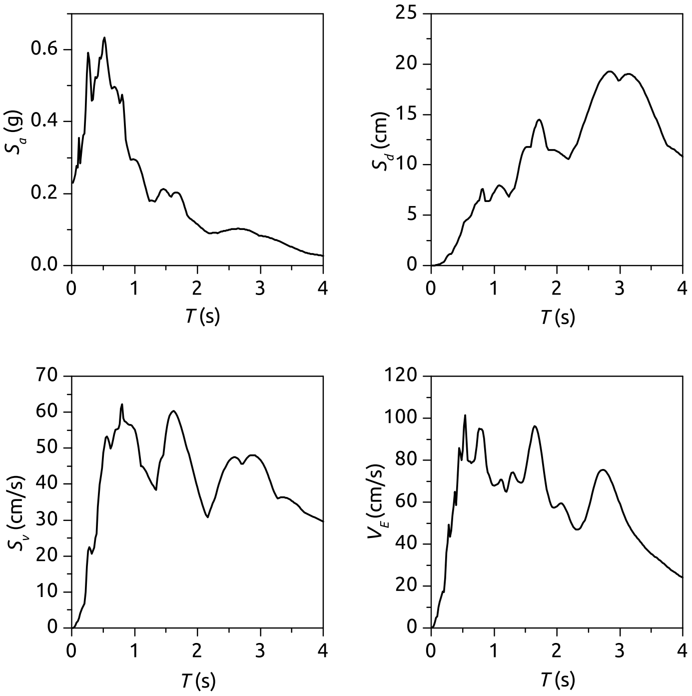

Figure A.8.: Elastic response spectra

A.5. Taft.

Earthquake	Station	Magnitud	Epicentral distance (km)	Fault distance (km)
Kern County	Taft Linncoln School Tunnel	7.5	46.4	-

Table A.5.: Seismological parameters

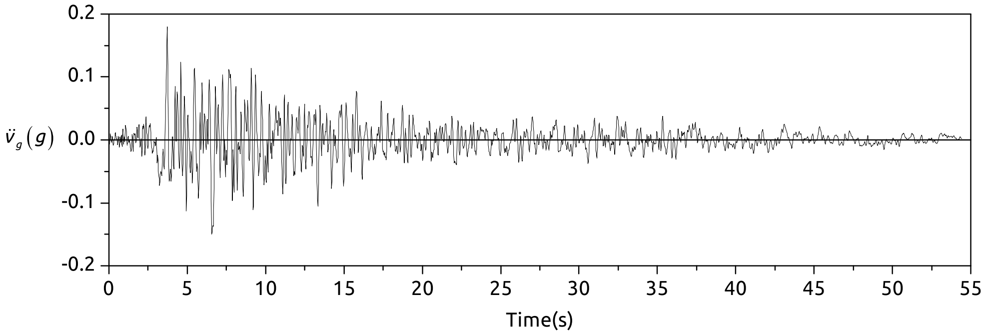

Figure A.9.: History of accelerations

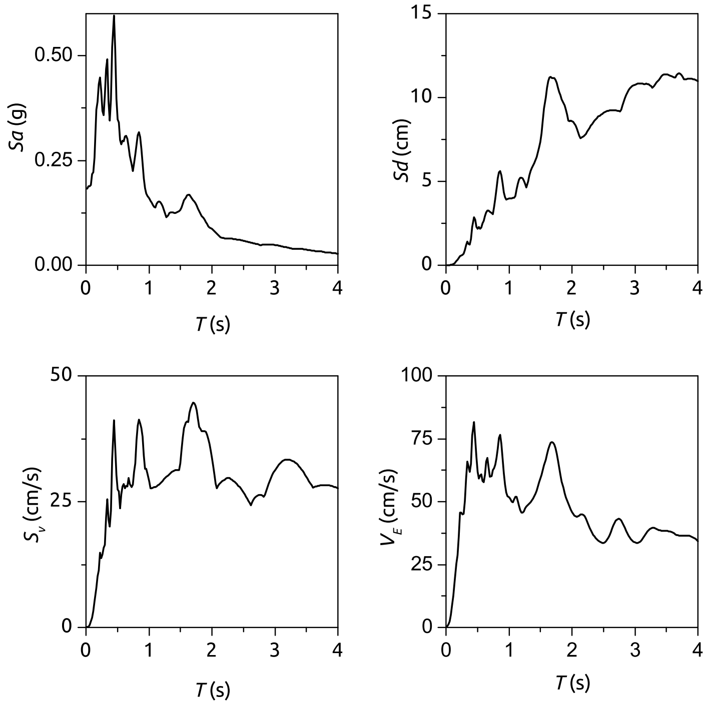

Figure A.10.: Elastic response spectra

A.6. Petrovac.

Earthquake	Station	Magnitud	Epicentral distance (km)	Fault distance (km)
Montenegro	Petrovac-hotel Oliva	6.9	25	3

Table A.6.: Seismological parameters

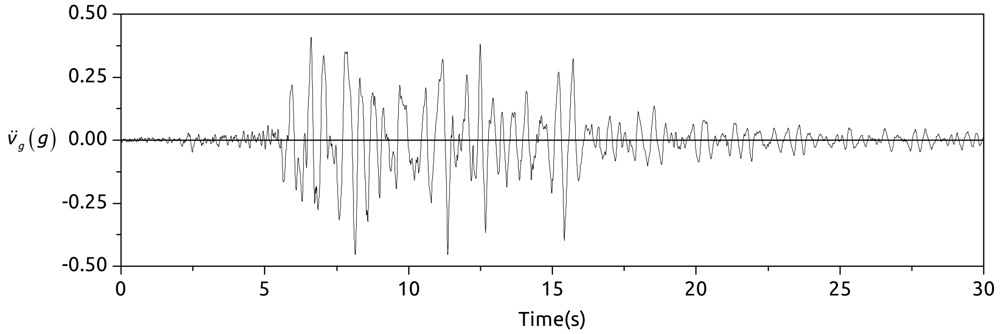

Figure A.11.: History of accelerations

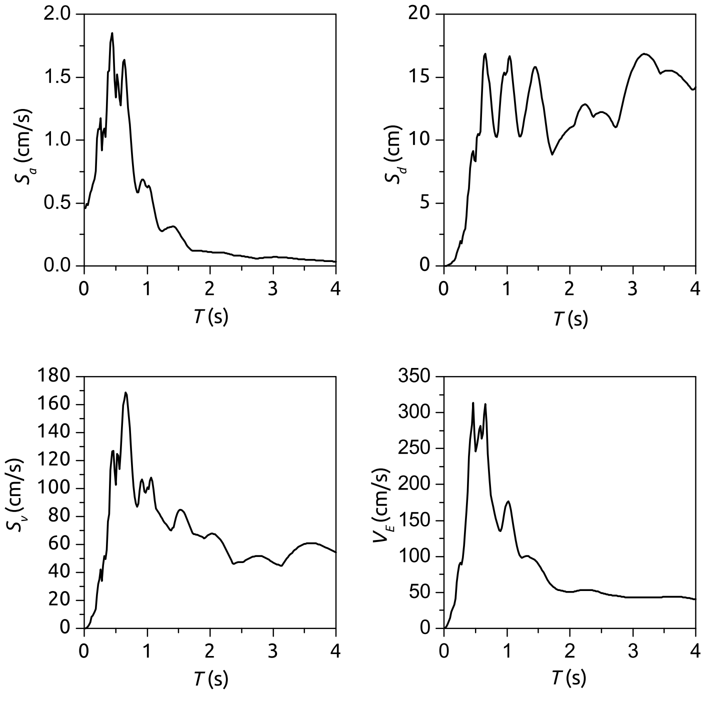

Figure A.12.: Elastic response spectra

A.7. Calitri

Earthquake	Station	Magnitud	Epicentral distance (km)	Fault distance (km)
Campano Lucano	Calitri	6.9	16	13

Table A.7.: Seismological parameters

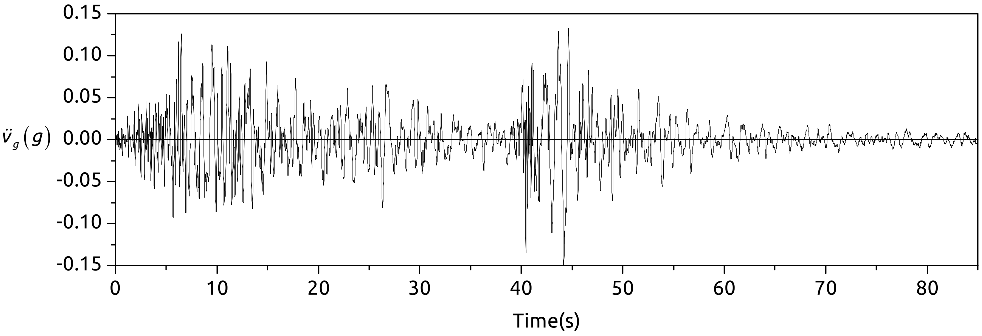

Figure A.13.: History of accelerations

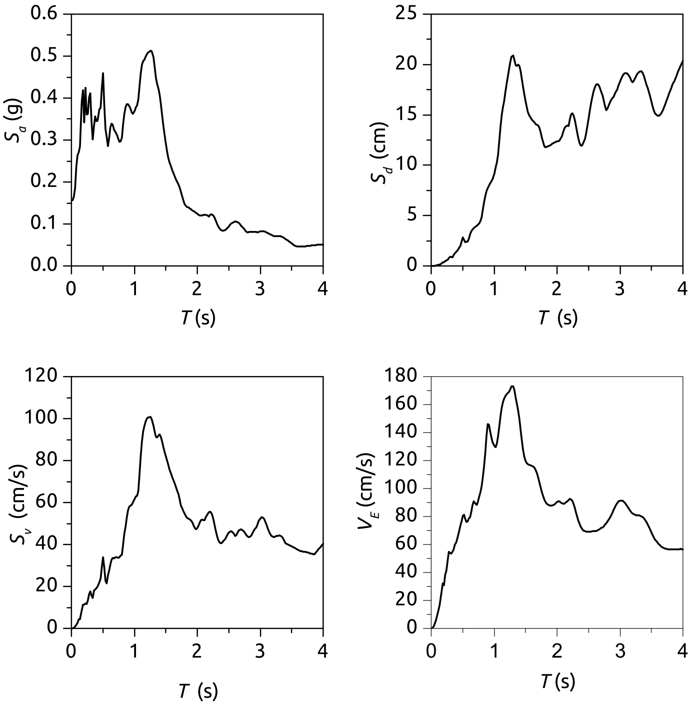

Figure A.14.: Elastic response spectra

A.8. Montebello

Earthquake	Station	Magnitud	Epicentral distance (km)	Fault distance (km)
Northridge	Montebello	6.4	46.3	43.1

Table A.8.: Seismological parameters

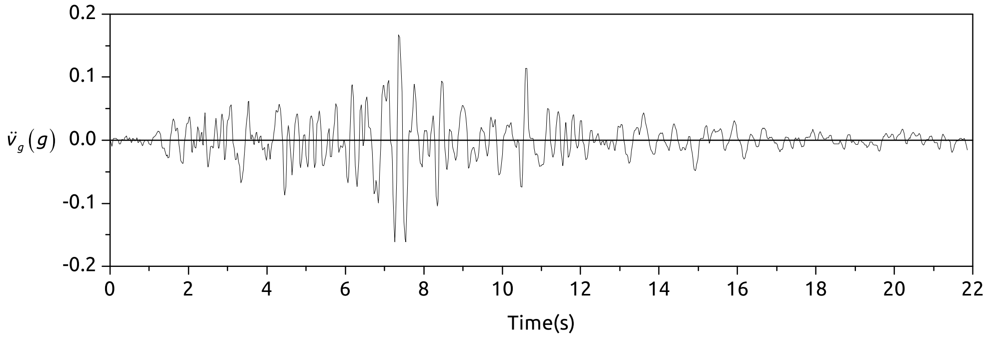

Figure A.15.: History of accelerations

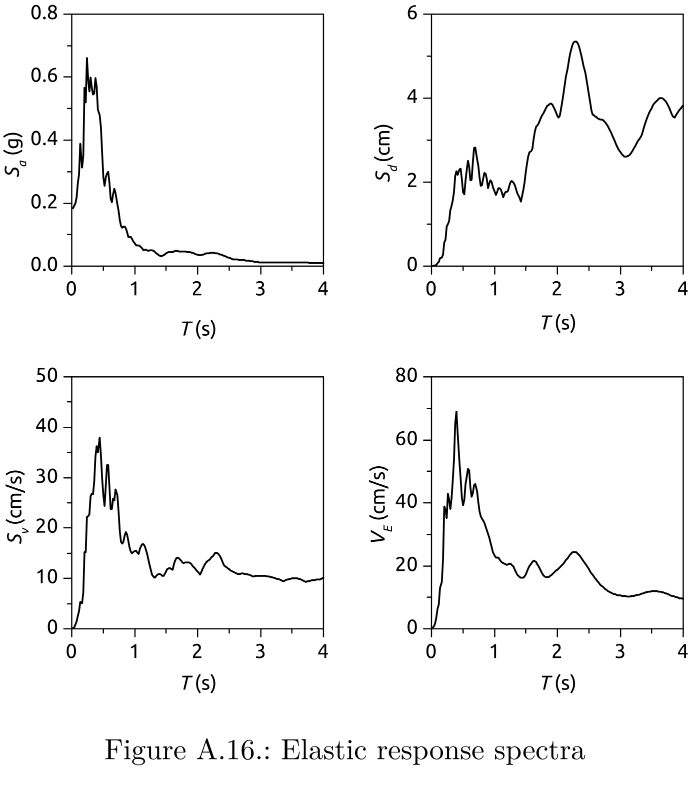

Figure A.16.: Elastic response spectra